Molecular Magnets in Nanoscopic Quantum Devices:

Theory & Experimental Comparisons

Ming-Yee Tsang

Supervisor:
Professor Lapo Bogani

University of Oxford
Department of Materials

Abstract

Quantum devices are quickly becoming the centrepiece of a novel generation of technological systems that could affect every aspect of our life, though we still do not understand how we may effectively interface molecular materials with nanoscopic quantum devices and control them. My aim in this thesis is to start exploring these issues, combining numerical and analytical theoretical methods to allow researchers to explore the properties of various molecular magnets, and predict and understand their behaviour when they are integrated into nanoscopic quantum devices. Maintaining a strong connection to real examples by considering specific molecular magnets, I cross-check the results with various characterisation techniques. I also consider commercially available molecular compounds and their possible practical use in actual quantum devices. In doing so, I also present and develop new methods of data analysis, to extend the information that can be extracted from experiments; throughout, I compare theory and experiments, corroborating the results. First, I mostly consider various compounds based on rare-earth metals, and deal with the challenges linked to numerically modelling the spin anisotropy of these systems. I demonstrate how careful treatment of the data can find the molecular anisotropy axes even in systems with high crystal symmetry. Moreover, I show how various methods allow us to predict the behaviour of single-molecule spin devices. Second, to investigate how the second-quantisation formalism impinges on the magnetisation's macroscopic dynamics, I consider a well-known, model spin system, Mn_{12}-acetate, and then explore in theory how we might expect a strongly coupled system to behave. Third and finally, I consider the theory of strongly coupled gadolinium-based systems, finding good agreement between experimental results and first-principles calculations, and explore what such systems could make possible for the future of quantum devices.

To my loving wife & unborn child

Contents

List of Initialisms vii

List of Symbols ix

List of Figures xii

List of Tables xiii

1 Motivation 1

2 Introductory concepts 6

2.1 Spin Hamiltonian 6

2.1.1 General theory 6

2.1.2 Spin Hamiltonians for rare-earths 13

2.1.3 How to calculate the parameters 15

2.2 Quantum coherence 19

2.3 Molecular magnetic materials 22

2.3.1 Quantum-coherence properties 22

2.3.2 Single-molecule magnets as quantum units 25

2.3.3 Properties of single-molecule magnets (SMMs) 27

2.4 Strong coupling 34

2.4.1 Second quantisation 34

2.4.2 The Hamiltonian 36

2.4.3 Experimental realisations 41

2.4.4 Spins in cavities . . . 43
2.5 Conclusion . . . 45

3 Methods 46

3.1 *Ab initio* methods . . . 46
3.1.1 Self-consistent field . . . 48
3.1.2 Configuration interaction . . . 54
3.1.3 Multi-configurational self-consistent field . . . 56
3.1.4 CASSCF . . . 57
3.1.5 RASSCF . . . 58
3.2 Comparison with other methods . . . 59
3.2.1 Density-functional theory (DFT) . . . 59
3.3 Spin Hamiltonian calculations . . . 60
3.3.1 Electron paramagnetic resonance (EPR) . . . 60
3.3.2 Crystal orientation and rotation . . . 61
3.4 Resolving experiment data . . . 61
3.5 Conclusions . . . 62

4 Determining magnetic anisotropy in rare-earth compounds 64

4.1 Overview . . . 64
4.2 Rare-earth compounds . . . 65
4.3 [Dy(dbm)$_3$phen] . . . 66
4.3.1 Ab initio calculations . . . 67
4.3.2 Analysing experimental magnetic data . . . 69
4.3.3 Classes of crystal symmetry . . . 73
4.4 Porphyrin complexes . . . 76
4.5 1-Dy . . . 77
4.5.1 Overview . . . 77
4.5.2 Ab initio calculations . . . 78
4.5.3 Comparison to transport measurements . . . 79

4.5.4 Simulation of magnetic-susceptibility measurements . 81
4.5.5 Calculation of dipolar coupling 84
4.6 1-Tb 86
4.6.1 Overview 86
4.6.2 Ab initio calculations 87
4.6.3 Simulation of torque-magnetometry experiments . . . 88
4.6.4 Simulation of SQUID measurements 91
4.7 Conclusion 95

5 Mn_{12}-acetate 97
5.1 Overview 97
5.2 Molecular properties 98
5.3 Magnetisation dynamics 99
5.4 The system 103
5.5 Photon-assisted tunnelling 107
5.6 Spin–photon hybrid bow-ties 111
5.7 Conclusion 118

6 Strong coupling of spin systems to light 120
6.1 Overview 120
6.2 [Gd(hfac)$_3$(^{t}Bubpy)] 122
6.2.1 Ab initio calculations 123
6.2.2 Q = 1 resonator at fixed orientation 124
6.2.3 EPR powder experiments in a low-Q resonator 126
6.2.4 High-Q resonator at different orientations 127
6.3 Gd-DOTA 139
6.3.1 Ab initio calculations 141
6.4 Conclusion 142

7 Conclusion 145

References **E.1**

A Tables **E.33**

A.1 General information E.33

A.2 Calculation results E.34

Glossary **E.39**

Acknowledgements **E.47**

List of Initialisms

BO Born–Oppenheimer

CASSCF complete-active-space self-consistent field

CFP crystal-field parameter

CI configuration interaction

DFT density-functional theory

EPR electron paramagnetic resonance

FWHM full width at half maximum

GNR graphene nanoribbon

HF Hartree–Fock

JCM Jaynes–Cummings model

MCSCF multi-configurational self-consistent field

QED quantum electrodynamics

QTM quantum tunnelling of the magnetisation

RASSCF restricted-active-space self-consistent field

RWA rotating-wave approximation

SCF self-consistent field

SIM single-ion magnet

SMM single-molecule magnet

SQUID superconducting quantum-interference device

ZFS zero-field splitting

List of Symbols

B Magnetic field

C Cooperativity

C Curie constant

D Axial anisotropy

E Rhombic anisotropy

$\Gamma_m^{m'}$ Incoherent-tunnelling rate

g Landé g factor (or related tensor, etc.)

h Planck's constant

$\hbar$ Reduced Planck's constant

J Total angular momentum

k_B Boltzmann constant

M Magnetisation

μ_o Permittivity of free space

μ_B Bohr magneton

m_S Total spin quantum number

N Number of molecules (sometimes per unit volume)

O_k^q Stevens operator

ψ Angle between molecular and crystal easy axes

Q Quality factor of a resonator cavity

S Total spin

S_{21} Transmittance in a resonator-cavity experiment

T Temperature

τ Relaxation time

τ Torque

ω Angular frequency

χ Magnetic susceptibility

ζ Ratio of susceptibilities, $\chi_{y'y'}/\chi_{z'z'}$

List of Figures

2.1 The Bloch sphere 20
2.2 $\Re(\chi), \Im(\chi)$ vs $\omega\tau$ 29
2.3 Magnetic relaxation 32
2.4 Avoided level crossing 33
2.5 Quantum tunnelling of the magnetisation in $Mn_{12}Ac$ 33
2.6 A schematic of a spin coupled to a cavity resonator 42

3.1 Configuration interaction in He 55
3.2 Orbital spaces of CASSCF 57
3.3 Orbital spaces and subspaces of RASSCF 59
3.4 A schematic of a transmission experiment 62

4.1 The unit cell in the [Dy(dbm)$_3$phen] crystal 66
4.2 Magnetic easy axis of [Dy(dbm)$_3$phen] 67
4.3 Dy(dbm)$_3$phen magnetic measurement data 72
4.4 Calculated angle ψ vs ζ, λ in Dy(dbm)$_3$phen 72
4.5 Calculated angle ψ vs ζ for some λ values in Dy(dbm)$_3$phen 73
4.6 Lanthanide–porphyrin compounds considered in this thesis 76
4.7 The unit cell in the 1-Dy crystal 77
4.8 Anisotropy of the 1-Dy molecule 78
4.9 Synthesis and setup of a 1-Dy nanodevice 79
4.10 Transport measurements of a 1-Dy nanodevice 80
4.11 Angular relation to single-ion anisotropy in 1-Dy 81

4.12 $\chi_m T$ vs temperature in 1-Dy powder 85
4.13 A dimerised lanthanide–porphyrin compound 85
4.14 The unit cell in the 1-Tb crystal 87
4.15 Anisotropy of the 1-Tb molecule 87
4.16 Orientation of the 1-Tb crystal in torque experiments 88
4.17 Torque vs angle in the $\hat{a}\hat{b}$-plane of the 1-Tb crystal 90
4.18 Torque vs angle in the $\hat{b}\hat{c}$-plane of the 1-Tb crystal 90
4.19 "Torque surface" in the 1-Tb crystal 91
4.20 Magnetisation vs magnetic field in 1-Tb 92
4.21 $\chi_m T$ vs temperature in 1-Tb crystal 93
4.22 $\chi_m T$ vs temperature in 1-Tb powder 94

5.1 The molecular structure of the Mn_{12} archetype 100
5.2 Double-well potential shift due to magnetic field 101
5.3 Finite-size simulation of on-chip resonator 105
5.4 Schematic of a Hall-bar setup to measure magnetisation 106
5.5 Schematic of photon-assisted tunnelling 110
5.6 Energy gap $E^{½}_{m,-m}$ vs coupling strength Ω in $Mn_{12}Ac$ 111
5.7 Tunnelling rate Γ_9^{-9} vs coupling strength Ω in $Mn_{12}Ac$ 111
5.8 Transition probabilities near a bow-tie crossing 114
5.9 Prediction of a polariton at zero field in $Mn_{12}Ac$ 115
5.10 Energy-level shifts vs δH at small detunings 116

6.1 Q-factor regimes 121
6.2 The unit cell in the $Gd(hfac)_3(^t Bubpy)$ crystal 122
6.3 $Gd(hfac)_3(^t Bubpy)$ lab axes in crystallographic frame 123
6.4 Data–calculation comparison in low-Q experiment 124
6.5 Prediction of low-Q transmission experiment 125
6.6 Prediction of and EPR data from a powder experiment 126
6.7 Transmission measurements along various directions 130

6.8 A single transition measurement 131
6.9 $S_{21}(\omega)$ full width at half maximum (FWHM) fit 133
6.10 Schematic of data treatment in transmission experiments 134
6.11 S_{21} fitting at various temperatures 135
6.12 Estimating crossing points by Newton's method 136
6.13 Data–calculation comparison of transition lines 137
6.14 Comparison of data to high-Q-experiment predictions 138
6.15 The unit cell in the Gd-DOTA crystal 140
6.16 Rotation of Gd-DOTA strongly coupled to a resonator 141

List of Tables

6.1 EPR powder-experiment features 128

A.1 Stevens operators in terms of S_z, $S_\pm$ E.33
A.2 Overview of the lanthanides E.34
A.3 Calculated Stevens coefficients in $Gd(hfac)_3(^tBubpy)$ E.35
A.4 Calculated Stevens coefficients in $Dy(dbm)_3phen$ E.36
A.5 Calculated Stevens coefficients in 1-Tb E.37
A.6 Calculated Stevens coefficients in 1-Dy E.38

1 Motivation

This thesis aims to better understand zero-dimensional magnetic systems from a theoretical perspective, and how they can be incorporated into quantum devices. To this end, I shall use a mixture of numerical computational methods and, to a lesser degree, pen-and-paper theory. These tools are then used to analyse datasets from magnetic measurements, and in some cases, to show how detailed information can be extracted well beyond what current, state-of-the-art data treatments are capable of.[1] Specific attention will be given throughout the whole thesis to considering not abstract objects or abstract spin centres, but rather real systems and real complex compounds that can be synthesised. Whenever possible, direct comparison will be made to datasets and previous reports, in order to keep the discussion grounded on experimentally relevant problems.

To further this experimentally driven direction, a specific focus of this thesis is the anisotropy of rare-earth magnets, which have seen growing applicability and increasing interest over the past few decades. On the other hand, there are specific and important challenges that hamper their numerical modelling. In this thesis, I will show how the behaviour of molecular systems based on rare-earth metals can be modelled accurately in order to reproduce or predict the response of hybrid quantum devices of very different kinds. I will start by considering the spin response of electronic-transport nanodevices, where a single molecule is placed between two electrodes. Using a second-quantisation approach, I will then move on to

predicting and explaining the behaviour of the strongly coupled system composed of rare-earth-based molecules and microwave cavity resonators.

My calculations also shed light on many properties of zero-dimensional systems that cannot easily be extracted from measurements, such as anisotropic terms with weaker effects, but which may still be very relevant for proper function in quantum devices. In some cases, I directly dealt with the problem of how to extract hidden information from careful examination of datasets obtained using various experimental techniques, such as angle-resolved magnetometry. Understanding magnetic systems, not only through their observable interactions in experimental setups, but also from first-principles calculations based on their chemical structure, allows us to better make sense of these magnets and design them for specific needs or to address specific problems.

The relevance of the results obtained in this thesis is thus rather broad, and touches several areas of fundamental research and prospective technological advancement. Since the 1980s, the development of increasingly smaller silicon semiconductor devices has increased the limit of what is computationally possible.[2] While the trajectory of transistor sizes has thus far followed Moore's law, periodically decreasing in size exponentially, because of their small size currently, quantum mechanical effects are becoming increasingly prominent, making it difficult to make them any smaller using silicon.[3]

What happens when a spin centre is placed inside these very small conducting elements is thus an area of very active research,[4–7] and molecular materials offer a potential alternative to the ubiquitous silicon,[8–10] particularly at the nanometre to sub-nanometre scale. At this scale, it is electron spin that governs the behaviour of devices and materials, and the quantum-mechanical effects of the spin centres can become apparent in macroscopic observables, such as the current.

These two facts – first, that electron spin governs behaviour, and second, that we can observe spin centres' effects macroscopically – have given rise to the field of molecular spintronics, which aims to create molecular electronic devices through precise control of these spin centres.[11] Single-molecule magnets (SMMs) are metal-organic compounds containing metal centres that behave as atomic magnets below a certain temperature, called the blocking temperature.[12] This magnetism comes from the angular momentum of unpaired electrons within the individual molecules, wherefore the metallic cores are aptly called spin centres. SMMs are especially versatile because their physical properties depend on the spin centres and surrounding ligands, which may be chemically adjusted.[13] Thus, one can control their magnetic properties using not only magnetic fields or temperature,[14] but also electric fields,[11], pressure,[15] and even visible light.[16, 17] Interaction with the SMMs, however, can sometimes lead to compound degradation or loss of SMM behaviour,[4, 18] so the development of robust SMMs is necessary. These weaknesses are especially prominent with electrical manipulation, which interacts with the electronic environment of SMMs. By contrast, using light as an external stimulus is particularly promising because it is clean and fast, directly interacting with electron spins, without affecting the external environment, which requires less robustness in the SMMs. This direct interaction with spins may also be a way to perform quantum logic operations, and indeed implementations of quantum algorithms have been proposed in SMMs.[14] The vast assortment of SMMs gives innumerable possibilities, which makes them a good choice for new molecular spintronic devices and observation of new light–matter coupling effects at low temperatures. As such, strongly coupling light to molecular magnetic materials gives another promising molecular quantum unit. Unlike merely interacting light with molecular magnetic materials, in the strong-coupling regime, molecular magnetic materials

form new states of matter entirely, so that the system cannot be treated as two independent subsystems, but one bound light–matter system. This is particularly promising in light of recent research on cavity resonators, such as the development of tunable, open-access microcavities, in which strong coupling effects such as polaritons have been observed.[19–21] Such microcavities have also been strongly coupled with nanographene,[22] and might also be strongly coupled to complex nanodevices to create more complex quantum systems.

In this thesis I consider two things: first, strong coupling to SMMs, and in particular how the light–matter quantum effects lead to macroscopic dynamical phenomena in these systems; second, strong coupling to molecular magnetic materials without a large magnetic anisotropy, which do not display the same slow-relaxing, macroscopic, dynamical effects, but can still provide a large Hilbert space, and thus might be effectively coupled to existing superconducting resonators. For this latter scheme, which was also implemented experimentally in the laboratory, I also developed the full data treatment of the results obtained by my colleagues, and the results are currently confidential, being at the core of a patent application for which large quantum-computing companies are expressing interest.

The thesis is structured in five chapters, aside from this introduction and the conclusion. I begin with a theoretical framework to understand the systems of interest, and this framework is then used throughout the thesis to discuss the salient properties of model molecular magnets and how to model them using a spin Hamiltonian. I then discuss how to calculate magnetic anisotropy from first principles, starting from the crystal structure, and the advantages and disadvantages of different methods, with particular attention to the challenges posed by rare-earth elements and their complexes, which are still an active area of computational research. I go on to show how the magnetic anisotropy of several of these systems

can be modelled, and compare the results to those of bulk magnetic measurements, and the quantum-transport behaviour of nanoscale devices at low temperature. I demonstrate how non-trivial data treatment can extract information that, until now, were not obtainable experimentally. Thereafter, I delve into a different class of quantum systems and a way of directly interfacing quantum molecular spin systems with nanoscale quantum devices, by considering the inclusion of molecular magnetic materials into resonators that are capable of strong-coupling effects. I first analyse the effects of strong coupling of light with SMMs, and how the Hamiltonian must be adjusted to model the entire light–matter system, to produce a different type of dynamical feature in the spin behaviour. I then move to molecular magnetic materials with low anisotropy included into fully quantum devices, for which I developed a full data treatment to compare predictions from first principles with experimental data, considering both second quantisation of the magnetic field and strong coupling. The appendix includes general information for understanding rare-earths and my results from first-principles calculations.

2 Introductory concepts

2.1 Spin Hamiltonian

2.1.1 *General theory and background*

The spin Hamiltonian is a phenomenological Hamiltonian used to interpret, classify, and predict spin systems without using fundamental theories: Researchers take advantage of symmetry properties of spin systems to eliminate orbital coordinates and replace them with spin coordinates.[23]

Using this model, we consider a magnetic centre with n unpaired electrons and thus total spin $S = n/2$. The $2S + 1$ spin levels of this multiplet will be split by their interactions with both each other and with an applied magnetic field. The former is called the crystal-field Hamiltonian, and the latter the Zeeman Hamiltonian. In general, the spin Hamiltonian may be given by

$$H_S = H_Z + H_{CF} + H_J + H_D + H_{HF} + H_{NQ} + H_{NZ}, \tag{2.1}$$

where H_Z is the Zeeman Hamiltonian, H_{CF} is the crystal-field Hamiltonian, H_J is the exchange-coupling Hamiltonian, H_D is the magnetic-dipole-coupling Hamiltonian, H_{HF} is the hyperfine-coupling Hamiltonian, H_{NQ}

is the nuclear-quadrupole Hamiltonian, and H_{NZ} is the nuclear-Zeeman Hamiltonian.

The Zeeman Hamiltonian describes the interaction of a spin $\vec{S}$ (the magnetic centre in this case) with a magnetic field $\vec{B}$, according to

$$H_{\mathrm{Z}} = \mu_B \vec{S} \cdot \bar{\bar{g}} \cdot \vec{B}, \tag{2.2}$$

where μ_B is the Bohr magneton, and $\bar{\bar{g}}$ is the second-rank, so-called g tensor describing the interaction of the spin with field. This tensor is related to the intrinsic spin angular momentum of a free electron, $g_e \approx 2.00232$. Despite the fact that the ground state of most molecules has zero orbital angular momentum, the g tensor is not simply the constant g_e because of admixing between the ground state and excited states as a result of spin–orbit coupling. The spin–orbit coupling does not need to be considered explicitly here, however, since its effects on Zeeman splitting can be represented by an anisotropic g tensor.[24]

A spin operator $\hat{S}$ may be expressed in terms of its Hermitian, Cartesian-component operators, $\hat{S}_x, \hat{S}_y, \hat{S}_z$. In spin-½ particles, these are the familiar Pauli spin matrices, whose (dimensionless) matrix forms are

$$\hat{\sigma}_x = \frac{1}{2}\begin{pmatrix} 0 & 1 \\ 1 & 0 \end{pmatrix}, \hat{\sigma}_y = \frac{1}{2}\begin{pmatrix} 0 & -i \\ i & 0 \end{pmatrix}, \hat{\sigma}_z = \frac{1}{2}\begin{pmatrix} 1 & 0 \\ 0 & -1 \end{pmatrix}.$$

The three are related by the commutation relations $[\hat{\sigma}_x, \hat{\sigma}_y] = i\hat{\sigma}_z$, $[\hat{\sigma}_y, \hat{\sigma}_z] = i\hat{\sigma}_x$, and $[\hat{\sigma}_z, \hat{\sigma}_x] = i\hat{\sigma}_y$, and all three spin matrices commute with the operator $\hat{\sigma}^2 = \hat{\sigma}_x^2 + \hat{\sigma}_y^2 + \hat{\sigma}_z^2$. It may therefore be simultaneously diagonalised with $\hat{\sigma}_z$, which defines a spherical basis, such that a complete set of kets is given by

$$\begin{aligned} \hat{\sigma}^2 |\pm\rangle &= |\pm\rangle, \\ \hat{\sigma}_z |\pm\rangle &= \pm |\pm\rangle. \end{aligned}$$

It is convenient also to define $\hat{\sigma}_\pm = \hat{\sigma}_x \pm i\hat{\sigma}_y$, which satisfy

$$\hat{\sigma}_\pm |\pm\rangle = C_\pm |\mp\rangle ,$$

for some constants $C_\pm$. These relate the two spinors explicitly with each other, which allows us to describe their interactions more directly. Simple algebra yields $C_\pm = 1$.

For higher-order spin operators, we retain the commutation relations and the property that $\hat{S}^2 = \hat{S}_x^2 + \hat{S}_y^2 + \hat{S}_z^2$ commutes with the three Cartesian-component operators. Again, $\hat{S}^2$ may be simultaneously diagonalised with $\hat{S}_z$, so that the complete set of kets is given by

$$\begin{aligned} \hat{\sigma}^2 |S, m_S\rangle &= S(S+1) |S, m_S\rangle , \\ \hat{\sigma}_z |S, m_S\rangle &= m_S |S, m_S\rangle . \end{aligned}$$

The form of $\hat{S}_z$ may be found using

$$(\hat{S}_z)_{ij} = \langle S, i|\hat{S}_z|S, j\rangle ,$$

where i, j are integers such that $-S \leq i, j \leq S$. Since $|S, m_S\rangle$ states are orthonormal, this yields,

$$(\hat{S}_z)_{ij} = i\delta_{ij},$$

where δ_{ij} is the Kronecker delta function, which defines a diagonal matrix, whose elements are its eigenvalues, $m_S = -S, -(S-1), \ldots, (S-1), S$. We again can define $\hat{S}_\pm$ to relate $|m\rangle$ to its neighbouring state $|m \pm 1\rangle$ through (non-Hermitian) ladder operators $\hat{S}_\pm = \hat{S}_x \pm i\hat{S}_y$:

$$\hat{S}_\pm |S, m_S\rangle = C_\pm |S, m_S \pm 1\rangle .$$

To find $C_\pm$, we consider the products of the ladder operators:

$$\hat{S}_\pm \hat{S}_\mp = (\hat{S}_x \pm i\hat{S}_y)(\hat{S}_x \mp i\hat{S}_y) = \hat{S}_x^2 + \hat{S}_y^2 \mp i[\hat{S}_x, \hat{S}_y] = (\hat{S}^2 - \hat{S}_z^2) \pm \hat{S}_z,$$

which allows us to express $C_\pm$ in terms of eigenvalues of $\hat{S}^2$ and $\hat{S}_z$ (the phases of $C_\pm$ are not physically significant, so we choose them to be positive and real, according to the Condon–Shortley phase convention):

$$C_\pm = S(S+1) - m_S^2 \pm m_S = S(S+1) - m_S(m_S \pm 1).$$

Hence,

$$\begin{aligned} \hat{S}_+ |S, m_S\rangle &= \sqrt{S(S+1) - m(m+1)}\, |S, m+1\rangle\,, \\ \hat{S}_- |S, m_S\rangle &= \sqrt{S(S+1) - m(m-1)}\, |S, m-1\rangle\,. \end{aligned} \tag{2.3}$$

With the spin operators established, we can formulate the Hamiltonian of the bound ion. Letting H_o be the Hamiltonian of the free ion, we assume the Hamiltonian of the bound ion to be of the form $H = H_o + V$, where V is an electrostatic potential that both satisfies the Laplace equation $\delta V = 0$ and has the symmetry of the surroundings of the ion. We can then expand V as a multipolar expansion in terms spherical coordinates, giving a sum of spherical harmonics:

$$V = \sum_{k=0}^{\infty} \sum_{q=-k}^{k} B_k^q r^k Y_k^q(\theta, \varphi),$$

where $Y_k^{-q} = (-1)^q Y_k^{q*}$. The orbital coordinates θ, φ may then be eliminated by expressing Y_k^q in Cartesian coordinates and replacing x, y, z with the spin operators $\hat{S}_x, \hat{S}_y, \hat{S}_z$, after which $\hat{S}_x, \hat{S}_y$ may be replaced with $\hat{S}_\pm$ using the property $\hat{S}_\pm = \hat{S}_x \pm i\hat{S}_y$. These give the Stevens-operator equivalents $\hat{O}_k^q$:

$$H_{\mathrm{CF}} = \sum_{k} \sum_{q=-k}^{k} B_k^q \hat{O}_k^q.$$

A table of the $k = 2, 4, 6$ Stevens operators is given in the Appendix (Table A.1).

The $\hat{O}_0^0$ term is always excluded, because it is isotropic and therefore does not contribute to the multiplet splitting. Relative to crystal-field effects, the magnitude of spin–orbit coupling is quite small for transition-metal

elements, but for lanthanides, its effects are non-negligible and cannot be ignored. The summands are components of irreducible tensors of rank k, whose matrix elements within a d^N (f^N) configuration with pure d (f) orbitals vanish for $k > 4$ ($k > 6$). Accordingly, for d multiplets $k > 4$ terms may be excluded from the sum, and for f multiplets, $k > 6$ terms may be excluded. Additionally, odd values of k describe the spectral intensity of induced electric-dipole transitions[25] and not the crystal-field splitting that we are ultimately interested in, and can be excluded by the requirement that the Hamiltonian have time-inversion invariance. Thus, for $3d^N$ ions, the non-zero elements are limited to $k = 2, 4$, and for trivalent lanthanide ($4f^N$) ions, the non-zero elements are limited to $k = 2, 4, 6$. Which values of q are non-zero depends on the point-group symmetry; for instance, for tetragonal symmetry, the only non-zero B_4^q are $q = 0, \pm 4$. Considering only the Zeeman and crystal-field Hamiltonians in Eq. (2.1), we then have

$$H(\vec{B}) = \sum_{k=2,\,4,\,6} \sum_{q=-k}^{k} B_k^q \hat{O}_k^q + g\mu_B \hat{S}\vec{B} \tag{2.4}$$

For simplicity, let us first consider only the second-order interactions in zero field. The crystal-field Hamiltonian may then be expressed in the simpler form,

$$H = \hat{S} \cdot \bar{\bar{D}} \cdot \hat{S},$$

where $\hat{S}$ is the total-spin operator and $\bar{\bar{D}}$ is a real, symmetric tensor. Because $\bar{\bar{D}}$ is real and symmetric, it must have three orthogonal eigenvectors, whereby it can be diagonalised into a basis such that

$$H = D_{xx}\hat{S}_x^2 + D_{yy}\hat{S}_y^2 + D_{zz}\hat{S}_z^2,$$

where $\hat{S}_x, \hat{S}_y, \hat{S}_z$ are the x, y, z components of $\bar{\bar{S}}$ in the eigenbasis of $\bar{\bar{D}}$. Because the physical properties of a system are dependent only on relative differences in energy, constants may be added or subtracted to the Hamil-

tonian without affecting its descriptive power. It is convenient, therefore, to subtract $\frac{1}{2}(D_{xx}+D_{yy})\bar{\hat{S}}(\bar{\hat{S}}+1) = \frac{1}{2}(D_{xx}+D_{yy})(\hat{S}_x^2+\hat{S}_y^2+\hat{S}_z^2)$, giving

$$H = D\hat{S}_z^2 + E(\hat{S}_x^2 - \hat{S}_y^2) = D\hat{S}_z^2 + \frac{E}{2}(\hat{S}_+^2 + \hat{S}_-^2), \tag{2.5}$$

where $D = D_{zz} - (D_{xx}-D_{yy})/2$ and $E = (D_{xx}-D_{yy})/2$. In this form, we see that in cubic symmetry, $D = 0$ because $D_{xx} = D_{yy} = D_{zz}$, and in axial symmetry, $D_{xx} = D_{yy}$ so that $E = 0$. The energies of the spin states of the system are split even at zero field according to the value of D (so-called zero-field splitting (ZFS)), and a non-zero value of E lifts the degeneracies between pairs of $|\pm m\rangle$ states if S is an integer. The value of D can be either positive or negative. If $D > 0$, the levels with lowest $|m|$ are ground states, giving easy-plane anisotropy; if $D < 0$, the levels with highest $|m|$ are ground states, giving easy-axis anisotropy. For this reason, D and E are respectively called the axial- and rhombic-anisotropy parameters. It is, however, conventional to subtract the constant $DS(S+1)/3$ from Eq. (2.5), giving

$$H = D\left[\hat{S}_z^2 - \frac{1}{3}S(S+1)\right] + \frac{E}{2}(\hat{S}_x^2 - \hat{S}_y^2), \tag{2.6}$$

which has the advantage that H is traceless, to physically correspond to the (traceless) second-order V term,

$$V = \sum(3z^2 - r^2).$$

Notably, the Eq. (2.6) may then equivalently be expressed

$$H = \frac{D}{3}\hat{O}_2^0 + E\hat{O}_2^2,$$

So the second-order interactions are sufficiently described by the Stevens operators with $k = 2$ (that is, O_2^q), and D and E are related to the coefficients B_2^q by $D = 3B_2^0$ and $E = B_2^2$. (Similarly, the cubic parameter a and fourth-order parameter F is related by $a = 24B_4^4, F = 180B_4^0 - 36B_4^4$.)[23]

In larger spin centres especially, it is important to consider the total angular momentum $\vec{J}$ of the system as well, defined as

$$\vec{J} = \vec{L} + \vec{S},$$

where $\vec{L}$ is the orbital angular momentum. Taking the dot product of this with itself, we obtain

$$\vec{J}^2 = \vec{L}^2 + \vec{S}^2 + 2\vec{L} \cdot \vec{S},$$

since $\vec{L}$ and $\vec{S}$ commute. The term $2\vec{L} \cdot \vec{S}$ is called the spin–orbit coupling. Relative to crystal-field effects, the magnitude of this coupling is quite small for transition-metal elements, but for lanthanides, its effects are non-negligible and cannot be ignored.

In situations where metal centres are not sufficiently magnetically shielded from one another, such as in molecules with multiple magnetic centres, the magnetic-dipole coupling may significantly contribute to Eq. (2.1), and its Hamiltonian is given by

$$H_D = \sum_{i \neq j} \hat{S}_i \bar{\bar{D}}_{ij} \hat{S}_j,$$

where the tensor $\bar{\bar{D}}_{ij}$ is the dipolar coupling between spins i and j with total-spin operators $\hat{S}_i$ and $\hat{S}_j$, respectively.

The hyperfine interaction, $H_{\mathrm{HF}} = \sum_i \vec{S} \cdot \bar{\bar{A}}_i \cdot \vec{I}_i$, is a very weak interaction compared to previously mentioned ones. It describes the magnetic dipole–dipole interactions between nuclear spins $\vec{I}_i$ and the spin of the system $\vec{S}$. The energy splittings due to hyperfine interaction are orders of magnitude smaller than those due to spin–orbit coupling, so they are neglected in this thesis. Nuclear quadrupole interactions, $H_{\mathrm{NQ}} = \sum_{i \neq j} \vec{I}_i \cdot \bar{\bar{P}}_{ij} \cdot \vec{I}_j$, arise only between nuclear spins of $I \geq 1$, which does not apply here, so this term may also be neglected. The nuclear Zeeman effect, described by $H_{\mathrm{NZ}} = \sum_i \mu_n g_{n,i} \vec{B} \cdot \vec{I}_i$ has $g_{n,i}$ values several orders of magnitude smaller

than the g value associated with H_Z, so it likewise will be neglected in this thesis.

2.1.2 *Spin Hamiltonians for rare-earths*

Spin systems based on lanthanides differ significantly in their electronic properties from the spin systems based on their transition-metal cousins. Their fully occupied 5s and 5p orbitals electrostatically shield the 4f electrons, making the effects from both the environment and coordinated ligands far smaller than the system's spin–orbit coupling, though some recent research has observed and quantified covalency and suggested it may have some role in determining magnetic properties of lanthanide complexes,[26, 27] though certainly the effect is less prominent than in transition-metal complexes. In cases where ignoring covalency does not accurately model the system, then this approximation would not be appropriate and covalent effects would then be considered as well. Hence, we take electronic transitions in lanthanide complexes to be essentially unaffected by their ligand environments, and the crystal fields generated by the ligands can be considered based on how they split the ground-state of the total angular momentum J into spin–orbit multiplets. The total angular momentum comes from unpaired 4f electrons of the compounds, and the strong spin–orbit coupling in lanthanides makes their magnetism strongly anisotropic. So the nature of the anisotropy, because it is governed by the splitting of the m_J sublevels, depends on the ligands coordinated to the lanthanide ion. Since the 5d and 6s orbitals participate the most in the mixing, one can safely neglect the mixing of f orbitals with ligand orbitals using crystal-field theory to calculate the m_J sublevels,[28, 29] since the outer shells electrostatically shield the f orbitals.

Equations (2.1), (2.2), and (2.3) are not good descriptions for lanthanides, however, because S is no longer a good quantum number. They

may, however, be recycled using J as the quantum number: for instance, Eq. (2.2) becomes

$$H_Z = \mu_B \vec{J} \cdot \bar{\bar{g}} \cdot \vec{B}, \tag{2.7}$$

where $\vec{J}$ is the total angular momentum.

The 4f electrons of the lanthanides are responsible for their different, individual properties. It is sometimes also useful to consider the other rare-earths, scandium, yttrium, and lanthanum, whose electron configurations are similar, lacking only the 4f electrons. In particular, they will share the properties of the lanthanides that do not depend specifically on the 4f electrons. The lanthanides have electron configurations of the form $[Xe]4f^n5d^16s^2$, which form trivalent compounds in solid form. Because 4f orbitals are internal, and hence mostly shielded by outer shells and not involved in bonding to ligands, the trivalent oxidation state is extremely stable, and magnetic exchange between 4f ions is often weak. In some cases, the magnetic exchange can be stronger, such as with an N_2^{3-} radical bridge[30] or certain more spherical f-electron densities,[31] but neither situation applies to the systems considered in this thesis.

In principle, crystal-field theory models the way in which ligands influence the splitting of d or f orbitals in metals. Ligand-field theory carries this model further by incorporating molecular-orbital theory, in essence considering covalent interactions between the metal and the ligands. Crystal-field theory was first proposed by Bethe[32] and Van Vleck[33] for d orbitals in transition-metal complexes, by considering interactions between metals and ligands in these complexes as purely electrostatic.[32, 34] Racah and Stevens then applied the Wigner–Eckart theorem to extend the theory to the many-electron case.[35, 36] Subsequently others extended the model to the f elements.[37] Thus, whereas in transition-metal complexes, the ZFS is induced by spin–orbit coupling with excited states,[38] in the f elements

it arises from the splitting of the lanthanide ion's ground J multiplet by the ligands and can be characterised by the crystal-field parameters (CFPs).

Thus, one may accurately model the behaviour of the m_J sublevels according to crystal-field theory using the spin Hamiltonian (Eq. (2.4)) with a $\hat{J}$ operator (and its projections) in place of the $\hat{S}$ operator. (For convenience, however, we will still denote the $\hat{J}$ operator with $\hat{S}$.) This method is useful because the spin Hamiltonian is a very simple model for how powerful it is, and magnetic behaviour of a complex may be easily described by calculated CFPs.

2.1.3 *How to calculate the parameters*

When the symmetry of the lanthanide complex is sufficiently high, the number of CFPs is reduced, so that they might be estimated phenomenologically by fitting to experimental data, such as from optical experiments.[25] If the complex has octahedral symmetry, for instance, only two CFPs are non-zero, and they can easily be estimated by calculating energies of the spin states and fitting to experimental data.[39] In the worst case, however, the complex may have no symmetries, so that the ZFS is governed by 27 independent parameters. In such cases, the fitting procedure becomes over-parameterised, so that several different sets of fitted parameters may be equally valid, thereby invalidating the entire derivation. In practice, at most only four or five parameters can be extracted by fitting magnetic and spectroscopic experimental data.[40–45] Hence, the CFPs must be determined by some other methods.

The first theoretical calculations in chemistry were by Walter Heitler and Fritz London in 1927, using valence-bond theory.[46] Important work by Linus Pauling and E. Bright Wilson,[47] Eyring, Walter, and Kimball,[48] Heitler,[49] and later Coulson[50] set the stage for decades to come in the early development of computational quantum chemistry.

A molecular formula represents a set of isomers, with each isomer being a local minimum on the potential-energy surface as a function of the coordinates of all the nuclei. A stationary point is a geometry such that the derivative of the energy with respect to all displacements of the nuclei is zero. This process of determining stationary points is called geometry optimisation. The determination of molecular structure by geometry optimisation became routine only after efficient methods for calculating the first derivatives of the energy with respect to all atomic coordinates became available. The total energy is determined by approximate solutions of the time-dependent Schrödinger equation, usually without relativistic effects, further simplified by separating electronic and nuclear motions using the Born–Oppenheimer (BO) approximation. The total energy is then evaluated as the sum of electronic energy at fixed nucleus positions and the repulsion energy of the nuclei.

Researchers have used various methods in the past to make predictions on lanthanide compounds, including density-functional theory (DFT)[51] and multireference methods,[52] which attempted to parameterise the lanthanide's entire energy spectrum. Later methods have focused on accurately predicting the crystal field that describes the splitting of the ground J multiplet.[53] These will be discussed in more technical depth in Chapter 3. Two of the central methods in dealing with lanthanide complexes now are complete-active-space self-consistent field (CASSCF) and restricted-active-space state interaction (RASSI) with spin–orbit coupling. These methods are able to predict energy levels and, with assistance from the other calculation libraries, also g-factors, CFPs, and other relevant quantities. They have made accurate predictions in many single-molecule magnets (SMMs) during the past decade.[54–60]

Semi-empirical quantum chemistry methods are based on the Hartree–Fock (HF) formalism, but use approximations and parameters from

empirical data to account for things such as correlation effects. They were very important in computational chemistry from the 1960s to the 1990s, especially for treating large molecules where the full HF method without the approximations were computationally too costly.

Methods that do not use any parameters derived from experimental data in their equations, but are derived only from theoretical principles, are called *ab initio* methods. This does not, however, mean that *ab initio* solutions are exact: they are still approximate quantum-mechanical calculations. But the approximations are rigorously defined on first principles and then solved within an error margin decided by the researcher.

The simplest type of *ab initio* electronic-structure calculation is the HF method, in which the correlated electron–electron repulsion is accounted for only by its average effect (see Section 3.1.1). The HF wavefunction, however, is a single configuration or determinant, and in some cases this is inadequate. Several configurations, then, must be considered, and both their coefficients and those of the basis functions are simultaneously optimised. As the basis-set size increases, the calculations tend toward the so-called HF limit. Many types of calculations (termed post-HF methods) begin with a HF calculation and subsequently correct for electron–electron repulsion, referred to also as electronic correlation. These methods approach the exact solution of the non-relativistic Schrödinger equation, but to obtain better agreement with experiment, it is necessary to include relativistic and spin-orbit effects, both of which are important for heavy atoms. In all of these approaches, researchers must also choose a basis set. This is a set of functions, usually centred on the different atoms in the molecule, which are used to expand the molecular orbitals with the linear combination of atomic orbitals (LCAO) molecular-orbital-method *ansatz*. *Ab initio* methods thus need to define both the choice of method and a basis set. A related class of methods, semi-empirical methods, build on *ab*

initio methods, making assumptions to further simplify models and taking parameters from empirical data.

There are several advantages to using *ab initio* calculations: (1) covalent effects can be taken into account, (2) all CFPs can be determined, even in cases of low symmetry, (3) the accuracy of crystal-field theory to modelling spectra can be assessed. Though the interaction between f-element ions and their coordinated ligands is indeed predominantly electrostatic, there is some evidence of weak covalency,[29, 61, 62] though less so than in actinides.[29] *Ab initio* calculations can produce results that accurately describe electrostatic effects and even weak covalent bonding effects. They have proven to be reliable tools for interpreting magnetic data of lanthanide complexes by predicting the nature of ground states and associated magnetic moments,[63] as well as describing low-lying multiplets with experimental accuracy.[55, 64] *Ab initio* calculations have even accurately described magnetic coupling between two lanthanide centres.[65]

For these calculations to be both efficient and accurate, it is critical that researchers make sensible choices regarding which orbitals are allowed to vary. In this regard, *ab initio* methods have an advantage over phenomenological and even semi-empirical quantum-chemistry methods (including DFT): By increasing the level of computation, the accuracy of the results can be systematically and rigorously improved (though at the cost of increased computation time). This can be done by, for instance, by considering additional terms in the calculation or otherwise making the model less simplified.

DFT is often considered to be an *ab initio* method for determining the molecular electronic structure. In reality, however, many of the most commonly used functionals have parameters derived from either empirical data or other calculations. In DFT, the total energy is expressed in terms of the total one-electron density rather than the wavefunction. In this type

of calculation, there is an approximate Hamiltonian and an approximate expression for the total electron density. DFT methods can be very accurate for little computational cost. Some methods combine the DFT exchange functional with the HF exchange term (see Section 3.1.1) and are called hybrid-functional methods. In the next chapter, the relationship between DFT and *ab initio* methods will be discussed further, and the two will be compared and contrasted.

2.2 Quantum coherence

Modern, classical computers store information in binary bits, with two states, 0 and 1. Quantum computers, by contrast, store information in superpositions of states, $a|0\rangle + b|1\rangle$. For a potential quantum system to be useful, then, it must be able to reliably generate, control, and read these superpositions of states, which must survive (persist) long enough for operations to be performed on them. In principle, any two-level system might satisfy these requirements, including the simple case of a spin-½ particle. In real systems, however, especially in the solid state, quantum superpositions are unstable and lose coherence quickly through interactions with the lattice, electric or magnetic noise, or more generally any interaction with their environments.

The possible quantum states for a single qubit can be visualised using a Bloch sphere (Figure 2.1). Here, the $|0\rangle$ and $|1\rangle$ states are respectively defined as the north and south poles of the sphere, and all other superpositions are points on the surface of the sphere. Notably, a pure qubit state $|\psi\rangle$ can be fully described as

$$|\psi\rangle = \cos\frac{\theta}{2}|0\rangle + e^{i\varphi}\sin\frac{\theta}{2}|1\rangle\,, \tag{2.8}$$

where θ governs the probability of the qubit being measured in the $|0\rangle$ or $|1\rangle$ states, and φ is the phase of the qubit.

When the qubit decoheres, however, it can no longer be described by a pure state. Instead, it is in a mixed state, which is a statistical combination or incoherent mixture of different pure states. Mixed states may be understood as points *inside* the Bloch sphere,

$$r(\cos\frac{\theta}{2}|0\rangle + e^{i\varphi}\sin\frac{\theta}{2}|1\rangle),$$

where r is the length of the vector representing the mixed state. This is not, however, a normalised state, so mixed states cannot be described by single ket vectors. Instead, they are described by a density matrix,

$$\rho = |\psi\rangle\langle\psi| = \sum_s p_s |\psi_s\rangle\langle\psi_s|,$$

where p_s is the fraction of the spin ensemble in each pure state $|\psi_s\rangle$. A density matrix, then, describes a pure state if and only if the square of the density matrix has unity trace, $\mathrm{Tr}(\rho^2) = 1$.

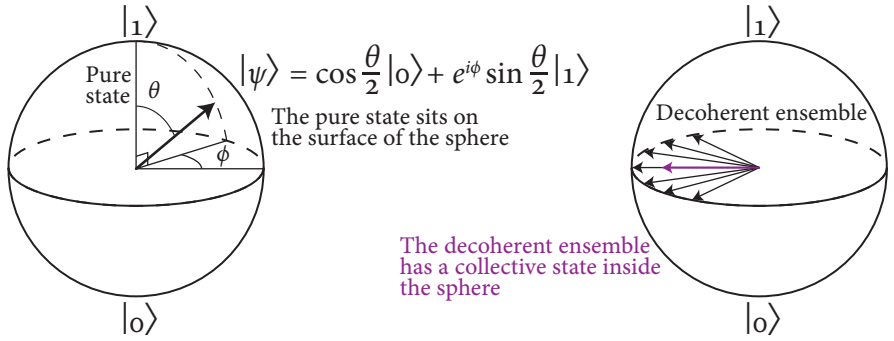


Figure 2.1: The Bloch sphere, a representation used to describe the state of a system, including both the magnitude of the $|0\rangle$ and $|1\rangle$ components and a phase ϕ. By convention, the coefficient of $|0\rangle$ is real. (Left) When the system is in a pure state, the representation sits on the sphere. (Right) When the system state is decoherent, the individual spin states are not in alignment, so that they span along on the surface. This then gives a collective state *inside* the sphere.

The off-diagonal elements of the density matrix represent the interaction between the energy levels by virtue of the relative phases of the amplitudes. For a generalised qubit as in Eq. (2.8), we can evaluate the density matrix using $\rho = |\psi\rangle\langle\psi|$ to find, for instance, $\rho_{01} = e^{-i\phi}\cos\theta\sin\theta$. Decoherence essentially causes the off-diagonal elements of the joint system's density matrix to vanish (for instance, $\rho_{01}(t) \propto e^{-\gamma t}$ for some decay constant γ). It irreversibly converts the pure state of the density matrix to a

reduced mixture, giving the appearance of a wavefunction collapse. When the system has not interacted with the environment, the joint system's density matrix may be denoted

$$\rho_{\text{total}} = |\psi\rangle \langle\psi| \otimes |e\rangle \langle e| ,$$

where $|e\rangle$ is the environment state. A partial trace of ρ over the basis of the environment gives the system's density matrix:

$$\rho_{\text{system}} = \text{Tr}_{\text{env}} = |\psi\rangle \langle\psi| \langle e|e\rangle = |\psi\rangle \langle\psi| .$$

After interaction with the system, the total density matrix becomes

$$\rho = \sum_{i,j} \langle i|\psi\rangle \langle\psi|j\rangle |i, e_i\rangle \left\langle j, e_j\right| = \sum_{i,j} \langle i|\psi\rangle \langle\psi|j\rangle |i\rangle \langle j| \otimes |e_i\rangle \left\langle e_j\right| ,$$

where the sums are taken over all states i, j of the system in any basis. Taking the partial trace of ρ again, we obtain

$$\begin{aligned}
\rho_{\text{system}} &= \text{Tr}_{\text{env}} \sum_{i,j} \langle i|\psi\rangle \langle\psi|j\rangle |i\rangle \langle j| \otimes |e_i\rangle \langle e_j| \\
&= \sum_{i,j} \langle i|\psi\rangle \langle\psi|j\rangle |i\rangle \langle j| \left\langle e_i|e_j\right\rangle \\
&= \sum_{i,j} \langle i|\psi\rangle \langle\psi|j\rangle |i\rangle \langle j| \delta_{ij} \\
&= \sum_{i} |\langle\psi|i\rangle|^2 |i\rangle \langle i| ,
\end{aligned}$$

which has no off-diagonal terms.

2.3 Molecular magnetic materials

2.3.1 *Quantum-coherence properties*

In order for a quantum device to be viable as a qubit, it must be able to maintain phase for a reasonable length of time, so that it might be used in a reasonably large number of quantum operations without the superposition states losing coherence, which would introduce errors. How long a device would be able to maintain phase coherence is dependent on its spin–spin relaxation (or coherence) time T_2. This requirement is one of the main technical challenges in the development of quantum devices, because most quantum systems are strongly susceptible to decoherence because of coupling to their environments.[66]

Spins, however, are relatively unaffected by fluctuations in electric fields, which are the primary cause of decoherence in both superconducting circuits[67] and trapped ions[68]. Hence, spins tend to have comparatively long coherence times when isolated from magnetic-field fluctuations (including from other spins in the environment). A number of molecular spin centres have been researched as possible systems for quantum computing. A few include ferrimagnetic chains,[69, 70] nitrogen-vacancy centres in diamond,[71] isotopic-impurity spins in silicon,[72] nitronyl nitroxide (NIT) groups, SMMs, and lanthanide-ion-based magnets. Ferrimagnetic chains, being one of the earliest researched, have models that can closely reproduce their behaviour,[69, 73] but interchain interactions make it difficult to study the one-dimensional properties in practice.[70] Nitrogen-vacancy centres in diamond[71, 74], isotopic-impurity spins in silicon[72, 75], and the more recent silicon-vacancy centres[76–79] have long coherence times and no nuclear-spin influence from their host lattices, but their electronic structures are difficult to tune, and the conditions for preserving quantum

coherence are strict, which limits coherent information exchange. Additionally, they are difficult to scale up and the spin systems tend to have low-dimension Hilbert spaces. This means that, in order to scale these up for quantum computation, the Hilbert space would have to be enlarged by efficient coupling between multiple systems, an additional complication. Such coupling, for instance, can often be hampered by inhomogeneity between qubits. NIT groups on the other hand, are fully organic (avoiding the complications of larger, metallic atoms), as well as being flexible and stable. They can also integrate onto graphene by edge functionalisation. They likewise suffer, however, from low-dimension Hilbert spaces, which require an efficient means of coupling them together for quantum computation.

The coordination-chemistry approach that drove much of the interest in ferrimagnetic chains, then, extended to design magnetic materials with spontaneous magnetisation below some critical temperature T_c (molecule-based magnets). Coordination chemistry allows researchers to design molecules bearing spin centres, including SMMs, which gives a greater flexibility compared with nitrogen-vacancy centres or isotopic impurities in silicon. Although other systems such as electron spins in NV centres in diamond can produce T_2 times exceeding 1 ms (which can even be extended to about 1 s with dynamic decoupling), they lack the flexibility that coordination chemistry gives. The flexibility of molecular spin qubits comes at a cost, typically having lower spin coherence times: An early example is $Cr_7NiF_6Piv_{16}$, which has T_2 on the order of 1 µs.

In order to create materials with large T_2 times, it is important to understand the primary limitations to coherence in molecular materials: interactions with (1) phonons, (2) nuclear spins in ligands and solvents, and (3) neighbouring spins.[80] Therefore, an intrinsic limitation of this molecular approach is the large coupling of phonons to qubit states, which

tends to be significant in these materials. In recent years, these effects have been somewhat mitigated, leading to millisecond coherence times.[81]

As a result, a lot of early research in SMMs as qubits focused on estimating their quantum coherence times. The first experimental estimates of quantum coherence in SMMs were published in 2000 for both Fe_8 and $Mn_{12}Ac$,[82] though these estimates were not from measurements using pulsed electron paramagnetic resonance (EPR). Though EPR experiments suggested a lower limit of 1 ns for coherence times in a Mn-based dimer,[83] estimates in SMMs were generally on the order of 10 ns.[83, 84] In 2007, however, T_2 times of up to 3.8 µs were observed in deuterated Cr_7Ni using pulsed ESR, and both long coherence times and quantum oscillations were observed in two SMMs, V_{15}[85] and Fe_4.[86] Schlegel *et al.* also found that modifications to the matrix surrounding SMMs can strongly increase the coherence time.[86] These observations showed that coherence times could continue to improve significantly. In the following decade, research in other transition-metal- and lanthanide-based magnets found coherence times between hundreds of nanoseconds and 15 µs,[85, 87–91] and even in the millisecond range.[81]

To mitigate the phononic effects, on the other hand, research is often conducted at low temperatures. Two other methods include (1) using rigid ligand molecules to increase the energies of vibrational modes,[92] and (2) using magnetic ions with half-integer spin states, which restricts some phononic transitions by time-reversal symmetry.[93] Lanthanide spin qubits, then, are a good choice. Their electronic ground state is often a doublet with an energy gap, which can be tuned using an electric field. In recent research, some spin levels have been observed to be tuneable while others are unaffectred. Hence, one proposed use of coupling between electric fields and spins is selective control of individual molecules in nanodevices.[94]

Lanthanides, as I will show in Chapter 4, are good choices for SMMs because their B_2^0 term can be negative, which produces specific properties, which I will discuss in the immediately following subsection.

2.3.2 *Single-molecule magnets as quantum units*

SMMs are magnetic compounds with one or more metal atom centres that display hysteresis without magnetic ordering. Their surrounding organic ligands act as a shield from their environment, so that the magnetic behaviour of each individual molecule is determined by the metal atom(s) only. In contrast to ferromagnets, there is no requirement of long-range cooperative exchange interaction. Hence, each molecule individually serves as a monomolecular magnet (hence the name), which makes them potentially useful for molecular spintronics[95] and quantum computation[14].

Because the spins of their metallic cores might be individually controlled and manipulated, SMMs are compelling choices for quantum units. Their microscopic size and large magnetic moment make them easier to control than single atoms, and their surrounding shell of organic ligands can be chemically tailored to bind them onto surfaces or junctions of prospective quantum devices.[96–98] Additionally, they can be assembled into dimers,[99, 100] trimers,[101] or larger aggregates[101, 102] to perform quantum operations.

One advantage of SMMs is their potential as multilevel qubits. Molecules with several accessible states are called "qudits" and have some advantages over qubits. The available Hilbert space is intrinsically higher in dimension in these systems, which allows more complex state interactions and computations within a single system. I will discuss this in greater detail in Chapter 6. With more than one state in qudits, quantum gates can be constructed without inter-qubit coupling,[103] the number of elementary quantum gates for given computation may be reduced,[104]

and information can stored in fewer physical units.[105] Qudits also have lower error rates than qubits,[106, 107] and they are able to act as complex quantum gates.[108, 109]

Another advantage of SMMs is their natural scalability. A useful quantum computation requires both a large number of qubits and a reliable way to integrate them into circuitry that can store information, process it, and implement it into quantum algorithms. A chemistry-based, bottom-up design naturally lends itself to both of these. SMMs can be chemically tailored to alter their anisotropy. They can also be replicated easily and organised using existing tools for self-assembly or supramolecular chemistry.

In order for a molecule to behave as an SMM, however, the energy barrier $U_{\text{eff}} \approx |D|S^2$ must be sufficiently large. The value of D depends on the electrostatic interactions between the magnetic centre(s) and the surrounding ligands. When D is negative, the ground state has a large m_S, giving a strong easy-axis anisotropy. Early attempts to increase this barrier by synthesising large exchange-coupled clusters failed were unfruitful, because despite increasing the spin S, they came at the cost of decreasing D, since the anisotropy terms of the individual spin centres in the large clusters counteracted each other.[110] For example, whereas the Mn_{19} cluster has $S = 83/2$, its barrier is $U_{\text{eff}} = 4\,\text{cm}^{-1}$, while $Mn_{12}Ac$ has $U_{\text{eff}} = 51\,\text{cm}^{-1}$, despite its smaller $S = 10$.[111] Some research has even suggested that D and S^2 cannot increase simultaneously.[112]

Later research therefore shifted to SMMs with single spin centres, to avoid this problem. In this case, the goal became increasing the anisotropy of a single ion. In these so-called single-ion magnets (SIMs), a subclass of SMMs, rather than a cluster of spin centres, there is a single high-spin centre with strong anisotropy. Lanthanide ions were a natural choice, because of their high orbital momentum, a direct consequence of both a strong spin–orbit coupling and a weak crystal field interacting with the

surrounding ligands. This is the opposite of 3d-transition-metal ions, in which crystal field is much stronger than the spin–orbit coupling, so that the orbital contribution is largely suppressed, resulting in small magnetic anisotropies. On account of this difference, the energy barriers of SIMs based on rare-earth metals are easily an order of magnitude higher than the energy barriers of their SMM cousins based on transition metals: some researchers have reported energy barriers as high as 1815 K.[113] In the last few years, magnetic hysteresis has even been observed at temperatures as high as 80 K,[114] showing good progress, but blocking temperatures for SMMs nonetheless remain too low currently to be practical. This is because at such small scales, these SMMs often still have fast relaxation, not only through quantum tunnelling, but also from interactions with the lattice.[115]

2.3.3 *Properties of single-molecule magnets (SMMs)*

When the D parameter in an SMM is negative, the spin states arrange themselves so that the higher-spin states have lower energy, with an energy barrier between them, and the $m_S = 0$ state has the highest energy. In the absence of an external magnetic field, the magnetic anisotropy does not favour either of the two ground states, which are degenerate in energy, though separated by an energy barrier U_{eff}. Hence, the magnetic moment usually has two stable, ground-state, high-spin orientations antiparallel to each other, and the energy barrier between them is the energy difference $U_{\text{eff}} \approx DS^2$ between the ground and $m_S = 0$ states. These stable orientations define the easy axis, or preferred magnetic orientation, of the molecule, while the directions perpendicular to this axis are called the hard plane. At finite temperatures T, there is a well-defined probability for the magnetisation to flip from one orientation to its opposite one, with a spin-flip rate, τ_0^{-1}. The corresponding relaxation time, takes a form similar to that

of superparamagnets,

$$\tau = \tau_0 \exp\left(\frac{U_{\text{eff}}}{k_B T}\right), \tag{2.9}$$

where U_{eff} is the energy barrier, k_B is the Boltzmann constant, and τ_0^{-1} is the rate of spins attempt to flip, which is connected to the efficiency of angular-momentum exchange between the spin and its environment, with vibrational effects playing a central role, so that an increase in phonon density leads to a decrease in τ_0.

From the total Hamiltonian, we obtain the spin levels as a function of the magnetic field, which are populated according to the Boltzmann distribution at a given temperature T. From this, we obtain the total magnetisation $\vec{M}$ as a function of field $\vec{B}$, and therefore the magnetic susceptibility $\bar{\bar{\chi}}$, defined according to

$$\chi_{ij} = \frac{\partial \vec{M}_i}{\partial \vec{B}_j}, \tag{2.10}$$

where i, j are directional components.

This describes the behaviour of the magnetization M in a static magnetic field B, and assumes an equilibrium response of the system to the introduction of an external field. On the other hand, a finite spin-flip time τ will generally lead to a delay in the spin response when subjected to variation in $\vec{B}$ at a frequency ω. The susceptibility $\chi(\omega)$ produced by $\vec{B}(\omega)$ can then be separated into its real and imaginary components, $\chi'(\omega)$, $\chi''(\omega)$:

$$\chi(\omega) = \chi'(\omega) + i\chi''(\omega).$$

The dependence of $\chi'(\omega)$ and $\chi''(\omega)$ on ω is then described by Kramers–Kronig relations, and the behaviour of $\chi''(\omega)$ is such that it has a peak when measured both versus ω and versus T.

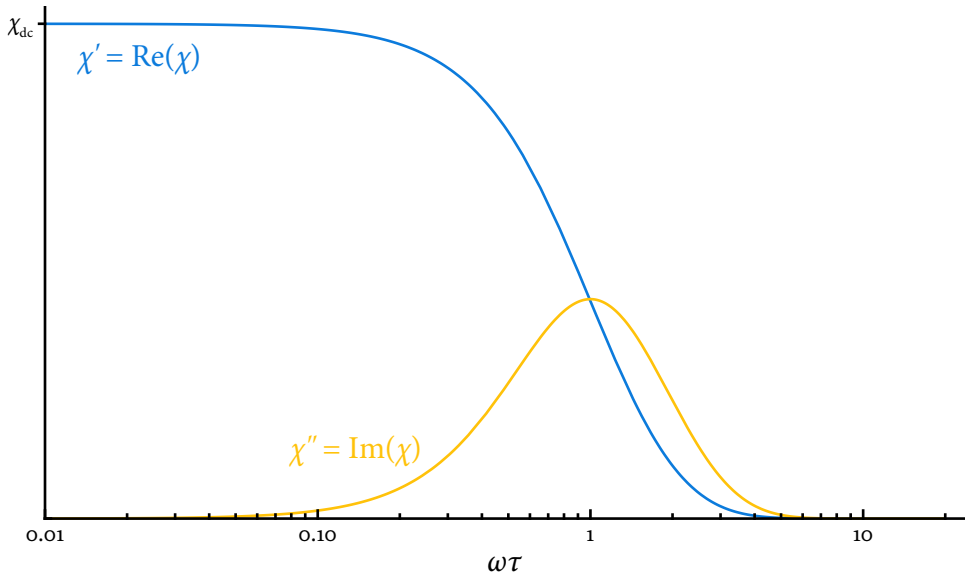


Figure 2.2: The real and imaginary parts of an example magnetic susceptibility χ as $\omega\tau$ is increased. The real and imaginary parts are related by the Kramers–Kronig relations, so that either one can be determined analytically if the other is known. Hence, measurement of one also gives values of the other.

The dependence of the peak on either the temperature T or ω can then be used to extract valuable information τ. If the dynamics are thermally activated, and thus τ follows the form given in (2.9), both the activation energy barrier Δ and the spin-flip attempt rate τ_o can be extracted from a plot of the peak frequencies $\log {}^1/_{\omega_{peak}}$ as a function of ${}^1/_T$.

The coupling of SMMs to the phonon bath of their environment, known as spin–phonon (or spin–lattice) coupling, allows the SMM to exchange both energy and angular momentum with the environment, which gives several possible mechanisms for magnetic relaxation. Sequential spin–phonon transitions therefore give rise to the energy barrier U_{eff}, resulting in the temperature dependence of the relaxation in Eq. (2.9). These transitions result in energy transfer from the spin centres to neighbouring molecules in the lattice, and the rate of energy transfer is quantified in the spin–lattice relaxation time, T_1. There are a few mechanisms by which the magnetisation can relax: (1) the direct process, (2) the Raman process, (3) the Orbach process, (4) quantum tunnelling, and (5) thermally assisted quantum tunnelling (Figure 2.3). While the first three are general processes for magnetic relaxation, the last two are specific to cases where there is an energy barrier between magnetic states of low energy. The relaxation that

arises from these first three mechanisms follow a summation relationship, where each term accounts for one of the mechanisms:[23]

$$\frac{1}{T_1} = A \coth \frac{h\omega}{2k_B T} + BT^n + \frac{C}{\exp \frac{\Delta}{k_B T} - 1}.$$

The first term describes the direct process, dominant at low temperatures, which is a one-phonon process where phonons of the same energy as some magnetic resonance $h\omega$ are absorbed or emitted by the spin system. At high temperatures ($T \gg h\omega/k_B$), the relationship is roughly linear, because $\coth(h\omega/2k_B T)$ may be approximated as $2k_B T/h\omega$. At low temperatures ($T \ll h\omega/k_B$), the relationship is roughly constant, with the relaxation time determined by the rate of spontaneous emission of phonons from the upper state when phonons of energy $h\omega$ are no longer thermally excited.

The second term describes the two-phonon Raman process, which involves virtual energy levels. More efficient at higher temperatures, this process works by absorbing a phonon of arbitrary energy to reach a virtual energy level and emitting a phonon to reach a lower energy level. Because of this, all phonons can participate in the process, which gives the strong temperature dependence. Values of the exponent n vary, depending on the system and temperature range: for non-Kramers doublets, $n = 7$, for Kramers doublets $n = 9$, and for multiplets for small splittings, $n = 5$.[23]

The third term describes the Orbach process, which is the absorption of a phonon by the direct process to a much higher energy level followed by the emission of a phonon of slightly different energy, such that the spin system goes from one energy state of a ground doublet to another.[23] At nonzero temperature, the spin states populate according to the Boltzmann distribution. When there is an energy barrier between the doublet states, phonons must induce spin transitions with $\Delta m_S = 1$ or $\Delta m_S = 2$ until the state at the top of the barrier is reached.[12] If T is high enough that the

thermal energy exceeds U_{eff}, thermal fluctuations dominate the system and the SMM behaves like a regular paramagnet. At low temperatures ($T \ll \Delta/k_B$, where Δ is the energy difference between the ground and excited states), the relationship approximately follows

$$1/T_1 = C\Delta^3 \exp(-\Delta/k_B T).$$

At sufficiently low temperatures, spin–phonon interactions are weak, and spins relax mostly by quantum tunnelling, which is a process that does not require overcoming the energy barrier, but still involves phonons in order to exchange momentum. The quantum-mechanical behaviour of the collective magnetisation of SMMs, however, is what is known as quantum tunnelling of the magnetisation (QTM), where the quantum-mechanical ground state is a linear superposition of the two classical ground states with equal and opposite magnetisation. Because of this QTM, the bonding and anti-bonding linear combination of these states forms an avoided level crossing, which separates them by a small energy difference, and defines a unique ground state.[12] This same effect also occurs for other pairs of higher-energy spin states, which lie on opposite sides of the energy barrier and have opposite magnetisation. Avoided level crossings occur whenever a Hamiltonian describing a quantum observable depends on N continuous, real parameters is measured on a manifold of less than $N - 2$ dimensions.[116] In practice, this means that when states of a system have quantum mechanical interactions, their energies may not be degenerate.

At slightly higher temperatures, the thermal energy may be below U_{eff} but high enough to easily excite spins from the ground state. The magnetisation may then relax through quantum tunnelling between higher-energy spin states. In this thermally assisted quantum tunnelling, the magnetisation relaxes through both thermal excitations and quantum tunnelling: phonons excite the spins to an excited state, the spins go through the energy

barrier by quantum tunnelling, and the spins fall back to the ground state (on the other side of the barrier).

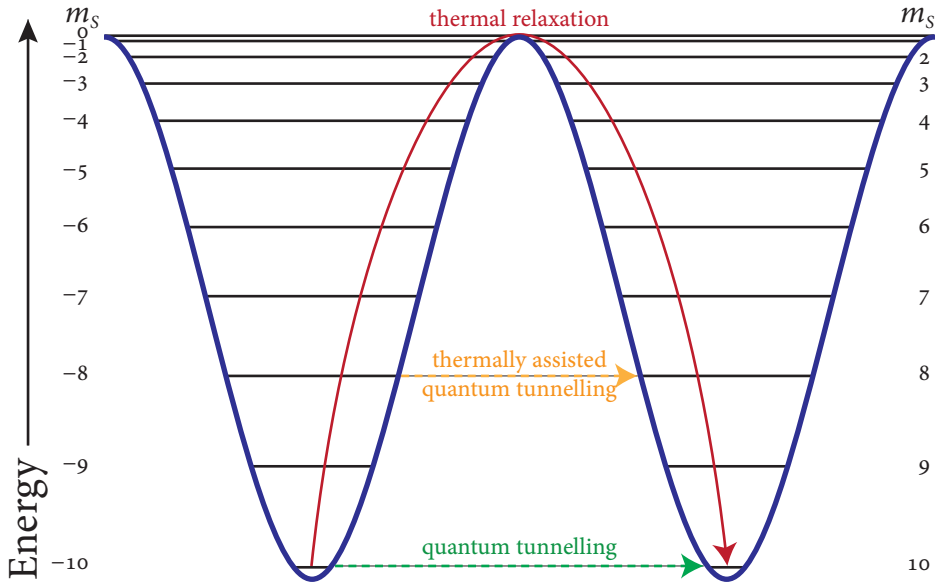


Figure 2.3: A schematic showing relaxation of magnetisation across a double-well potential for a system with $S = 10$. At high temperatures, the system can easily relax thermally over the barrier. At low temperatures where the energy is lower than the potential barrier, the system can relax through quantum tunneling, either thermally assisted or not, depending on the amount of energy available for thermal excitations.

The simplest case of a two-level system demonstrates this effect analytically. Consider the two-state Hamiltonian H with only diagonal elements E_1 and E_2. Its eigenvalues are E_1 and E_2, and the two unit vectors, $\langle 1, 0\rangle$ and $\langle 0, 1\rangle$, form its eigenbasis and designate the two states of the system. If the states have an interaction, which we will consider a perturbation with only off-diagonal elements $\Delta, \Delta^\dagger$ (to ensure the Hamiltonian remains Hermitian) for simplicity, the new Hamiltonian becomes

$$H' = \begin{pmatrix} E_1 & \Delta \\ \Delta^\dagger & E_2 \end{pmatrix},$$

whose eigenvalues are

$$E_\pm = \frac{E_1 + E_2}{2} \pm \sqrt{(E_1 - E_2)^2 + 4|\Delta|^2}.$$

We notice that, whereas before, H could have degenerate energies if $E_1 = E_2$, it is not possible for $E_\pm$ to be degenerate as long as $\Delta \neq 0$. When $\Delta E = E_1 - E_2$ is varied, then, $E_\pm$, form a hyperbola, separated by a minimum distance $2|\Delta|$ (Figure 2.4).

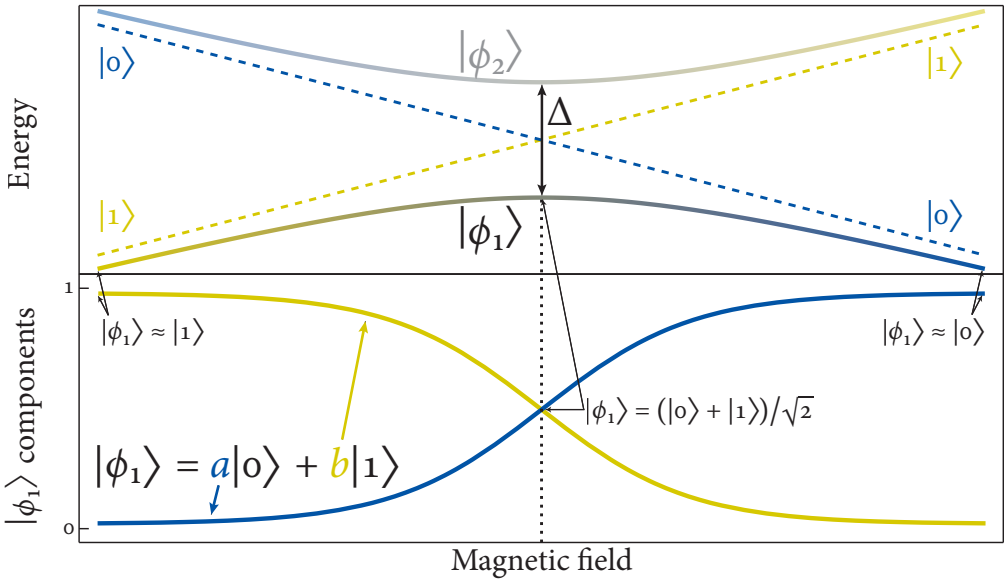


Figure 2.4: An avoided level crossing in a two-state system. (Top) In their pure states, the energy levels would simply cross (dotted lines), but the off-diagonal elements of the Hamiltonian introduce mixing between the states, so that they are no longer pure, and the energy levels of the states instead "avoid" each other, with an energy gap Δ. (Bottom) This gives $|\phi_1\rangle$ (and $|\phi_2\rangle$) that has components of $|0\rangle$ and $|1\rangle$, from a (nearly) pure $|1\rangle$ state to a (nearly) pure $|0\rangle$ state, as the magnetic field increases through the avoided level crossing.

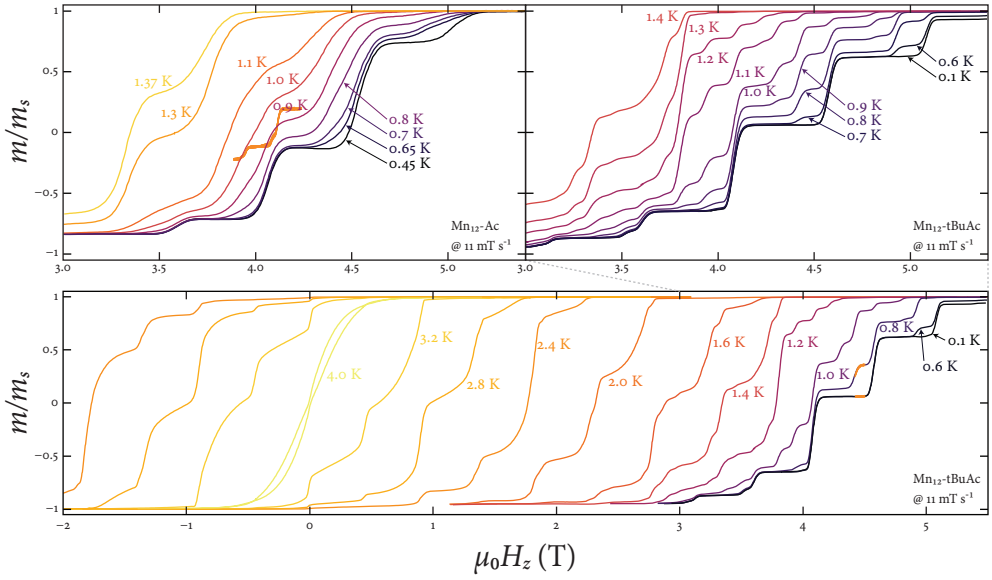


Figure 2.5: Quantum tunnelling of the magnetisation (QTM) causes the magnetisation of an SMM such as Mn_{12}Ac to change in a stepped pattern, as a magnetic field is slowly applied. The fields at which these steps occur coincide with avoided level crossings between spin levels. Shown here are also is the QTM in a sister SMM, Mn_{12}-tBuAc, which shows more pronounced steps. The magnetisation forms a hysteresis curve as the field is swept back and forth, because of the barrier between the high-spin ground states. Figure reproduced from [117].

As a result of QTM, somewhat similarly to quantum tunnelling of single electrons in double quantum wells, the magnetisation can tunnel through the barrier despite this tunnelling being classically forbidden. Thus, for sufficiently low temperatures, the magnetisation of SMMs follows a stepped hysteresis loop with respect to an applied magnetic field, because the quantised energy of the m_s states, which shift according to Zeeman splitting, giving another channel for relaxation when they are close in energy (Figure 2.5).

When U_{eff} is large and T is small, the relaxation time expected by Orbach processes becomes much larger than what is experimentally observed. The effect of the vibrational bath on the tunnelling probabilities has been considered in detail in the literature, and shall be examined in some detail in Chapter 5 when calculating the transition probabilities associated with quantum tunnelling in the presence of a strongly coupled electromagnetic field. In order to do this, we shall follow the literature and consider again the spin Hamiltonian (Eq. (2.4)), with the addition of a spin–phonon perturbation term,[118]

$$H_{\text{sp}} = i \sum_{q,\lambda} \sqrt{\frac{\hbar}{2m_c \omega_{q,\lambda}} V_{q,\lambda}} \bar{\bar{S}} (C_{q,\lambda} - C^{\dagger}_{q,\lambda}), \tag{2.11}$$

where ω, q, and λ are the phonon frequency, wave vector, and polarisation, $\hbar$ is the Planck constant, m_c is the unit-cell mass, $V_{q,\lambda}$ is the spin–phonon interaction potential, $C_{q,\lambda}$, $C^{\dagger}_{q,\lambda}$ are the operators for phonon creation and annihilation, and the sum runs over the Brillouin zone. We shall see that deeply understanding these processes is thus crucial to extending the relaxation time for SMMs, to make them practical for use as qubits.

2.4 Strong coupling

2.4.1 *Second quantisation*

A one-dimensional oscillator of mass m and frequency ω is described by the Hamiltonian

$$H = \frac{\hat{p}^2}{2m} + \frac{1}{2} m\omega^2 \hat{x}^2,$$

where the momentum operator $\hat{p}$ and position operator $\hat{x}$ obey the commutator relation

$$[\hat{x}, \hat{p}] = i\hbar\,.$$

We can then use second quantisation and define the ladder operators

$$\hat{a} = \sqrt{\frac{m\omega}{2\hbar}}\left(\hat{x} + \frac{i}{m\omega}\hat{p}\right), \tag{2.12}$$

$$\hat{a}^\dagger = \sqrt{\frac{m\omega}{2\hbar}}\left(\hat{x} - \frac{i}{m\omega}\hat{p}\right). \tag{2.13}$$

The operators $\hat{a}$ and $\hat{a}^\dagger$ satisfy the bosonic relation $[\hat{a}, \hat{a}^\dagger] = \hat{a}\hat{a}^\dagger - \hat{a}^\dagger\hat{a} = 1$. Using these operators, the Hamiltonian of the harmonic oscillator becomes

$$H = \hbar\omega\left(\hat{a}^\dagger\hat{a} + \frac{1}{2}\right).$$

Accordingly, we can consider a solution to the Schrödinger equation with some eigenstate $|m\rangle$ and energy E_m,

$$H|m\rangle = \hbar\omega\left(\hat{a}^\dagger\hat{a} + \frac{1}{2}\right)|m\rangle = E_m|m\rangle.$$

Multiplying both sides of the latter equality by $a^\dagger$ on the left gives

$$\begin{aligned}
\hbar\omega\left(\hat{a}^\dagger\hat{a}^\dagger\hat{a} + \tfrac{1}{2}\hat{a}^\dagger\right)|m\rangle &= E_m\hat{a}^\dagger|m\rangle \\
\Rightarrow \hbar\omega\left(\hat{a}^\dagger(\hat{a}\hat{a}^\dagger - 1) + \tfrac{1}{2}\hat{a}^\dagger\right)|m\rangle &= E_m\hat{a}^\dagger|m\rangle \\
\Rightarrow \hbar\omega\left(\hat{a}^\dagger\hat{a}\hat{a}^\dagger - \hat{a}^\dagger + \tfrac{1}{2}\hat{a}^\dagger\right)|m\rangle &= E_m\hat{a}^\dagger|m\rangle \\
\Rightarrow \hbar\omega\left(\hat{a}^\dagger\hat{a}\hat{a}^\dagger - \tfrac{1}{2}\hat{a}^\dagger\right)|m\rangle &= E_m\hat{a}^\dagger|m\rangle \\
\Rightarrow \hbar\omega\left(\hat{a}^\dagger\hat{a} - \tfrac{1}{2}\right)\hat{a}^\dagger|m\rangle &= E_m\hat{a}^\dagger|m\rangle \\
\Rightarrow \hbar\omega\left(\hat{a}^\dagger\hat{a} + \tfrac{1}{2}\right)\hat{a}^\dagger|m\rangle &= (E_m + \hbar\omega)\hat{a}^\dagger|m\rangle.
\end{aligned}$$

This gives another solution to the Schrödinger equation with eigenstate $\hat{a}^\dagger|m\rangle$ and energy $(E_m + \hbar\omega)$. This means that for every eigenstate $|m\rangle$ with energy E_m, there is another eigenstate $|m+1\rangle = \hat{a}^\dagger|m\rangle$ with energy $E_{m+1} = E_m + \hbar\omega$, which gives an infinite, equally spaced ladder of energy levels in the harmonic oscillator, for which $\hat{a}^\dagger$ acts as a "creation operator"

that shifts the energy level upward. Similarly, the operator $\hat{a}$ acts as a "destruction operator" (or "annihilation operator") that shifts the energy level downward, $H\hat{a}\,|m\rangle = (E_m - \hbar\omega)\hat{a}\,|m\rangle$. The destruction operator, however, has a lower bound given by the ground state, which we denote $|0\rangle$, because the energy eigenvalues are not allowed to be negative. Thus, $H\hat{a}\,|0\rangle = (E_0 - \hbar\omega)\hat{a}\,|0\rangle$ should have as its only consistent solution $\hat{a}\,|0\rangle = 0$ since E_0 should be the lowest allowable energy. Expanding the Schrödinger equation for the ground state gives

$$H\,|0\rangle = \hbar\omega\left(\hat{a}^\dagger\hat{a} + \frac{1}{2}\right)|0\rangle = \cancel{\hbar\omega\hat{a}^\dagger\hat{a}\,|0\rangle} + \frac{1}{2}\hbar\omega\,|0\rangle = E_0\,|0\rangle\,,$$

which means that $E_0 = \frac{1}{2}\hbar\omega$. Therefore,

$$E_m = \hbar\omega\left(m + \frac{1}{2}\right).$$

2.4.2 *The Hamiltonian*

In the simplest formulation for cavity quantum electrodynamics (QED), the interaction between an ideal two-level system (a qubit) and a single electromagnetic field mode inside a cavity is given by the Jaynes–Cummings model (JCM).[119] In this formulation, the two-level system may be in either its ground state $|g\rangle$ or its excited state $|e\rangle$, separated by some $\hbar\omega$, and the cavity may be in either the state $|n-1\rangle$ or $|n\rangle$, where n is the number of photons in the cavity. When the two interact, the total Hamiltonian is

$$\mathcal{H} = H_S + H_\Phi + H_I, \tag{2.14}$$

where H_S is the Spin Hamiltonian that describes the matter, H_Φ is the Hamiltonian describing the light to which the matter is coupled, and H_I is the interaction Hamiltonian. Because the JCM assumes that the systems have only two levels, the component Hamiltonians can be expressed ex-

plicitly rather simply. The spin system is given by $H_S = \hbar\omega\hat{\sigma}^+\hat{\sigma}^-$, where $\hat{\sigma}^+ = |e\rangle\langle g|, \hat{\sigma}^- = |g\rangle\langle e|$ are the raising and lowering operators for the two-level system, respectively; The light, in the form of photons trapped in a resonator cavity, is described by the usual harmonic-oscillator Hamiltonian,

$$H_\Phi = \hbar\omega\left(\hat{a}^\dagger\hat{a} + \frac{1}{2}\right), \tag{2.15}$$

where ω is the natural resonant frequency of the resonator, and $\hat{a}^\dagger, \hat{a}$ are the operators for photon creation and annihilation (or resonator raising and lowering), respectively, as given in Equations (2.12) and (2.13).

In general, free atoms can interact with an infinite number of radiation modes, but because the system we are considering confines the spin system to a resonator cavity, it can interact only with modes of the cavity. In particular, we consider only the single, fundamental mode. In the Coulumb gauge, then, the dipole interaction between a spin and an electric field is given by

$$H_I = \vec{D}\cdot\vec{E} = \sqrt{\frac{\hbar\omega_k}{2\epsilon_0 V}}D\sin(kx)(\hat{a}+\hat{a}^\dagger),$$

where ω_k is the mode frequency, V is the volume of the cavity, k is wave number of the electromagnetic wave, $D = \vec{D}\cdot\hat{x}$ is the component of the dipole moment in the direction of the cavity $\hat{x}$, and x is . For a two-level system, we can express D as

$$D = |0\rangle\langle 0|D|1\rangle\langle 1| + |1\rangle\langle 1|D|0\rangle\langle 0| = D_0|0\rangle\langle 1| + D_0|1\rangle\langle 0| = D_0(\sigma^- + \sigma^+),$$

where $D_0 \equiv \langle 0|D|1\rangle = \langle 1|D|0\rangle$ is a constant (since D is a constant). The dipole interaction Hamiltonian is, then,

$$H_I = \hbar\Omega(\hat{\sigma}^+ + \hat{\sigma}^-)(\hat{a}+\hat{a}^\dagger),$$

where

$$\Omega = \sqrt{\frac{\omega_k}{2\hbar\epsilon_0 L}} D_0 \sin(kx).$$

In the rotating-wave approximation (RWA), the $\hat{\sigma}^+\hat{a}$ and $\hat{\sigma}^-\hat{a}^\dagger$ terms, which do not conserve energy, are dropped, so the interaction Hamiltonian becomes

$$H_I = \hbar\Omega\left(\hat{\sigma}^+\hat{a} + \hat{\sigma}^-\hat{a}^\dagger\right), \tag{2.16}$$

where Ω can be understood as the coupling strength. In the RWA, the total Hamiltonian is given by the thus-named Jaynes–Cummings Hamiltonian,[119] given in Equation (2.14), which thus predicts that such a coupled system has two hybridised "dressed states", $|g, n\rangle$ and $|e, n-1\rangle$. Intuitively, this means that an absorption of a photon by the spin system from the resonator both excites the spin system $|g\rangle \to |e\rangle$ and decreases the number of photons in the cavity ($|n\rangle \to |n-1\rangle$).

In principle, the JCM is limited to one two-level system interacting with a resonator field, which would preclude its use for a high-spin system (such as SMMs) that have more than two levels. In practice, however, it is still useful to describe multi-level systems where there is one transition of interest that is tuned to the cavity mode and other transitions are sufficiently detuned from that mode. It also does not include spontaneous decays of the system or loss of photons from the resonator.

The JCM, however, is still limited to a single system. An extension of the model is the Tavis–Cummings model, which considers N two-level systems. The Tavis–Cummings Hamiltonian is

$$\mathcal{H} = \underbrace{\frac{\hbar}{2}\sum_{i=1}^{N}\omega_i\hat{\sigma}_i^+\hat{\sigma}_i^-}_{H_S} + H_\Phi + \underbrace{\hbar\sum_{i=1}^{N}\Omega_i\left(\hat{\sigma}_i^+\hat{a} + \hat{\sigma}_i^-\hat{a}^\dagger\right)}_{H_I}, \tag{2.17}$$

where the i^{th} two-level system has transition frequency ω_i and is coupled to

the resonator with strength Ω_i. In the case where the two-level systems are an ensemble of identical systems, $\omega_i \equiv \omega$ for some ω over all i. Additionally, coupled ensembles in circuit QED produce a $\sqrt{N}$ enhancement to the coupling rate Ω,[120–126] because of the two-level systems in the resonator are indistinguishable. Thus, when a photon in the resonator is absorbed, no single system absorbs it, but rather the total system is in a superposition state of each individual system being excited.

This can be analytically shown using the operators

$$\Sigma^{\pm} = \frac{1}{\sqrt{N}} \frac{\sum_{i=1}^{N} \Omega_i \hat{\sigma}_i^{\pm}}{\frac{1}{N}\sum_{i=1}^{N} \Omega_i}, \tag{2.18}$$

where the denominator of latter fraction is the average over all Ω_i, which we shall define to be Ω. Like $\sigma^{\pm}$, these operators obey the bosonic commutation relation $\left[\Sigma^{+}, \Sigma^{-}\right] = 1$,[127] so that the collective excitation of the system behaves like a harmonic oscillator. This gives, for the interaction term H_I of Equation (2.17),

$$H_I = \hbar\Omega\sqrt{N}\left(\hat{\sigma}^{+}\hat{a} + \hat{\sigma}^{-}\hat{a}^{\dagger}\right),$$

which, compared to Equation (2.16), we notice contains an additional factor of $\sqrt{N}$.

Thus, we can model an ensemble of spins by considering only a single spin system with coupling strength appropriately scaled, since the difference will only be a scaling factor in coupling strength.

Because the electric field of a cavity is quantised, single excitations between the atom and cavity will coherently oscillate at the vacuum Rabi frequency. These oscillations have been observed both in Rydberg atoms in three-dimensional microwave cavities[128] and in alkali atoms in small optical cavities.[129] Quantum effects in these cavities can then be manipulated,[130–133] and when they are strongly coupled to spin systems, the two coherently interact so that coherent superpositions of the two can be gen-

erated,[134] and excitations can be coherently exchanged.[135] Coherent superpositions and excitation exchange are vital for quantum information processing, as they allows operations to be performed between qubits without them losing coherence, so such cavities may be a good candidate for building quantum gates.

The coupling between a cavity and a spin system may also produce virtual states at much higher energies, through which the spins may virtually pass. This allows spin systems to go from one state to another, even when such a transition would normally be forbidden. This happens despite the fact that the system never actually enters the high-energy state, much like in a Raman transition.

Since this involves large energy detunings, the RWA is inaccurate, so the Hamiltonian must instead be expressed as

$$\mathcal{H} = H_s + \hbar\omega a^\dagger a + \hbar\Omega(\hat{S}_- + \hat{S}_+)(\hat{a}^\dagger + \hat{a})/2.$$

In this hybrid system, the energy splitting between levels m and m' is given by[136]

$$E_{mm'} = 2\left|\sum_{\substack{\phi_i \\ m_i \neq m,m'}}^{N}\left(\frac{V_{m,m_1}U_{m,\phi_1}}{(\epsilon_m-\epsilon_{m_1})(\epsilon_m-\epsilon_{\phi_1})}\times\prod_{i=1}^{N-1}\frac{V_{m_i,m_{i+1}}}{\epsilon_m-\epsilon_{m_{i+1}}}\frac{U_{m_i,\phi_{i+1}}}{\epsilon_m-\epsilon_{\phi_{i+1}}}V_{m_N,m'}U_{m_N,\phi}\right)\right|,$$

where $m > m_i > m'$, and V_{m_i,m_j} and U_{m_i,ϕ_j} are the off-diagonal elements of $\mathcal{H}$ resulting from $\hat{O}_k^q$ and H_I contributions, respectively. We see here a sum over all possible paths between $|m\rangle$ and $|m'\rangle$ in the larger Hilbert space of the hybrid system, comprising both $|m\rangle$ and $|\phi\rangle$ levels. Notably, even levels not mixed by $\hat{O}_k^q$ operators become mixed: strong coupling introduces photon-induced tunnelling in the spin system through cavity paths that contain first-order ladder operators and admixes any $|m\rangle$, $|m'\rangle$ by virtual processes. The efficiency of these new quantum processes depends on Ω and the particular levels involved, since the polaronic up-shift effect can partially compete with pure spin–phonon processes arising from Eq. (2.11),

given by[136]

$$W_{m\pm1,m} = \frac{A^2 s_{\pm1}}{12\pi\rho c^5\hbar^4}\frac{(\epsilon_{m\pm1}-\epsilon_m)^3}{e^{\beta(\epsilon_{m\pm1}-\epsilon_m)}-1},$$

$$W_{m\pm2,m} = \frac{17A^2 s_{\pm2}}{192\pi\rho c^5\hbar^4}\frac{(\epsilon_{m\pm2}-\epsilon_m)^3}{e^{\beta(\epsilon_{m\pm2}-\epsilon_m)}-1}.$$

From both processes, nevertheless, we may find the photon-assisted tunnelling rate,[136]

$$\Gamma_m^{m'} = E_{mm'}^2 \frac{W_m + W_{m'}}{4\xi_{mm'}^2 + \left(W_m + W_{m'}\right)^2},$$

where W_m is the total phononic contribution from state $|m\rangle$, and $\xi_{mm'}$ is the difference in energy between the pure $|m\rangle$ and $|m'\rangle$ levels (in the absence of off-diagonal interactions terms in the Hamiltonian).

Because phononic processes can efficiently promote the spin reversal opened by the strong-coupling channel, $\Gamma_m^{m'}$ is enhanced. This is evident even at small spin–cavity couplings.

2.4.3 *Experimental realisations*

In its archetypical form, a cavity is formed by two mirrors separated by some fixed distance d, which in principle will allow only discrete modes to resonate. Hence, if some photon of an allowed mode enters the cavity, it will remain trapped for some time, characterised by the cavity decay rate κ. As a result, a spin system placed inside of such a cavity will interact most strongly with allowed modes (Figure 2.6). If the cavity mode is on resonance with the decay mode of the spin system, the interaction between the trapped photons and the spin system will enhance the latter's radiating decay because of the Purcell effect,[137] thereby allowing the spin system and the cavity to coherently exchange of photons.[138]

In practice, cavities can be either 2-D or 3-D. Moreover, the spacing of the energy levels in many spin systems of interest corresponds to microwave

frequencies, so cavities are usually constructed so that their fundamental mode falls in the microwave regime.

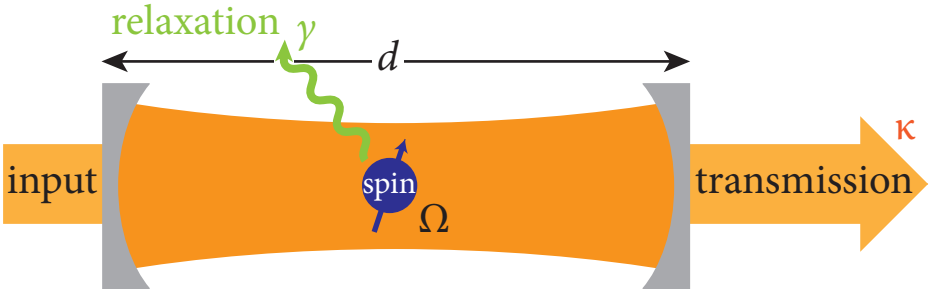


Figure 2.6: A schematic of a spin coupled to a cavity resonator. Some input light is incident on a cavity with characteristic length d, with cavity decay rate κ, which can be measured. The spin in the resonator will couple to the photons with coupling rate Ω and relax at rate γ.

3-D cavity resonators. The most straightforward manifestation of the theoretical cavity, this is formed using highly reflective materials to enclose a small volume, with an input and a readout. The volume of the cavity will affect the field strengths, the reflectivity of the materials will determine the quality factor, and the dimensions will determine the modes.

2-D cavity resonators. A special realisation using circuit QED, these are constructed using a waveguide with small gaps that act as mirrors, and a coplanar, superconducting thin film surrounding it. Here, a single microwave photon can be stored in the on-chip cavity and coherently coupled to things placed in the resonator, such as a spin system or an ensemble of spin systems. Though the resonator as a whole is two-dimensional, the waveguide effectively reduces the microwaves into one-dimensional standing waves. The superconducting surfaces prevent magnetic flux, effectively linearly polarising the microwaves as well. These resonators produce concentrate the magnetic and electric fields to much higher values and in much smaller regions[128, 139] because of the small effective mode volume.[140]

While in theory, a resonant cavity allows only discrete frequencies that are multiples of its fundamental mode, in practice, near each resonant frequency ω_c, the power transmission spectrum follows a Lorentzian shape,

$$T(\omega) = \frac{2}{\pi} \frac{\Gamma_c}{4(\omega - \omega_c)^2 + \Gamma_c^2},$$

where Γ_c is the bandwidth, or the frequency's full width at half maximum (FWHM) of transmission. Both ω_c and Γ_c are properties of the cavity, and their ratio gives the quality factor Q, defined as

$$Q \equiv \frac{2\pi \langle E_s \rangle}{E_l} = \frac{\omega_c}{\Gamma_c},$$

where $\langle E_s \rangle$ is the average (over time) energy stored in the cavity and E_l is the energy loss per cycle. The experimental sensitivity scales with the quality factor: If less energy is lost and more is retained in the cavity, smaller signals are resolved better. One way energy may be lost is through the walls of the cavity, where microwaves can induce currents.

2.4.4 *Spins in cavities*

Using the JCM, Sanchez-Mondragon *et al.* predicted the emission spectrum of a two-level atom interacting with a single-mode electromagnetic field in an ideal cavity, showing that the result of strong coupling between the two would resolve as two spectral peaks, which they called the vacuum-field Rabi splitting.[141] This splitting also occurs when N atoms couple to a photon, and as mentioned before, the strength of the coupling is then enhanced by a factor of $\sqrt{N}$.[142, 143] Chiorescu *et al.* later showed that, in the case of n photons and N two-level systems, the splitting effect is still enhanced by $\sqrt{N}$ if $n \ll N$.[144]

In a given spin–cavity system, the system dynamics are quantified by the atomic decay rate γ, the cavity decay rate κ, and the coupling strength Ω (see Figure 2.6). The coupling strength may also be thought of as a coupling *rate,* which measures the rate of energy exchange between the cavity and the spin system's state transitions. The strength of the interaction between the two can be quantified by a dimensionless cooperativity parameter C,

$$C = \frac{g^2}{\kappa\gamma},$$

from which we can define by three regimes of coupling: (1) the weak coupling regime, (2) the intermediate regime, and (3) the strong coupling regime.

In the weak-coupling regime, the coupling rate is much smaller than the decay rates of both the spin-level decay rate γ and the cavity's photon decay rate κ, $\Omega \ll \gamma, \kappa$, which we find also that $C \ll 1$. Since the two decay rates are much faster than the rate of energy exchange between the spin system and the cavity in the weak coupling regime, no coherent effects are observable. In the intermediate regime, at least one of the two decay parameters is slower than the coupling rate so that $C > 1$. In this regime, coherent effects such as the Purcell effect manifest.[145] In the strong-coupling regime, the coupling rate is much larger than both decay rates, $\Omega \gg \gamma, \kappa$, which allows the spin system and cavity to coherently exchange excitations. In this regime, vacuum Rabi splitting manifests,[135] and it is the resulting vacuum Rabi oscillations that coherently exchange energy (and states) between the spins and the cavity.

The coupling of spins to resonators is a basis for a handful of theoretically proposed and experimentally studied qubits. In many cases, the resonators are fabricated onto chips, making them easier to produce in bulk and tailor specifically. This also allows researchers to make cavities extremely small, which concentrates the microwaves in much smaller regions, making their coupling effects more pronounced, so that in some cases single spins can even be detected.[146–149] One method of coupling these qubits, then, is coupling them to an intermediate quantum bus, often a microwave cavity resonator. This has been done in transmons,[150–152] xmons,[153] and other qubits.[154–156] The same coupling can also be used to control and read out qubit states.

Some research has reported coupling between cavity photons and spin ensembles, caused by inducing weak magnetic-dipole transitions in

low-spin systems.[122, 157–159] By contrast, however, SMMs have large spins.

2.5 Conclusion

In this chapter I laid out the groundwork and the background that will constitute the foundations of the theoretical work developed during this thesis. From this discussion, I highlight how there is presently considerable interest in molecular magnetic materials, and the complex Hamiltonian, and thus Hilbert spaces, that can arise from them. I discussed here the numerical methods that can be used to model the magnetic anisotropy of spin centres, starting from the structural configuration. I have then discussed the theoretical tools used to describe strong light-matter coupling, a problem that is usually approached in an analytical manner.

We shall then see in the upcoming chapters how these two theoretical approaches, the numerical and analytical ones, can be combined to produce a detailed and common picture of the magnetic properties of molecular systems, improve the understanding of their experimental behaviour, and guide their integration into quantum devices. The following chapters will thus use the background laid out in this chapter to delve with multiple magnetic systems, compare them one with another, and investigate how closely their predicted behaviour matches the observed properties in a variety of quantum systems.

3 Methods

3.1 *Ab initio* methods

A variety of theoretical and computational methods exist to numerically predict the properties of chemical systems and molecules. In this chapter, I begin first by introducing the formalism. Second, I describe a method of writing wavefunctions called the Slater determinant. Thirdly, I explain the principles of the self-consistent fields (SCFs), or Hartree–Fock (HF), methods, which are the basis of *ab initio* wavefunction methods, and I will briefly describe density-functional theory (DFT) and its related methods. Fourthly, I describe the configuration interaction (CI) method. Finally, I describe the methods of multi-configurational self-consistent fields (MCSCFs) that are considered and used in this thesis.

The time-independent Schrödinger equation for a single electron is

$$\hat{H}\psi(\vec{r}) = E\psi(\vec{r})\,,$$

where $\psi(\vec{r})$ is the electron wavefunction, normalised so that $|\psi(\vec{r})|^2$ is the probability of finding the electron at position $\vec{r}$. For a many-bodied wavefunction with N electrons and M nuclei, the wavefunction is more complex, so that

$$\Psi = \Psi(\vec{r}_1, \ldots, \vec{r}_N; \vec{R}_1, \ldots, \vec{R}_M)\,.$$

For this wavefunction, assuming proper normalisation, $|\Psi|^2$ tells us the

probability of finding all N electrons at the respective positions $\vec{r}_i$, given the positions $\vec{R}_i$ of the M nuclei. Thus, the probability of finding some electron (because of indistinguishability) at some position with no consideration given to the positions of the remaining electrons is given by a sum over all possibilities:

$$n(\vec{r}) = N \int |\Psi(\vec{r}, \vec{r}_2, \ldots, \vec{r}_N; \vec{R}_1, \ldots, \vec{R}_M)|^2 \mathrm{d}\vec{r}_2 \cdots \mathrm{d}\vec{r}_N \mathrm{d}\vec{R}_1 \cdots \mathrm{d}\vec{R}_M \,.$$

This is thus the electron-density function. Having thus defined this, in principle, we can calculate it by solving

$$\hat{H}\Psi = [K + U]\Psi = [K_\mathrm{n} + K_\mathrm{e} + U_\mathrm{ne} + U_\mathrm{ee} + U_\mathrm{nn}]\Psi = E\Psi \,.$$

Expanding the Hamiltonian further, we find

$$\hat{H} = -\sum_{A<M} \frac{1}{2m_A} \nabla_A^2 - \frac{1}{2} \sum_{i<N} \nabla_i^2 + \sum_{A<M} \sum_{B>A} \frac{Z_A Z_B}{r_{A,B}} + \sum_{i<N} \sum_{j>i} \frac{1}{r_{i,j}} - \sum_{A<M} \sum_{i<N} \frac{Z_A}{r_{A,i}} \,,$$

where the A, B indices correspond to nuclei, the i, j indices correspond to electrons, M_A is the mass of nucleus A, Z is the nuclear charge, and $r_{i,j} = |\vec{r}_i - \vec{r}_j|$ is the distance between the two particles i and j.

No analytical solutions are obtainable for all but the simplest of systems, and it becomes necessary to make approximations. One such approximation is the Born–Oppenheimer (BO) approximation, also known as the adiabatic approximation, which assumes that electrons relax immediately to their instantaneous ground-state configurations when there are changes to nucleus positions. This approximation arises from the fact that nuclei are several orders of magnitude heavier than electrons and therefore move very slowly in comparison to the electrons that surround them.

One remaining difficulty is the Coulomb repulsion between electrons, expressed by the potential term

$$U_{ee} = \frac{1}{2} \sum_{i \neq j} \frac{e^2}{4\pi\epsilon_0} \frac{1}{|\vec{r}_i - \vec{r}_j|} \,. \tag{3.1}$$

Different methods have differing ways to deal with this problem.

3.1.1 *Self-consistent field*

Self-consistent-field (SCF) methods, also known as Hartree–Fock (HF) methods, are a class of methods that are often used to find a numerical approximation for the solution by convergence to some defined convergence limit. These methods are variational (iterative) methods of approximation for the wavefunction and energy of a quantum many-bodied, stationary-state system. They inherently assume the BO approximation and typically ignore relativistic effects using a non-relativistic momentum operator.[a] For fermions (such as electrons), these methods also assume that the exact N-body wavefunction of the system can be approximated by a single Slater determinant, an antisymmetrised product of one-electron wavefunctions (orbitals).

[a] Scalar relativistic effects can be included in related, more advanced methods.

The method is predicated on the variational principle, which posits that expected energy of a given wavefunction is always greater than or equal to the exact energy, with equality only when the wavefunction is the ground-state function:

$$\forall \psi \neq \psi_0 : \; E > E_0 \,.$$

In principle, then the method optimises *ansatz* wavefunctions to minimise their energy,

$$E = \langle \psi | \hat{H} | \psi \rangle \,,$$

assuming a normalised wavefunction ψ.

An important property of these wavefunctions, however, is that they must satisfy the Pauli exclusion principle. Accordingly, the wavefunction must be antisymmetric on pairwise exchange of electron coordinates, since electrons are fermions and therefore indistinguishable. Thus, wavefunctions for single particles are often expressed in spin-orbitals, a product of a spatial orbital and a spin function,

$$\psi(\vec{x}) = \phi(\vec{r})\sigma(s_z)\,,$$

where $s_z \in \{-s + i\}_{i=0}^{2s}$ is the spin quantum number, or the projection of the particle spin on the z axis. For an electron, $s = 1/2$, so $s_z = \pm 1/2$, which are thus said to "spin up" ($\uparrow$) and "spin down" ($\downarrow$). Around an atom, a wavefunction for a given electron also depends on its set of quantum numbers, n, l, m_l, m_s, which we will denote by $\vec{\kappa}$, so that the spin-orbital of an electron with quantum numbers n, l, m_l, m_s is given by

$$\psi_{\vec{\kappa}}(\vec{x}) \equiv \psi_{n,l,m_l,m_s}(\vec{x}) = \phi_{n,l,m_l}(\vec{r})\sigma_{m_s}(s_z)\,,$$

where the spatial orbital ϕ depends only on the set of quantum numbers n, l, m_l, the spin orbital function is $\sigma_{m_s}(s_z) = \delta_{m_s,s_z}$, where $\delta_{i,j}$ is the Kronecker delta function

By the Pauli exclusion principle, each spatial orbital can be occupied by at most two electrons, one of each spin. In this way, different electron wavefunctions are orthogonal, so that an *ansatz* for the two-electron wavefunction may be given by the Hartree product,

$$\Psi(\vec{x}_1, \vec{x}_2) = \psi_{\vec{\kappa}_1}(\vec{x}_1)\psi_{\vec{\kappa}_2}(\vec{x}_2)\,.$$

This, however, is not antisymmetric ($\Psi(\vec{x}_1, \vec{x}_2) \neq -\Psi(\vec{x}_2, \vec{x}_1)$), so the wavefunction must be rectified by taking a linear combination of both Hartree products:

$$\begin{aligned}\Psi(\vec{x}_1,\vec{x}_2) &= \tfrac{1}{\sqrt{2}}\left(\psi_{\vec{\kappa}_1}(\vec{x}_1)\psi_{\vec{\kappa}_2}(\vec{x}_2) - \psi_{\vec{\kappa}_1}(\vec{x}_2)\psi_{\vec{\kappa}_2}(\vec{x}_1)\right)\\ &= \frac{1}{\sqrt{2}}\begin{vmatrix}\psi_{\vec{\kappa}_1}(\vec{x}_1) & \psi_{\vec{\kappa}_2}(\vec{x}_1)\\ \psi_{\vec{\kappa}_1}(\vec{x}_2) & \psi_{\vec{\kappa}_2}(\vec{x}_2)\end{vmatrix}.\end{aligned}$$

The latter expression is known as a Slater determinant. In the multi-electron case, this can be generalised to

$$\begin{aligned}\Psi(\vec{x}_1,\ldots,\vec{x}_N) &= \frac{1}{\sqrt{N!}}\begin{vmatrix}\psi_{\vec{\kappa}_1}(\vec{x}_1) & \cdots & \psi_{\vec{\kappa}_N}(\vec{x}_1)\\ \vdots & \ddots & \vdots\\ \psi_{\vec{\kappa}_1}(\vec{x}_N) & \cdots & \psi_{\vec{\kappa}_N}(\vec{x}_N)\end{vmatrix}\\ &\equiv \tfrac{1}{\sqrt{N!}}\left|\psi_{\vec{\kappa}_1}(\vec{x}_1)\cdots\psi_{\vec{\kappa}_N}(\vec{x}_N)\right|\\ &\equiv \left\langle\vec{x}_1,\ldots,\vec{x}_N|\psi_{\vec{\kappa}_1},\ldots\psi_{\vec{\kappa}_N}\right\rangle,\end{aligned}$$

where each $\psi_{\vec{\kappa}_i}$ corresponds to a different set of n, l, m_l, m_s quantum numbers. The latter two are compact notations for Slater determinants. In the determinant, the columns share spin-orbital functions, and the rows share coordinates. As in the two-electron case, anti-symmetry enforces the Pauli exclusion principle. HF theory assumes that the total wavefunction Ψ is indeed given by a single configuration and can therefore be expressed by a Slater determinant.

An optimal set of spin-orbitals for a wavefunction can be found solving the Schrödinger equation. HF theory assumes that each electron moves in an effective potential due to the nuclei and other electrons, and, being a variational method, it iteratively solves an effective *one*-electron Schrödinger equation until satisfactory convergence.

While one-electron HF problems have analytical solutions, many-electron ones do not. In practice, atomic orbitals are often used as initial *ansatz* functions to find numerical solutions, and linear combinations of such orbitals can lead to molecular orbitals that may be used for many-electron problems.

With the assumptions of HF, the considered Hamiltonian is

$$\mathcal{H} = T_e + U_{eN} + U_{ee}, \tag{3.2}$$

where T_e is the electron kinetic energy, U_{eN} is the potential describing the electron–nucleus interactions, and U_{ee} is the potential describing electron–electron interactions (Eq. (3.1)). The HF wavefunction is then assumed to be expressable as a single Slater determinant, so that the energy is given by

$$E_{HF} = \langle \Psi | \mathcal{H} | \Psi \rangle . \tag{3.3}$$

The variational principle then provides that such symmetric energy expressions are always an upper bound to the true energy of the system. We can therefore obtain progressively better approximations for the wavefunction Ψ by varying parameters until the energy is minimised within a given functional space. Thus the correct molecular orbitals are those that minimise Eq. (3.3), so that the HF energy is the minimal energy for a single Slater determinant, made up of one spin orbital per electron. This energy can be rewritten in terms of one- and two-electron integral operators:

$$E_{HF} = \sum_i \langle i|h|i\rangle + \frac{1}{2}\sum_{ij} \left([ii|jj] - [ij|ji] \right), \tag{3.4}$$

where the one-electron integral is

$$\langle i|h|i\rangle = \int \chi_i^*(\vec{x}_1) h(\hat{r}_1) \chi_j(\vec{x}_1)\, \mathrm{d}\vec{x}_1, \tag{3.5}$$

where $\hat{h} = T_e + U_{eN}$, and the two-electron integral in chemists' notation is

$$[ij|kl] = \int \chi_i^*(\vec{x}_1)\chi_j(\vec{x}_1) r_{12}^{-1} \chi_k^*(\vec{x}_2)\chi_l(\vec{x}_2)\, \mathrm{d}\vec{x}_1\, \mathrm{d}\vec{x}_2. \tag{3.6}$$

Since the energy expression is symmetric, the variational principle guarantees that the Slater determinant with the lowest energy is the best approximation for the true wavefunction using a single Slater determinant. Hence Eq. (3.3) must be mimimised with respect to changes in the orbitals

$\chi_i \to \chi_i + \delta\chi_i$. The orbitals χ are taken to be orthonormal, and the variational procedure to mimimise them must retain this property. This can be done using Lagrange's method of undetermined multipliers, defining a functional

$$\mathcal{L}[\{\chi_i\}] = E_{\text{HF}}[\{\chi_i\}] - \sum_{ij} \epsilon_{ij}(\langle i|j\rangle - \delta_{ij}), \tag{3.7}$$

where ϵ_{ij} are the undetermined Lagrange multipliers. If we set the first variation $\delta\mathcal{L} = 0$, we obtain the HF equations:

$$h(\vec{x}_1)\chi_i(\vec{x}_1) + \sum_{j\neq i}\left[\int |\chi_j(x_2)|^2 \hat{r}_{12}^{-1}\, \mathrm{d}x_2\right]\chi_i(\vec{x}_1) - \sum_{j\neq i}\left[\int \chi_j(x_2)\hat{r}_{12}^{-1}\chi_i(x_2)\, \mathrm{d}x_2\right]\chi_j(x_1) = \epsilon_i\chi_i(\vec{x}_1), \tag{3.8}$$

where ϵ_i is the energy eigenvalue of orbital χ_i. The first summation in Eq. (3.8) gives the Coulomb interaction of an electron in orbital χ_i with the *mean* charge distribution of all the other electrons. Hence HF assumes a mean-field approximation. This term is called the Coulomb term, and it is therefore appropriate to define

$$\mathcal{J}_i(\vec{x}_1) = \int |\chi_j(\vec{x}_2)|^2 \hat{r}_{12}^{-1}\, \mathrm{d}\vec{x}_2 \tag{3.9}$$

as the Coulomb operator, which describes at $\vec{x}_1$ the average potential due to the charge distribution from the electron in orbital χ_j. The second summation in Eq. (3.8) accounts for the requirement that wavefunctions must be antisymmetric. It exchanges orbitals χ_i and χ_j and is therefore called the exchange term. It is similarly appropriate to define

$$\mathcal{K}_i(x_i)\chi_i(x_i) = \left[\int \chi_j(x_2)\hat{r}_{12}^{-1}\chi_i(x_2)\, \mathrm{d}x_2\right]\chi_j(x_i) \tag{3.10}$$

as the exchange operator, describing its action on an arbitrary orbital χ_i. Eq. (3.8) can then be more conveniently expressed as

$$\left[h(\vec{x}_1) + \sum_{j\neq i} \mathcal{J}_i(\vec{x}_1) - \sum_{j\neq i} \mathcal{K}_j(\vec{x}_1)\right]\chi_i(\vec{x}_1) = \epsilon_i\chi_i(\vec{x}_1). \tag{3.11}$$

Since $\mathcal{J}_i(\vec{x}_1) - \mathcal{K}_i(\vec{x}_1)]\chi_i(\vec{x}_1) = 0$, the restriction that $j \neq i$ can be removed, and we can define the Fock operator,

$$\hat{f} = \hat{h} + \hat{v}^{\text{MF}}, \tag{3.12}$$

where v^{MF} is the so-called mean-field potential,

$$\hat{v}^{\text{MF}} = \sum_i \mathcal{J}_i - \sum_i \mathcal{K}_i. \tag{3.13}$$

This allows us to express Eq. (3.11) as

$$\hat{f}(\vec{x}_1)\chi_i(\vec{x}_1) = \epsilon_i\chi_i(\vec{x}_1). \tag{3.14}$$

This is not a true eigenvalue problem, since the Fock operator $\hat{f}$ is itself a function of χ_i through the mean-field potential term. Hence, after some initial guess for the orbitals χ_i, the Fock operator $\hat{f}$ is fixed, the eigenvalue problem is solved, and the new values for χ_i are taken for the next iteration. This is continued until the changes $\delta\chi_i$ are below some predetermined threshold for convergence.

To summarise, the assumptions and simplifications of HF are: (1) the BO approximation, (2) relativistic effects are ignored, (3) the solution is assumed to be a linear combination of a finite number of basis functions, (4) the energy eigenfunction is describable with a single Slater determinant, and (5) the mean-field approximation. As mentioned previously, the HF energy found will always be an upper bound of the true ground-state energy, and HF is subject to two limitations: (1) the HF limit, and (2) the full-configuration-interaction (full-CI) limit. The former is a complete (infinite) basis set, limited by the third assumption of HF, since a complete basis set is computationally impossible; the latter is consideration of all CIs, which is a relaxation of the fourth and fifth assumptions.

3.1.2 *Configuration interaction*

Because electron motions are correlated, the true wavefunction describing a system will not be simply one configuration of the electrons. Rather, it can be expressed in the form

$$\Psi = \sum_i c_i \Phi_i = c_0 \Phi_0 + c_1 \Phi_1 + \dots . \tag{3.15}$$

The first term in Eq. (3.15) is the ground state, and while in principle, Ψ is simply the ground state eigenfunction, in reality, there is small mixing with the excited state, but this small mixing accounts for most of the interesting magnetic behaviour in, for instance, a molecular compound's spin centre.

Hence, though the CI method, like the HF method, is based on the variational principle, it considers more than one configuration. In its simplest form, it treats the wavefunction as a spin and a linear combination of Slater determinants, which are known as configuration state functions (CSFs), whose coefficients are determined by requiring an energy minimum. In practice, the molecular orbitals used to build the excited CSFs are assumed from an initial HF estimate and held fixed, though more modern techniques may opt to use guess orbitals derived from DFT results or other calculations instead. Then,

$$\Psi_{\text{CI}} = \sum_{i=0}^{\infty} C_i^{\text{CI}} \Phi_i = C_0^{\text{CI}} \Phi_{\text{HF}} + \sum_{i=1}^{\infty} C_i^{\text{CI}} \Phi_i \,, \tag{3.16}$$

where the i^{th} term is describes the i^{th} excited CSF, relative to the HF configuration. Hence, each Ψ_i term describes some particular configuration of the electrons, up to infinite excitation, which is called the full-CI limit (see Figure 3.1).

Substituting Eq. (3.16) into the Schrödinger equation, we obtain

$$\left\langle \Psi_{\text{CI}} | \hat{H} | \Psi_{\text{CI}} \right\rangle = \sum_{i=0} \sum_{j=0} C_i^{\text{CI}} C_j^{\text{CI}} \left\langle \Phi_i | \hat{H} | \Phi_j \right\rangle .$$

When the molecular orbitals are orthogonal, such as are produced by the

HF method, $\langle \Phi_i | \Phi_j \rangle = \delta_{ij}$ (where δ is the Kronecker delta function), so we obtain characteristic equations of the form

$$\hat{H} C^{\text{CI}} = E C^{\text{CI}} .$$

This can be otherwise expressed as

$$\begin{pmatrix} H_{00} - E & H_{01} & \cdots & H_{0i} & \cdots \\ H_{10} & H_{11} - E & \cdots & H_{1i} & \cdots \\ \vdots & \vdots & \ddots & \cdots & \cdots \\ H_{i0} & H_{i1} & \vdots & H_{ii} - E & \cdots \\ \vdots & \vdots & \vdots & \vdots & \ddots \end{pmatrix} \begin{pmatrix} C_0^{\text{CI}} \\ C_1^{\text{CI}} \\ \vdots \\ C_i^{\text{CI}} \\ \vdots \end{pmatrix} = \begin{pmatrix} 0 \\ 0 \\ \vdots \\ 0 \\ \vdots \end{pmatrix} .$$

The CI ground-state energy is given by the smallest eigenvalue of the matrix, and its respective eigenvector contains the C_i^{CI} coefficients in Φ_{CI}. The i^{th}-smallest eigenvalue similarly gives the energy of the $(i-1)^{\text{st}}$ excited state.

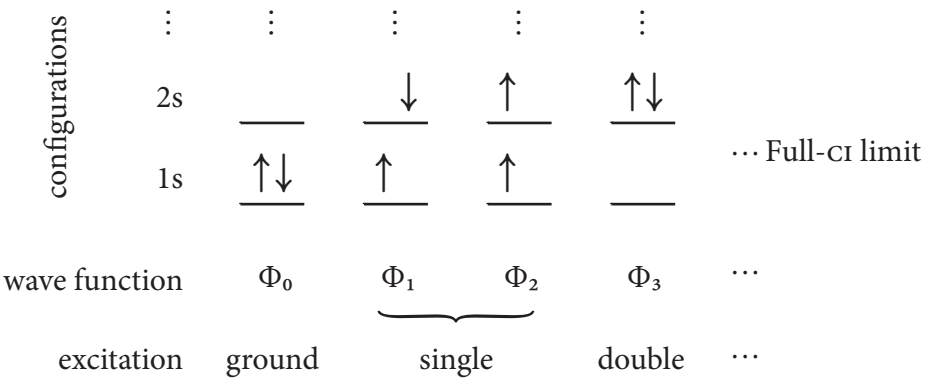


Figure 3.1: A schematic of the ground and some excited configurations in helium. Each electronic configuration can be expressed as a single Slater determinant, but multiple must be considered in the CI method, as they will mix (interact). In practice, because the computational space grows very quickly, this method is limited to very small systems, and is limited by the full-CI limit, which accounts for all (infinite) configurations. Naturally, this is computationally impossible, and the space must be truncated at some point, which will introduce inaccuracy. For large systems, this inaccuracy will be significant.

The excited CSFs are computed by considering electrons in the HF reference wavefunction moving from occupied orbitals to virtual orbitals, so the number of such CSFs scales with $n_{\text{electrons}}!$, which is computationally intractable.

The results are generally qualitatively correct and recover a "static" part of the correlation, which effectively considers near-degeneracy (con-

figurations with similar energy). One weakness in the CI method, as with HF, is its neglect of the correlation energy between electrons, or dynamic correlation. Both static and dynamic correlation effects, however, can be taken into account by considering more Slater determinants.

3.1.3 *Multi-configurational self-consistent field*

MCSCF is a class of methods in quantum chemistry that generate reference states in molecules that are *qualitatively* correct. It is most useful in cases where HF and DFT are inadequate, such as systems where the ground state is a superposition of different electron configurations (see Section 3.1.2) or where there are states that are nearly degenerate in energy (see Section 3.2.1). As its name implies, MCSCF combines the CI method with the SCF method (i.e., the HF method). This mitigates the weaknesses of both the CI method, where the molecular orbitals are not varied, and the HF method, where only one Slater determinant is considered. Because this combination greatly increases wave-function complexity, restrictions are usually placed on the calculation space. Some core orbitals may be held constant, for instance, or the calculations may be carried out on only a small subset of configurations.

As an extension of HF, where the wavefunction is taken to be expressible as a single Slater determinant, MCSCF is considered a multi-determinant method. Because a Slater determinant represents a single configuration, by nature, it accounts for only *average* electron–electron interactions. Hence, by using only one Slater determinant, HF neglects the correlation energy between electrons.

Like the CI method, MCSCF methods construct wavefunctions from CSFs, but determine the coefficients and orbitals used to construct the CSFs by minimising the energy of the wavefunction

$$\Phi_{\text{MCSCF}} = \sum_{i=0} C_i^{\text{MCSCF}} \Psi_i^{\text{CSF}}.$$

There are many approaches to selecting CSFs, which collectively form the class of MCSCF methods. Many of these are included in the `molcas` package, which we use for *ab initio* calculations in this thesis.

3.1.4 CASSCF

In complete-active-space self-consistent field (CASSCF), all possible CSFs are considered from a chosen set of so-called "active orbitals", which are often chosen to be the highest occupied and lowest unoccupied molecular orbitals from a HF calculation (at the full-CI limit); Conversely, an inactive space consists of the lowest-energy orbitals from inner doubly occupied shells and a virtual space consists of high-energy virtual orbitals (see Figure 3.2).

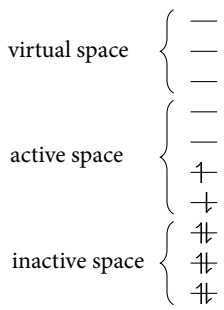


Figure 3.2: A schematic representation of the three orbital subspaces of a complete-active-space self-consistent field (CASSCF) *ansatz*.

The most successful approaches using multiple determinants begin by using the CASSCF method to determine a reference wavefunction. For atoms from all over the Periodic Table, this method used together with second-order perturbation theory provides accurate results on molecules in both ground and excited states.[160–167] In theory, CASSCF can be applied to any electronic problem, but in practice, the size of the active space used in CASSCF presents a limitation on the computational tractability.

3.1.5 *RASSCF*

For an active space of m spatial orbitals, $n_\uparrow$ up spins, and $n_\downarrow$ down spins, the total number of CSFs is given by

$$n_{\text{total}} = \binom{m}{n_\uparrow}\binom{m}{n_\downarrow},$$

which for large m is roughly exponential in m. Since, therefore, the number of CSFs increases exponentially with the number of active orbitals, for even medium-sized molecules, the computational cost of CASSCF is prohibitively large: supercomputer implementations can partially converge only up to an active space of 22 electrons in 22 orbitals[168]. The restricted-active-space self-consistent field (RASSCF) method allows larger active spaces to be used for the reference wavefunction, giving access to a wider variety of chemical problems. Like CASSCF, there are an inactive space, a virtual space, and an active space. In RASSCF, however, the active space is split up into three subspaces: RAS1, RAS2, and RAS3, which each have restrictions on excitations (see Figure 3.3).

RAS2 behaves exactly like the active space in CASSCF; RAS1 comprises orbitals which are doubly occupied except for some specified maximum number of holes and RAS3 comprises orbitals which are unoccupied except for some specified maximum number of electrons. In essence, excitations from RAS1 into RAS2 and from RAS2 into RAS3 are considered only, restricting the space of interactions considered, thereby reducing the computational cost. These subspaces must be chosen judiciously, therefore, to give useful results while keeping computation time feasible. This should be done based on how the orbitals are expected to behave with orbitals of neighbouring atoms.

VIRTUAL	Orbital occupation number = 0
RAS3	Orbital occupation number $\in [0, 2]$; $n_{\text{subspace electrons}} \leq N$
RAS2	Orbital occupation number $\in [0, 2]$
RAS1	Orbital occupation number $\in [0, 2]$; $n_{\text{subspace holes}} \leq N$
INACTIVE	Orbital occupation number = 2

Figure 3.3: A schematic representation of the spaces (and subspaces) in the restricted-active-space self-consistent field (RASSCF) method, and the conditions on orbitals contained within them.

3.2 Comparison with other methods

3.2.1 *Density-functional theory* (DFT)

DFT is an *ab initio*, iterative, computational modelling method that predicts behaviour on the basis of only quantum-mechanical considerations. Like in HF, the molecular nuclei are held fixed (though some recent work has suggested using DFT without assuming the BO approximation[169]). In principle, DFT is formally derived from the time-independent Schrödinger equation, with a reduction of a many-body problem with an electron–electron interaction energy to a single-body problem without it.

The weaknesses of DFT lie in the approximations it must make, including to the exchange- and correlation-energy functionals. In particular, the delocalisation error of these approximations, which arise from a dominating Coulomb term, result in underestimates of chemical-reaction barriers and material band gaps, and overestimates of binding energies in charge-transfer complexes. DFT also fails to describe electron–electron interaction, because electron density does not adequately describe it.[170]

DFT, however, is very fast compared to some other *ab initio* methods, and empirically, it can be very accurate or powerfully predictive in many situations. In many ways, it is similar to HF because of the computational similarity of solving the Kohn–Sham equations of DFT to solving the equations for HF, and this similarity has aided its rapid rise. With SCF methods,

the main objective is to full-CI wavefunction; DFT attempts to minimise the energy over some density ρ, assuming some exact functional $E[\rho]$. Since DFT in principle does not distinguish between systems to decide what functional to apply (the researcher might, but the method does not), it is the functional that is of the same complexity as doing a full-CI on all possible systems. In essence, the computational challenge of CI calculations for the wavefunction in SCF methods and their successors into a theoretical challenge to find some universal functional that is exact for all densities.

3.3 Spin Hamiltonian calculations

3.3.1 *Electron paramagnetic resonance (EPR)*

To predict the results of transmission experiments, we turn to electron paramagnetic resonance (EPR) simulations. We do this by explicitly determining the transition probability of every pair of states at each field strength by brute force. This has the advantage of not relying on approximations and including all transitions, allowed or forbidden. The linewidth of the EPR spectra is assumed to follow a pseudo-Voigt shape,

$$V(\Delta E, \eta, \nu) = \nu \frac{2\eta/\pi}{1 + 4\left(\frac{\Delta E}{\eta}\right)^2} + (1-\nu)\frac{2\eta\sqrt{\ln 2/\pi}}{\exp\left(-(4\ln 2)\left(\frac{\Delta E}{\eta}\right)^2\right)},$$

where $\Delta E = \left||E_i - E_j| - E_{\mathrm{MW}}\right|$ is the difference in energy between the microwave signal and the energy gap $|E_i - E_j|$ between spin eigenstates j and i (in the presence of some external magnetic field $\vec{B}$), η is the EPR resonance linewidth, and ν is the Voigt parameter.

The absorption, accordingly, is then given by

$$A(\vec{B}) = \sum_{i<j} \left|\langle i|H(\vec{B})|j\rangle\right|^2 \frac{\exp\left(-\frac{E_i}{k_B T}\right) - \exp\left(-\frac{E_i}{k_B T}\right)}{Z(\vec{B})} V(\Delta E, \eta, \nu),$$

where Z is the partition function, defined as

$$Z(\vec{B}) = \sum_i \exp\left(-\frac{E_i(\vec{B})}{k_B T}\right).$$

3.3.2 *Crystal orientation and rotation*

The spin operator $\hat{S}$ in the Zeeman term assumes a Cartesian basis. Since it is applied to a magnetic-field term $\vec{B}$, the coordinate basis most convenient is often the coordinate frame in which magnetic measurements are conducted. Accordingly, the rest of the Hamiltonian must also be expressed in the same basis. A set of Stevens coefficients for a molecule, then, only have physical meaning when the coordinate basis is also specified. In a typical crystal, however, there are multiple inequivalent molecules (that is, those not related by inversion) per unit cell, and calculations will give the Stevens coefficients in the basis of only one given molecule. Hence, to find a meaningful result for a crystal, it is necessary also to determine the transformation between inequivalent molecules of a unit cell. Then, by rotating the Stevens coefficients of each inequivalent molecule so that they share a common coordinate basis, the effects of each inequivalent molecule can be calculated independently and superposed to find the total behaviour of a crystal.

3.4 Resolving experiment data

In a particular orientation relative to the crystal structure of the externally applied magnetic field, the response of the spin-level energies of a compound is determined by its crystal-field parameters B_k^q and its g-tensor. For a transmission experiment on a crystal strongly coupled to a microwave cavity resonator, the experimental data will show avoided level crossings between the energy levels of the crystal's spin levels and the resonant energy of the cavity (Figure 3.4). This effectively allows us to probe the spin levels

as the magnetic field is varied. Additionally, the crystal (or equivalently magnetic field) may be rotated to give a better picture of the spin levels. This can then be compared to *ab initio* or other theoretical calculations to verify our understanding of the spin system.

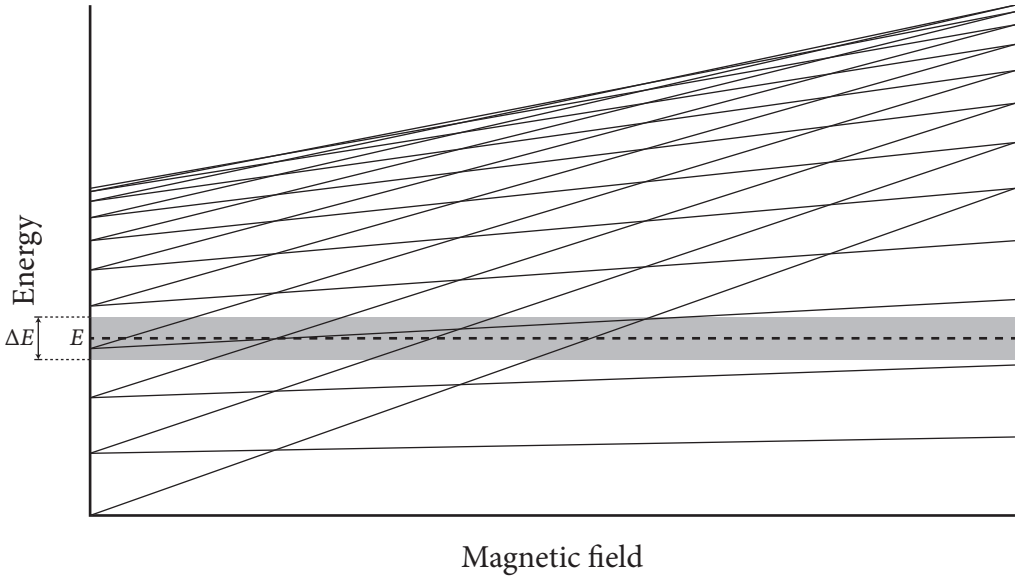


Figure 3.4: A schematic representation of the portion of the energy-splitting picture that is probed by a transmission experiment in an example spin system strongly coupled to a microwave cavity resonator of a given energy E and energy width ΔE, which depends on the quality factor Q of the resonator. The spin levels whose energy lines that cross the energy of the resonator will couple with the resonator when on-resonance (at the appropriate magnetic-field strength) and be experimentally detectable this way. A resonator with a lower Q probes more of the picture, but the interaction between the spin system and resonator will be weaker.

The analysed experimental data were taken from a $[Gd(hfac)_3(^tBubpy)]$ crystal, with transmission measurements conducted over a field range of ~−0.6 T–+0.6 T[b] and an energy range of 12.0656 GHz–12.0956 GHz, at orientations along the xy-, yz-, and xz-planes (in an arbitrary lab coordinate frame) in 2° intervals. This will be discussed in greater depth in Section 6.2.4.

[b] Some of these measurements were conducted over −0.55 T–+0.55 T instead.

3.5 Conclusions

In this chapter I have given an overview of the methods that are going to be applied in the following chapters in order to numerically calculate the magnetic properties of molecular systems. I started by describing the general features of *ab initio* methods and the usual approximations that are introduced in the evaluation of the Hamiltonian from an early stage. I then moved to considering self-consistent field methods, and

examined the descriptions of the orbitals that are necessary to achieve an accurate reproduction of the systems without incurring in unmanageable computational burdens.

The limitations of the different numerical approaches, the necessary checks, and the strengths of the different methods are important in order to understand why these approaches were followed for the specific samples examined. In the upcoming chapters I am going to use the methods here described to calculate specific properties, and to make predictions about the magnetic and quantum behaviour of molecular systems. We shall see how the numerical approaches can be combined with analytical descriptions of the quantum interactions in order to see novel phenomena arise, and to account for the inclusion and integration of molecular materials into quantum devices.

4 Determining magnetic anisotropy in rare-earth compounds

4.1 Overview

The compounds thus far described represent a possible class of technologies, such as spintronic devices. To use such compounds in future technology, however, engineers and scientists need to know the spin states of the compounds and how they would interact with proposed device designs. Understanding their magnetic anisotropy and being able to predict their magnetic behaviour, concretely, is critical to understanding the spin states. In this chapter, we examine how *ab initio* calculations and data analysis can be used to characterise the magnetic anisotropy of a system, and therefore predict its magnetic behaviour. The larger question concerns the energy levels of a high-spin magnetic system and dynamics involving them. Accordingly, in Chapter 5 we shall investigate the effects of strongly coupling a resonator to a magnetic system, and in Chapter 6 we shall look

more closely at alterations to the static properties in a Gd(III) crystal from strong coupling, and what further possibilities this may afford. All this, however, requires that we be able to accurately predict the magnetic anisotropy of a given compound, which will allow us to model the change of the energy levels from external influences. Often such prediction is not possible from experiments: because the many molecules contribute to the overall magnetic behaviour in different directions, the magnetic axes of individual molecules cannot be discerned from experiment. For example, in low-symmetry crystals containing more than two molecules per unit cell, it is impossible in principle to ascertain the magnetic easy axes of the individual molecules from magnetic measurements on the crystal. This difficulty raises two relevant questions: (1) Is it possible, then, in some cases to estimate the magnetic easy axes of an individual molecule from magnetic measurements within an acceptable error? (2) And can we reliably predict magnetic anisotropy and behaviour for rare-earth centres from first principles and crystallographic data?

4.2 Rare-earth compounds

Rare-earth compounds tend to crystallise in low-symmetry configurations. This makes it difficult to characterise their anisotropy, because the crystal axes may give no information about the magnetic axes. In monoclinic crystals, for instance, we are guaranteed by symmetry that a principal magnetic axis lies along the $\vec{b}$ crystal axis, but have no guarantees of further information, including whether the axis is a hard magnetic axis or an easy magnetic axis.

In this chapter, I will first look at a compound, considering only anisotropic behaviour. Second, I will look at compounds with functionalities, such as those that can be included into single-molecule devices. Among

all possible choices, I will specifically focus on compounds based on porphyrins with rare-earth centres.

4.3 [Dy(dbm)$_3$phen]

The [Dy(dbm)$_3$phen] compound is a monoclinic system, with four spin centres in the unit cell related by an inversion centre and a 2_1 screw axis along $\vec{b}$ (Figure 4.1). They are extremely common building blocks,[60, 171] but their anisotropy has been largely unexplored. This is because anisotropic behaviour of molecular constituents in materials is characterised using either dedicated diffraction methods,[172] which requires large-scale facilities and big crystals, or angle-resolved measurements, the latter of which has required specific crystal symmetries.[173] Because of their lower crystal symmetries, monoclinic crystals have thus far been limited to the former.

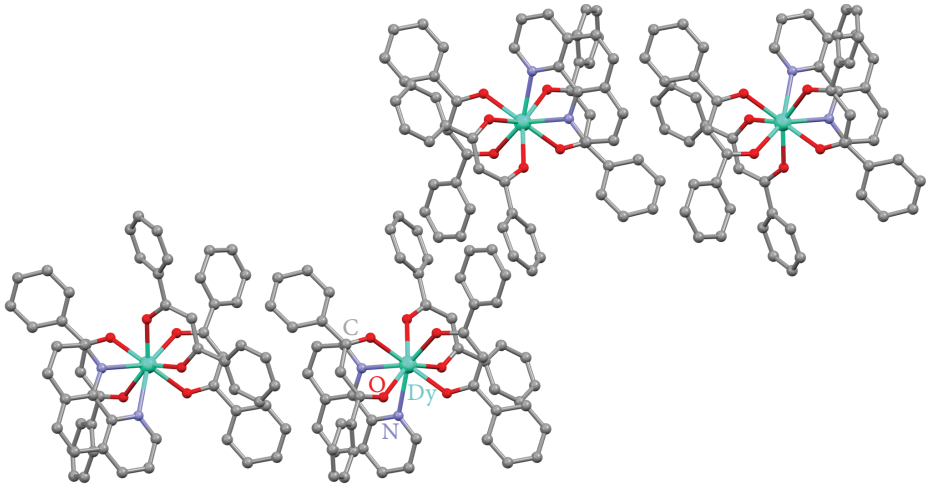


Figure 4.1: The unit cell of a [Dy(dbm)$_3$phen] crystal, which is monoclinic. There are four molecules per unit cell, related by inversion and a mirror plane (or equivalently, inversion and a screw axis), giving two inequivalent molecules per unit cell, with no higher symmetry. Hydrogen atoms have been omitted for clarity.

While the general magnetic properties of dysprosium β-diketonates are documented, the aforementioned symmetry problems have limited knowledge of the magnetic principal axes to only a few cases.[174] The Dy^{III} ion is coordinated by six oxygen atoms of the β-diketonate pair, which induces strong uniaxial magnetic anisotropy in the ion.[175–180]

The conventional symmetry restrictions, however, ignore the possibilities of analysing temperature of frequency, which are governed by the molecular anisotropy. Once a few conditions are met, the molecular anisotropy can be determined with high accuracy, up to uncertainties from sensitivity limits in standard methods of measurement and not crystal symmetry, even in situations where it would have been considered intractable. This method is applicable to rare-earth-based molecular magnets, and addresses the problems surrounding monoclinic systems, which accounts for about half of all known molecular crystals.[181] We then compare the results of analysis directly to results from *ab initio* calculations, to verify their accuracy.

4.3.1 *Ab initio calculations*

Ab initio calculations were performed using post-Hartree–Fock (HF) with the relativistic quantum CASSCF–RASSI–SINGLE_ANISO method implemented in MOLCAS (see Chapter 3), predicting strong easy-axis magnetic anisotropy. The ground doublet well is isolated from excited states, with an energy gap of about 150 cm^{-1} from the first excited states. The resulting components of the effective g-value for the ground Kramers doublet, determined along the molecular principal axes, were 19.39, 0.0097, and 0.0058. The anisotropy is therefore strongly axial, with one component more than three orders of magnitude larger than the others. The easy axis is perpendicular to the phen ligand, in the plane of the two dbm ligands (Figure 4.2), as we expect from simple electrostatics.[175]

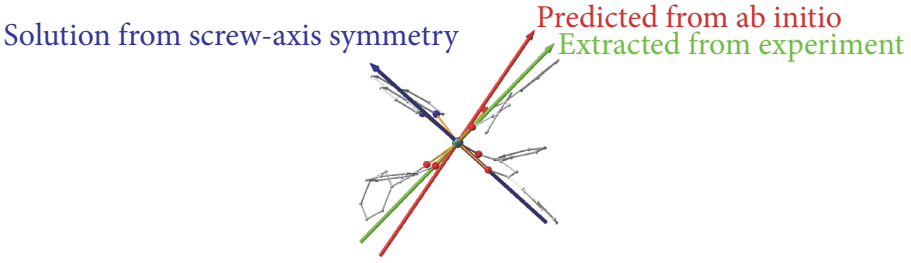


Figure 4.2: The easy axis of the [Dy(dbm)$_3$phen] molecule, as predicted by the symmetry of the screw axis (blue), *ab initio* calculations (red), and analysis of experimental magnetic data (green). Hydrogens have been omitted for clarity.

From the crystal symmetries, we can express a transformation T between two non-equivalent molecules in the crystal structure. Here we will choose those related by the 2_1 screw axis. In the $\hat{a}, \hat{b}, \hat{c}^*$ basis of the crystal, then,

$$T = \begin{pmatrix} 1 & 0 & 0 \\ 0 & -1 & 0 \\ 0 & 0 & 1 \end{pmatrix}.$$

This allows us to then determine the magnetic anisotropy of all four molecules in the unit cell, where for any $\bar{\bar{g}}$ component $\vec{g}_i$, the four values in the unit cell will be given by

$$\vec{g}_i, T\vec{g}_i, -T\vec{g}_i, -\vec{g}_i.$$

For magnetic measurements, however, when two molecules are related to each other by inversion, these two molecules experience effective magnetic fields in opposite directions. The overall g measured experimentally, then, will be given by

$$\bar{\bar{g}}_{\text{crystal}} = 2(\bar{\bar{g}} + T\bar{\bar{g}}),$$

and the angle ψ between the molecular and crystal magnetic easy axes can be found by

$$\psi = \arccos(\hat{g}_{\text{easy}} \cdot \hat{g}_{\text{crystal,easy}}) \approx 39.2202°.$$

4.3.2 *Analysing experimental magnetic data*

The magnetisation $\vec{M}$ of the crystal is given by

$$\vec{M} = \bar{\bar{\chi}}\vec{H},$$

where $\bar{\bar{\chi}}$ is the magnetic-susceptibility tensor and $\vec{H}$ is the external magnetic field. In some laboratory coordinate system, this can be expressed

$$\vec{M} = H_0 \begin{pmatrix} \sin\theta\cos\phi \\ \sin\theta\sin\phi \\ \cos\theta \end{pmatrix}^{\mathrm{T}} \begin{pmatrix} \chi_{xx} & \chi_{xy} & \chi_{xz} \\ \chi_{yx} & \chi_{yy} & \chi_{yz} \\ \chi_{zx} & \chi_{zy} & \chi_{zz} \end{pmatrix} \begin{pmatrix} \sin\theta\cos\phi \\ \sin\theta\sin\phi \\ \cos\theta \end{pmatrix},$$

where H_0 is the magnitude of the magnetic field, $\theta = \arccos \hat{H} \cdot \hat{z}$ is the azimuthal angle, ϕ is the polar angle, and χ_{ij} are the components of $\bar{\bar{\chi}}$ in the lab frame. The magnetic susceptibility has eigenvectors $\vec{\lambda}_1$, $\vec{\lambda}_2$, and $\vec{\lambda}_3$, which define the crystal's magnetic principal axes. When the unit cell contains more than one asymmetric unit, the magnetic susceptibility of one molecule m be related to another m' through a symmetry operation $S_m^{m'}$, such that

$$\bar{\bar{\chi}}^{m'} = S_m^{m'} \bar{\bar{\chi}}^m S_m^{m'\dagger},$$

where $\bar{\bar{\chi}}^m$, $\bar{\bar{\chi}}^{m'}$ are the molecular magnetic susceptibilities. The total (crystal) magnetic susceptibility is, then,

$$\bar{\bar{\chi}} = \sum_{m'} \bar{\bar{\chi}}^{m'} = \sum_{m'} S_m^{m'} \bar{\bar{\chi}}^m S_m^{m'\dagger}.$$

When molecular symmetry is low, however, elements of the sum cancel out, leading to the rule of thumb that molecular susceptibility can be determined experimentally only when there is a single molecule in the asymmetric unit from which the others are generated by inversion centre or high-symmetry position.[57, 173, 182]

From both observation of single-molecule magnet (SMM) behaviour and the *ab initio* calculations, however, we know that the compound exhibits strong molecular Ising anisotropy. Consider the molecular frame of reference $\hat{x}', \hat{y}', \hat{z}'$ such that $\bar{\bar{\chi}}^m$ is diagonal with $\chi^m_{z'z'} \gg \chi^m_{y'y'} \approx \chi^m_{x'x'}$. By symmetry, when a molecule has uniaxial anisotropy, one of the molecular hard axes, $\hat{x}'$ and $\hat{y}'$, must lie in the $\hat{a}\hat{c}'$ plane along the crystal hard axis, $\hat{\lambda}_3$,[183] which without loss of generality we shall take to be $\hat{x}'$. Defining ψ as the angle between the molecular easy axis $\hat{z}'$ and the crystal easy axis $\hat{\lambda}_1 = \hat{b}$ we then have for the two non-equivalent molecules in the unit cell,

$$\begin{pmatrix} \hat{x}' \\ \hat{y}' \\ \hat{z}' \end{pmatrix} = T_1 \begin{pmatrix} \hat{\lambda}_1 \\ \hat{\lambda}_2 \\ \hat{\lambda}_3 \end{pmatrix} = \begin{pmatrix} \cos\frac{\pi}{2} & \cos\frac{\pi}{2} & \cos 0 \\ \cos\left(\frac{\pi}{2} - \psi\right) & \cos(\pi - \psi) & \cos\frac{\pi}{2} \\ \cos\psi & \cos\left(\frac{\pi}{2} - \psi\right) & \cos\frac{\pi}{2} \end{pmatrix} \begin{pmatrix} \hat{\lambda}_1 \\ \hat{\lambda}_2 \\ \hat{\lambda}_3 \end{pmatrix},$$

$$\begin{pmatrix} \hat{x}'' \\ \hat{y}'' \\ \hat{z}'' \end{pmatrix} = T_2 \begin{pmatrix} \hat{\lambda}_1 \\ \hat{\lambda}_2 \\ \hat{\lambda}_3 \end{pmatrix} = \begin{pmatrix} -\cos\frac{\pi}{2} & \cos\frac{\pi}{2} & \cos 0 \\ -\cos\left(\frac{\pi}{2} - \psi\right) & \cos(\pi - \psi) & \cos\frac{\pi}{2} \\ -\cos\psi & \cos\left(\frac{\pi}{2} - \psi\right) & \cos\frac{\pi}{2} \end{pmatrix} \begin{pmatrix} \hat{\lambda}_1 \\ \hat{\lambda}_2 \\ \hat{\lambda}_3 \end{pmatrix}.$$

The crystal magnetic susceptibility tensor $\chi = \frac{1}{2}\left(T_1^\dagger \chi^m T_1 + T_2^\dagger \chi^m T_2\right)$, then, is

$$\chi = \begin{pmatrix} \chi^m_{z'z'}\cos^2\psi + \chi^m_{y'y'}\sin^2\psi & 0 & 0 \\ 0 & \chi^m_{z'z'}\sin^2\psi + \chi^m_{y'y'}\cos^2\psi & 0 \\ 0 & 0 & \chi^m_{x'x'} \end{pmatrix},$$

where χ^m is the diagonalised molecular susceptibility tensor and $\chi^m_{x'x'}$,$\chi^m_{y'y'}$, and $\chi^m_{z'z'}$ are the respective diagonal elements. In the $\vec{\lambda}_1\vec{\lambda}_2$ plane, then,

$$\chi^m_{z'z'}\cos^2\psi + \chi^m_{y'y'}\sin^2\psi = \lambda_1, \tag{4.1}$$

$$\chi^m_{z'z'}\sin^2\psi + \chi^m_{y'y'}\cos^2\psi = \lambda_2, \tag{4.2}$$

where $\psi = \arccos(\hat{z}' \cdot \hat{\lambda}_1)$ is the angle between the molecular and crystal magnetic easy axes. Defining the ratios $\zeta = \chi^m_{y'y'}/\chi^m_{z'z'} \neq 1$ and $\lambda = \lambda_1/\lambda_2 \neq 1$, we can solve Equations (4.1) and (4.2):

$$\psi = \arctan\left(\sqrt{\frac{1-\lambda\zeta}{\lambda-\zeta}}\right).$$

Though ζ is unknown in principle, this gives an exact solution for ψ in the limit of pure molecular Ising anisotropy ($\zeta \to 0$ or $\zeta \to \infty$).

The sensitivity of the angle ψ to the values of ζ and λ depends on the values of ζ and λ:

$$\frac{\partial\psi}{\partial\zeta} = -\frac{(\lambda-1)\sqrt{\frac{\lambda\zeta-1}{\zeta-\lambda}}}{2(\zeta-1)(\lambda\zeta-1)}.$$

For $\lambda \approx 1$, then, the change in ψ relative to changes in either ζ or λ is quite small. Taking $\lambda = 1+\epsilon$, we find

$$\frac{\partial\psi}{\partial\zeta} = -\frac{\epsilon\sqrt{\frac{\zeta+\epsilon\zeta-1}{\zeta-\epsilon-1}}}{2(\zeta-1)(\zeta+\epsilon\zeta-1)}.$$

In order for ψ to be insensitive to changes in ζ, we must have $\left|\frac{\partial\psi}{\partial\zeta}\right| \ll 1$. Solving, we find the condition

$$\epsilon \ll \frac{2(1-4\zeta+6\zeta^2-4\zeta^3+\zeta^4)+2\sqrt{O(\zeta^4)+4\zeta^5+4\zeta^6-4\zeta^7+\zeta^8}}{1+4\zeta-8\zeta^2+4\zeta^3},$$

which can be approximated as $\epsilon \ll \zeta$ for $\zeta \gg 1$ and $\epsilon \ll 2$ for $\zeta \ll 1$. Hence, under this condition, the direction of the easy axis, which is parameterised by ψ, is roughly the same for even large variations in the susceptibility of the crystal. We can also see this graphically (Figure 4.4), where even large variations in ζ produce relatively small variations in ψ, tightly clustered around one value. Thus, when independent evidence indicates strong molecular Ising anisotropy, we can estimate the direction of the easy axis within the limits of confidence even from experimental results.

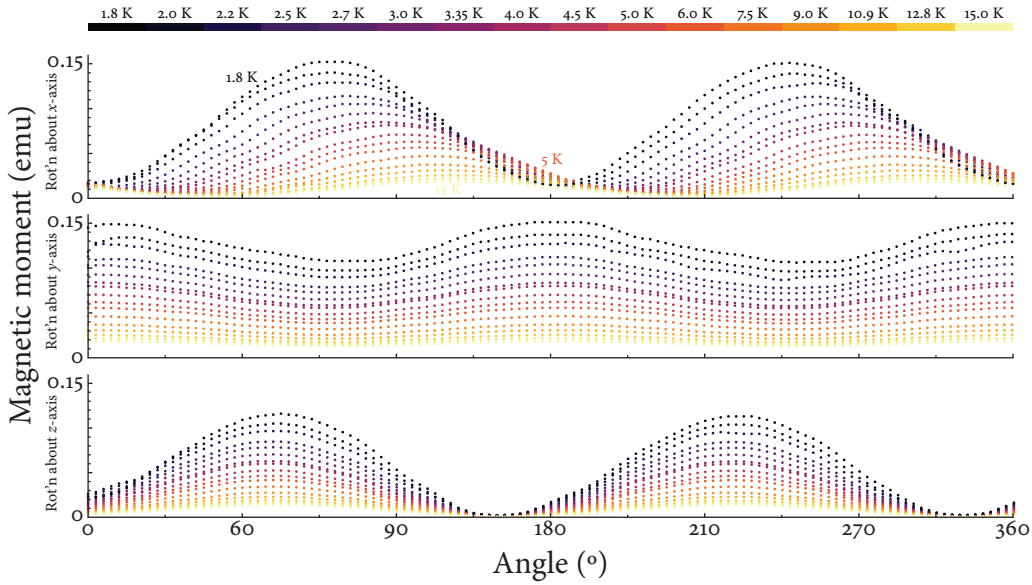


Figure 4.3: A plot of the experimental data from magnetic measurements by Michael Slota and Shang-Da Jiang. These measurements were taken at different rotations about three arbitrary but orthogonal and fixed axes. These data were fit according to Eqs. (4.1) and (4.2), with the experimental uncertainties giving bounds on the estimated angle ψ (see Figure 4.4). Measurements were conducted at various temperature, of which a few are marked in the figure. From darkest to lightest, the temperatures were: 1.8 K, 2 K, 2.2 K, 2.5 K, 2.7 K, 3 K, 3.35 K, 3.5 K, 4 K, 4.5 K, 5 K, 6 K, 7.5 K, 9 K, 10.9 K, 12.8 K, and 15 K.

In this case, after magnetic measurements were run on a crystal of Dy(dbm)$_3$phen by Michael Slota and Shang-Da Jiang, and the data (Figure 4.3) obtained by him were fit according to Equations (4.1) and (4.2), both the experimental results and *ab initio* calculations confirmed the Ising-type anisotropy, and within the region experimental error, the value of ψ was determined to be $39.4 \pm 1.0°$.

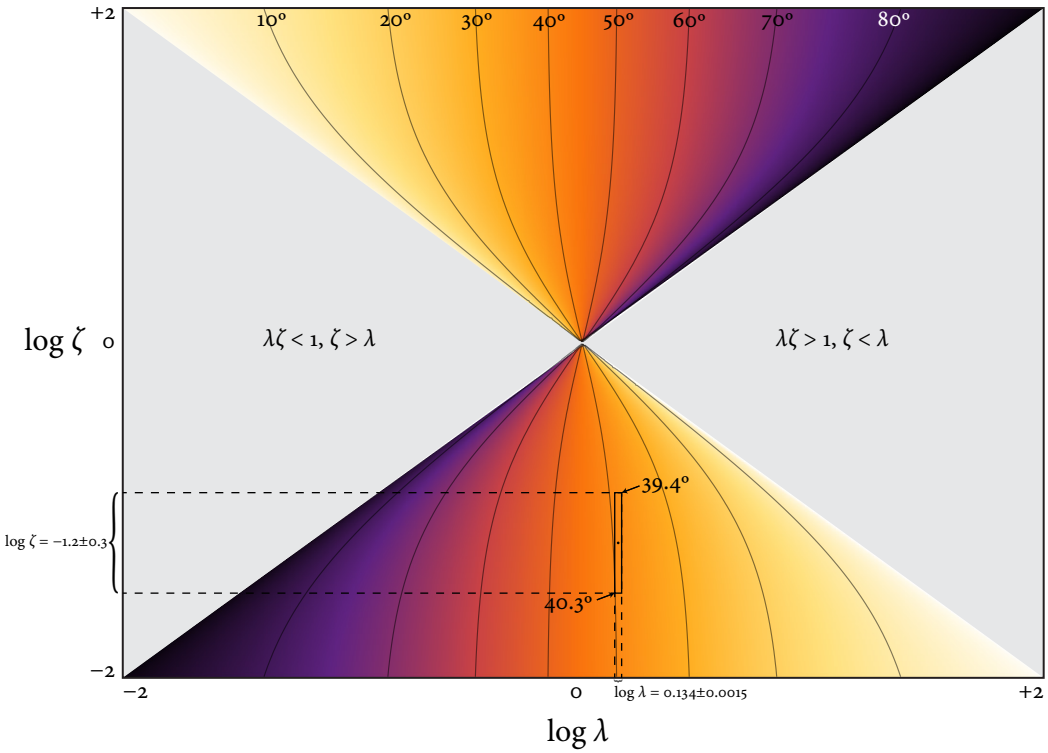


Figure 4.4: A plot of the calculated angle ψ between the molecular and crystal axes as a function of the logarithm of $\zeta = \chi^m_{y'y'}/\chi^m_{z'z'}$, the ratio of the $y'y'$ and $z'z'$ molecular magnetic susceptibilities, and the logarithm of $\lambda = \lambda_1/\lambda_2$, the ratio of the calculated eigenvalues of the susceptibility tensor. The value of ψ is undefined in the gray regions, and the angle gets arbitrarily close to 0° and 90° as $\zeta\lambda \to 1$ and $\zeta \to \lambda$, respectively. The uncertainty in lambda is determined from the experimental error, and we see here that even when an extremely large uncertainty in ζ is assumed, the uncertainty in ψ is quite small.

This method of estimating ψ is limited by accuracy in the lesser of $|\log\zeta|$ and $|\log\lambda|$. In this case, though significantly increasing the uncertainty in λ (tripling the error in the logarithmic scale) increases uncertainty by only 1°, the effect is still significantly more than increasing the uncertainty in ζ (Figure 4.5). The insensitivity of ψ to changes in ζ persists, in fact, until ζ approaches λ in magnitude, or equivalently, as long as $\zeta \ll \lambda$, $\zeta \gg \lambda$, $\lambda\zeta \ll 1$, or $\lambda\zeta \gg 1$.

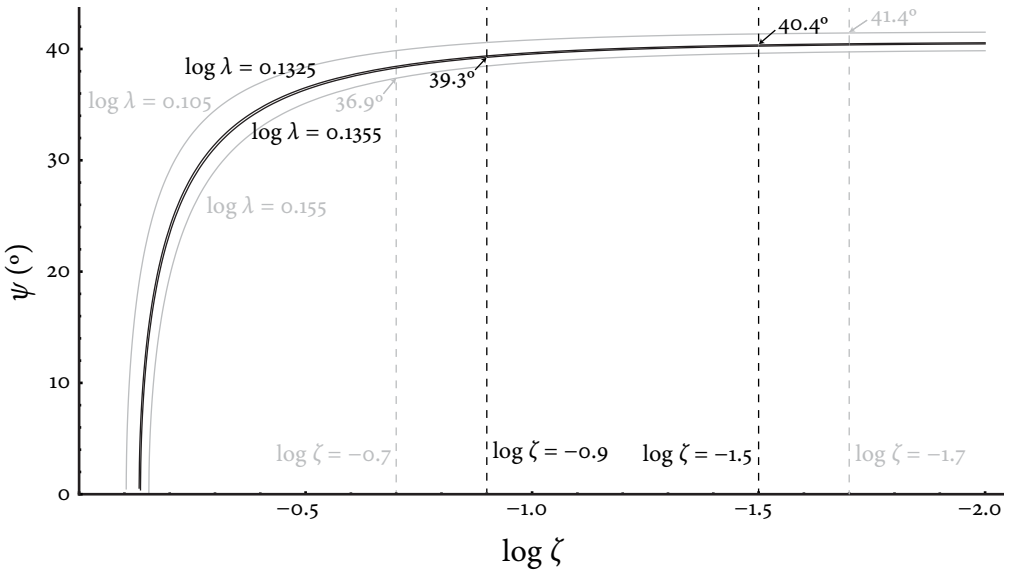


Figure 4.5: A plot of the calculated angle ψ between the molecular and crystal axes as a function of the logarithm of $\zeta = \chi^m_{y'y'}/\chi^m_{z'z'}$, the ratio of the $y'y'$ and $z'z'$ molecular magnetic susceptibilities, for various values of logarithm of $\lambda = \lambda_1/\lambda_2$, the ratio of the calculated eigenvalues of the susceptibility tensor. The value of ψ is somewhat insensitive to uncertainty of λ, within reasonable experimental errors, but it is far more insensitive to uncertainty in ζ, as long as $|\log\zeta|$ significantly differs from $|\log\lambda|$.

4.3.3 *Classes of crystal symmetry*

The method detailed above is relevant to more than just monoclinic systems. I give here a brief discussion of the crystal symmetry classes and the impact this method has on them and therefore the body of known crystals.

Triclinic. This class accounts for approximately one-fifth of all known molecular crystals,[181] and has been the most investigated to date, always giving a solution through previously known methods. There are only two point groups in triclinic systems: C_1 for $P1$ and C_i for $P\bar{1}$. Even though the lowest possible symmetry of a molecule is C_1, the symmetry of its magnetic properties cannot be lower than C_i, since the magnetic susceptibility of a

paramagnetic system must have inversion symmetry. It is therefore always possible to precisely determine the axes of a molecule's magnetic anisotropy, as long as there is only one independent paramagnetic centre in the unit cell. In the case of a $P\bar{1}$ space group, which has two magnetic centres related by an inversion operation, it is also possible to determine the axes of the molecules' magnetic anisotropy using the same method.

Monoclinic. This class accounts for approximately one-half of all known molecular crystals,[181] including the one treated above. The characteristic symmetry elements of a monoclinic system are one two-fold screw axis parallel to the $\hat{b}$-axis, or equivalently, glide planes whose normals are parallel to the $\hat{b}$-axis. Existing literature described ways to determine the axes of the molecules' magnetic anisotropy when the magnetic centres were located on either the screw axes or along the glide planes. Our method above demonstrates a method to determine the anisotropy axes to high accuracy even in cases when this is not true (with the magnetic centres in general locations in the unit cell), so long as the molecular anisotropy is strongly uniaxial.

Orthorhombic. This class accounts for approximately one-fifth of all known molecular crystals.[181] The characteristic symmetry elements of an orthorhombic system are two-fold axes parallel to the crystal axes, or equivalently, glide planes whose normals are parallel to the crystal axes. Standard treatment in the literature can determine the axes of the molecules' magnetic anisotropy only when the magnetic centres are located on at least two characteristic symmetry elements. This is very rare, however, making it impossible to determine the anisotropic axes in most cases. Using our method above, in cases where the magnetic centre is located on at least *one* characteristic symmetry element, we can determine the anisotropic axes to high accuracy, as long as the molecular anisotropy is uniaxial. The solution, in fact, is a special case of the discussion for monoclinic system

because of Neumann's principle, which states that one of the magnetic principal axes is determined by the symmetry element on which the spin centre is located, whereby one crystallographic axis must coincide with a molecular magnetic axis. Focusing on the plane normal to this axis, then, as long as the magnetic anisotropy is sufficiently large, we can determine the molecules' magnetic easy axis in the plane normal to this hard axis, in exactly the same way as we have demonstrated for Dy(dbm)$_3$phen above.

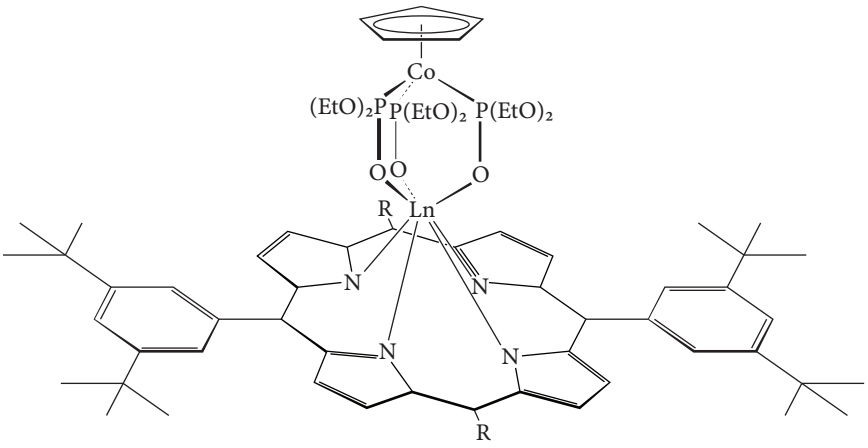
Uniaxial. These classes – trigonal, tetragonal, and hexagonal – together account for less than one-twentieth of all known molecular crystals.[181] The only characteristic symmetry elements are a single three-fold, four-fold, or six-fold axis (for trigonal, tetragonal, and hexagonal, respectively). In many cases, the magnetic centre is located on this axis. If this is true, and if both the molecule has Ising-type anisotropy and the mangetic easy axis is parallel to the crystal axis, known methods in the literature can be used to determine the axes of the molecules' magnetic anisotropy. In all other cases, there were no known methods to determine the magnetic easy axis. Using our method above, however, we can determine the magnetic easy axis even when the magnetic centre is not located on the crystal axis, as long as there is either a glide plane or a two-fold axis normal to the crystal axis.

Cubic. This class accounts for 0.5 % of all known molecular crystals.[181] Neither known methods in the literature nor our above method can be used to determine the axes of the molecules' magnetic anisotropy, but this is small fraction of known molecular systems.

4.4 Porphyrin complexes

For the following sections, some compounds have a rare-earth centre (Dy and Tb here considered) coordinated to Kläui's tripodal ligand, $Ln[CpCo\{P(=O)(OEt)_2\}_3]$,[a] and either (1) a porphyrin complex, 5,15-diphenyl-10,20-bis(3,5-dimethylphenyl)-(21,23-porphyrin)Ln, which we call 1-Ln for simplicity, or (2) a biporphyrin complex, 5,15′-diphenyl-10,10′,20,20′-tetrakis(3,5-dimethylphenyl)-3,17′-cyclo-7,13′-cyclo-5,15′-bi[(21,23-porphyrin)Ln], which we call 2-Ln for simplicity. The 1-Ln porphyrin complex is shown in Figure 4.6. While Kläui's tripodal ligand has a C_3 symmetry and the porphyrins have a C_2 symmetry, despite appearances at first glance, the compounds themselves have no rotational symmetry.

[a] Cp refers to cyclopentadienyl, C_5H_5, and Et is the ethyl group, CH_2CH_3.



1-Ln

Figure 4.6: The groups bound to the rare-earth porphyrin compounds in this chapter. The monomers 1-Tb and 1-Dy have a Tb and Dy centre, respectively, bound to the *porphyrin 1* group at the Ln sites, and all of the compounds have their rare-earth centres bound to Kläui's tripodal ligand (at the Ln site). R is a group that will vary depending on the lanthanide centre that affects mainly crystalisation, and Et denotes the ethyl group, CH_2CH_3.

Since the two metal centres we will be considering in this compound will primarily be Dy and Tb, the compounds accordingly will be called 1-Dy and 1-Tb, and so on, in the following sections.

4.5 1-Dy

4.5.1 *Overview*

The 1-Dy compound crystallises in a triclinic unit cell, with two molecules per unit cell. Two of the molecules are related to the other two by inversion, giving two inequivalent molecules per unit cell that are related by a 2_1 screw axis along $\vec{b}$ (or equivalently, a glide plane with normal $\vec{b}$). The cell axes $\vec{a}, \vec{b}, \vec{c}$ have respective lengths of 16.1981(3) Å, 23.3852(4) Å, and 25.4730(5) Å, with α, β, γ being 73.821(2)°, 89.254(2)°, and 86.965(1)°, respectively. As mentioned previously, the molecule does not exhibit any rotational symmetry. This is because, while porphyrin and Kläui's tripodal ligand both exhibit rotational symmetry, the former is two-fold and the latter is three-fold. The length of the butyronitrile groups in the groups functionalised to the porphyrin, moreover, result in orientations on either side of the porphyrin that are not reflectively symmetric either, so while the porphyrin complex itself and Kläui's tripodal ligand would suggest that the molecule would exhibit reflection symmetry, it actually does not. Moreover, the two molecules in the unit cell are not even related by any rototranslation operation.

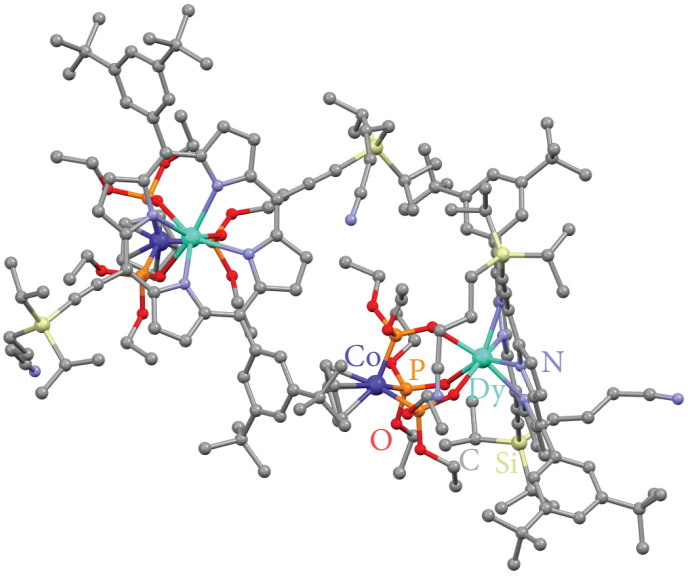


Figure 4.7: The unit cell of the 1-Dy crystal. There are two molecules per unit cell having no symmetry relation between them, giving two inequivalent molecules per unit cell, with no higher symmetry. Here, the R group of Figure 4.6 is the ethynyldiisopropylsilyl butyronitrile group, $C_2Si[CH(CH_3)_2]_2[C_4H_7N]$. Hydrogen atoms have been omitted for clarity.

4.5.2 *Ab initio calculations*

Because the molecule is too large to efficiently model, the calculations using MOLCAS excluded orbitals of extremely high energy. We considered only the lowest-lying 18 sextets and the lowest-lying 99 quartets.[184] Even the lowest-lying doublet has an extremely high energy, so all doublets were excluded. The geometry could have been simplified instead, but we opted to exclude orbitals instead, because the literature suggested that this set of orbitals would produce good results, without simplifications to the geometry being needed. The results of the calculated anisotropy of the molecule overlayed on the molecule itself are shown in Figure 4.8. As is the case with 1-Tb (Section 4.6), the molecule lacks true rotational symmetry, so its crystal-field Hamiltonian's isoenergy surface is likewise not rotationally symmetric around the pseudo-axis of the molecule. Because the functional group is large and itself asymmetric, however, the atoms of the groups on each side will orient themselves differently, so that the porphyrin part of the molecule is not exactly symmetric either, so unlike in 1-Tb, the axis of rotational symmetry of the isoenergy surface is not exactly tilted along what would otherwise by the plane of reflection symmetry of the molecule.

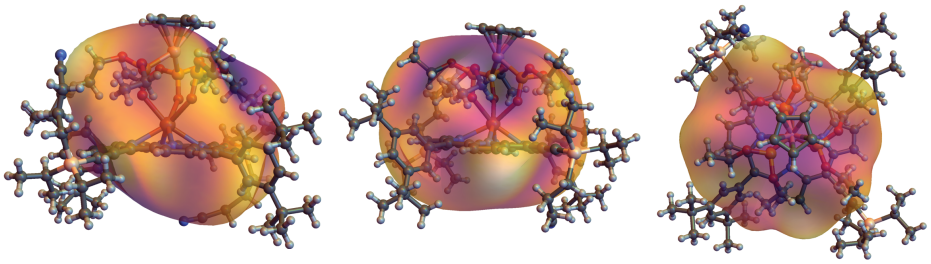


Figure 4.8: An isoenergy surface of the 1-Dy molecule's crystal-field Hamiltonian, overlayed on the molecule, as viewed along three directions. Higher-order contributions ($k \geq 6$) have been exaggerated to more clearly show higher-order differences in the energy surface.

4.5.3 *Comparison to transport measurements*

A transport measurement by Tian Pei was conducted in a single-molecule nanodevice (Figure 4.9) containing 1-Dy (and 1-Y, for reference), which was synthesised by James Thomas and Harry Anderson.

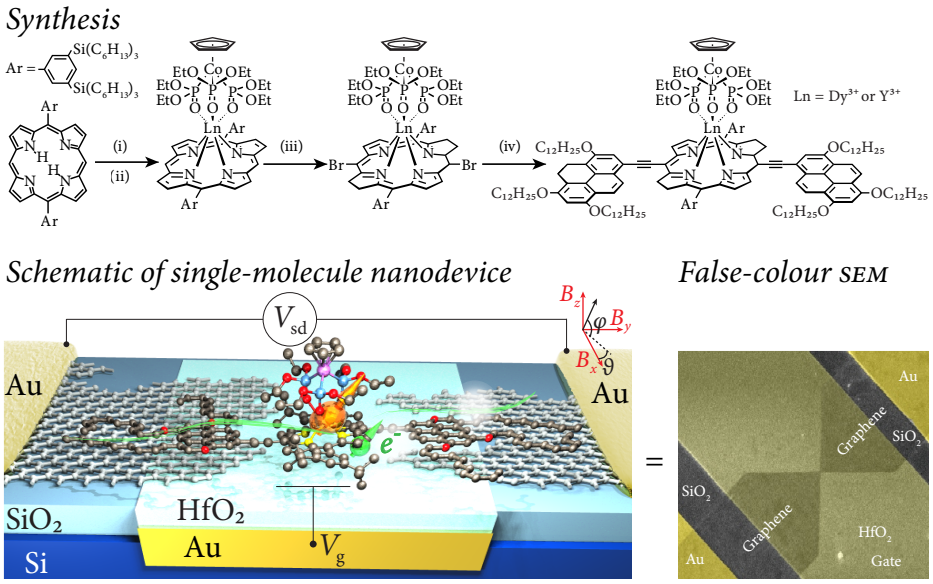


Figure 4.9: (Top) A scheme of the synthetic route to the 1-Dy and 1-Y compounds and the setup for their integration into a nanodevice. (Bottom left) A schematic of the transistor, with the molecule bridging the source and drain leads, which experimentally are graphene leads. The source–drain voltage V_{sd} is indicated, as well as the gate voltage V_g that can be applied from underneath through a gold strip, which is buried into Si and SiO_2 and separated from the molecule by a 10 nm HfO_2 layer. The experimental frame of reference for the vector magnetic field is also depicted, together with the angles θ and ϕ. (Bottom right) Figure adapted from **??**.

In the 1-Ln molecule, there is intramolecular exchange coupling J between the Ln spin centre and an unpaired electron in the porphyrin radical cation. When the molecule is integrated into the nanodevice, this coupling splits the degeneracy of the conduction channel through the porphyrin, even in the absence of magnetic field. The energies of these two resulting conduction channels shift when the gate voltage V_g is changed. When one of the energies corresponds to the energy gap between the source and drain of the nanodevice, which is adjusted by changing source–drain voltage V_{sd}, a spin-polarised current is allowed to flow. This current manifests as conductance lines in the transport measurements (Figure 4.10). The oxidation state of the molecule changes depending on V_g (1-Ln or 1-Ln^+ in the figures). In the transport measurement results of the 1-Dy device, an additional line (as compared with the 1-Y measurements) can be seen that meets the Coulomb diamond edge on the 1-Dy^+ side. This line indicates

an excitation of the 1-Dy$^+$ state and not of the 1-Dy state, and we thus call it 1-Dy$^+$ ·.

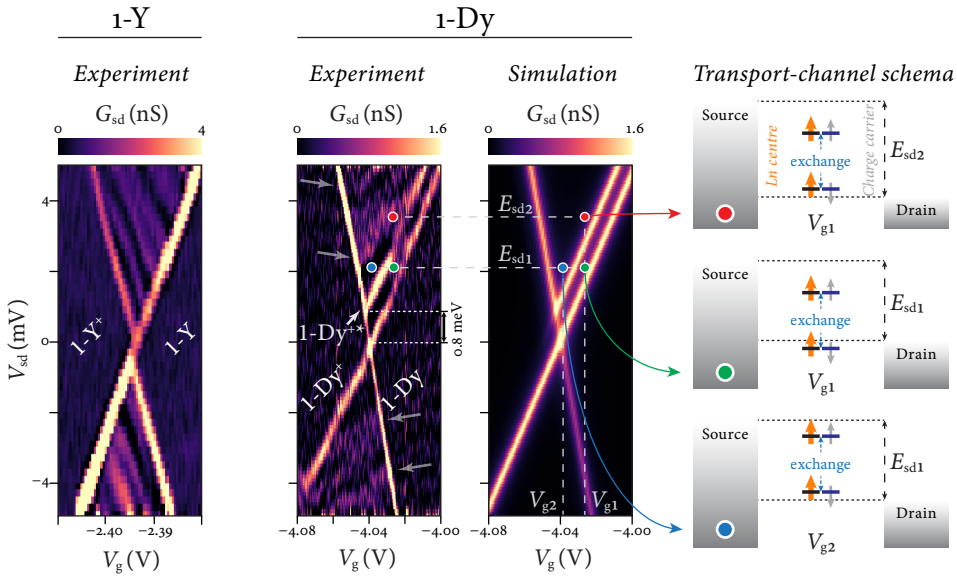


Figure 4.10: (Left) Map of the differential conductance $G = \frac{\partial I_{sd}}{\partial V_g}$ vs V_{sd} and V_g for 1-Y, showing regions of blocked conductance (dark) separated by ridges of high conductance (bright) where the molecular levels fall into the transport window. No spin level is observed. (Middle) The map of the differential conductance is also shown for 1-Dy, displaying the same regions of blocked conductance and a high conductance ridge where the molecular spin level produced by the exchange interaction is visible (arrow). The measurements can be compared to a simulated map of the transport, courtesy of James Thomas and Tian Pei. (Right) The energy-level diagrams corresponding to several configurations of the single-molecule transistor are depicted on the right, with the charge-carrier ½-spin in grey and the Dy ⁱ⁵⁄₂-spin in orange, and the parallel and antiparallel configurations split by the exchange interaction between the spins. All data were taken at 20 mK and zero field.

Exchange interactions depend on the relative orientations of the spins in the porphyrin radical cation and the Ln centre. Since the spin of the latter is extremely sensitive to its large anisotropy, experimental measurements can also probe the orientation of the molecular easy axis. Measurements of the source–drain current I_{sd} at various orientations along two planes show that, while it has no appreciable dependence on θ, it has a non-monotonous dependence on ϕ, with several local energy minima and maxima (Figure 4.11). These relations suggest that the axial anisotropy of the Dy centre lies roughly along the laboratory frame's z axis, which is perpendicular to the graphene plane. The lack of θ dependence also indicates, by symmetry, that there is no twist between the side groups and the porphyrin, so that the porphyrin and all its side groups are coplanar.

A calculation of the magnetic anisotropy from *ab initio* results found a tilt of ~ 70° from the plane of the porphyrin. A much less structured evolution is expected in the plane of the porphyrin because of the axial anisotropy of the lowest Kramers doublet. A fit of the energy data from

the transport measurement gives energy minima that indicate a tilted magnetic easy-cone anisotropy of the Dy centre tilted at an angle of $\phi_t = 68°$, which agrees with our result from *ab initio* calculations. The anisotropy energies that are extracted from torque measurements show similar energy dependences on ϕ, with the exception of the feature around $\phi = \pi/2$: In the neutral system, there is no unpaired spin in the porphyrin. Comparing the behaviours of the nanodevice and molecular crystal, we can see that the single-ion anisotropy affects the magnetoresistive signal of transport electrons because of exchange interaction, and this effect will modulate the transport characteristics of molecular spintronic devices.

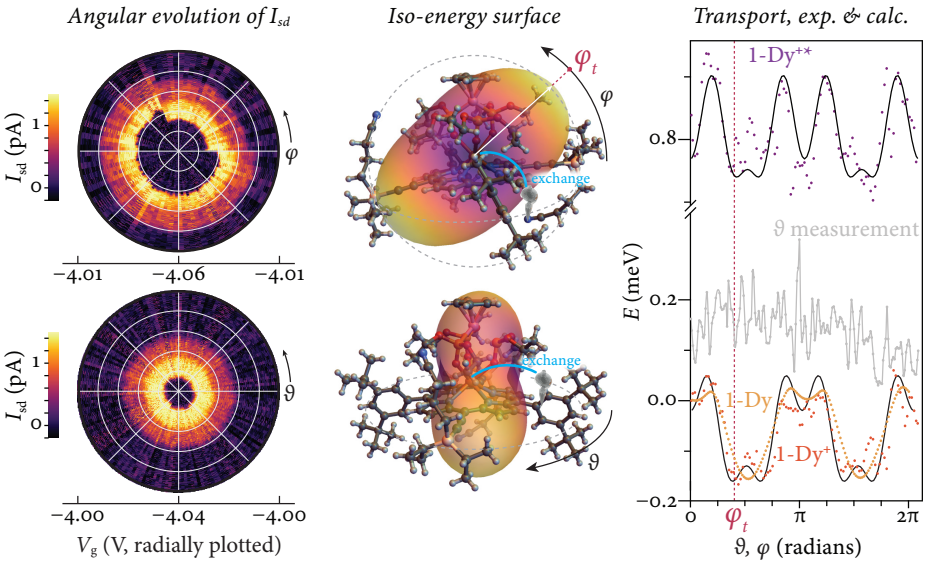


Figure 4.11: (Left) Angular evolution of the source–drain current for the azimuthal ϕ (top) and polar θ (bottom) angles, acquired at $V_{sd} = 1.5\,\text{mV}$ at a constant magnetic-field strength $|\vec{B}| = 1\,\text{T}$, on scanning V_g (radial direction), courtesy of Tian Pei. (Middle) The isoenergy surface for the 1-Dy complex's crystal-field Hamiltonian, as seen from two different orientations, with the polar angles indicated and the easy axis indicated with ϕ_t. (Right) The calculated and measured angular evolution of the anisotropic transport behaviour and the torque anisotropy are depicted for different molecular oxidation states.

4.5.4 *Simulation of magnetic-susceptibility measurements*

While the molecules are not identical, the slight twist of Kläui's tripodal ligand in one relative to another should intuitively result in only a rotation of the anisotropy axis with respect to the molecule's pseudo-axis. Hence, we cannot easily determine the magnetic behaviour of a crystal without running separate *ab initio* calculations on the second inequivalent molecule and simulating them independently, but we can still reasonably predict

the magnetic behaviour of a powder sample. We notice, however, that different twists in the tripodal ligand ought to produce approximately the same magnetic anisotropy but oriented differently, and this orientation difference would be taken into account from the random orientations of molecules when considering a powder sample.

The Curie law also gives that

$$M(B) \approx \frac{C}{T}B, \tag{4.3}$$

at high T, where C is the material-dependent Curie constant,

$$C = \frac{N\mu_o\mu_B^2}{3k_B}g_J^2 J(J+1), \tag{4.4}$$

where N is the number of magnetic atoms or molecule per unit volume, μ_o is the permeability of free space, μ_B is the Bohr magneton, k_B is the Boltzmann constant, g_J is the g-factor, and J the angular-momemtum quantum number. In principle, this means that $\chi_m T$ should be constant for temperatures above the Curie temperature T_C,

$$\chi_m T = \text{constant} \approx C.$$

Some paramagnetic materials, however, may follow the adapted Curie–Weiss law,

$$M(B) \approx \frac{C}{T - T_C}B, \tag{4.5}$$

but at sufficiently high temperatures $T \gg T_C$, the ratios should converge. In any case, we can define effective magnetic moment μ_{eff} according to

$$\mu_{\text{eff}} = \sqrt{\frac{3k_B}{N\mu_o\mu_B^2}}\sqrt{\chi_m T} \approx 797.727\sqrt{\chi_m T}, \tag{4.6}$$

which is effectively dimensionless but sometimes given in units of μ_B. We expect, then, that

$$\mu_{\text{eff}} = g_J\sqrt{J(J+1)}, \tag{4.7}$$

though in practice, the experimentally observed value may be slightly different (see Table A.2). We expect, then, that $\chi_{\text{m}}T$ should converge with

$$\lim_{T\to\infty}\chi_{\text{m}}T = \mu_{\text{eff}}^2\sqrt{\frac{N\mu_{\text{o}}\mu_B^2}{3k_{\text{B}}}} \approx \frac{\mu_{\text{eff}}^2}{797.727^2}. \tag{4.8}$$

We can thus apply Equation (4.7) to find an expected $\mu_{\text{eff}} \approx 10.6$, given in terms of μ_{B} as usual, which falls around the experimentally observed value of $\mu_{\text{eff}}^{\text{exp}}$ in the range 10.2–10.6. From Equation (4.8), then, the corresponding range of $\chi_{\text{m}}T$ is

$$0.163\times10^{-3}\,\text{m}^3\,\text{mol}^{-1}\,\text{K} \overset{\text{Dy}^{3+}}{\leq} \lim_{T\to\infty}\chi_{\text{m}}T \overset{\text{Dy}^{3+}}{\leq} 0.177\times10^{-3}\,\text{m}^3\,\text{mol}^{-1}\,\text{K}.$$

We can now consider the behaviour of the compound in a powder, which should be an average over all orientations of the crystal, and predict how $\chi_{\text{m}}T$ will change as a function of T and compare again to experimental data. Such a prediction can be done stochastically with a Monte Carlo simulation, though care must be taken to sample points uniformly over the surface of the unit sphere.

Alternatively, the average can be carried out numerically using integration. Taking the basis for which the matrix representation of $\bar{\bar{\chi}}$ is diagonal, with values χ_{xx}, χ_{yy}, and χ_{zz}, the average susceptibility can be expressed as

$$\begin{aligned}\chi_{\text{m}}^{\text{avg}} &= \int_S(\bar{\bar{\chi}}(\hat{v})\hat{v})\cdot\hat{v}\,\mathrm{d}\hat{v}\\ &= \frac{2}{\pi}\int_{\text{o}}^{\frac{\pi}{2}}\int_{\text{o}}^{\frac{\pi}{2}}\left(\chi_{xx}(\hat{v})\hat{v}_x^2+\chi_{yy}(\hat{v})\hat{v}_y^2+\chi_{zz}(\hat{v})\hat{v}_z^2\right)\sin\phi\,\mathrm{d}\theta\,\mathrm{d}\phi,\end{aligned} \tag{4.9}$$

where S is the surface of the unit sphere, $\hat{v}_x = \hat{v}\cdot\hat{x} = \cos\theta\sin\phi$, $\hat{v}_y = \hat{v}\cdot\hat{y} = \sin\theta\sin\phi$, and $\hat{v}_z = \hat{v}\cdot\hat{z} = \cos\phi$, as in the usual spherical-coordinates trans-

formation. The second integral trivially follows because $\bar{\bar{\chi}}$ is real symmetric, which guarantees its eigenvectors are orthogonal and span $\mathbb{R}^3$, and we may take $\hat{x}, \hat{y}, \hat{z}$ to lie along the eigenbasis of $\bar{\bar{\chi}}$ without loss of generality.

A formula for the average susceptibility that is computationally less intensive is given in the literature,[185, 186]

$$\chi_{\mathrm{m}}^{\mathrm{avg}} \approx \frac{1}{3}(\chi_{xx} + \chi_{yy} + \chi_{zz}), \tag{4.10}$$

assuming it to simply be the arithmetic mean of the eigenvalues of $\bar{\bar{\chi}}$ at the small applied field oriented in an arbitrary direction. This estimate, however, is not robust, and assumes that the magnetic susceptibility does not change significantly over all orientations. Indeed, if we instead take

$$\begin{aligned}\chi_{\mathrm{m}}^{\mathrm{avg}} &= \int_S (\bar{\bar{\chi}}(\hat{v}_{\mathrm{o}})\hat{v}) \cdot \hat{v} \, \mathrm{d}\hat{v} \\ &= \frac{2}{\pi}\int_{\mathrm{o}}^{\frac{\pi}{2}}\int_{\mathrm{o}}^{\frac{\pi}{2}} \left(\chi_{xx}(\hat{v}_{\mathrm{o}})\hat{v}_x^2 + \chi_{yy}(\hat{v}_{\mathrm{o}})\hat{v}_y^2 + \chi_{zz}(\hat{v}_{\mathrm{o}})\hat{v}_z^2\right) \sin\phi \, \mathrm{d}\theta \, \mathrm{d}\phi, \end{aligned} \tag{4.11}$$

the integral simply evaluates to $(\chi_{xx}(\hat{v}_{\mathrm{o}}) + \chi_{yy}(\hat{v}_{\mathrm{o}}) + \chi_{zz}(\hat{v}_{\mathrm{o}}))/3$, matching the form of Equation (4.10).

We use Equations (4.10) and (4.11) to estimate $\chi_{\mathrm{m}} T$ in a powder sample, which are shown in Figure 4.12. The predicted values fall in the range expected from experimental values of μ_{eff}, suggesting that the predicted results are reasonable (and hence the crystal-field parameters (CFPs) determined from *ab initio* calculations).

4.5.5 *Calculation of dipolar coupling*

We consider now the situation of a single, dimerised porphyrin molecule, 2-Dy. The two independent spins can act as a spin valve in a single molecule, which can be incorporated into a quantum device. Collaborators have continued investigations using this molecule, in two of its isomers, as

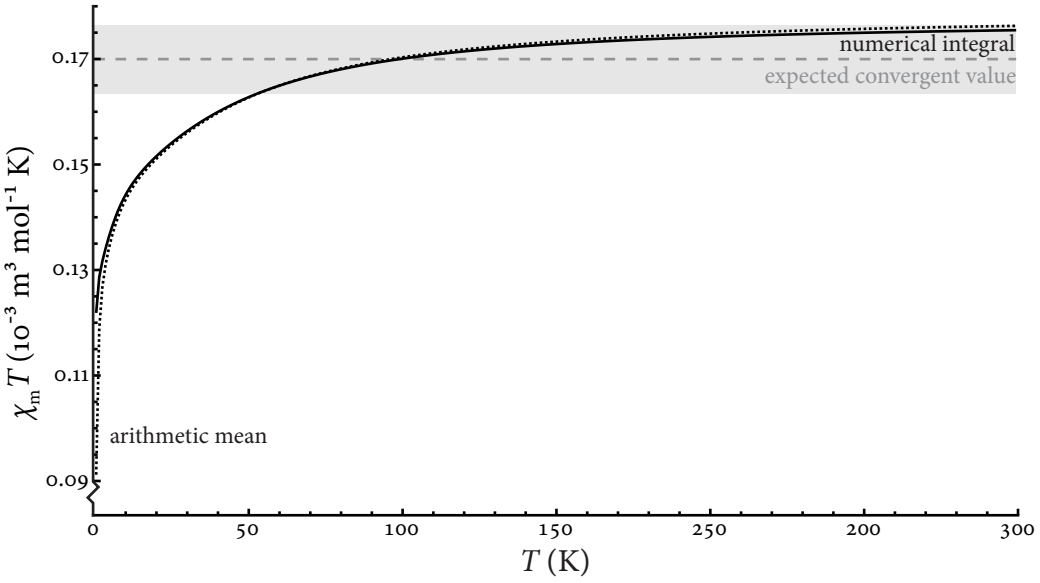


Figure 4.12: Predicted values for $\chi_m T$ vs T in a powder sample of 1-Dy. The predicted values are calculated both using a simpler arithmetic mean method (Equation (4.10)) and a more accurate numerical integral method (Equation (4.9)).

well as a fused trimer, but we will consider here a simple investigation of this molecule. While we might expect this molecule to have a plane of symmetry between the two porphyrins, it in fact is slightly unsymmetrical. Thus, a truly accurate result can only be found by considering running two calculations on the entire dimer with each Dy replaced with its closest diamagnetic analogue, to find the anisotropy for each Dy centre, and determine their interaction using the exchange-interaction and dipolar-interaction Hamiltonians.

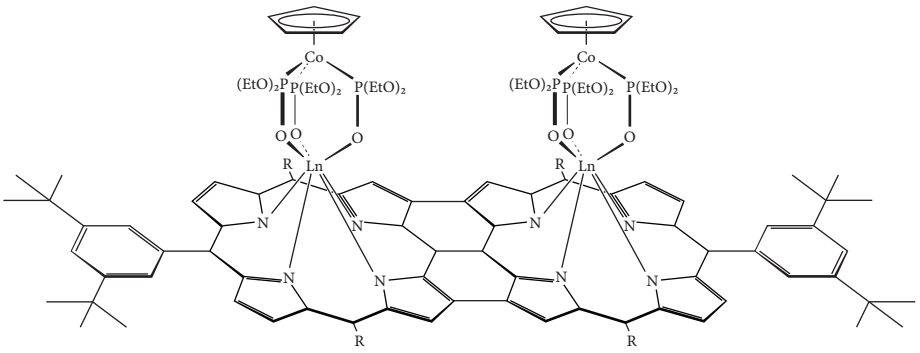


Figure 4.13: A dimerised porphyrin compound, 2-Ln, which combines two components of 1-Ln, removing a methyl group between them and linking the porphyrins. This can be done singly or triply, though triple linkage is considered here. The compound has two isomers, of which the *syn* isomer is shown here and considered.

This, however, is computationally an intensive task. We can, however, assume symmetry to produce a preliminary result, recognising that it will be somewhat inaccurate, so I opted to do this instead. Accordingly, I

assume the magnetic anisotropy of the two Dy centres behave as if they were in two properly rotated, separate monomers with coplanar porphyrins, but in the location of the Dy centres of the dimer. Then, using the equation

$$\bar{\bar{D}}_{12} = -\frac{\mu_0}{4\pi}\frac{\mu_B^2}{2|\vec{r}|^3}(\bar{\bar{g}}_1\bar{\bar{g}}_2 - 3(\bar{\bar{g}}_1\cdot\hat{r})(\bar{\bar{g}}_2\cdot\hat{r})^T),$$

with $|\vec{r}| = 8.5576$ Å, we found, in the molecular basis of 2-Dy,[b] that

$$\bar{\bar{D}}_{12} = \begin{pmatrix} -375.989 & -28.2988 & -190.038 \\ -145.007 & -926.213 & 792.034 \\ 77.4515 & -857.751 & 856.059 \end{pmatrix},$$

expressed in MHz, which has eigenvalues of −578.046 MHz, 134.047 MHz, and −2.1442 MHz.

[b] That is, with the porphyrin plane parallel to $\hat{x}z$ plane and the Dy metal centres lying on the $\hat{z}$ axis.

4.6 1-Tb

4.6.1 *Overview*

The 1-Tb compound crystallises in a monoclinic unit cell, with four molecules per unit cell. Two of the molecules are related to the other two by inversion, giving two inequivalent molecules per unit cell that are related by a 2_1 screw axis along $\vec{b}$ (or equivalently, a glide plane with normal $\vec{b}$). The cell axes $\vec{a}, \vec{b}, \vec{c}$ have lengths 31.4746(6) Å, 16.1160(2) Å, and 19.5145(2) Å, with $\beta = 107.246(2)°$. As mentioned previously, the molecule does not exhibit any rotational symmetry. This is because, while porphyrin and Kläui's tripodal ligand both exhibit rotational symmetry, the former is two-fold and the latter is three-fold. They do, however, have reflection symmetry, so we expect any anisotropy to be on or normal to the symmetry plane of the molecule.

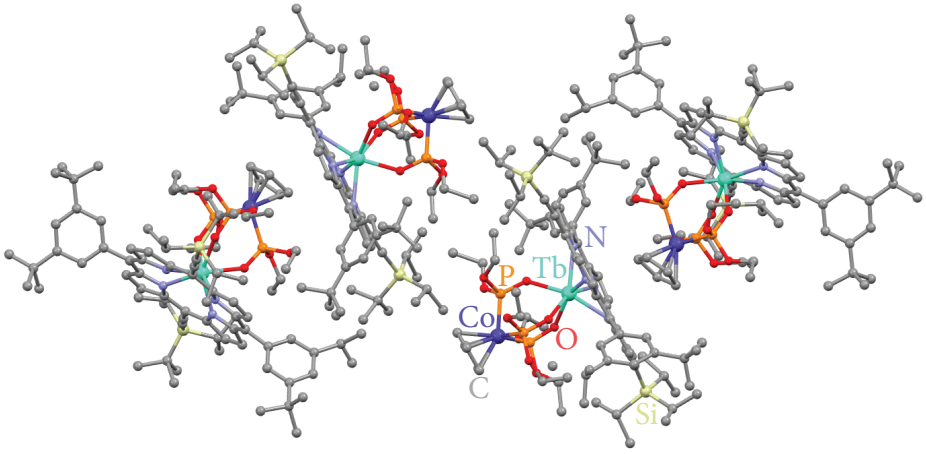


Figure 4.14: The unit cell of the 1-Tb crystal. There are four molecules per unit cell, related by inversion and a mirror plane (or equivalently, inversion and a screw axis), giving two inequivalent molecules per unit cell, with no higher symmetry. Here, the R group of Figure 4.6 is the ethynyltriisopropylsilyl group, $C_2Si[CH(CH_3)_2]_3$. Hydrogen atoms have been omitted for clarity.

4.6.2 *Ab initio calculations*

Because of the size of the molecule, the calculations using MOLCAS excluded orbitals of extremely high energy. We considered only the lowest-lying 7 septets, 105 quintets, and 112 triplets. Even the lowest-lying singlet has an extremely high energy, so all singlets were excluded. The results of the calculated anisotropy of the molecule overlayed on the molecule itself are shown in Figure 4.15. The axis of rotational symmetry of the isoenergy surface does not match the pseudo-axis of the molecule because the molecule lacks true rotational symmetry. Instead, the isoenergy surface's axis of rotational symmetry is tilted along the molecule's plane of reflection symmetry, where we would expect it to lie.

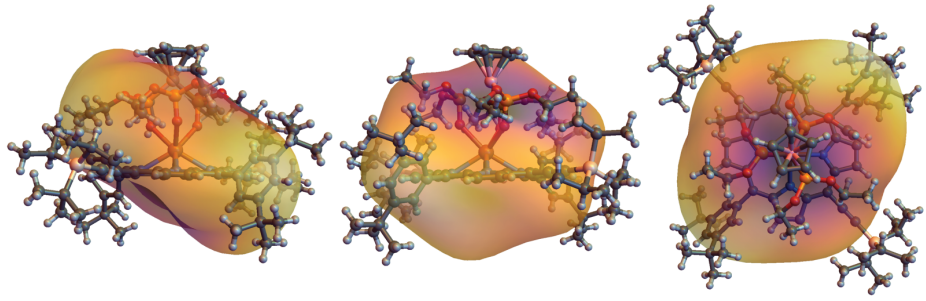
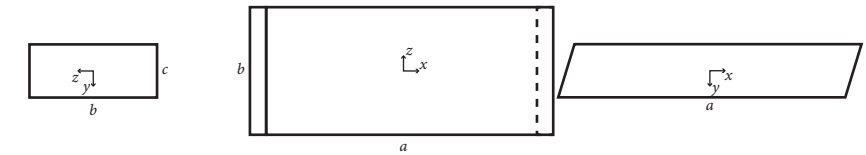


Figure 4.15: An isoenergy surface of the 1-Tb molecule's crystal field Hamiltonian, overlayed on the molecule, as viewed along three directions. Higher-order contributions ($k \geq 6$) have been exaggerated to more clearly show higher-order differences in the energy surface.

4.6.3 *Simulation of torque-magnetometry experiments*

Now having *ab initio* predictions for the crystal-field parameters, we can then use them to calculate theoretical responses to torque magnetometry measurements, which we can then compare with experimental results. To do this, as before, we first rotate the CFPs into the lab coordinate basis used by the experiments. Having done this, we can find the energies of one molecule's spin levels according to the usual method with the Spin Hamiltonian (Equation (2.4)),

$$H(\vec{B}) = \sum_{k=2,\,4,\,6} \sum_{q=-k}^{k} B_k^q \hat{O}_k^q + g\mu_B \hat{S}\vec{B}\,.$$



View along $+x$ View along $+y$ View along $+z$

Figure 4.16: The orientation of the crystal of 1-Tb in the torque measurements whose data were compared to simulations in this section. The crystal axes length are approximate and not to scale, but reflect the relative lengths of the grown crystal (and not the unit cell), with the principal growth axis being $\hat{a}$ and with $\hat{b}$ being a secondary axis.

We can then find the magnetisation $\vec{M}$ according to

$$\vec{M}(\vec{B}) = \frac{\sum_m \vec{\nabla} E_m(\vec{B}) \exp\left(\frac{E_m(\vec{B})}{T}\right)}{\sum_m \exp\left(\frac{E_m(\vec{B})}{T}\right)}\,, \tag{4.12}$$

where the summations are taken over eigenenergies $E_m(\vec{B})$ of the Hamiltonian of a given molecule m in the unit cell. The gradients are estimated numerically. The magnetisations for each molecule can be found individually, or else they can be determined simply by symmetry operation. The total torque due to magnetic field that acts on the system, then, is given by

$$\vec{\tau}(\vec{B}) = \sum_m \vec{M}_m(\vec{B}) \times \vec{B}\,, \tag{4.13}$$

where the summation is taken over all inequivalent molecules m of the unit cell.

The experimental data were gathered through a torque-magnetometry experiment by Simen Sopp, whose 1-Tb sample was synthesised by Alicia Götz, Xuelin Yao, and Dimitris Alexandropoulos. The crystal was oriented such that the $\hat{a}$ and $\hat{b}$ axes were parallel to the $\hat{x}$ and $\hat{z}$ lab directions, respectively, with the $\hat{c}$ axis going in the $-\hat{y}$ direction (Figure 4.16). In this setup, the sample crystal is attached to a cantilever, and torque induced on the crystal will move it and the cantilever arm. A short distance from the cantilever face is another metal plate, and the two form a capacitor, whose capacitance can be measured. For small deflections of the cantilever face, (1) the capacitance scales linearly with deflection, and (2) the cantilever arm acts as a Hookian spring, so that the distance deflected scales linearly with the torque applied. We can determine this by calculating the capacitance. Consider a cantilever with arm length a, plate length l, plate width w, initial separation z_0, deflection θ, twist ϕ, and permittivity ϵ. We assume zero thickness of the plates, neglect edge effects, and assume the charge distributes uniformly over the plates. This then gives us

$$C = \int_0^l \int_{-w/2}^{w/2} \frac{\epsilon \, \mathrm{d}y \, \mathrm{d}x}{z_0 + (a+x)\tan\theta + y\tan\phi}.$$

Evaluating the integral and Taylor expanding around $\theta = 0$ and $\phi = 0$, we obtain

$$C = \frac{\epsilon l w}{z_0} + \frac{\epsilon l w^2 \phi^2}{12 z_0^3} - \frac{\epsilon l w (2a + l)\theta}{2 z_0^2},$$

or

$$\Delta C = \frac{\epsilon l w^2 \phi^2}{12 z_0^3} - \frac{\epsilon l w (2a + l)\theta}{2 z_0^2},$$

so that, at small angles, the change in capacitance is indeed linear to first order in the deflection of the cantilever arm.

Because the spring constant of the cantilever arm and the precise mass of the sample were not measured, however, the absolute magnitude of the torque is unknown, and thus the values are given in arbitrary units. This does, however, still allow us to consider the relative magnitudes of the torque at different orientations. Comparing, then, predicted results from measurements to those obtained from experiments, we find them to be in good agreement (Figures 4.17 and 4.18).

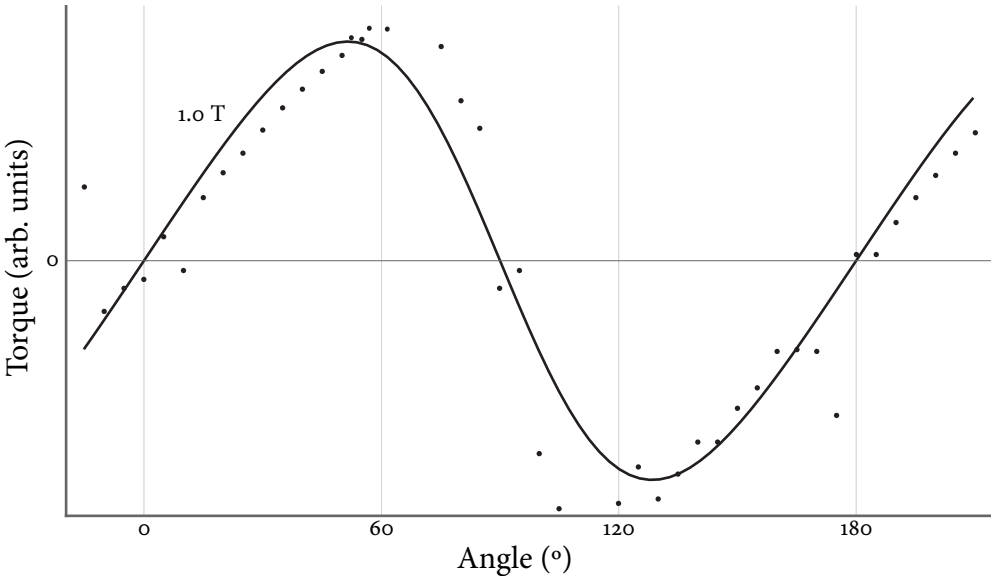


Figure 4.17: A torque measurement along the $\hat{a}\hat{b}$-plane of the 1-Tb crystal at 500 mK. The points denote experimental data acquired by Simen Sopp (in arbitrary units because the stiffness of the cantilever was unknown) and the lines denote calculated predictions from *ab initio* calculations. Notice the the slightly steeper slope around the $\hat{b}$ direction, indicating that $\hat{b}$ is comparatively easier than $\hat{a}$.

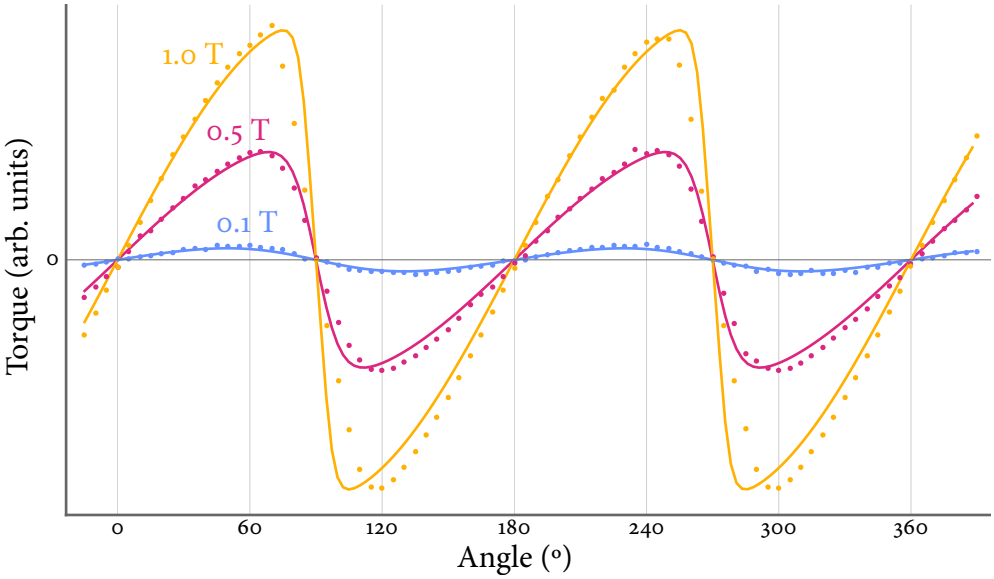


Figure 4.18: A torque measurement along the $\hat{b}\hat{c}$-plane of the 1-Tb crystal at 500 mK. The points denote experimental data acquired by Simen Sopp (in arbitrary units because the stiffness of the cantilever was unknown) and the lines denote calculated predictions from *ab initio* calculations. Notice the much steeper slope around the $\hat{c}$ direction, indicating that $\hat{c}$ is an easy axis and $\hat{b}$ is a hard axis. Hence, taken with Figure 4.17, the $\hat{a}\hat{b}$-plane is likely a hard plane.

Since the $\hat{a}\hat{c}$-plane is a glide plane, when a magnetic field is applied parallel to it, the induced magnetisation must also lie parallel to the plane, so that the induced torque lies parallel to $\hat{b}$. Since the torque experiments measured components along $\hat{a}$, the theoretical torque should always be 0.

This can be a result of an induced twist ϕ in the plate of the cantilever or, more likely, a slight misalignment of the crystal on the cantilever face.

These induced torques were measured with the magnetic field applied along three planes only, but in principle, any direction of the magnetic field might induce a torque. We can therefore produce a "torque surface" of the magnitude of the induced torque as a function of the direction of the magnetic field (Figure 4.19).

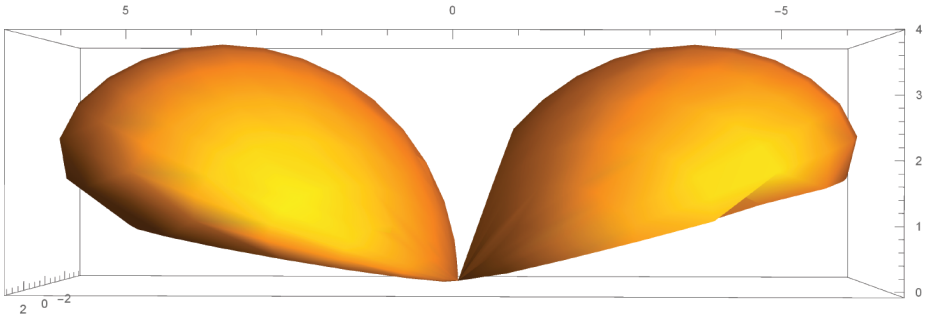


Figure 4.19: A three-dimensional representation of the "torque surface" of 1-Tb. For any given direction $\hat{v}$, the distance from the origin represents the magnitude of the torque in the $\hat{a}$ direction when a magnetic field is applied along $\hat{v}$.

4.6.4 *Simulation of SQUID measurements*

From Equation (4.12), we can also determine the behaviour of the magnetisation as a function of magnetic field strength along the easy axis and perpendicular to the easy axis. This we compared with measurements in a superconducting quantum-interference device (SQUID) experiment run by Michael Slota and Dimitris Alexandropoulos (Figure 4.20). Magnetisation, however, is dependent on crystal size, which we could not reliably and accurately measure, so only the magnitudes relative to magnetic saturation could be compared. These were found to be in good agreement, although slightly underestimated.

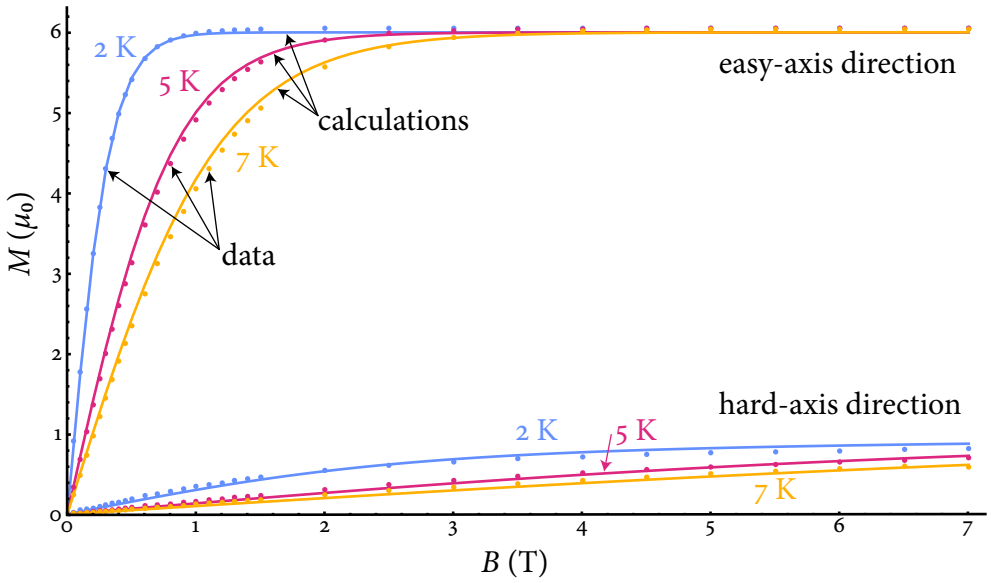


Figure 4.20: Magnetisation vs magnetic field in 1-Tb at 2 K, 5 K, and 7 K in easy-axis and hard-axis directions. Experimental data, acquired by Michael Slota and Dimitris Alexandropoulos, are denoted with points and calculated values are denoted by the lines. While saturation for a single molecule is known, saturation for the crystal is not, so the theoretical results have been roughly scaled to the experimentally observed saturation.

We note here, that the magnetisation saturates at about $6\mu_0$ in the easy-axis direction. For a molecule with a trivalent Tb centre, which has $J = 6$ and $g_J = \frac{3}{2}$, we expect that the magnetisation saturates at $9\mu_0$ in the molecular easy axis. The molecular easy axes, however, do not align with the crystal easy axis in general. In this crystal, there is a misalignment of roughly 42.6° between the molecular and crystal easy axes, taking only into account the ground doublet of the Tb centre. This then corresponds to a saturation (per molecule) in the crystal easy axis of $9\mu_0 \cos 42.6° \approx 6.6\mu_0$. Both the temperatures at which these measurements were conducted and the temperatures input in the calculations, however, are somewhat high, so excited states could easily cause a slight further misalignment to give the slightly lower predicted saturation of $\sim 6.05\mu_0$, which corresponds to a misalignment of 47.8°.

The magnetic-susceptibility tensor $\bar{\bar{\chi}}$, moreover, can be found according to

$$\vec{M}(\vec{B}) = \bar{\bar{\chi}}(\vec{B})\vec{B}. \tag{4.14}$$

This allows us to compute the quantities $\bar{\bar{\chi}}_{\hat{a}\hat{a}}T$ and $\bar{\bar{\chi}}_{\hat{b}\hat{b}}T$ as a function of the temperature T (Figure 4.21). We find that here too, the predictions are

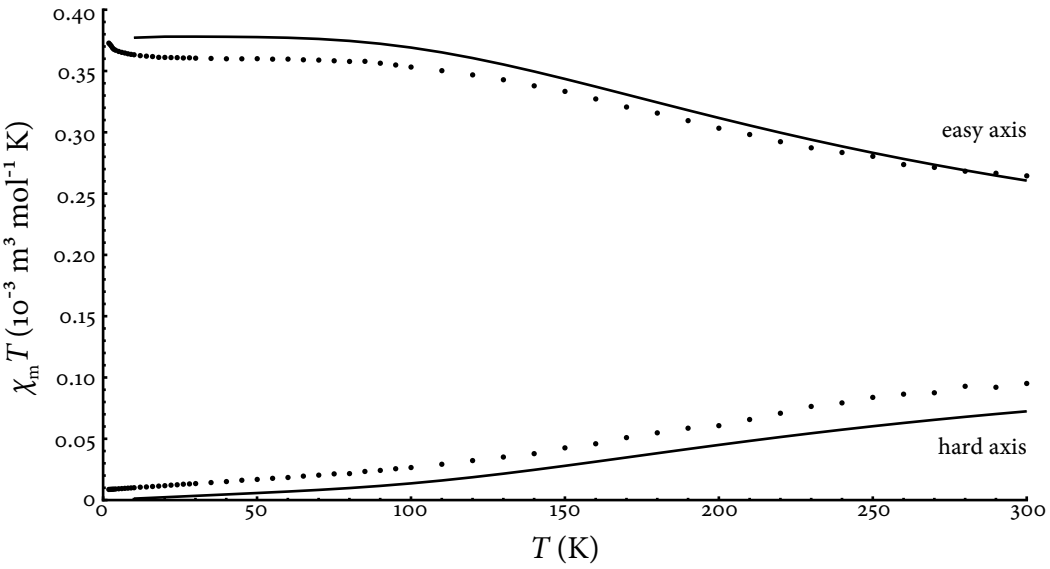


Figure 4.21: Experimental data (points) acquired by Michael Slota and Dimitris Alexandropoulos, and predicted values (curves) for $\chi_m T$ versus T along both the easy axis and a hard axis of the 1-Tb crystal.

in good agreement with experiment. Although the data differ slightly from the theoretically predicted values, even a slight misalignment in the crystal placement significantly alters the shape of $\chi_m T$.

For Tb^{3+}, the experimentally observed value of $\mu_{\text{eff}}^{\text{exp}}$ is 9.7–9.8, around what we expect theoretically from Equation (4.7), which gives $\mu_{\text{eff}} \approx 9.721$. Thus,

$$0.152 \times 10^{-3}\,\text{m}^3\,\text{mol}^{-1}\,\text{K} \overset{\text{Tb}^{3+}}{\leq} \lim_{T\to\infty} \chi_m T \overset{\text{Tb}^{3+}}{\leq} 0.154 \times 10^{-3}\,\text{m}^3\,\text{mol}^{-1}\,\text{K}.$$

We again apply the two methods used in Section 4.5 of estimating $\chi_m T$ in a powder sample. Both predictions are shown in Figure 4.22. Here, we see that in practice, because the magnetic susceptibility is measured at a small applied field, the orientation of a given molecule affects the magnetic susceptibility it experiences, so that for large variations in the magnetic susceptibility, as we have here, the difference between the more precise integral method of Equation (4.9) and the simpler arithmetic-mean method of Equation (4.10) can be quite stark (3–6% error down to 10 K, and up to 11% error at 1 K for this compound). In the same figure we have also experimental values for several 1-Tb compounds. The predicted

values are in good agreement with the experimental data from a 1-Tb graphene nanoribbon (GNR) powder sample, but slightly underestimate the experimental data from a simple powder sample of the 1-Tb monomer. The latter data set, however, does not make physical sense, as the values for $\chi_m T$ at T = 300 K are the $\chi_m T$ limit we expect (and therefore would be higher still at higher temperatures).

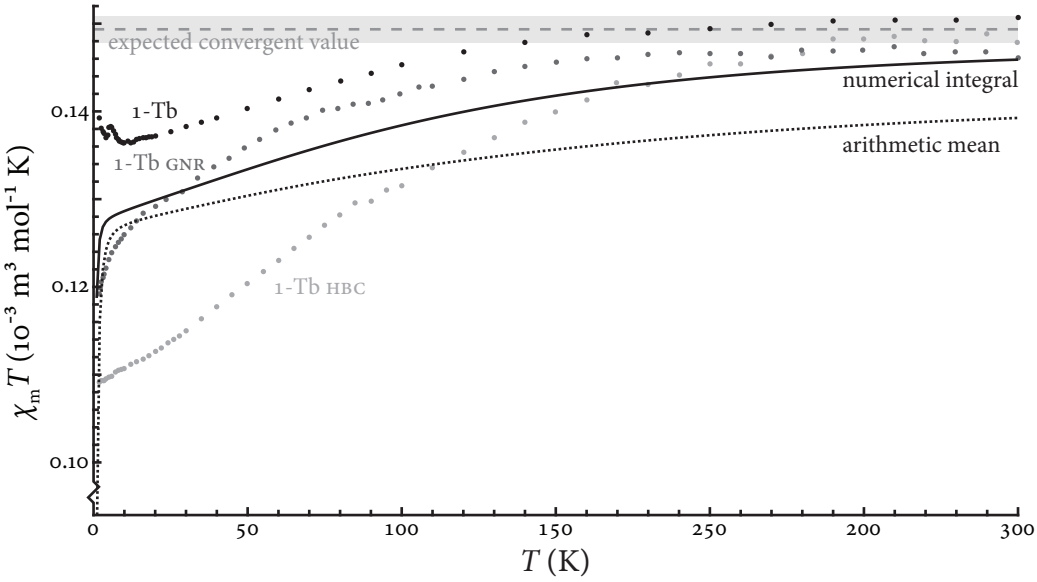


Figure 4.22: Experimental data and predicted values for $\chi_m T$ vs T in three powder samples: (1) 1-Tb monomer, (2) 1-Tb functionalised onto a GNR, and (3) 1-Tb functionalised onto hexabenzocoronene (HBC). The predicted values are calculated both using a simpler arithmetic mean method (Equation (4.10)) and a more accurate numerical integral method (Equation (4.9)).

One possible explanation is that the 1-Tb monomer sample had trace amounts of solvent remaining when weighed, giving an overestimate of the mass and hence $\chi_m T$, which would shift higher the calculated values for $\chi_m T$. Indeed, the experimental data for the functionalised samples suggest that the $\chi_m T$ for the monomer is too high, giving credibility to the supposition that experimental error shifted the values up. The shape of the data from the monomer sample, however, best match the predicted shape, albeit with the difference of the aforementioned shift, and the samples with 1-Tb functionalised onto graphene give similar results (though with slightly differing shapes), suggesting that the predicted results are quite accurate (and hence the CFPs determined from *ab initio* calculations).

4.7 Conclusion

In this chapter, I have demonstrated various computational techniques for characterising magnetic properties of compounds based on rare-earth metals. This chapter's very first result, given in Section 4.3, showed *ab initio* calculations to be very effective for predicting accurately the behaviour of rare-earth compounds, particularly with certain crystal symmetries. I gave an accurate calculation of the crystal's magnetic anisotropy from first principles, and I also demonstrated a novel method for determining the individual anisotropies of the molecules within a crystal from only experimental results. The method's novelty has important implications for a large number of crystals, since the method can be applied to most crystals known. Existing methods in the literature can determine individual molecular anisotropies in only two kinds of crystals: either those with high symmetry or those with only one molecule per unit cell. The new proposed method now makes it possible, in the majority of known crystals, to isolate magnetic anisotropy axes of individual molecules from magnetisation data alone.

Another notable result, described in Section 4.5, was the *ab initio* characterisation of rare-earths: these were found to be accurate and useful for single-molecule nanodevices, where the presence of a molecule with an anisotropic centre acts as a spin valve that affects the flow of electrons within the device. When the anisotropy is known, the interaction of the rare-earth centre with the flowing electrons can also be predicted and even tailored by chemical engineering of the molecule. It is even possible that further predictions may be made about larger, multi-centre molecules, such as the dimer considered in Section 4.5.5, though more study will be necessary to determine and fine-tune the accuracy of my preliminary calculation.

The next result, shown in Section 4.6, demonstrated that *ab initio* methods are useful not only for determining the anisotropy in Dy centres, but also in other rare-earth centres, such as Tb. The results from calculations were in good agreement with both torque-magnetometry measurements and SQUID magnetic measurements on the 1-Tb compound. From these results, it was also possible to calculate the torque response in arbitrary directions, giving predictions in a breadth of directions much more readily than measurements might be obtained in the same compound. Notably, torque-magnetometry experiments in most of the literature were conducted at temperatures above 2 K. In our case, we wanted to compare our results to measurements performed in the millikelvin range, where measurements are much more sensitive and show more features, and are therefore more likely to make apparent any inaccuracies in calculations. These results thus offer a stronger validation of modern computing techniques than much of the previous literature, and provide a reassuring picture of the level of accuracy that is now available in the modelling of magnetic centres.

In Chapter 6, we will also see this is true for Gd, but in general, these calculations are quite accurate and useful for predicting the anisotropic behaviour of rare-earths. In the following chapter, we will first examine the theoretical behaviour of large-spin magnetic centres strongly coupled with light, using a well-studied molecule, Mn_{12}.

5 Mn_{12}-acetate

5.1 Overview

Usually, electron spins can be brought into an excited state only individually; strong coupling, however, causes electron spins to exhibit superradiance, a collective behaviour wherein an ensemble of spins acts as a bloc. This collective behaviour can be observed even macroscopically, so that macroscopic observations give us a window into quantum behaviour. In this chapter, I examine how second quantization and the inclusion of a high-quality resonator around a molecular magnetic system can alter its quantum properties. I have chosen the Mn_{12}Ac single-molecule magnet (SMM) as a model system because it is well understood and described in the literature. In the thesis as a whole I am examining how both external influence and magnetic anisotropy of a magnetic system change the two possible aspects of a magnetic system: the static energy-level splitting and the dynamics of the system's spin state through these energy levels. The possibilities offered by the alteration of the static properties will be studied in detail in Chapter 6 for a novel, multi-level system based on Gd(III), a magnetic molecule that does not give rise to relevant magnetization dynamic effects. Such systems are thus excellent ways in which to explore the properties that the strong coupling makes available for quantum manipulation and computing purposes. On the other hand, as explained in Chapter 1, many molecular magnetic systems behave as single-molecule magnets and display very

prominent, slow dynamics of the magnetisation, which at low temperatures lead to spin-reversal times much longer than the experimental timescales. The unusual behaviour of strongly coupled systems raises three relevant questions: (1) Why does the strong coupling to a quantised electromagnetic field alter the dynamic properties such as quantum tunnelling behaviour? (2) How are these affected by the electromagnetic field? (3) If the strong coupling can be used to alter the magnetisation dynamics, can magnetic measurements in turn be used to quantify the strong-coupling regime? This last question is all the more relevant because SMMs show macroscopic quantum effects, and researchers can thus exploit the quantum regime to change the thermodynamic properties of a large macroscopic system. In this chapter, I pay attention to all these questions, and provide a theoretical framework to answer them.

5.2 Molecular properties

For this study I chose to examine the effect of the strong coupling to one of the most studied and better known SMMs, $Mn_{12}O_{12}(OAc)_{16}(H_2O)_4$[a] (often abbreviated "$Mn_{12}Ac$"). $Mn_{12}Ac$ was the first SMM discovered, [111, 187, 188] and it is considered the archetypical "Mn_{12}" SMM, i.e. the system that first evidenced the macroscopic quantum tunnelling of the magnetisation, Berry-phase interference, and related effects.[189]

[a] OAc denotes the acetate anion, CH_3COO^-.

The structure of the molecule is shown in Figure 5.1. The molecule contains a central cuboid made of four Mn^{IV} ions with electronic configuration $[Ar]3d^3$, connected by four bridging oxygen atoms, and thus total spin $S = 3/2$. This core is surrounded by a shell of eight Mn^{III} spin centres, which have $[Ar]3d^4$ electronic configuration, and has $S = 2$. Each Mn centre of the shell is connected to the central cuboid by further bridging oxygen atoms, and its coordination sphere is completed by two acetate ligands, so that the molecule is neutral. The surrounding sphere of acetate ligands can

be exchanged with different ligands, and this possiblity of exchange has been used to attach Mn_{12}-based molecules onto surfaces, or to alter the anisotropy terms of the molecule, as described below.

In $Mn_{12}Ac$, the oxygen-bridging ligands cause the Mn metal centres to be magnetically coupled by strong superexchange interactions. All the central Mn^{III} centres are coupled ferromagnetically one to another, while the surrounding Mn^{IV} centres couple antiferromagnetically to the core and ferromagnetically one to another. This configuration thus gives rise to a total spin of $S = 8(2) + 4(-3/2) = 10$ for the molecule. Because exchange interactions are much higher than the thermal energy, at the temperatures of interest, the whole molecule can thus be considered a giant spin. This so-called giant-spin approximation is customary for molecular magnetic clusters, and allows the molecular system to be treated as one magnetic centre shielded from its neighbouring molecules by its surrounding ligands, with a multi-dimensional Hilbert space, where the transverse terms of the anisotropy are connected to the structural features by symmetry rules, as described below. The resulting system also sees all molecules perfectly aligned, in a crystallographic lattice, so that a magnetic field can be applied either parallel to the easy axis of the magnetisation or perpendicular to it. We shall see in the next sections that this can have dramatic consequences for the dynamics, because of quantum states that would otherwise be separated becoming admixed.

5.3 Magnetisation dynamics

Alternating-current (AC) *susceptibility.* In an AC-susceptibility experiment, a sample is exposed to a small, oscillating magnetic field (typically 1 G or less, with a frequency between 25 Hz and 1000 Hz). While the magnetic moments of simple paramagnets will oscillate in phase with the applied field, $Mn_{12}Ac$ complexes produced an out-of-phase signal χ''_m at

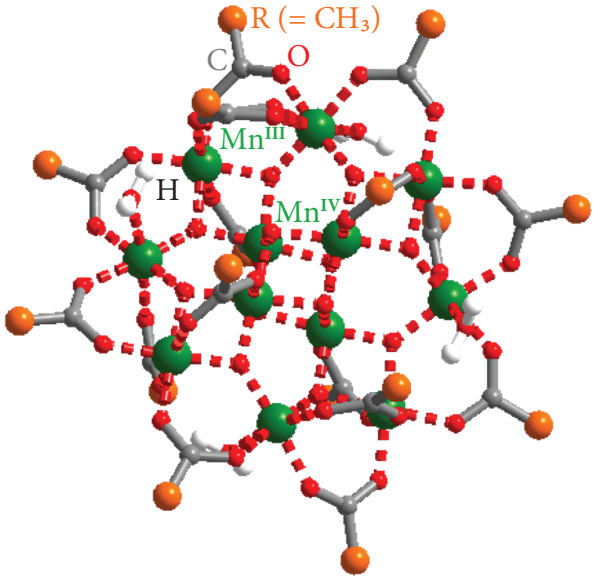


Figure 5.1: The structure of the Mn_{12} archetype of SMMs, viewed slightly off the S_4 axis. The one under consideration in this chapter has a methyl group, CH_3, as R. The water molecules of crystallisation have been included.

low temperatures. The values of χ'' (or χ') at different frequencies ω of the magnetic-field oscillation can then be fit to the expression $1/(1 + i\omega\tau)$, to give the relaxation time τ. The logarithm $\log \tau$ at various temperatures T then has a linear relationship with $1/T$, because the fit function is proportional to $\exp(-U_{\text{eff}}/k_B T)$; since $U_{\text{eff}} = DS_z^2$, we can use this method to also find the anisotropy parameter D. Research using this method has indicated both slow relaxation on the timescales of the field oscillations and a large relaxation barrier.

Quantum tunnelling of the magnetisation (QTM). One defining feature of SMMs is the anisotropy barrier, which forms a double-well potential, and the resulting quantum tunnelling of the magnetisation (QTM) in applied magnetic fields. As discussed in Section 2.3.3, at zero field, the spin states of the system are such that the highest-energy state has $S = 0$. For $Mn_{12}Ac$, the lowest-energy states are $S = \pm 10$, which lie on opposite sides of the energy barrier DS_z^2. At low temperatures, as the magnetic field is swept, the magnetisation of a single crystal of $Mn_{12}Ac$ flips in discrete steps, in a "staircase" structure, with the steps occurring at values of the applied field where different energy levels of the spin system coincide. As Thomas *et al.* explains, "at these special values of the field, relaxation from one spin state

to another is enhanced above the thermally activated rate by the action of resonant quantum-mechanical tunnelling."[190] This is a result of the double-well potential shifting in the presence of a magnetic field, which aligns different pairs of energy levels at specific field strength, as shown in Figure 5.2.

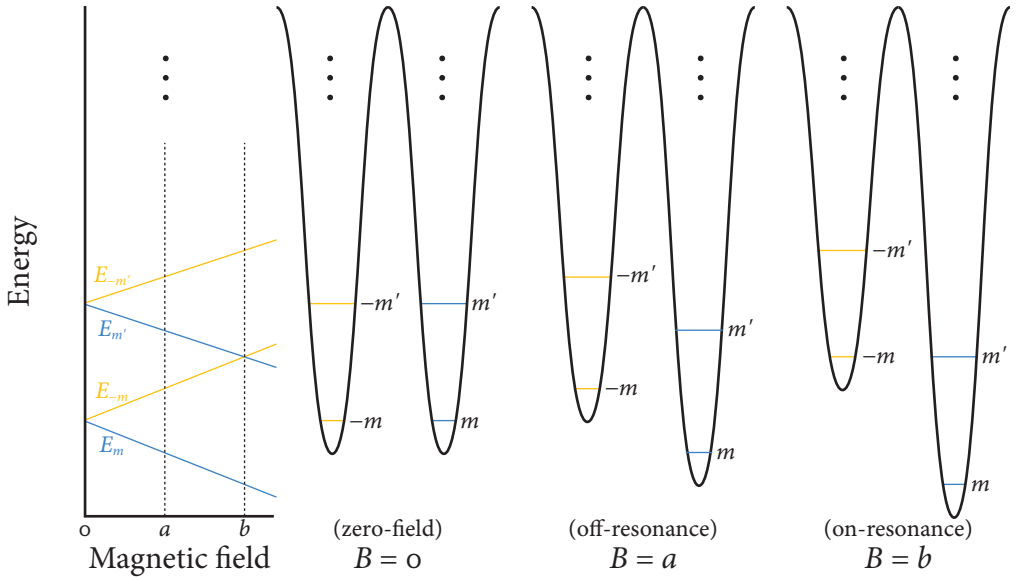


Figure 5.2: In the absence of an external magnetic field, $|\pm m\rangle$ states are degenerate in energy. When a field is applied, the potential wells shift, and along with them the energies of the spin levels. In general, the energies of the spin levels will not match (a), but at certain field values, different pairs of spin levels may be degenerate in energy (b). Only four spin levels $|\pm m\rangle$ and $|\pm m'\rangle$ are drawn in the figure, for simplicity.

As the field is increased, then, what was the ground state at zero field matches the energy of other states on the other side of the barrier, starting with the highest spin and progressively moving down. This produces a stepped hysteresis curve that is characteristic of high-spin SMMs (see Section 2.3.3).

Transverse magnetic anisotropy. At low temperatures, in the absence of transverse magnetic fields, a spin system governed by $\mathcal{H} = D\hat{S}_z^2 - g\mu_B H\hat{S}_z$ has no terms which do not commute with $\hat{S}_z$. Hence, the energy levels will not have anticrossings as a function of field and thus no coupling between there is no coupling among the spin states. As a result, no tunnelling through the barrier can happen. Experimentally, however, the observed tunnelling rate exceeds what would be expected from just dipolar or hyperfine fields, suggesting that there is coupling among levels, and thus

terms that do not commute with $\hat{S}_z$. Second- and fourth-order transverse anisotropies can be introduced, giving

$$H = D\hat{S}_z^2 + E(\hat{S}_x^2 - \hat{S}_y^2) + \frac{B}{2}(\hat{S}_+^4 + \hat{S}_-^4) - g\mu_B H\hat{S}_z.$$

Here, the E term governs transitions between states whose m_S differ by multiples of 2, and the B term governs transitions between states whose m_S differ by multiples of 4. In principle, the value of E should vanish due to the fourfold symmetry of the $Mn_{12}Ac$ cluster. The number and arrangement of hydrogen-bound acetate ligands, however, can differ, giving six different isomeric forms of $Mn_{12}Ac$, some of which have non-zero E. Cornia *et al.* confirmed in a spectroscopy study using high-field electron paramagnetic resonance (EPR) that $Mn_{12}Ac$ has symmetry lower than tetragonal, giving rise to quadratic anisotropy, which was distributed around discrete values two orders of magnitude lower in strength than the axial anisotropy.[191] Odd transitions, however, are likely a result of small transverse magnetic fields.[192–195] Dipolar coupling,[196] easy-axis tilting,[197] and distributions of molecular environments,[191] are likely not strong contributors to such fields, though asymmetric spin–orbit exchange might be.[198] Barra *et al.* did further spectroscopy experiments using high-field EPR, finding that the transverse anisotropy in axial SMMs originated from both the multispin nature of the system and the breakdown of the strong-exchange approximation, with the tilting of single-ion easy axes with respect to the cluster's axis of symmetry playing a major role.[199] They also did angular-dependency measurements to determine the sixth-order anisotropy, finding that it was three orders of magnitude weaker than fourth-order anisotropy. For high-field transitions, such as $m_S = -7 \rightarrow m_S = -6$, however, the deviation between experiment and simulation is significant if sixth-order terms are neglected.[199]

Magnetic-field sweep rate. In the limit where magnetic field is varied infinitely slowly as a function of time (adiabatically), the state of the system will traverse a single path as it approaches and leaves an avoided level crossing, gradually changing from one spin state into another. At finite speeds (diabatic transitions), however, the probability of transition becomes nonzero, so that the system might "jump" between paths. The dynamics of these transitions are governed by the Landau–Zener formula, which gives the probability of a diabatic process:

$$P = \exp\left(-2\pi \frac{\Delta^2}{4\hbar v_{\mathrm{LZ}} \frac{\partial}{\partial B}(E_2 - E_1)}\right),$$

where Δ is the splitting between the levels (or twice the off-diagonal element in the Hamiltonian), B is the strength of the external magnetic field, E_1, E_2 are the energies of the states which are having an avoided level crossing, and v_{LZ} is the so-called Landau–Zener velocity, given by

$$v_{\mathrm{LZ}} = \frac{\mathrm{d}B}{\mathrm{d}t}.$$

This situation becomes much more interesting and complex when multiple levels cross, for example in a bow-tie scheme.

5.4 The system

The scheme that we consider is a $Mn_{12}Ac$ system that is strongly coupled to a cavity. As the coupling to the magnetic field of the cavity mode cannot be strong enough to be detected for a single molecule, we consider the coupling of the cavity to a crystal containing N $Mn_{12}Ac$ molecules, all isoaligned as per the crystallographic orientation. This leads to an enhancement factor of $\sqrt{N}$ of the resonator–molecule coupling strength, and we thus consider in the following the presence of a small crystal of $Mn_{12}Ac$ molecules. The use of an ensemble inside the cavity, although a fully quan-

tum, second-quantization scenario, raises the question of whether, at a certain temperature, the whole system of both the cavity and the molecules can be kept in a coherent superposition. This issue thus imposes an upper temperature limit, below which the considerations are valid. This temperature limit can be estimated by considering the fraction of $Mn_{12}Ac$ molecules that are in an excited spin state, and not in the spin ground state, at a given temperature, simply by Boltzmann statistics. This indicates that there is a practical upper limit to the size of a crystal that can be effectively used, limited by coherence. For a sufficiently large crystal, the excitations would prevent the system from being coherent and effectively make useless the $\sqrt{N}$ enhancement. Since the population distribution in a group of molecules across the energy levels follows

$$p_i \propto \exp\left(-\frac{E_i}{k_B T}\right),$$

for a system of N molecules, we expect the number of molecules in the ground state to be

$$N_g = \frac{N}{\sum_i \exp\left(-\frac{E_i}{k_B T}\right)}, \tag{5.1}$$

or, equivalently, the number of molecules in an excited state to be

$$N_e = 1 - \frac{N}{\sum_i \exp\left(-\frac{E_i}{k_B T}\right)} = \frac{N \sum_{i>0} \exp\left(-\frac{E_i}{k_B T}\right)}{\sum_i \exp\left(-\frac{E_i}{k_B T}\right)} \tag{5.2}$$

For sufficiently low temperatures T, we can reasonably neglect the higher excited states ($i > 1$) of Eq. (5.2), so that

$$N_e \approx \frac{N \exp\left(-\frac{E_1}{k_B T}\right)}{1 + \exp\left(-\frac{E_1}{k_B T}\right)}. \tag{5.3}$$

Since we want $N_e \ll 1$, we can solve Eq. (5.3) to give the crystal-size limit,

$$N \ll \frac{1 + \exp\left(-\frac{E_1}{k_B T}\right)}{\exp\left(-\frac{E_1}{k_B T}\right)} = 1 + \exp\left(\frac{E_1}{k_B T}\right). \tag{5.4}$$

Since $1 \ll \exp(E_1/k_B T)$ at sufficiently low T, we can more succinctly express Eq. (5.4) as

$$N \ll \exp\left(\frac{E_1}{k_B T}\right). \tag{5.5}$$

From the practical point of view, one of the possible implementations of this scheme uses a superconducting coplanar resonator, such as produced by 150 nm-thick NbTi superconductors on sapphire substrates. The superconductor of choice is, ideally, relatively resistant to an applied magnetic field, and the synthetic sapphire substrate is chosen in order to minimise the loss and dispersion of the photons. Such schemes have different advantages: (1) they ensure compatibility with current schemes for quantum computation, as implemented by most companies such as Google and IBM;[200–202] (2) they also ensure good interaction of the molecular system with the cavity electromagnetic field, as shown by simulations (see Figure 5.3 for simulations by Conrad Clauß[203]) using finite-size elements methods; and (3) they allow single crystals of molecular magnets to be placed directly onto resonators, and thus the possibility of having collective coupling of a macroscopic crystal, rather than coupling to single atoms or molecules.

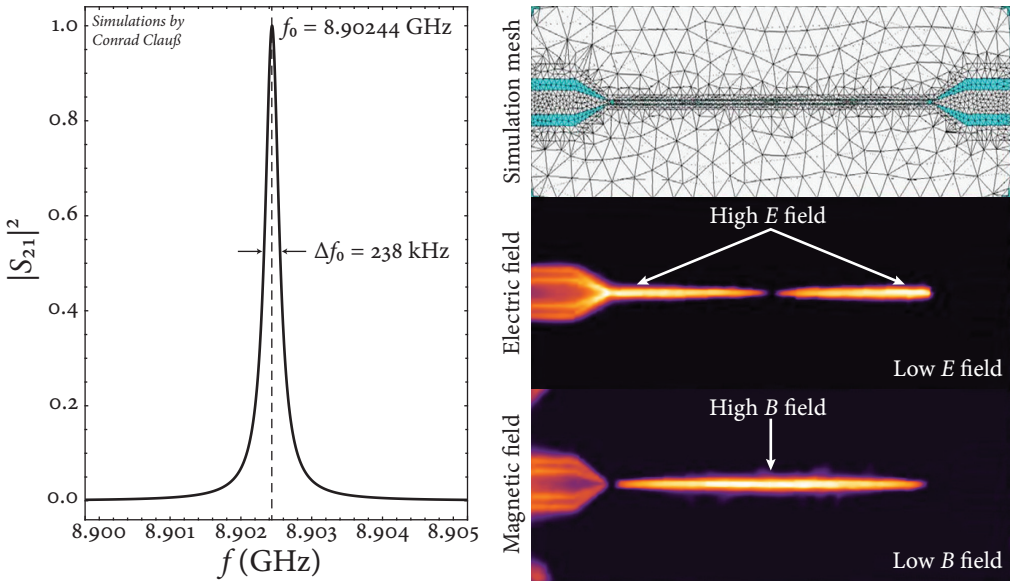


Figure 5.3: A finite-size simulation of the magnetic and electric fields in an on-chip superconducting resonator, done by Conrad Clauß.[203] The S_{21} parameter is simulated and has a clear Lorentzian shape (left), and this is used alongside a mesh (top right) to simulate the electric (middle right) and magnetic (bottom right) fields. The electric field has a node in the middle of the waveguide, while the magnetic field has an antinode.

Moreover, using this scheme, it is conceivable to bury a magnetic probe below the cavity, so as to allow the detection of the magnetisation of the molecular system, and its time dependence, while in the cavity. One possible implementation of this scheme, depicted in Figure 5.4, is the creation of a Hall-bar gradiometer within the sapphire substrate, separated from the superconductor cavity by a thin insulation layer. Gradiometers can be nanofabricated to widths down to a few nanometres (e.g. by using focused-ion-beam technology), in a process that both enhances their sensitivity, and minimises the capacitive interaction of the gradiometer with the cavity. Such nanofabricated systems have already been used to detect the magnetisation reversal of molecular magnets and microcrystals of $Mn_{12}Ac$ in crystals as small as 100 µm,[204] and are sensitive up to magnetic signals less than $10^6 \mu_B$.[205, 206] They are thus excellently suited for the detection of the magnetisation of the crystals while the strong coupling is in place.

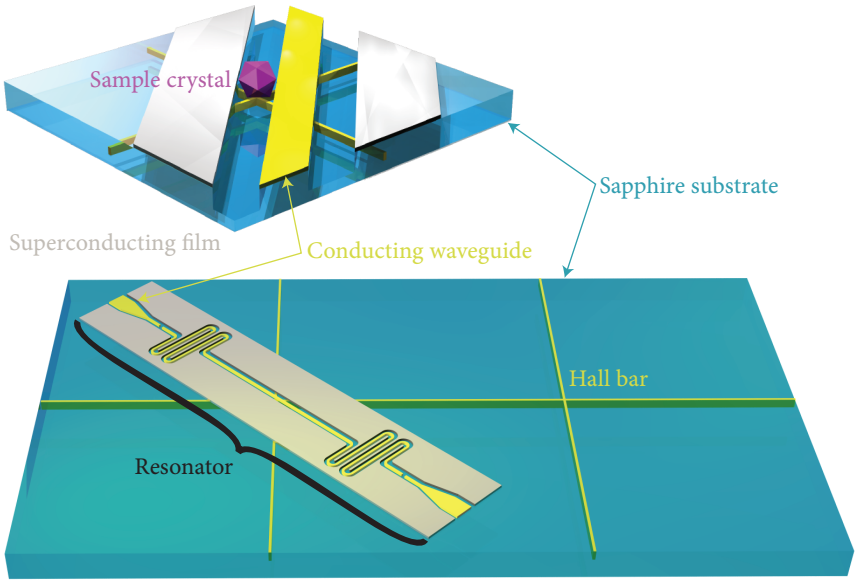


Figure 5.4: A schematic of a Hall-bar setup to measure magnetisation. A 2D resonator with a sample crystal is placed on one intersection of the small bar, and strong coupling will be induced between the crystal and the resonator. The energy of the resonator can be adjusted by fabrication, and the magnetisation can precisely measured using the Hall effect.

It is very interesting to notice that the coupling and detection schemes here envisaged lead to the possibility of observing strong coupling, second-quantization effects on the *macroscopic* properties of a crystal. The implementation of the schemes here described can thus lead to the direct

observation of quantum effect on the thermodynamic properties of a large macroscopic crystal, rather than on the microscopic energy levels usually considered. This is a qualitative difference that entails profound implications. Rather than the observation of quantum mechanical behaviour being limited to small scales (what we often think of as the so-called "quantum regime), it would now become possible to observe quantum mechanical behaviours in macroscopic systems, limited only by the coherence of the crystal, as imposed by the condition of Eq. (5.5).

5.5 Photon-assisted tunnelling

The Hamiltonian of the cavity plus $Mn_{12}Ac$ crystal is given by Eq. (2.14):

$$\mathcal{H} = H_S + H_\Phi + H_I,$$

where again, H_S is the Hamiltonian of the spin system, H_Φ is the Hamiltonian of the resonator, and H_I is the Hamiltonian of the interaction between the two. In the rotating-wave approximation (RWA), this can be expressed

$$\mathcal{H} = \sum_{k=2,4,6} \sum_{q=-k}^{k} B_k^q \hat{O}_k^q + \hbar\omega \left(\hat{a} + \hat{a}^\dagger\right) + \hbar\Omega \left(\hat{\sigma}^+ \hat{a} + \hat{\sigma}^- \hat{a}^\dagger\right). \tag{5.6}$$

In certain cases, the strong coupling between the photon and the energy levels creates a polariton, a quasi-particle that is an expression of level repulsion as a result of strong coupling between electromagnetic waves and an electric or magnetic dipole-carrying excitation.

We shall consider first, however, what this entails for a large mismatch between the resonator and spin-level energies. Even for high energy mismatches of the resonator, the lack of a polariton does not prevent the photon from playing a role in the behaviour of the system. In such cases, the strong coupling produces virtual states at the much higher energies of the resonator. While the spin system may never really occupy these

states, their presence alters the quantum-mechanical probability that the system has of changing from one m_S spin state to another. The tools to address this problem are to be found in a perturbation treatment of the spin Hamiltonian.

We consider the system Hamiltonian

$$\mathcal{H} = H_S + H_\Phi + H',$$

where H_S and H_Φ are the spin-system and cavity Hamiltonians, respectively, and H' is a perturbation Hamiltonian with coupling strength Ω, which will also be act as the perturbation parameter.

A spin system can thus evolve from one state to another, despite the fact that the system never actually enters the high-energy state that are intermediate, much like in a Raman transition, in optics. To understand how the introduction of the cavity modes changes the paths that connect the states on the two sides of the well, we must thus explore the effect considering the full Hilbert space, and all the virtual states associated.

When considering the case of large detunings Δ, the RWA no longer holds, since it relies on the assumption that the detuning is much less than the sum of the light-field and atomic frequencies, $\Delta \ll \omega_L + \omega_0$. In the RWA, the term $\omega_L + \omega_0$ appears in rapidly oscillating exponentials, so that they so that they quickly average to 0, as compared to the Δ terms. When this is no longer the case, the RWA may not be assumed. The expanded Hamiltonian must thus instead be expressed as:

$$\mathcal{H} = H_S + \hbar\omega a^\dagger a + \hbar\Omega \left(\hat{S}_- + \hat{S}_+\right)\left(\hat{a}^\dagger + \hat{a}\right)/2\,.$$

In a hybrid system, the energy splitting between levels m and m' is given by:[136]

$$E_{mm'} = 2\left|\sum_{\substack{\phi_i \\ m_i \neq m,m'}}^{N}\left(\frac{V_{m,m_1}U_{m,\phi_1}}{(\epsilon_m-\epsilon_{m_1})(\epsilon_m-\epsilon_{\phi_1})}\times\prod_{i=1}^{N-1}\frac{V_{m_i,m_{i+1}}}{\epsilon_m-\epsilon_{m_{i+1}}}\frac{U_{m_i,\phi_{i+1}}}{\epsilon_m-\epsilon_{\phi_{i+1}}}V_{m_N,m'}U_{m_N,\phi}\right)\right|,$$

where $m > m_i > m'$, and V_{m_i,m_j} and U_{m_i,ϕ_j} are the off-diagonal elements of $\mathcal{H}$ resulting from $\hat{O}_k^q$ and H_I contributions, respectively. This expression displays a sum over all possible paths between $|m\rangle$ and $|m'\rangle$ in the larger Hilbert space of the hybrid system comprising both $|m\rangle$ and $|\phi\rangle$ levels. For instance, in a four-state system with states $|0\rangle, |1\rangle, |2\rangle, |3\rangle$, there are 4 possible paths between $|0\rangle$ and $|3\rangle$:

1. $|0\rangle \to |3\rangle$
2. $|0\rangle \to |2\rangle \to |3\rangle$
3. $|0\rangle \to |1\rangle \to |3\rangle$
4. $|0\rangle \to |1\rangle \to |2\rangle \to |3\rangle$

Thus, in general, between states $|m\rangle$ and $|m'\rangle$, there are

$$\sum_{i=0}^{m-m'-1}\binom{m-m'-1}{i} = 2^{m-m'-1}$$

total possible paths considered in the sum.

Notably, even levels not mixed by $\hat{O}_k^q$ operators (e.g., $|\pm 9\rangle$) now become mixed: strong coupling introduces phonon-induced tunnelling in the spin system through cavity paths that contain first-order ladder operators and admixes any $|m\rangle, |m'\rangle$ by virtual processes. The efficiency of these new quantum processes depends on the coupling strength Ω and the particular levels involved, since the polaronic up-shift effect can partially compete with pure spin–phonon processes, given by[136]

$$W_{m\pm1,m} = \frac{A^2 s_{\pm1}}{12\pi\rho c^5\hbar^4}\frac{(\epsilon_{m\pm1}-\epsilon_m)^3}{e^{\beta(\epsilon_{m\pm1}-\epsilon_m)}-1},$$

$$W_{m\pm2,m} = \frac{17A^2 s_{\pm2}}{192\pi\rho c^5\hbar^4}\frac{(\epsilon_{m\pm2}-\epsilon_m)^3}{e^{\beta(\epsilon_{m\pm2}-\epsilon_m)}-1}.$$

These expressions consider spin transitions between $|m\rangle$ and both $|m\pm1\rangle$ and $|m\pm2\rangle$ from phononic processes, described by Eq. (2.11).

From both processes, nevertheless, we may find the photon-assisted tunnelling rate,

$$\Gamma_m^{m'} = E_{mm'}^2 \frac{W_m + W_{m'}}{4\xi_{mm'}^2 + (W_m + W_{m'})^2},$$

where W_m is the total phononic contribution from state $|m\rangle$,

$$W_m = W_{m-2,m} + W_{m-1,m} + W_{m+1,m} + W_{m+2,m}.$$

In this way, dynamic paths that would normally be forbidden can now happen (See Figure 5.5).

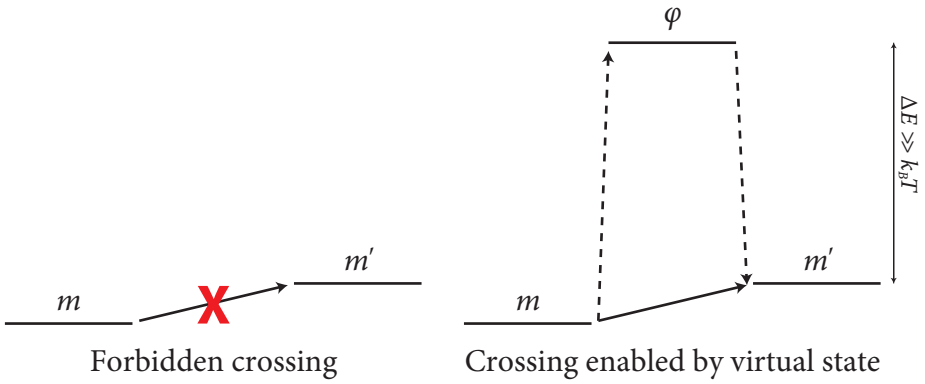


Figure 5.5: A schematic of photon-assisted tunnelling. For two states $|m\rangle$ and $|m'\rangle$ between which transitions are normally forbidden, a virtual pathway through a resonator level, even a highly detuned one, opens a pathway between the two states.

Because phononic processes can efficiently promote the spin reversal opened by the strong-coupling channel, energy splittings between levels are increased as the coupling rate increases ($E_{m,-m}^{½}$ versus Ω shown in Figure 5.6), so that $\Gamma_m^{m'}$ is enhanced. Even at small spin–cavity couplings, the resulting photon-assisted tunnelling rates Γ_9^{-9} (for the normally unmixed $|\pm 9\rangle$ levels) can reach 10^5 Hz at $\Omega \sim 10^{-2}$ cm^{-1} through otherwise prohibited relaxation channels (Figure 5.7).

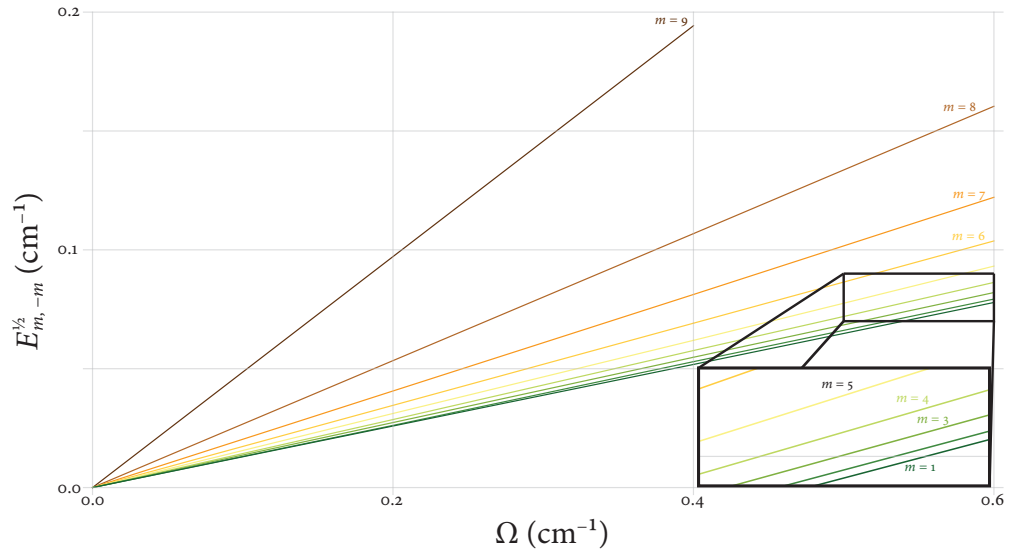


Figure 5.6: The energy gap $E^{1/2}_{m,-m}$ between degenerate spin states $|\pm m\rangle$ in $Mn_{12}Ac$ at zero field, as a function of the coupling strength Ω. As the coupling strength increases, so too does the gap between degenerate spin states, even for a highly detuned resonator state, because of coupling through a virtual pathway with the resonator state (Figure 5.5).

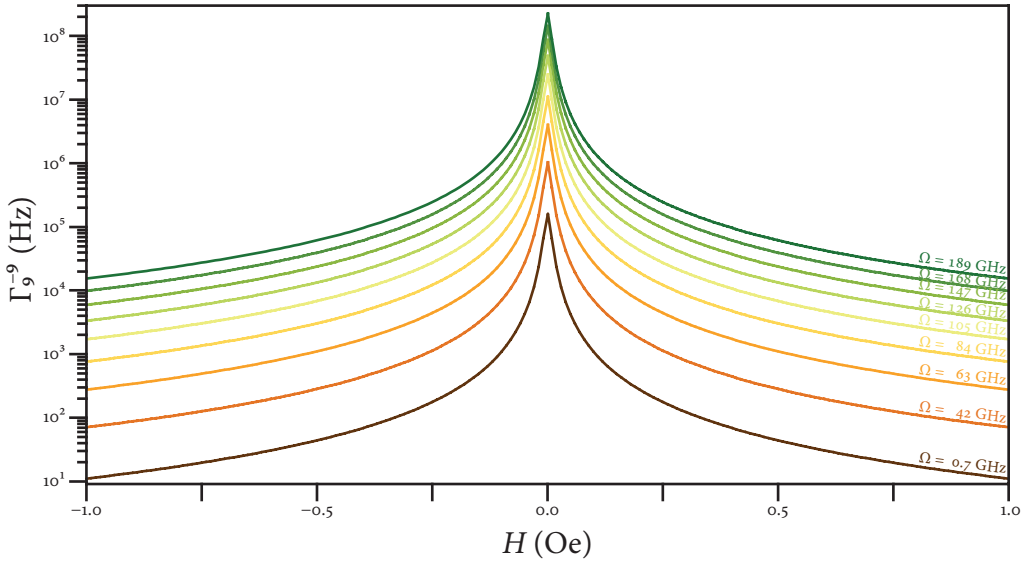


Figure 5.7: A plot of the photon-assisted, incoherent tunnelling rate Γ_9^{-9} between states $|9\rangle$ and $|-9\rangle$ as a function of the coupling strength Ω in $Mn_{12}Ac$. While normally, the $|9\rangle \rightarrow |-9\rangle$ transition is forbidden by the Stevens operators $\hat{O}_k^q$ alone, coupling with the cavity resonator opens up this channel. For even weak increases coupling strength, the tunnelling rate is boosted by orders of magnitude.

5.6 Spin–photon hybrid bow-ties

One of the most studied, and interesting, situations in quantum mechanics arises when several quantum states become degenerate in presence of a mixing term in the Hamiltonian. In this case, even for very small mixing terms, the dynamic properties display starkly quantum behaviours. The effect on the dynamics of a two-level system was studied in the early '30s by Lev Landau, Clarence Zener, Ernst Stueckelberg, and Ettore Majorana, and has since become one of the hallmarks of quantum behaviour: the

mixing of the two resonant levels can lead to underbarrier tunnelling from one to another, in a process that is prohibited classically.

We shall describe Landau–Zener theory, with particular attention to three-level transitions and Bloch oscillations. Consider first an avoided level crossing of a two-level system, with energies E_1 and E_2, which evolve over time. In order for the equations of motion for the system to be solved analytically, the system is simplified through a set of assumptions collectively called the Landau–Zener approximation: (1) The perturbation parameter in the Hamiltonian is a known, linear function of time, (2) The energy separation of the diabatic states varies linearly with time, and (3) The coupling in the diabatic Hamiltonian matrix is independent of time. The first assumption means that the approximation is semi-classical. In the case of a spin system in a magnetic field, the strength of the field becomes a classical variable that can be measured during the transition and varies over time. The second assumption allows for the substitution,

$$\Delta E = E_2(t) - E_1(t) = \alpha t,$$

where α is some constant. Again, in the case of a spin system in a magnetic field, this corresponds to a linear change in the magnetic field with respect to time. An important value in this formulation is the so-called Landau–Zener velocity,

$$v_{\mathrm{LZ}} = \frac{\frac{\partial}{\partial t}|E_2 - E_1|}{\frac{\partial}{\partial q}|E_2 - E_1|} \approx \frac{\mathrm{d}q}{\mathrm{d}t},$$

where q is the perturbation variable, which is the magnetic field in the case of a spin system in a magnetic field. A large v_{LZ} gives a large diabatic transition probability and vice versa. The probability of a diabatic transition is given by

$$P_D = e^{-2\pi\Gamma},$$

where Γ is an adiabaticity parameter given by

$$\Gamma = \frac{V_0/\hbar}{\frac{\partial}{\partial t}(E_2 - E_1)} = \frac{V_0/\hbar}{\frac{dq}{dt}\frac{\partial}{\partial q}(E_2 - E_1)} = \frac{V_0^2}{\hbar|\alpha|},$$

where V_0 is the off-diagonal element in the two-level system's Hamiltonian that couples the states. The minimum energy difference ΔE is achieved when $E_1 = E_2$ in the unperturbed system and satisfies

$$\Delta E = 2V_0.$$

The situation becomes considerably more complex when more than two levels are in resonance, in what is called a "bow-tie" tunnelling system. In this section we examine what happens when a bow-tie tunnelling is made possible by the concomitant presence of two spin levels and a resonator level, all coupled to each another by the strong-coupling and spin-mixing terms (Figure 5.8). The time-dependent evolution for such multistate systems can have exact solutions that are polynomials of the solutions of the corresponding two-state models, which can give simple, analytic descriptions for the time-dependent control. Let us consider now a time-dependent, three-level system, by neglecting all other levels and putting $k = k_0 - Ft$, where t is the time. Centring the crossing around $t = 0$ and $E = 0$, we obtain the linearised Hamiltonian

$$H = \begin{pmatrix} 2Ft & \frac{V_0}{2} & 0 \\ \frac{V_0}{2} & 0 & \frac{V_0}{2} \\ 0 & \frac{V_0}{2} & -2Ft \end{pmatrix}. \tag{5.7}$$

This is the three-level extension of the Landau–Zener model, and it has been solved analytically in a more generalised form by Carroll and Hioe.[207]

We can then consider an operator $\hat{P}$ that takes initial probability amplitudes squared (at $t \to -\infty$) to their final probability amplitudes squared (at $t \to \infty$). Under this Hamiltonian, the bare and dressed states become

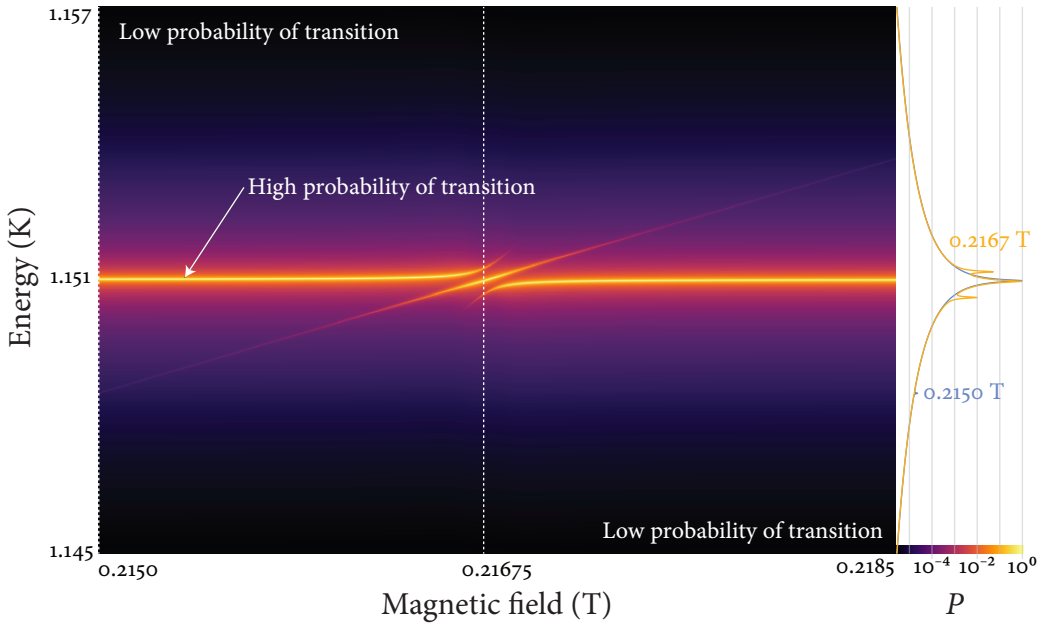


Figure 5.8: A plot of the probability P (on a logarithmic scale) of a transition at a given photon energy E and magnetic-field strength B for a toy system. A bow-tie crossing can be seen here, because the energy of the resonator has been tuned to meet the avoided level crossing. Notice that, near the crossing point, the probability of transitions to *three* states is high, with state admixing between the $|0\rangle$, $|1\rangle$, and $|\phi\rangle$states.

identical as $t \to \pm\infty$, and thus the matrix representation of $\hat{P}$ has identical elements in both the basis of the bare and the basis of the dressed states. Thus, for bare states, we have

$$\begin{pmatrix} |p_{-1}^{\infty}|^2 \\ |p_{0}^{\infty}|^2 \\ |p_{+1}^{\infty}|^2 \end{pmatrix} = \begin{pmatrix} P^2 & 2P(1-P) & (1-P)^2 \\ 2P(1-P) & (1-2P)^2 & 2P(1-P) \\ (1-P)^2 & 2P(1-P) & P^2 \end{pmatrix} \begin{pmatrix} |p_{-1}^{-\infty}|^2 \\ |p_{0}^{-\infty}|^2 \\ |p_{+1}^{-\infty}|^2 \end{pmatrix},$$

where only one of $|p_{-1}^{-\infty}|^2, |p_{0}^{-\infty}|^2, |p_{+1}^{-\infty}|^2$ is non-zero. The probability P is given by

$$P = e^{-\Gamma/2},$$

where Γ is the same adiabaticity parameter as in the original Landau–Zener model, $\Gamma = \pi V_0^2/4F$. In the limit of $t \to \pm\infty$, the eigenvalues of the Hamiltonian (Eq. (5.7)) are $-\infty$, 0, and ∞, and the three states are not coupled. With the full Hamiltonian of Eq. (5.6), however, in the approximation $k = k_0 - Ft$, there are periodic crossings, and the adiabatic eigenenergies always have finite differences, so that the states are always coupled. Three-level systems have been proposed and sought experimentally for magnetic

traps with cold quantum gasses,[208] cavity quantum electrodynamics (QED),[209] chains,[210] and quantum-dot systems.[211]

One possible situation when a bow-tie can be created in a solid-state device is as follows. The polaritonic effects near zero field, as produced by strong coupling to the cavity, can result in a triply admixed system between two spin states and a photonic state (Figure 5.9).

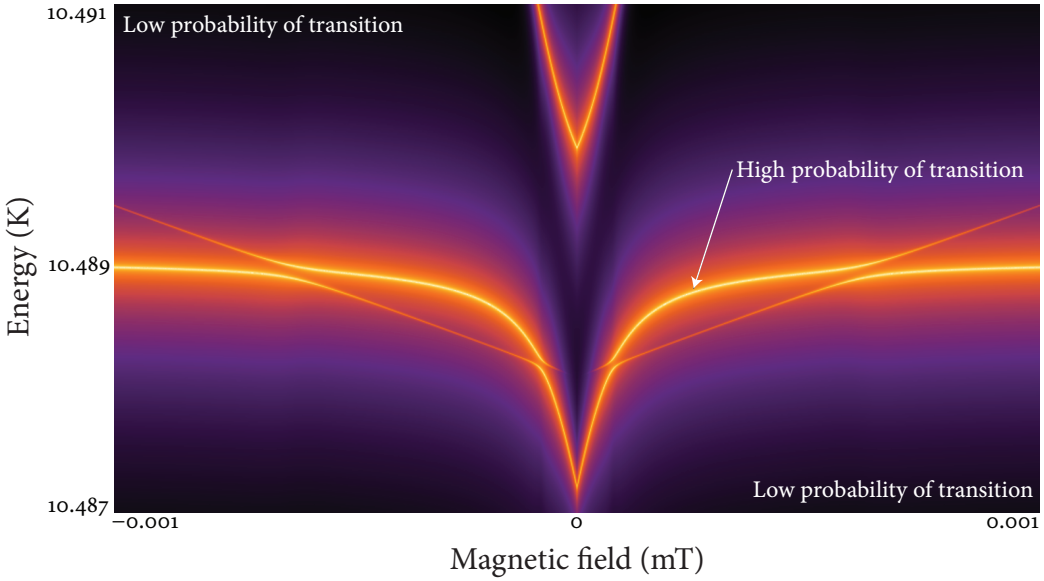


Figure 5.9: A plot of the probability P (on a logarithmic scale) of a transition at a given photon energy E and magnetic-field strength B. A polariton, a quasi-particle, can be seen here, both forcing down the energy of the lower-energy spin state and forcing up the energy of the higher-energy spin state, with the photon state having avoided level crossings with both spin states.

Consider again the situation of the $Mn_{12}Ac$ molecule in a resonator cavity. When the detuning of the cavity frequency is small, the resonator energy is close to the energy spacing between the spin levels, giving rise to more striking effects. If the field is so set that the resonance condition is achieved, the resonator and spin levels split symmetrically around their resonant energy. Sweeping the field, then, progressively shifts the resonance lines, giving the usual signature of strong coupling (see Figure 5.10). This means that the interaction term of Hamiltonian is mixing the $|\phi\rangle$and $|m\rangle$ levels, which forms a coherent superposition of the cavity and molecular states.

Because of the symmetry of the $Mn_{12}Ac$ molecule, it must have non-zero crystal-field parameters (CFPS) for only $k = 2, 4$ (in a basis which

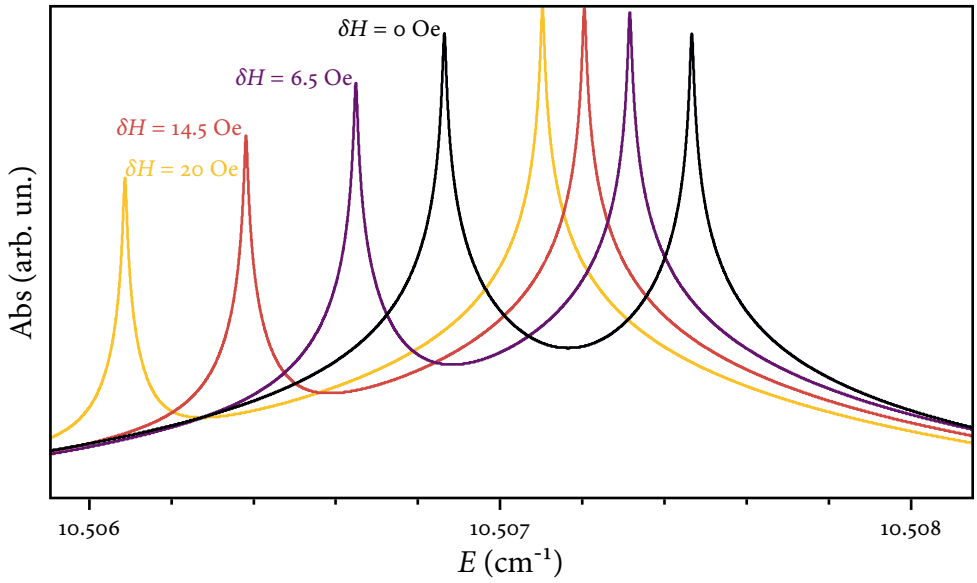


Figure 5.10: At small detunings of the cavity frequency, sweeping δH shifts the energies of the resonator and spin levels in the usual signature of strong coupling, as a result of the mixing of the $|\phi\rangle$and $|m\rangle$ levels, which forms a coherent superposition of the cavity and moleculare states.

exhibits that symmetry about the z-axis). The Zeeman splitting behaviour of the molecule, then, will not show avoided level crossings between levels whose spins differ by an odd number; that is, there is no coupling between state $|m\rangle$ and state $|m'\rangle$ if $|m - m'| \notin 2\mathbb{Z}$. For two such states, however, if an energy level of the resonator cavity is tuned near the crossing point of their energies at some field B,

$$E_{|\phi\rangle} \approx E_{|m\rangle}(B) = E_{|m'\rangle}(B),$$

the resonator state $|\phi\rangle$ interacts with both the $|m\rangle$ and $|m'\rangle$ states, creating a triple-well mixing process. The resonator state $|\phi\rangle$ can thus act as a bridge between the two states $|m\rangle$ and $|m'\rangle$, inducing mixing among all three states. This, then, produces a coupling between the two states so that even when the resonator state is removed (the spin system is decoupled from the resonator), the two spin states that are normally decoupled can remain coupled.

This bow-tie crossing is significantly different from the standard behaviour of Landau–Zener tunnelling, and together with the Klein paradox constitutes a fundamental test of quantum tunnelling. In SMMs, transitions between $|m\rangle$ and $|m'\rangle$ are now possible by coupling between the spin and

the dissipative phonon bath. To analytically characterise the behaviour, we consider the situation when the double-resonance condition is fulfilled exactly and the field detuning from the avoided level crossing δH is small. The probability amplitudes $\vec{\Psi}$ will follow the time-dependent Schrödinger equation, $i\dot{\vec{\Psi}}(t) = \mathcal{H}'(t)\vec{\Psi}(t)$:

$$i\frac{\mathrm{d}}{\mathrm{d}t}\begin{pmatrix}\psi_{|m\rangle}\\ \psi_{|\phi\rangle}\\ \psi_{|m'\rangle}\end{pmatrix} = \begin{pmatrix}\mu_{\mathrm{B}} m v t & U_{m,\phi} & V_{m,m'}\\ U_{\phi,m} & \epsilon & U_{\phi,m'}\\ V_{m',m} & U_{m',\phi} & g\mu_{\mathrm{B}} m' v t\end{pmatrix}\begin{pmatrix}\psi_{|m\rangle}\\ \psi_{|\phi\rangle}\\ \psi_{|m'\rangle}\end{pmatrix},$$

where $\mathcal{H}'(t)$ describes the hybrid system's temporal evolution as a function of the time, with field-sweep rate $v = \frac{\mathrm{d}B}{\mathrm{d}t}$ mapped onto the threefold basis and $\epsilon \ll U_{i,j}, V_{i,j}$ for all i, j is a negligibly small detuning from perfect degeneracy. Starting from occupancy $\psi_{|m\rangle} = 1$ at $t \to -\infty$, we divide $\mathcal{H}'(t)$ into diagonal and off-diagonal components according to $\mathcal{H}'(t) = H^{\mathrm{d}}t + \xi H^{\mathrm{off}}$. We then use a Wentzel–Kramers–Brillouin analysis based on Borel resummation techniques to obtain

$$\psi_i(t) = \xi \exp\left(\frac{\xi}{\mathbb{I}}\int_0^t H_i^{\mathrm{d}} t\,\mathrm{d}t\right)(H_j^{\mathrm{d}}t - H_i^{\mathrm{d}}t)^{L_{j,i}}(H_k^{\mathrm{d}}t - H_i^{\mathrm{d}}t)^{L_{k,i}}(\hat{u}_i + O(\xi)),$$

where the indices i, j, k run over $|m\rangle, |\phi\rangle, |m'\rangle$, $L_{i,j} = \mathbb{I}|H_{ij}^{\mathrm{off}}|^2/(H_j^{\mathrm{d}} - H_i^{\mathrm{d}})$, $\hat{u}_i$ is a unit vector and $\mathbb{I} = \sqrt{-1}$ is the imaginary unit for clarity. The general S matrix which connects solutions ψ_i from $t \to -\infty$ to $t \to +\infty$ can then be obtained:

$$\begin{pmatrix}\Lambda_{m,\phi}\Lambda_{m,m'} & a_{m,m',\phi}\dfrac{\Lambda_{\phi,m'}^2}{\Lambda_{m,\phi}^2} - a_{m,\phi}\dfrac{1}{\Lambda_{\phi,m'}^2} & a_{m,m'}\dfrac{1}{\Lambda_{m,\phi}^2} + a_{m,m'}\\ -a_{\phi,m}\dfrac{1}{\Lambda_{m,m'}} & -a_{m',\phi,m}a_{m,m'}\dfrac{\Lambda_{\phi,m'}}{\Lambda_{m,\phi}} + \Lambda_{\phi,m}\Lambda_{m,\phi} & (a_{\phi,m,m'} - a_{\phi,m'})\dfrac{1}{\Lambda_{m,\phi}}\\ -a_{m',m}\dfrac{\Lambda_{m,\phi}}{\Lambda_{\phi,m'}} & -a_{\phi,m'}\dfrac{1}{\Lambda_{m,m'}} & \dfrac{1}{\Lambda_{\phi,m'}\Lambda_{m,m'}}\end{pmatrix},$$

where $\Lambda_{i,j} = \exp(\mathbb{I}\pi L_{i,j})$,

$$a_{i,j} = H_{ij}^{\text{off}} \frac{\mathbb{I}\sqrt{2\pi}}{\Gamma(1 \pm L_{i,j})\sqrt{(H_j^{\text{d}} - H_i^{\text{d}})e^{f\mathbb{I}\pi/2}}} (\sqrt{2}\xi)^{f2L_{i,j}} e^{-(f-\frac{1}{2})\mathbb{I}\pi L_{i,j}} \left[\frac{e^{\mathbb{I}\pi L_{ij}} e^{\frac{\mathbb{I}\xi^2}{2H_i^{\text{d}} - 2H_j^{\text{d}}}}}{(2H_j^{\text{d}} - 2H_i^{\text{d}})^{L_{i,j}}} \left(\frac{H_k^{\text{d}} - H_j^{\text{d}}}{H_j^{\text{d}} - H_i^{\text{d}}} \right)^{L_{j,k} - L_{i,k}} \right]^f,$$

$a_{i,j,k} = a_{i,j} a_{j,k}$, and

$$f = \begin{cases} 1, & (i,j) \in \{(m,\phi),(\phi,m'),(m,m')\}; \\ -1, & \text{otherwise.} \end{cases}$$

This leads to the tunnelling probability

$$P_{m,m'}^{\Phi} = 1 - \exp\left(-\frac{\pi \left(E_{m,m'}^{\Phi}\right)^2}{2\hbar g \mu_{\text{B}} |m - m'| v} - \left(\frac{\pi \left(E_{m,m'}^{\Phi}\right)^2}{4\hbar g \mu_{\text{B}} |m - m'| v} \right)^2 \right),$$

which, compared to the standard Landau–Zener case, has both an increased transition rate and a different dependence on v.

5.7 Conclusion

In this chapter, I have started exploring the inclusion of molecular magnetic materials into quantum devices, from a theoretical perspective. I explored theoretically what results when a multilevel system interacts with a resonator. I first demonstrated, in Section 5.5, that otherwise-forbidden transitions between spin levels are opened by a virtual path through even a highly detuned photon level. Such an interaction between the photon and a pair of spin levels opens up a gap between the spin levels, a gap that increases as the coupling between the photon and spin system strengthens. This interaction in turn increases the rate at which the spin system's state tunnels between such spin levels, as the coupling between the spin system and the resonator grows stronger.

In Section 5.6, I showed that when the resonator level crosses two spin levels at their intersection, the three-level system that forms from

their interaction results in a bow-tie crossing, even at zero field. Bow-tie crossings have been proposed in quantum gasses[212, 213] and are highly sought after in solid-state systems, because the means to strongly couple three or more energy levels for quantum coherent transport is required for advanced quantum information protocols in the solid state, so a resonator–spin system could fill this need.

The resulting collective behaviour is a polariton, which both forces down the lower spin levels' energy and forces up the higher spin levels' energy. We also determined analytically the tunnelling probability in such a three-level system, thus showing the effect of polaritons not only on level splittings in a spin system, but also on their dynamic properties. Such a resonator–spin system may make possible, for the first time, a macroscopic quantum system, based on the quantum coupling between a resonator and a crystal's entire ensemble of molecules. In such a multi-level system, the tunnelling probability between a pair of spin levels has a different relationship with respect to the sweep rate, and the transition rate is boosted. This means that forming such systems can, in general, boost transitions between a selected pair of levels by careful application of a magnetic field and a properly engineered resonator.

In the next chapter, I will further explore this concept. Using both theoretical and experimental results, I will investigate the so-called strong-coupling regime by examining the behaviour of a Gd-based crystal strongly coupled to a microwave resonator.

6 Strong coupling of spin systems to light

6.1 Overview

In this chapter we examine in greater detail how a multi-level system with a Gd(III) centre is affected by strong coupling. In particular, we examine the ways in which both temperature and rotation change the joint resonator–spin system's energy levels and its cooperativity, which is a measure of the interaction due to the strong coupling. When a resonator and a spin system strongly couple, their energy levels are affected by their interaction in such a way that they "repel" each other in the energy–magnetic field space, creating an anticrossing, or avoided level crossing. It is true that this behaviour is well understood and has been studied for decades for two-level systems, and even systems with many levels can be understood as two-level systems close to any anticrossing between pairs of levels. But the addition of a tunable resonator energy makes it possible to easily construct a multi-crossing merely by forcing an anticrossing between a resonator level and an existing anticrossing between the spin system's levels. Such a multi-crossing involving a resonator level gives an avenue into manipulating the system's various spin states, including superpositions among them, through

excitations using the resonator. This possibility raises five questions: (1) How does temperature affect strong coupling? (2) How is strong coupling affected as the system is rotated? (3) How shall we characterise cooperativity in a multi-crossing system? (4) How do two-level crossings interact as they move closer together? (5) And how can we predict some of this behaviour from *ab initio* calculations on simply the crystal structure of the multi-level system and resonant mode of the resonator?

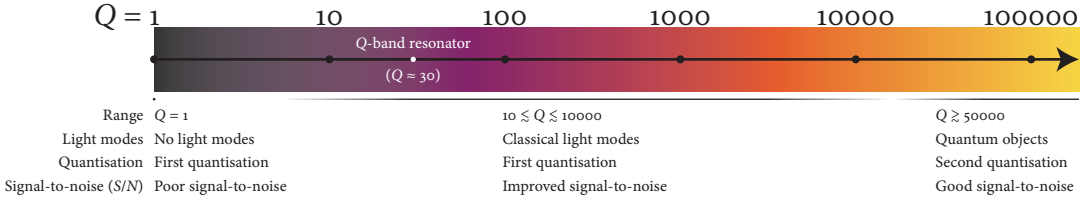


Figure 6.1: Different regimes of a resonator's quality factor. At $Q = 1$, there are no light modes in the resonator, the light is described by first quantisation, and measurements have poor signal-to-noise. At higher Q, light modes become measureable, and signal-to-noise improves. At very high Q, in addition to significantly improving signal-to-noise, the light becomes second quantised, and the quantum-mechanical coupling between light and matter causes them to effectively become quantum objects.

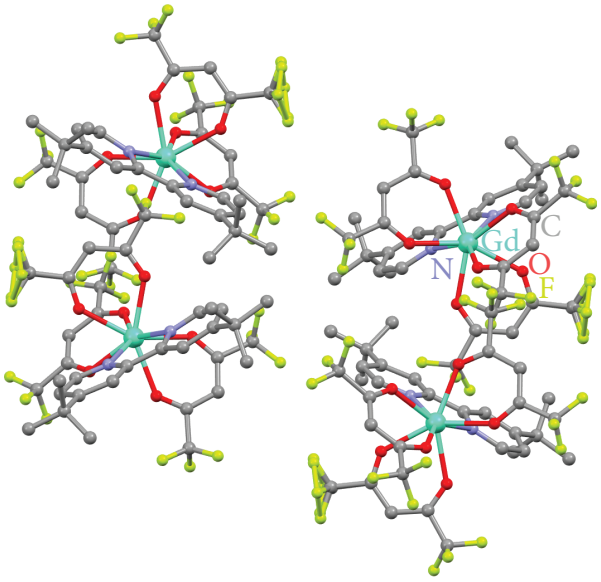
To investigate these questions, and to compare our results meaningfully to experimental data, we must overcome a substantial challenge: we need to be able to simulate the behaviour and response of molecular magnetic systems in different regimes of light–matter coupling.

On increasing the quality factor (or Q factor) of a resonator, the behaviour of a molecule–resonator system can fundamentally change (Figure 6.1). For $Q = 1$, a situation that can be experimentally realised by placing a crystal on a conducting stripline, there is actually no resonator, and one is able to freely scan the frequency of the incoming electromagnetic radiation. The system is thus completely described by the standard textbook light–matter interactions for first quantization. Because there is no signal-to-noise enhancement, such experiments rely purely on the population difference produced by Boltzmann statistics, and must thus be conducted at temperatures that are much lower than the energy of the incoming radiation. On increasing Q, which is the situation that is most commonly found in experiments, such as for electron paramagnetic resonance (EPR), the signal-to-noise ratio improves, but one is limited by the bandwidth of the resonator,

and thus only a few transitions might be observable. If Q is increased much further, in addition to measurements giving a significantly increased signal-to-noise ratio, the assumptions that allow perturbative treatment of light–matter interactions are no longer accurate. We thus fall into a completely different physical regime, were the joint molecule–resonator system needs to be treated as a whole, in a fully quantum-mechanical, second-quantisation approach. We are most interested in the evolution of the physics from one regime to another, and in particular we will examine the situation when the entire molecule–resonator system becomes quantum-mechanically coupled. In the following sections, we will explore and describe properties of the molecular magnetic compound at different light–matter couplings using resonators of different Q.

6.2 [Gd(hfac)$_3$(^{t}Bubpy)]

[Gd(hfac)$_3$(^{t}Bubpy)], which we abbreviate Gd(hfac)$_3$, is a single-ion magnet with a single Gd^{3+} metallic-ion centre surrounded by three hexafluoroacetylacetonate[a]ligands, which are well known to efficiently block magnetic interactions with the environment, and coordinated to the 5,5′-di-t-butyl-2,2′-bipyridine[b] ligand, which also provides magnetic shielding.



[a] Hexafluoroacetylacetonate is the chemical compound $CF_3C(O)C(H)C(O)CF_3$, which coordinates at the two O sites.

[b] 

Figure 6.2: The unit cell of a [Gd(hfac)$_3$(^{t}Bubpy)] crystal, which is monoclinic, as viewed along the crystallographic $\hat{a}$ axis. There are four molecules per unit cell, related by inversion and a mirror plane (or equivalently, inversion and a screw axis), giving two inequivalent molecules per unit cell, with no higher symmetry. Hydrogen atoms have been omitted for clarity.

Gd(hfac)$_3$ crystallises in a monoclinic unit cell, with four molecules per unit cell. Two of the molecules are related to the other two by inversion, giving two inequivalent molecules per unit cell that are related by a 2_1 screw axis along $\vec{b}$ (or equivalently, a glide plane with normal $\vec{b}$). The cell axes $\vec{a}, \vec{b}, \vec{c}$ have lengths 13.0696(2) Å, 22.9794(4) Å, and 14.5283(3) Å, with $\beta = 109.295(2)°$.

6.2.1 *Ab initio calculations*

The molecule was sufficiently small that all configurations of the Gd centre's valence electrons could be considered in the *ab initio* calculations of the molecule. Once the crystal-field parameters (CFPs) were obtained, they were rotated into the laboratory frame (for Section 6.2.4 only), with $\hat{x}$ in the $(\bar{1}\,0\,\bar{1})$ direction and $\hat{z}$ in the $(0\,\bar{1}\,0)$ direction, and both inequivalent orientations of the molecule in the cystal unit cell were considered in all further calculations.

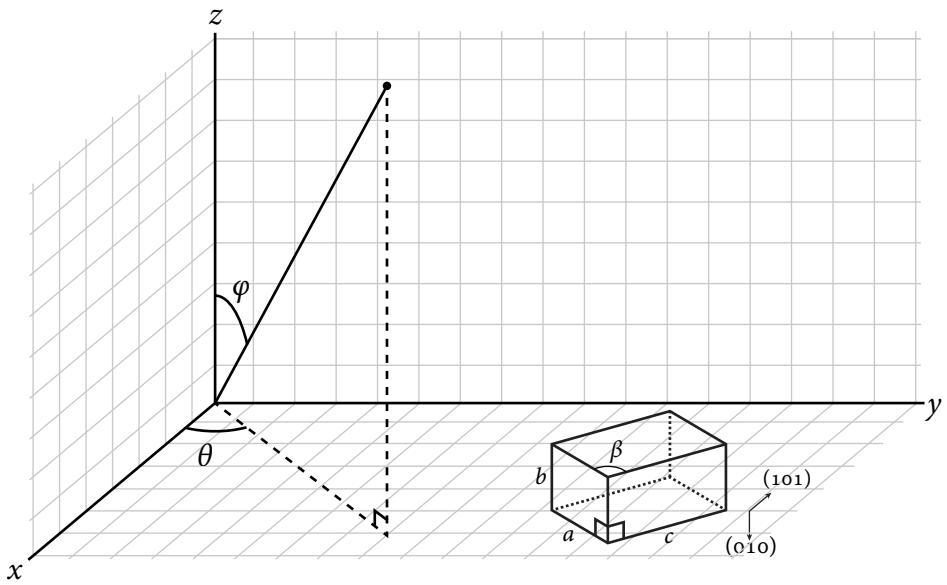


Figure 6.3: The definition of the lab frame in this chapter, with azimuthal angle ϕ measured from the z axis and polar angle θ measured from the x axis. The orientation of the Gd(hfac)$_3$(^{t}Bubpy) crystal in the strong-coupling measurements considered in Section 6.2.4 is also shown. The drawing is approximately to scale for the unit cell, and not the physical crystal grown.

6.2.2 $Q = 1$ *resonator at fixed orientation*

An experiment with a low-Q resonator was conducted at 22 mK by Conrad Clauß, whose Gd(hfac)$_3$ crystal was synthesised by Lapo Bogani, at a fixed orientation over large energy and magnetic-field ranges. This more clearly shows the energies of the spin transitions as magnetic field is varied, rather than only around a given, fixed energy, as with a high-Q resonator.

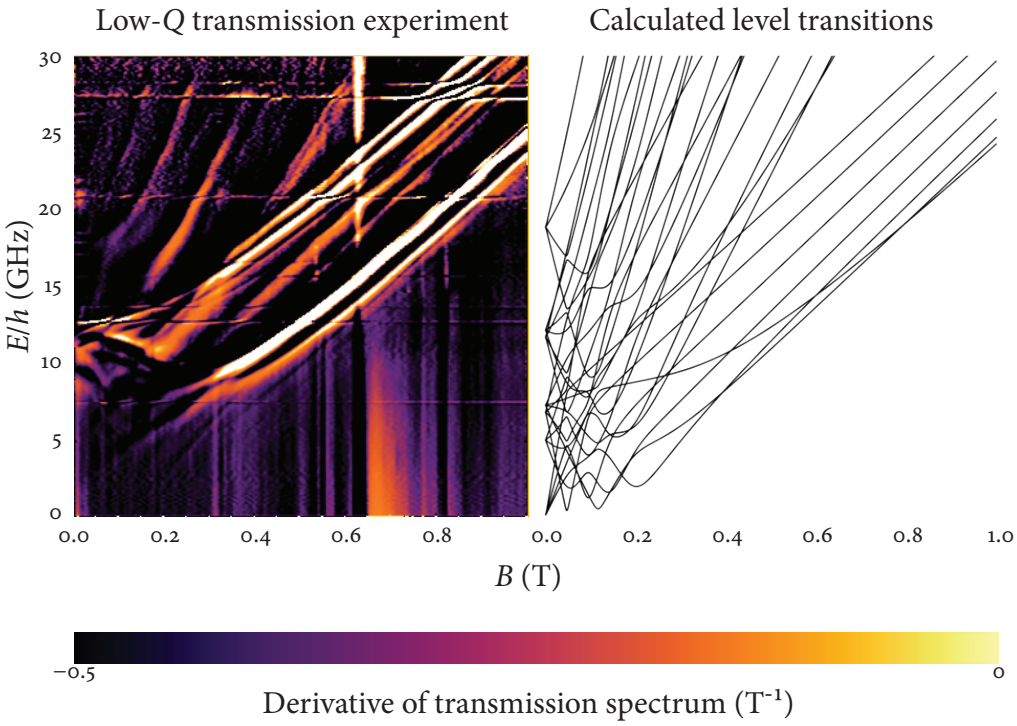


Figure 6.4: A comparison between (Left) a low-Q transmission experiment at 22 mK (plot of derivative of averaged transmission spectrum that has been low-pass filtered[203], $-0.5\ \mathrm{T}^{-1}$ $0\ \mathrm{T}^{-1}$), which sweeps a large range of the energy and magnetic field, and (Right) the level transitions as calculated from *ab initio* results, at an orientation of the polar angle at $\theta = 80°$ and the azimuthal angle at $\phi = 40°$, chosen by visual inspection to roughly match the spead of the experimental data, since the exact orientation of the crystal was not known. The transitions between high-spin states are less likely and therefore appear less prominently in the data.

Because the exact orientation of the crystal was unknown in the experiment, it is impossible to perfectly compare the results of the *ab initio* calculations with those of the experiment. The energies at zero field, however, are not orientation dependent, nor are the energy levels' macroscopic change due to Zeeman interaction. Because *ab initio* calculations of this kind can sometimes slightly underestimate energies by a multiplicative factor, we compared the results of the *ab initio* predictions to the zero-field energies observed in experiment. Then, scaling all the CFPs from the calculations by 1.8 (estimated by visual inspection), we observed that the

predictions were in good agreement with measurements, the exact crystal orientation notwithstanding (Figure 6.4). All further calculations were thus conducted using these scaled CFPs, which are reported in Table A.3.

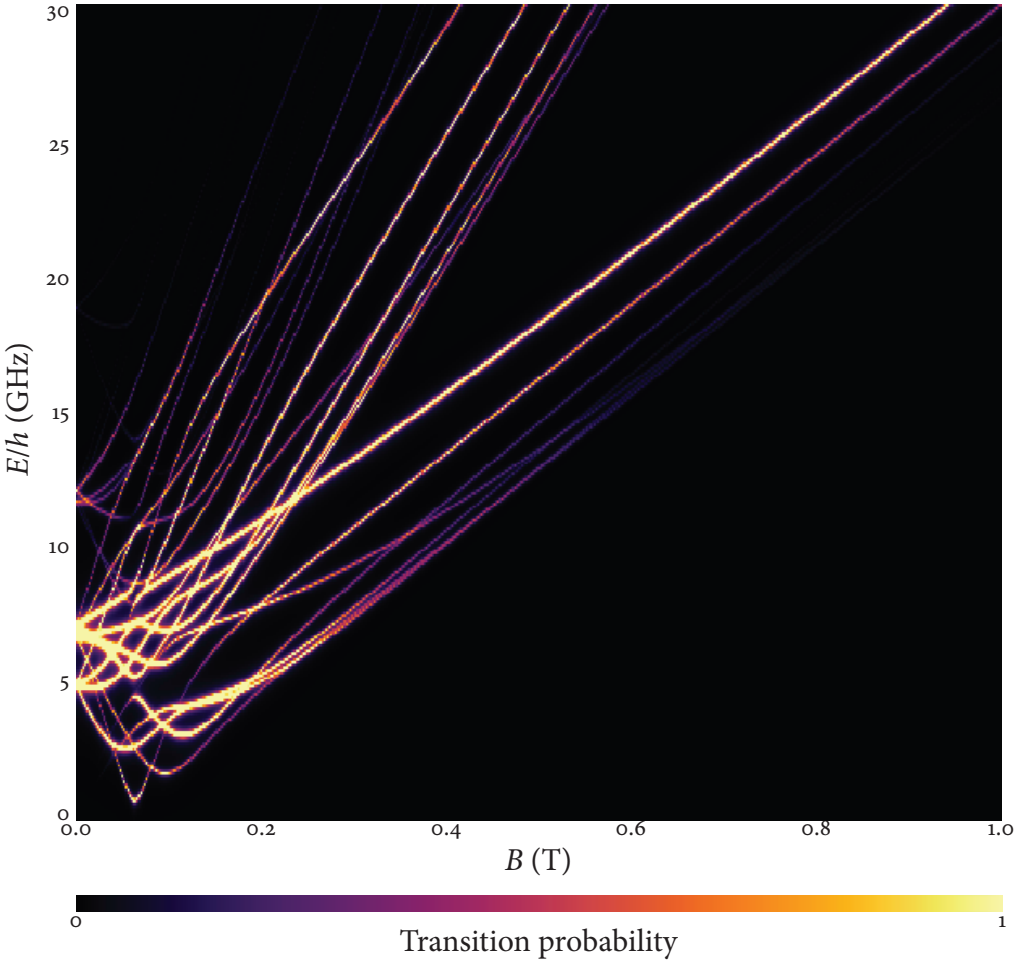


Figure 6.5: A prediction of a low-Q transmission experiment, at the same orientation as in Figure 6.4. Here, the transition probabilities are taken into account for the pair of energy levels that give rise to each transition energy found. As expected, the transitions between high-spin states have low probability, except when they are close in energy to a transition between lower-spin states (because of state mixing).

The transitions detected through the experiment are in relatively good agreement with the predicted transition energy lines as a function of field, though there are many more possible transitions than observed experimentally. This is because some transition energies may correspond to transitions that are unfavourable (very low probability) or quantum mechanically forbidden. We can take into account transition energies as well by calculating the probabilities of an EPR transition at each energy and field for the system (Figure 6.5).

6.2.3 *EPR powder experiments in a low-Q resonator*

With the CFPs calculated for the crystal, it is also possible to simulate EPR powder experiment data by calculating the magnetic response in random orientations of the field relative to the molecule. We compare here the data from an echo-detected field-sweep (EDFS) EPR experiment conducted at 5 K to a simulation in PHI[214] for a powder sample using a linewidth of 0.075 GHz and powder-simulation parameter $N = 6$, which generates 377 orientations according to the Zaremba-Conroy-Wolfsberg (ZCW) scheme.[215]

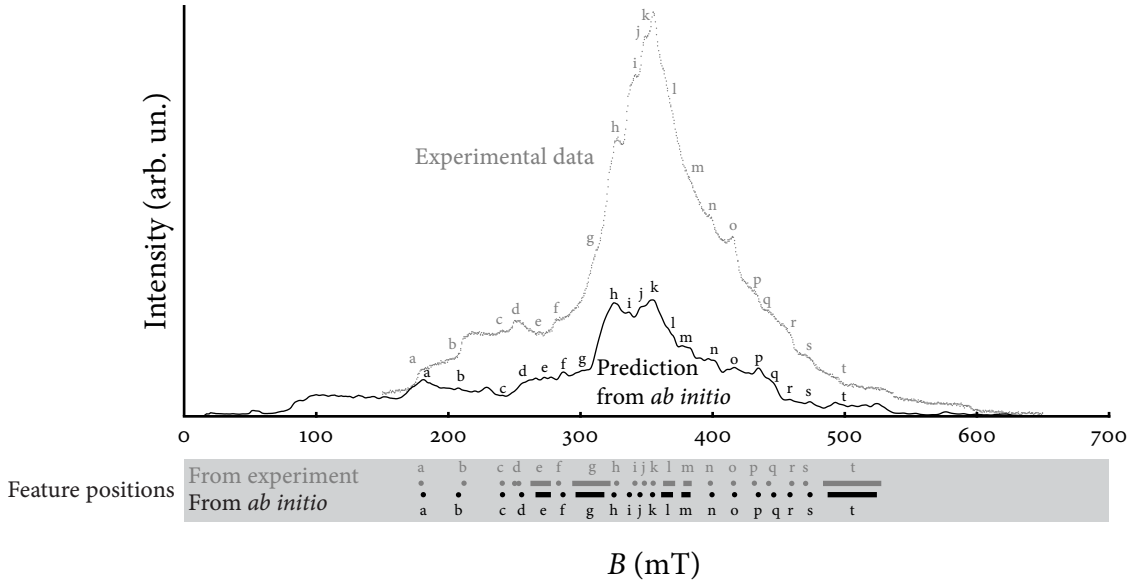


Figure 6.6: EPR powder simulation compared to data from an echo-detected field-sweep (EDFS) EPR experiment at 9.792674 GHz and 5 K. The powder simulation was conducted in PHI with a linewidth of 0.075 GHz and $N = 6$ as the ZCW parameter. Since EPR data have arbitrary intensities, the y-axis scale is arbitrary and has been omitted. Because of the nature of EDFS experiments, we are focus only on peak locations, which have been roughly marked. The labelled features are discussed in greater detail in Table 6.1.

Because of the hard pulses used by EDFS, the measured response is not in general linear in the strength of the transition but may in fact include higher order terms. This means that peak intensities, even relative to each other in the spectrum, are unreliable. The positions of peaks are still generally somewhat reliable, however. It is most useful, therefore, to broadly compare features between simulations and experiments, as we have done in Figure 6.6. We see that, for instance, though *ab initio* calculations predict the EPR response at peaks h and k to be of similar magnitude, the

EDFS data do not reflect that. Though there is some misalignment between the features as predicted by simulation and as visible in the data, they appear to always be within 5 mT of each other (Table 6.1). The discrepancy is most prominent far away from the main peak (around 355 mT), and at the higher fields (above 420 mT), the peaks wash out almost entirely and are not easily visible in the data, though we have tried to identify slopes and small bumps in the data that are likely a result of nearby peaks. Many of the strong responses, however, have discrepancies of 3 mT or less, showing good agreement between the data and the simulation.

6.2.4 *High-Q resonator at different orientations*

When a crystal of Gd(hfac)$_3$ is placed in a microwave cavity resonator, the spin-level transitions will strongly couple with the resonant modes of the cavity. When the cavity has a high quality factor, it will absorb (and transmit) photons at energies near its resonant frequencies, with transmission profiles that are approximately Lorentzian, centred about its resonant frequencies. When coupled to a spin system, however, the transmission "band" will have small gaps due to avoided level crossings (as a function of magnetic field) with the transition-energy levels of the spin system. Thus the transition energies of a spin system that it is coupled to microwave cavity resonator can be observed when the transition energies are approximately that of the cavity's resonant modes. When the cavity has a very low quality factor, conversely, the Lorentzian "smears out", so that the transition-energy levels interact with the cavity and are visible at a greater range of energies of light.

The limitation to low-Q experiments, however, is that high-energy spin levels may be difficult to observe in practice. This is because the lower the quality factor of a cavity, the greater the dependence on population differences among the levels. Thus, while a high temperature reduces

Name	Sim. feature (mT)	Exp. feature (mT)
a	Peak, 181	Slope, 175–179
b	Peaks, 208	Slope, 207–211
c	Peaks, 241	Peak, 241
d	Slope, 249–256	Peaks, 250, 253
e	Peak sequence, 266–278	Peak sequence, 262–278
f	Peak, 287	Peak, 283
g	Peak sequence, 296–318	Slope, 294–323
h	Peak, 325	Peak, 327
i	Peak, 337	Peak, 341
j	Peak, 345	Peak, 348
k	Peak, 355	Peak, 355
l	Slope, 361–370	Slope, 362–372
m	Peak sequence, 376–383	Slope, 378–384
n	Peaks, 397, 400	Peak, 398
o	Peak, 417	Peak, 416
p	Peak, 435	Slope, 432–437
q	Slope, 442–454	Slope, 442–453
r	Peak, 459	Slope, 456–462
s	Peak, 474	Slope, 470–476
t	Peak sequence, 487–524	Peak sequence, 484–528

Table 6.1: A comparison of some notable features in Figure 6.6. Some of the peaks in the data were slightly washed out or merged together, and likewise, some peaks in the simulation were not very prominent. In such cases, the washed-out peaks or group of peaks was treated as a single feature, and noted as such. Feature positions were approximately estimated visually.

the difference in spin-state populations, a low temperature will prevent high-energy levels from having appreciable population, in accordance to Boltzmann statistics. High-Q experiments, on the other hand, do not suffer from this limitation, and the resonator can be appropriately tuned to high energies as necessary.

When the quality factor of the resonator is high, the coupling strength increases, and the contributions to coupling strength of the individual spin systems in an ensemble (such as in the Gd(hfac)$_3$ crystal) can be combined to estimate the collective coupling strength according to:

$$C = \sqrt{\sum_i C_i^2},$$

where C_i are the coupling strengths between the individual spin systems and the photons. If the C_i are taken to be equal, we find

$$C = \sqrt{N} C_i^2.$$

In other words, the coupling strength of an ensemble increases as the square-root of the size (number of molecules) of the ensemble.

Hence, transmission experiments were conducted in a high-Q resonator at 16 mK, 500 mK, and 1 K by Wenjing Yan, whose Gd(hfac)$_3$ crystal was synthesised by Lapo Bogani and Dimitris Alexandropoulos, at different rotations along three planes well-defined with respect to the crystal structure (xy-plane results shown in Figure 6.7). Each experiment measured the transmission of photons through the resonator at a given direction of magnetic field, with a varying magnetic field strength and photon energy. The energy was chosen to be near the fundamental mode of the resonator.

In each orientation, therefore, the profile of the transmission strength should be approximately Lorentzian, except near any avoided level crossings (see Figure 6.8).

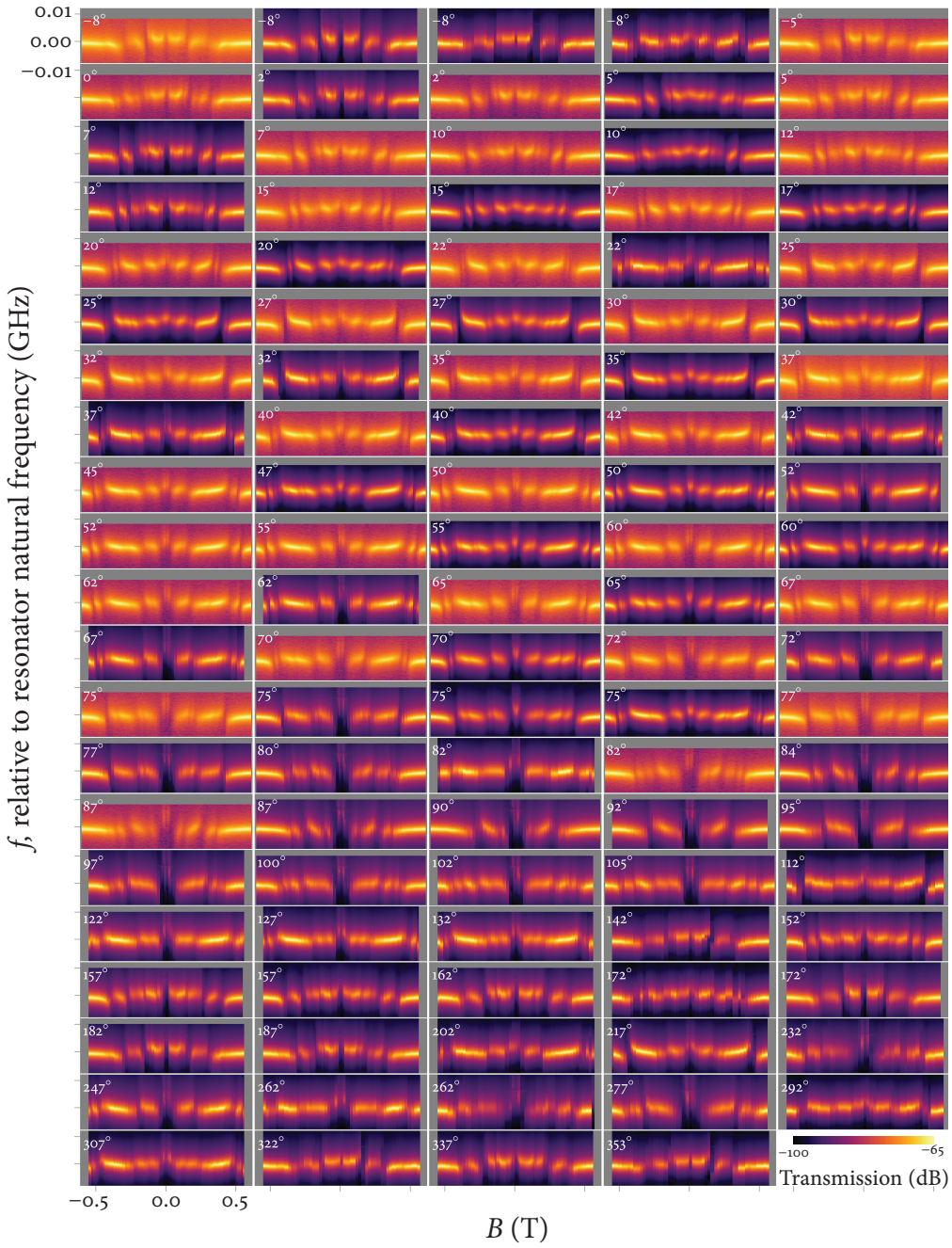


Figure 6.7: A series of 16 mK transmission measurements at different orientations in the xy-plane, with different values of θ as defined in Figure 6.3. Frequencies are given relative to the natural frequency of the resonator, 12.081 GHz. The darker colours indicate lower transmission, while the lighter colours indicate higher transmission. These measurements were taken over two sessions, giving the slightly different groups of colouration and differing energy and field ranges.

In order to understand the angular and magnetic-field dependence of these data, it is important to be able summarise the data across the range of photon energies, at each magnetic field strength and orientation. Two methods were used, with qualitatively comparable success, which we shall call them the "Averaging Method" and the "S_{21} Method". While the latter is more rigorous and has been used in the literature, the former is computationally less intensive and guaranteed to work. The disadvantages

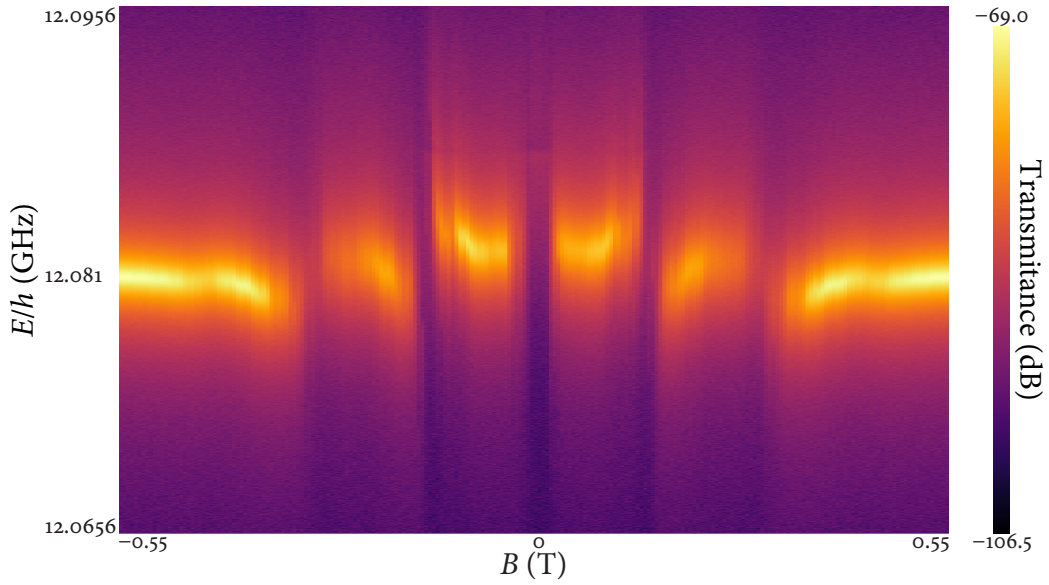


Figure 6.8: An enlarged single transmission measurement at −8° in the xy-plane. The avoided level crossings can clearly be seen here, creating breaks in the resonator line, which otherwise would be a constant, horizontal line at 12.081 GHz. The picture is symmetric, since magnetic responses in compounds are symmetric with respect to inversion of the magnetic field, and some avoided level crossings are more apparent, while some are weaker (~0.5 T).

of the latter are that, because it involves a parameter-fitting step, (1) the fitting may fail to converge, (2) the fitting may converge on a local minimum that does not describe the data well, and (3) the fitting may be considerably slower.

Averaging Method. By visual inspection, we define an energy band of interest around the resonant mode of the cavity. Then, at each field strength, the transmission strength across that band of energies is averaged to produce a single "average transmission strength" for that field strength. This then gives a value for each orientation and strength of the magnetic field.

S_{21} *Method.* At each field strength, the transmission data across the entire range of energies (with frequency ω) measured at is fit to a standard input–output model,[124]

$$|S_{21}(\omega)| = \left| \frac{\kappa_e}{i(\omega_c - \omega) + \frac{\kappa_c}{2} + \frac{g_k^2}{i(\omega_k - \omega) + \gamma_k}} \right|, \tag{6.1}$$

where κ_e is the coupling rate to the microwave resonator, ω_c is fundamental frequency of the cavity, $\kappa_c = \omega_c/Q$ is the total relaxation rate of the resonator (Q is the quality factor), g_k is effective ensemble coupling be-

tween the molecular spins and the resonator, $\omega_k = g\mu_B B/\hbar$ is the frequency associated with the magnetic field B, and γ_k is the spin-dephasing rate.

The results in both of the above methods are qualitatively very similar, though they have individual strengths and weaknesses. The S_{21} method does not rely on a choice of an energy band, but for weak signals, may not reliable be able to produce good fits. It is, however, derived from a standard model, and the numbers therefore have more useful physical meaning. The averaging method will successfully give a result for all data sets, though it relies on a good choice of energy band and the quantitative values found are less physically meaningful. It will also tend to flatten and broaden the crossing areas slightly, though the crossing points indicated should not shift. A quantitative comparison of the two was not considered, since for the data considered here, the more rigorous S_{21} method was able to reliably produce good fits, and was therefore chosen in favour of the averaging method.

In any case, in principle, either gives some calculated value as a function of the magnetic field B. Since this is for some particular orientation, we can plot all the values as a function of both B and θ for each of the planes of rotation along which measurements were taken, giving us the energy-level crossings as a function of field and orientation.

We can also determine the cooperativity C from the S_{21} fitting parameters according to

$$C = \frac{2g_k^2}{\kappa_c \gamma_k}. \tag{6.2}$$

This formalism assumes that crossings are well isolated from one another, and the cooperativity C is also only well defined between a resonator and one magnetic level. The full widths at half maximum (FWHMs) of the Lorentzian fits of S_{21} will themselves follow Lorentzian shapes as a function

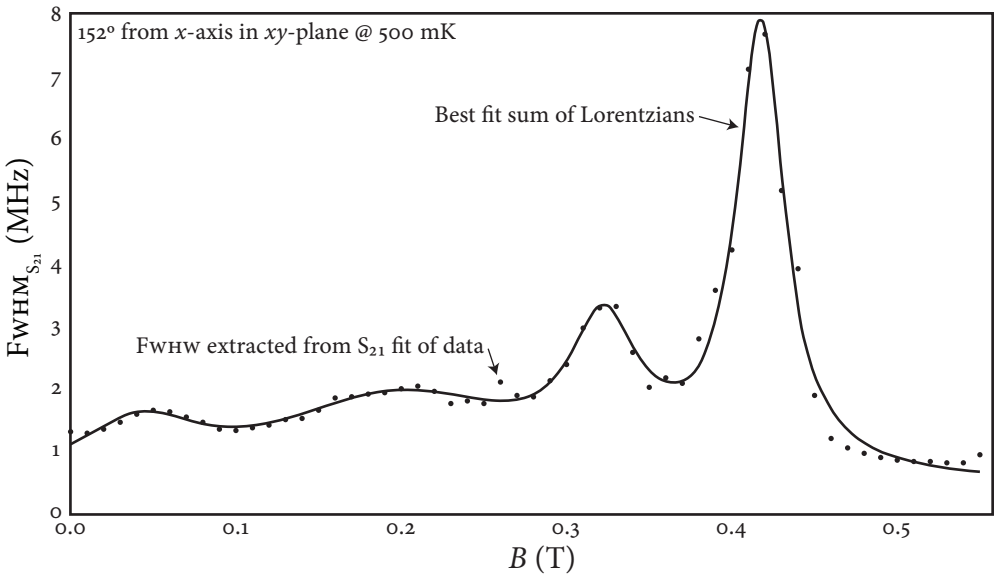


Figure 6.9: The full width at half maximum (FWHM) of $S_{21}(\omega)$ fitted to the energy spectrum at each magnetic-field strength are plotted as points, and the line is a fit to a sum of Lorentzian curves, in this case a sum of four Lorentzian curves.

of magnetic field. In the general form of a Lorentzian distribution given by

$$f(x) = \frac{A}{\pi\gamma\left[1 + \left(\frac{x-\bar{x}}{\gamma}\right)\right]^2} + c,$$

the cooperativity from a single Lorentzian can equivalently be expressed as

$$C = \frac{A}{\pi c \gamma}.$$

When crossings are sufficiently close, however, the interactions between the Lorentzians may be non-negligible, so that the shape of the FWHMs of the Lorentzian fits must be expressed as

$$f(x) = \sum_i \frac{A_i}{\pi\gamma_i\left[1 + \left(\frac{x-\bar{x}_i}{\gamma_i}\right)\right]^2} + c_i,$$

where i is taken over the number of crossings, or equivalently Lorentzians (see Figure 6.9). This can equivalently be expressed as

$$f(x) = \sum_i \frac{A_i}{\pi\gamma_i\left[1 + \left(\frac{x-\bar{x}_i}{\gamma_i}\right)\right]^2} + c,$$

where

$$c = \sum_i c_i,$$

and in a simultaneous fit to this function from data, it is impossible to extract the individual c_i. Thus, the cooperativity for a given crossing,

$$C = \frac{A_i}{\pi c_i \gamma_i},$$

cannot be found exactly, since c_i is indeterminable. We are guaranteed, however, that $c_i \leq c$ for all i, so that

$$C \geq \frac{A_i}{\pi c \gamma_i}.$$

Thus, we can still determine a lower bound for the cooperativity between the resonator and a given magnetic level of the system.

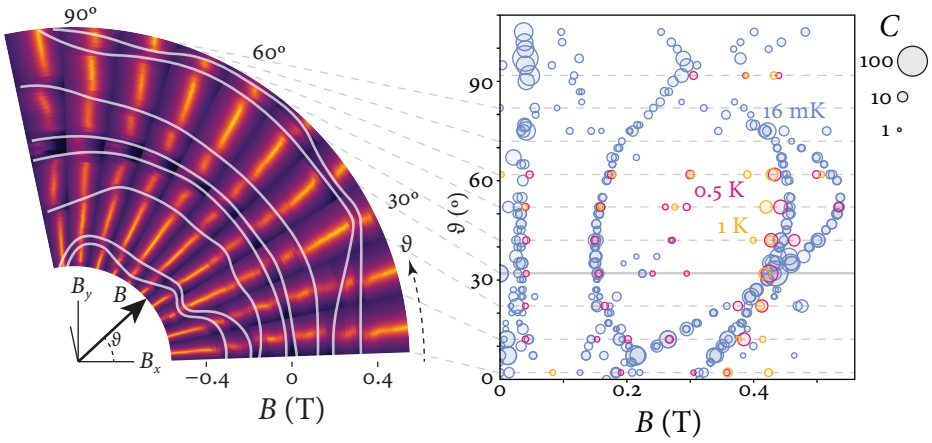


Figure 6.10: A schematic of the data-treatment process, with (Right) a few measurements arranged radially along the directions they were conducted in, and (Left) the lower-bound cooperativities extracted from the S_{21} fits of the data at various temperatures. In general, the cooperativities weaken at higher temperatures, though some crossings become more prominent, and others shift. This is clearly visible in the $\theta = 32°$ fit (Figure 6.11).

We can then plot this lower bound cooperativity across different temperatures as a function of both magnetic field and angle (Figure 6.10). The cooperativities at low temperatures (16 mK and 500 mK) are relatively consistent as the angle varies, but when two crossings cross, producing a three-level crossing among the resonator and the two spin levels, the cooperativity is "boosted" because both cooperativities are active. Computationally when the peaks were sufficiently close, the fitting process was unable to differentiate the distinct peaks, and the two Lorentzians would

therefore sum into a large Lorentzian. In the limiting case when two peaks were to coincide exactly, we would indeed have, near the crossing,

$$f(x) = \frac{A}{\pi\gamma\left[1+\left(\frac{x-\bar{x}}{\gamma}\right)\right]^2} + \frac{B}{\pi\gamma\left[1+\left(\frac{x-\bar{x}}{\gamma}\right)\right]^2} + c = \frac{C}{\pi\gamma\left[1+\left(\frac{x-\bar{x}}{\gamma}\right)\right]^2} + c,$$

where $C = A + B$, so that there is only a single Lorentzian. We also expect this physically, since there is cooperativity between the resonator and each of the two crossings, which gives an overall cooperativity that is boosted by both. At higher temperatures, new peaks may appear while old ones diminish (e.g., at $\theta = 60°$ in Figure 6.10). This likely results from a change of which transitions are favoured, according to the Boltzman distribution.

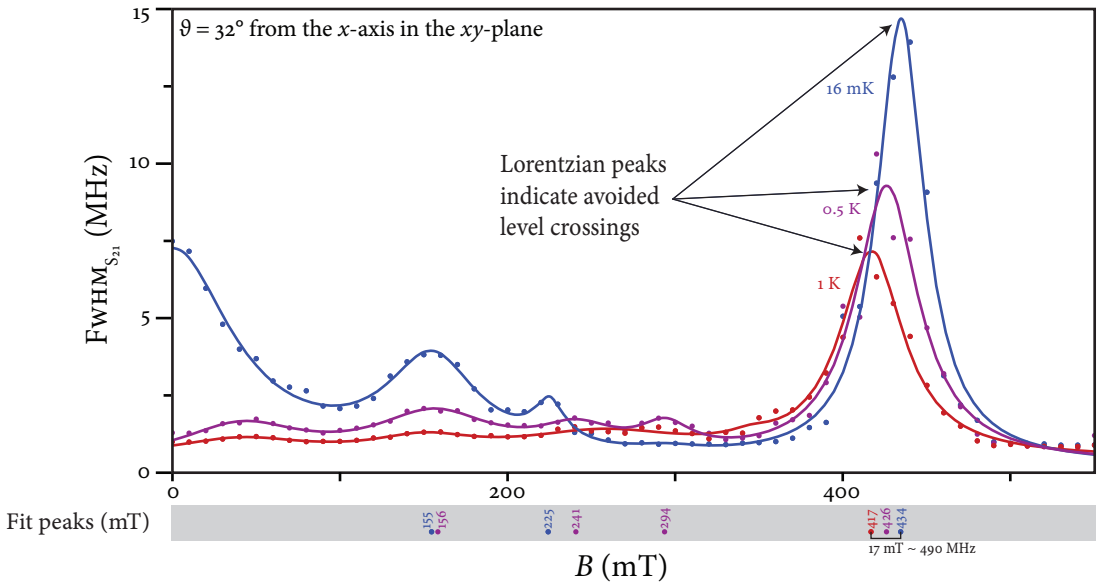


Figure 6.11: An example of the fitting process for various temperatures. As the temperature is varied, the coupling strengths at the various crossings changes (indicated roughly by the sharpness of the peaks), certain peaks disappear and others arise (as a result of different transitions being favoured), and the locations of some peaks shift slightly (on the order of 0.5 GHz).

Interestingly, in addition to decreasing the height of the peaks (and therefore the cooperativity), increasing the temperature also shifts the peaks as well (Figure 6.11). This is a robust shift, not an artifact from the fitting process, as is visible visually from the data. The shift from 16 mK to 1 K is roughly 0.017 T, which corresponds to an energy difference of roughly 490 MHz. This may be a result of a residual magnetorestriction or a thermorestrictive effect.

The experimental results from the high-Q resonator were more difficult to simulate outright, because essentially, the crossings observed by the experiment satisfy

$$E = \lambda_j - \lambda_i,$$

for the resonator energy E and λ_i, λ_j satisfying

$$\mathrm{Det}\left(I - \lambda H(\vec{B})\right) = 0.$$

While there is a closed-form expression for λ, the characteristic polynomial found by expanding the determinant, we in fact need values of $\vec{B}$ such that

$$\prod_{\lambda_i,\lambda_j} (\lambda_j - \lambda_i - E) = 0,$$

which cannot be solved from an analytical expression of $H(\vec{B})$.

For a given orientation of $\vec{B}$, however, it is possible to try to approximate values of the magnitude B until some transition energy crosses the desired E. This can be done by assuming the energy levels vary linearly with magnetic field, which is true when they are far apart from each other, and applying Newton's method (Figure 6.12).

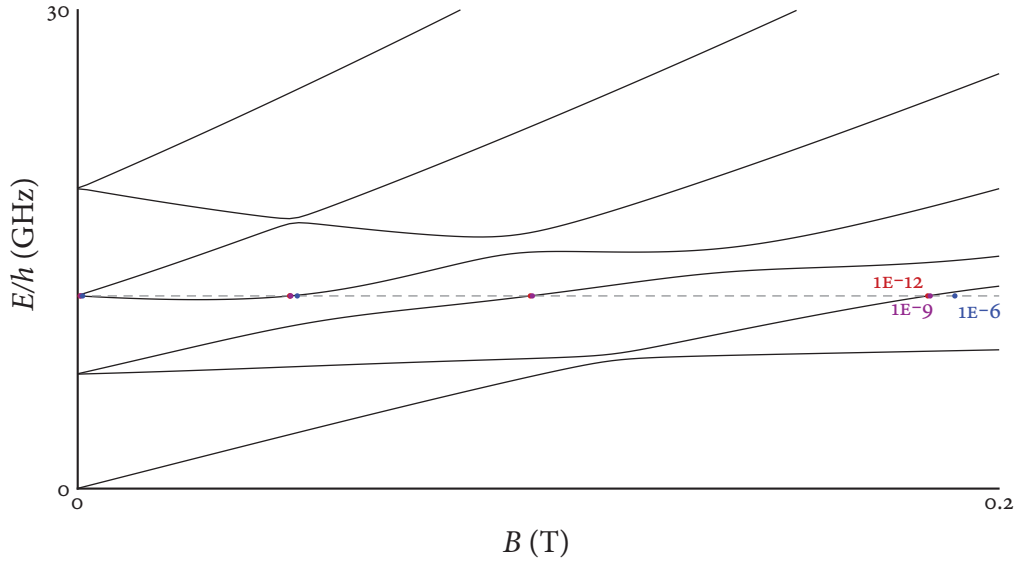


Figure 6.12: Because of mixing among the states, the magnetic field at which energy levels cross a given energy is not a solution to a linear equation and cannot be solved analytically. We can assume, however, that for points far from an anticrossing, the energy levels vary roughly linearly with field. When this hold true, we can estimate the crossing points using Newton's method, up to a specified tolerance. The results of applying this method using three tolerances, 1×10^{-6}, 1×10^{-9}, and 1×10^{-12}, are shown here.

This is, however, extremely computationally intensive, when we consider the fact that at lower fields, the transition energies are relatively close together, leading to non-linear behaviour. While Newton's method is still able to converge to a crossing, it takes a long time and does not generally prove to be a computationally efficient method. Another difficulty of this method is that a given line, indexed by its magnitude relative to others, may cross a given energy at multiple points, making it difficult to determine if more points need to be found. While on its face, this might be mitigated by indexing instead by the spin states the transition involves, near anticrossings, the spin states may not be pure and therefore cannot be indexed.

Nevertheless, the method can still be attempted with the assumption simply that certain crossing points may be missed in the search (Figure 6.13). At low energies especially, the field strengths found may be grouped tightly near zero field, so the values found may be somewhat unreliable because of the nature of the convergence method.

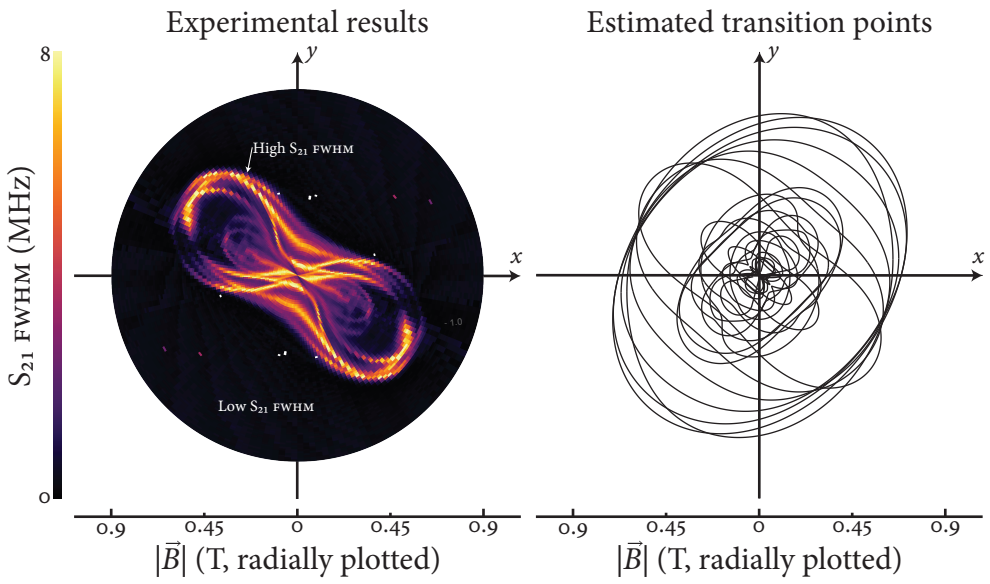


Figure 6.13: A comparison of the S_{21} experimental results found to the transition points found numerically, as a function of magnetic-field orientation and strength. For clarity in the figure, the transition points were found considering only a single molecule in the unit cell. In the xy plane of the lab frame, however, the contribution of each non-equivalent molecule of the unit cell is very similar, so the two results can still be comfortably compared. There are far more numerically determined transition lines than what appears in the S_{21} result, because the former were determined without taking into account the likelihood of the transitions.

In addition to the aforementioned problems, another key problem with this method is that the magnetic field is found for *any* transition energy

matching E, regardless of the likelihood of that transition. Hence, many more lines may appear from this method than are visible from experimental results. Another method, then, is to simulate data from EPR measurements.

Here, the results are shown for several different temperatures, 22 mK, 100 mK, and 200 mK, and otherwise in the same conditions as the experiment (magnetic field directions and magnitude, Q factor of resonator cavity, etc.).

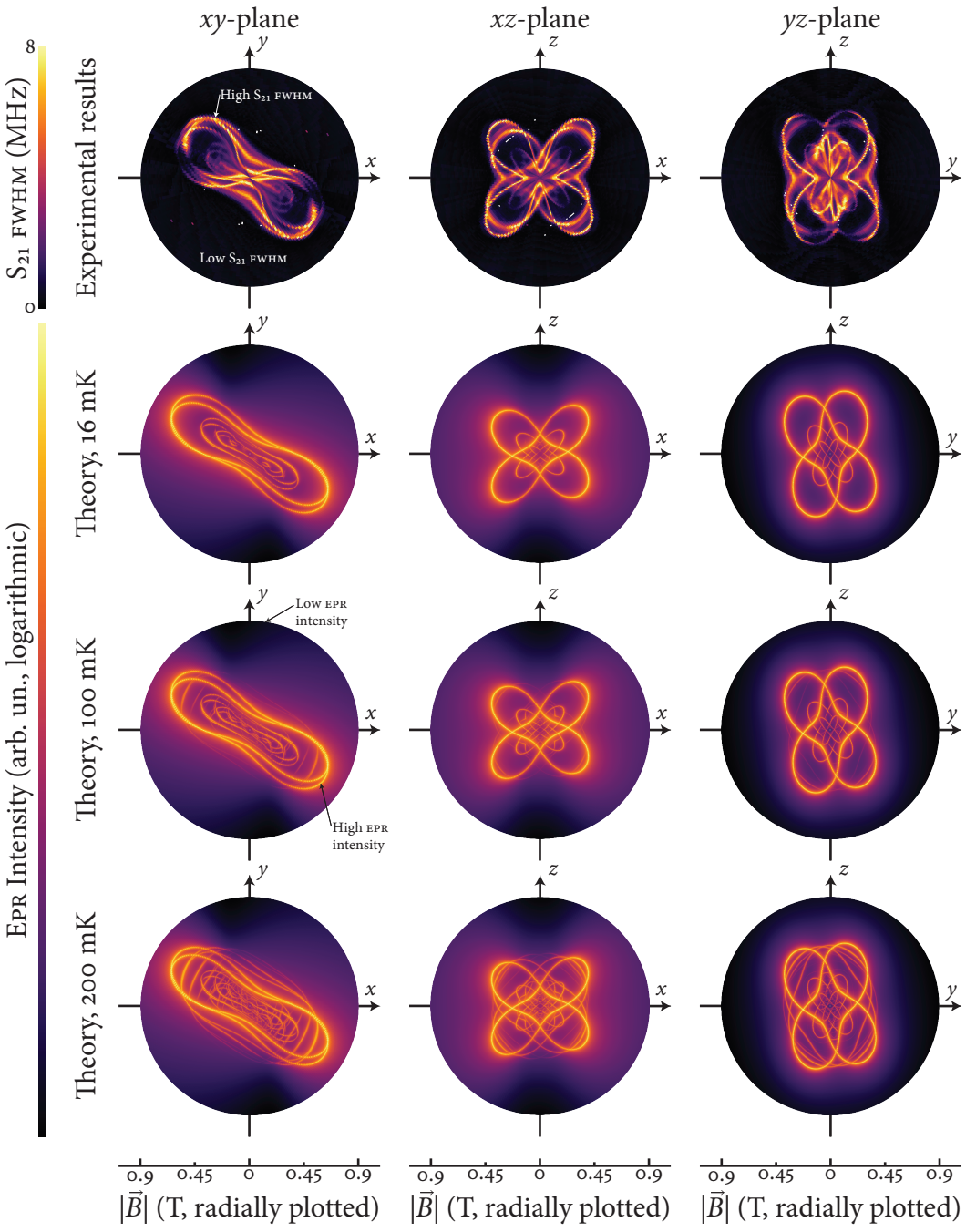


Figure 6.14: A comparison of the S_{21} experimental results to the theoretical EPR transition intensities at 16 mK, 100 mK, and 200 mK. Although experiments were conducted at 16 mK, not all lines visible in the experimental results appear in the theoretical results at the same temperature. The temperature, however, was maintained for the experiment stage and the sensor would not detect slight heating of the sample from the applied magnetic field. Thus, the experimental lines do appear in the theoretical results at higher temperatures.

Thus, since for every $\vec{B}$, we can determine the EPR intensity of some transition of energy E, we can plot these as a function of field strength and direction, along the same planes as the experiments were conducted. Any transitions should then correspond to a resonator anti-crossing, since such an avoided level crossing would likewise arise only from a transition at that magnetic field having an energy of E. This theoretically calculated result indeed matches the results from experiments quite well (Figure 6.14), with most identifiable features of the experimental results visible also in the theoretically predicted results. There are some features, however, that are not visible in the 16 mK prediction but are in predictions at higher temperatures, but are present in the experimental results. This is likely a result of slight heating of the sample from the applied magnetic field. While the experimental set-up in principle assured a temperature of 16 mK, the measurement device is only able to give the temperature of the mounting stage, and not of the sample itself. Applying a changing magnetic field would more than account for a small temperature difference which would produce the lines absent in the 16 mK. At even 100 mK, there appear to be more features present in the predictions than in the experimental results, suggesting that this heating put the sample temperature somewhere between 16 mK and 100 mK.

6.3 Gd-DOTA

The Gadoliunium(III) 1,4,7,10-Tetraazacyclododecane-1,4,7,10-tetraacetate ($[GdC_{16}H_{24}N_4O_8]$) compound, which we abbreviate Gd-DOTA, is a single-molecule magnet (SMM) with a single Gd^{3+} metallic-ion centre surrounded by the tetraazacyclododecane-1,4,7,10-tetraacetate (or DOTA)[c] ligand, which is well known to efficiently block magnetic interactions with the environment.

[c] DOTA, or tetraxetan, is the chemical compound $(CH_2CH_2NCH_2CO_2H)_4$, with a central 12-membered tetra-aza ring which coordinates at the four N sites. It is an acronym of dodecane tetraacetic acid.

Gd-DOTA crystallises in a triclinic unit cell, with one molecule per unit cell. The cell axes $\vec{a}, \vec{b}, \vec{c}$ have lengths 8.711(1) Å, 9.111(1) Å, and 15.711(2) Å, with α, β, γ being 82.86(1)°, 85.47(1)°, and 81.50(1)°, respectively.

Commonly used as an MRI contrast agent, it gains a magnetic moment when under the influence of an externally applied magnetic field, which increases signal intensity in MRI imaging. Understanding its magnetic properties, therefore, can give greater insight into how it might be used in both the medical fields and magnetism.

While lanthanide complexes with the DOTA ligand have been studied and used for a long time as contrast agents and luminescent materials, their low-temperature magnetic behaviour has only recently been investigated. Dy-DOTA was discovered to be a single-molecule magnet, though Gd-DOTA is not because of its quenched orbital angular momentum.

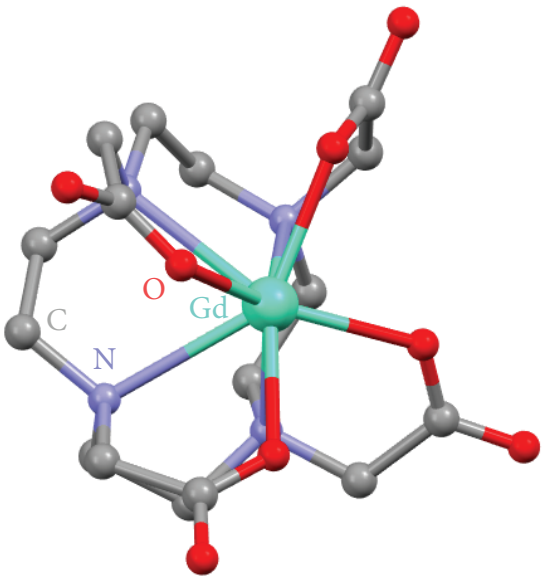
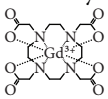


Figure 6.15: The unit cell of a Gd-DOTA crystal, which is triclinic, as viewed along the crystallographic $\hat{a}$ axis (with $\hat{b} - \hat{b} \cdot \hat{a}$ pointing up). There is one molecule per unit cell. Hydrogen atoms have been omitted for clarity. Chemical structure:



6.3.1 *Ab initio calculations*

Using CFPs from *ab initio* calculations to run EPR simulations, we can again consider the rotational response of the crystal in a resonator. Results for the CFPs are given by Briganti *et al.* in the $\hat{a}\hat{b}'\hat{c}^*$ frame.[216] We use these results to predict the rotational dependency of the crystal strongly coupled to a resonator of natural frequency 12.081 GHz as before. The results are shown in Figure 6.16.

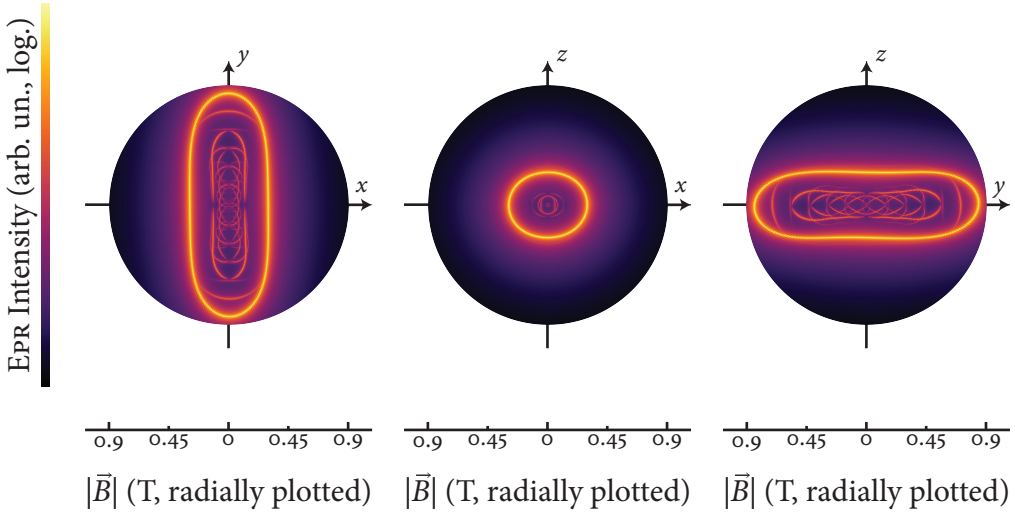


Figure 6.16: The prediction of a measurement on a Gd-DOTA crystal strongly coupled to a resonator of natural frequency 12.081 GHz at 100 mK, using EPR predictions based on CFPs that Briganti *et al.* have calculated.[216]

It is worth noting that the CFP results by Briganti *et al.* accurately reproduce the resonance fields but fail to reproduce the experimental temperature dependence of the X-band EPR spectra.[216]

These results are consistent with the approximate shape of the iso-energy surface produced by the same CFPs: There is an easy axis and a nearly symmetric hard plane. Briganti *et al.* do not describe the compound as having strong easy-axis anisotropy, but this is in comparison to its sister lanthanide compounds. In actuality, it does exhibit slight easy-axis anisotropy along the $\hat{y}$ direction, which is consistent with the anisotropic result of Figure 6.16, and the approximately radially symmetric hard plane is also likewise consistent.

6.4 Conclusion

In this chapter, I have explored how multi-level systems could be interfaced practically with microwave resonators to create quantum hybrid systems. To this end I examined the behaviour of a system that could be implemented experimentally, and has very low magnetic anisotropy. In particular, therefore, I analysed Gd-based systems strongly coupled to resonators and paid special attention to two things: deriving theoretical results that could be compared to datasets, and developing programmes for analysing the data themselves. Throughout the chapter, I have discussed how the interaction between light and matter depends on the strength of the coupling between them, up to what was experimentally achievable, in order to do something never attempted before: verifying step by step the theoretical tools' applicability.

In Section 6.2.2, using *ab initio* calculations, I analysed the interaction with a $Q = 1$ resonator, which has the added capability of allowing a scan of the incoming frequency as well as of the magnetic field magnitude. As a result, we could compare our calculations to a complete map of the spin levels, with a richness of detail that was until now unachieved. We were able to reasonably reproduce the measurement results of a $Gd(hfac)_3$ crystal and all the basic features were replicated, including the transition energies at zero field, which are independent of orientation. Discrepancies still arose, especially at low energies and low fields, in agreement with what has already been noticed by Briganti *et al.*.[216]

We later moved to systems with $Q > 1$, and using the same *ab initio* results, we were then able in Section 6.2.3 to reproduce most major features of an EPR spectrum on a $Gd(hfac)_3$ powder sample; except for minor inaccuracies in the peaks within 5 mT, our predictions were all accurate.

The calculations allowed us to identify some peaks more clearly than the data could, because of some experimental line broadening in the data.

I eventually considered the domain of strong coupling in Section 6.2.4, which showed the angular dependence of the energy-level behaviour by analysing data from high-Q transmission experiments conducted at various orientations of a $Gd(hfac)_3$ crystal, along the three Cartesian planes as defined in the lab frame. Fitting the data to the input–output model, we found the cooperativities of the crossings between the energy levels and the resonator level as we varied the field strength and orientation. When we varied the experimental temperature, we found not only changes in the resonator and crystal's cooperativity but also small changes in the resonance field of the crystal's spin transitions. While cooperativity is well defined for two-level crossings, the meaning and definition are hazier in crossings of more than two levels. In such cases, I characterised the cooperativity among the levels analytically, and gave a first way of treating data from such crossings. It is possible that the full rotating-wave approximation (RWA) breaks down in such situations, so further work is necessary.

I was then able to reproduce the angular dependence seen in experimental results using both numerical diagonalisation of the Hamiltonian (to find the resonance field of all transitions) and EPR calculations. The former showed many more transition lines than the experiments could, because the experiments were conducted at temperatures orders of magnitude lower than the corresponding energies of many of the transitions, according to Boltzmann statistics, but the lines in the experiment agreed with the resonance fields predicted from the Hamiltonian. The latter, on the other hand, produced features in extremely good agreement with the angular-dependency results produced from experimental data: when calculated at temperatures slightly higher than the temperatures at which the experiments were conducted, EPR calculations were able to reproduce most

major features, likely because application of the field heated up the crystal sample a little, which would not necessarily be detected by experimental temperature sensors.

In Section 6.3, we applied the same methodology of Section 6.2.4, using CFPs for the crystal derived from *ab initio* calculations to determine, using EPR calculations, the theoretical angular dependence of the energy levels in a Gd-DOTA crystal. The major feature of the results, namely the relative widths of the shapes seen, were consistent with the iso-energy surface found in the literature.

Strongly coupling such spin systems to resonators has possible applications in quantum computing. The ensemble of molecules in a crystal coupled to a resonator acts as a macroscopic system that is fully described by quantum mechanics; it also boosts the collective system's cooperativity, and this result is desirable for quantum coherence across quantum operations in a device. Additionally, because of the high spin in these rare-earth centres, such a setup would increase the number of qubits in a resonator above what is typically seen currently, thereby expanding the dimension of the Hilbert space available to such a device. This is particularly promising because of recent research on cavity resonators, such as the development of tunable, open-access microcavities, in which strong coupling effects such as polaritons have been observed[19–21] Such microcavities have also been strongly coupled with nanographene,[22] and further research could consider microcavities strong coupled to complex nanodevices.

These results can now be used to consider how to develop more efficient ways of performing quantum computation using the molecular-resonator hybrids. Following our input, a full scheme of such calculations has been developed by collaborators in the Department of Physics (Dr Martin Kiffner, Prof. Dieter Jaksch, and Michael Hughes), and it is being considered for patenting.

7 Conclusion

Current research, shifting towards quantum devices, requires greater understanding of how molecular systems behave and what role they might play in the development of such devices. It would be useful to be able to interface these molecular systems with these devices, because one would then be able to build hybrid quantum devices combining multiple systems capitalizing on each system's advantageous aspects. This thesis has offered a first perspective on how to use numerical and analytical methods to consider how molecular quantum systems are, or can be, interfaced with and included in hybrid quantum devices. To this end, I investigated various possible molecular systems, all using the same general spin Hamiltonian; then, examining some real-life examples, I investigated compounds and directly compared theoretical predictions with experimental datasets, and compounds' integration into several quantum systems.

Using a novel method for determining the individual anisotropies of the molecules within a crystal from only experimental results, in Section 4.3 I first showed *ab initio* calculations to be very effective for making accurate predictions in the behaviour of rare-earth compounds, particularly with certain crystal symmetries. This new proposed method enables one to isolate magnetic anisotropy axes of individual molecules from only magnetic-measurement data for the majority of known crystals.

The *ab initio* characterisation of rare-earths, described in Section 4.5, was then found accurate and useful for single-molecule nanodevices, where

the presence of a molecule with an anisotropic centre acts as a spin valve that affects the flow of electrons within the device. This result opens up the possibility of studying and predicting the behaviour of molecular spintronic devices, and in particular the anisotropy of the current flow through such devices when they are subjected to a magnetic field. When the anisotropy is known, the interaction of the rare-earth centre with the flowing electrons can also be predicted and even tailored by chemical engineering of the molecule. It is even possible that predictions may be extended to larger, multi-centre molecules, such as the Tb–porphyrin dimer considered in Section 4.5.5, though more studies are necessary to determine and fine-tune the accuracy of this preliminary calculation.

I then expanded in Section 4.6 the use of *ab initio* methods from determining the anisotropy in Dy centres to determining the anisotropy in other rare-earth centres, such as Tb. I checked the reliability of these numerical results against precise magnetometry measurements. The results from calculations were in good agreement with both torque-magnetometry and superconducting quantum-interference device (SQUID) magnetometry data on the 1-Tb compound. These results also enable one to calculate the torque response in arbitrary directions, giving predictions in a breadth of directions much more readily than experimental measurements could be obtained in the same compound. While torque-magnetometry experiments in most of the literature were conducted at temperatures above 2 K, I aimed to compare our results with measurements taken in the millikelvin range, where measurements are much more sensitive and show more features, and are therefore more likely to make apparent any inaccuracies in calculations. The results thus validate modern computing techniques more firmly than much of the previous literature, and provide a reassuring picture of the level of accuracy now available in the modelling of magnetic centres.

We saw in Chapter 6 that this is also true for trivalent Gd ions, but in general, one result of this thesis is that these calculation methods are quite accurate, precise, and reliable for predicting the anisotropic behaviour of rare-earths.

I next proceeded and examined the theoretical behaviour of large-spin magnetic centres strongly coupled with light, using a well-studied molecule, Mn_{12}, exploring theoretically what results when a multilevel system interacts with a resonator. I first demonstrated in Section 5.5 that transitions between otherwise-forbidden spin levels are opened by a virtual path through even a highly detuned photon level. Such an interaction between the photon and a pair of spin levels opens up a gap between the spin levels, a gap that increases as the coupling between the photon and spin system strengthens. This interaction in turn increases the rate at which the spin system's state tunnels incoherently between such spin levels as the coupling between the spin system and the resonator grows stronger.

I then showed in Section 5.6 that when the resonator level crosses two spin levels at their intersection, the three-level system that forms from their interaction gives a bow-tie crossing, even at zero field. Bow-tie crossings have been proposed in quantum gasses, and are highly sought after in solid-state systems, so a resonator–spin system could fill this need. The resulting collective behaviour is a polariton, which both forces down the lower spin level's energy and forces up the higher spin level's energy. I also determined analytically the tunnelling probability in such a three-level system, thus showing the effect of polaritons not only on level splittings in a spin system, but also on the spin system's dynamic properties. Such a resonator–spin system may make possible, for the first time, a macroscopic quantum system, based on the quantum coupling between a resonator and a crystal's entire ensemble of molecules.

In such a three-level system, the tunnelling probability between a pair of spin levels has a different relation with respect to the sweep rate, and the transition rate is boosted. This means that forming such systems by carefully applying a magnetic field to a spin system coupled to a properly engineered resonator can, in general, boost transitions between two selected levels.

I then further explored this concept by examining both theoretical and experimental results in a Gd-based crystal strongly coupled to a microwave resonator. Using *ab initio* calculations, I managed to reproduce in Section 6.2.2 the transmission measurement of a $Gd(hfac)_3$ crystal with unknown orientation in a $Q = 1$ resonator.

Using the same *ab initio* results, I then managed in Section 6.2.3 to reproduce most major features of electron paramagnetic resonance (EPR) spectra of a $Gd(hfac)_3$ powder sample; except for minor inaccuracies in the peaks within 5 mT, our predictions were all accurate. The calculations allowed us to identify some peaks more clearly than the data could, because of some smearing out in the data.

I also managed in Section 6.2.4 to reproduce the angular dependence of the energy-level behaviour by analysing data from high-Q transmission experiments conducted at various orientations of a $Gd(hfac)_3$ crystal, along the three Cartesian planes as defined in the lab frame. Fitting the data to the input–output model, I found the cooperativities of the crossings between the energy levels and the resonator level as I varied the field strength and orientation. Varying the experimental temperature, I found not only changes in the cooperativity between the resonator and crystal, but also small changes in the resonance field of the spin transitions of the molecules in the crystal. In the case of multi-level crossings, moreover, I characterised the cooperativity among the levels analytically, and proposed a method to treat data from such crossings. Because the full

rotating-wave approximation (RWA) may not hold in such situations, further work is necessary.

I then managed to reproduce the angular dependence seen in experimental results using both numerical diagonalisation of the Hamiltonian (to find the resonance field of all transitions) and calculations of EPR transitions. The former showed many more transition lines than the experiment could, because the experiment was conducted at temperatures low enough that many of the transitions were very improbable according to Boltzmann statistics. The latter, on the other hand, produced features in extremely good agreement with the angular-dependency results produced from experimental data: when calculated at temperatures slightly higher than the temperatures at which the experiments were conducted, EPR calculations were able to reproduce most major features, likely because application of the field heated up the crystal sample a little.

In Section 6.3, I applied the same methodology of Section 6.2.4 to determine the theoretical angular dependence of the energy levels in a Gd-DOTA crystal. This is a fist, preliminary step in considering the possible use of commercially available molecules (Gd-DOTA is a commercial contrast agent) for quantum interfaces.

Strongly coupling such spin systems to resonators has possible applications in quantum computing. The ensemble of molecules in a crystal coupled to a resonator acts as a macroscopic system that is fully described by quantum mechanics; it also boosts the collective system's cooperativity, and this result is desirable for quantum coherence across quantum operations in a device. Additionally, because of the high spin in these rare-earth centres, such a setup would increase the number of qubits in a resonator above what is typically seen currently, thereby expanding the dimension of the Hilbert space available to such a device.

Strong coupling has been studied in a number of different systems,[217–219] and there are proposals for how to use nanomagnets and resonators to build quantum gates,[220] implement quantum error correction,[221–225] and scalably produce quantum processors for computation[226–228] Extensive research is also underway on how to optimise resonators themselves to decrease size and increase coupling strength.[229] One major hurdle thus far has been characterising different spin systems, including understanding their behaviour at different orientations of an applied magnetic field, and how strongly coupling them to light changes their behaviour. Understanding this is necessary to finely control the quantum state of any device based on such a system, in order to store information and perform quantum computations.

The confinement of electrons to fewer than three dimensions gives rise to topological states of matter, which behave quantitatively and qualitatively differently than free electrons. Some two-dimensional systems of note are topological insulators and graphene, one-dimensional systems include spin chains and graphene nanoribbons (GNRs), and zero-dimensional systems include quantum dots and single-molecule magnets (SMMs). Each of these has unique properties that make them advantageous or disadvantageous for potential use in electronic devices, but regardless of the system, the principal question is how to control the magnetic spins. Here we have investigated zero-dimensional systems, but further research can examine the behaviours and properties of one- and two-dimensional systems and how these might also be useful for building quantum devices.

References

[1] John F. Nye. *Physical Properties of Crystals: Their Representation by Tensors and Matrices*. Oxford University Press, Oxford, 1957. Cited on page 1.

[2] Thompson, S.E., and Parthasarathy, S. Moore's law: The future of Si microelectronics. *Mater. Today*, 9(6):20–25, June 2006. ISSN 1369-7021. doi:10/d6hw7c. Cited on page 2.

[3] Mack, C.A. Fifty Years of Moore's Law. *IEEE Trans. Semicond. Manuf.*, 24(2):202–207, May 2011. ISSN 1558-2345. doi:10/dx78gh. Cited on page 2.

[4] Gao, S., editor. *Molecular Nanomagnets and Related Phenomena*, volume 164 of *Structure and Bonding*. Springer, Berlin, Heidelberg, 2015. ISBN 978-3-662-45722-1. doi:10.1007/978-3-662-45723-8. Cited on pages 2 and 3.

[5] Fu, T., *et al.* Single-Molecule Junction Formation in Break-Junction Measurements. *J. Phys. Chem. Lett.*, 12(44):10802–10807, November 2021. doi:10/gnbfgg. Cited on page 2.

[6] Aradhya, S.V., and Venkataraman, L. Single-molecule junctions beyond electronic transport. *Nat. Nanotechnol.*, 8(6):399–410, June 2013. ISSN 1748-3395. doi:10/gfx27h. Cited on page 2.

[7] Coronado, E. Molecular magnetism: From chemical design to spin control in molecules, materials and devices. *Nat. Rev. Mater.*, 5(2): 87–104, February 2020. ISSN 2058-8437. doi:10/ghqbpq. Cited on page 2.

[8] Zhou, W., and Coleman, J.J. Semiconductor quantum dots. *Current Opinion in Solid State and Materials Science*, 20(6):352–360, December 2016. ISSN 1359-0286. doi:10/ggvp2z. Cited on page 2.

[9] Hanson, R., *et al.* Spins in few-electron quantum dots. *Rev. Mod. Phys.*, 79(4):1217–1265, October 2007. doi:10/bf8h2m. Cited on page 2.

[10] Zhang, J.L., *et al.* Towards single molecule switches. *Chem. Soc. Rev.*, 44(10):2998–3022, May 2015. ISSN 1460-4744. doi:10/gqw4ks. Cited on page 2.

[11] Gaita-Ariño, A., *et al.* Molecular spins for quantum computation. *Nat. Chem.*, 11(4):301–309, April 2019. ISSN 1755-4349. doi:10/gf8v2x. Cited on page 3.

[12] Gatteschi, D., Sessoli, R., and Villain, J. *Molecular Nanomagnets*. Number 5 in Mesoscopic Physics and Nanotechnology. Oxford University Press, Oxford ; New York, March 2006. ISBN 978-0-19-856753-0. Cited on pages 3, 30, and 31.

[13] Affronte, M., *et al.* Single molecule magnets for quantum computation. *J. Phys. D: Appl. Phys.*, 40(10):2999–3004, May 2007. ISSN 0022-3727. doi:20070511031311. Cited on page 3.

[14] Leuenberger, M.N., and Loss, D. Quantum computing in molecular magnets. *Nature*, 410(6830):789–793, April 2001. ISSN 1476-4687. doi:10/cspqcg. Cited on pages 3 and 25.

[15] Briganti, M., and Totti, F. Magnetic anisotropy on demand exploiting high-pressure as remote control: An ab initio proof of concept. *Dalton Trans.*, 50(30):10621–10628, August 2021. ISSN 1477-9234. doi:10.1039/D1DT01719E. Cited on page 3.

[16] Sato, O., Tao, J., and Zhang, Y.Z. Control of Magnetic Properties through External Stimuli. *Angew. Chem. Int. Ed.*, 46(13):2152–2187, 2007. ISSN 1521-3773. doi:10/bctqhw. Cited on page 3.

[17] Feng, X., *et al.* Tristability in a Light-Actuated Single-Molecule Magnet. *J. Am. Chem. Soc.*, 135(42):15880–15884, October 2013. ISSN 0002-7863. doi:10/f5gjzs. Cited on page 3.

[18] Kahle, S., *et al.* The Quantum Magnetism of Individual Manganese-12-Acetate Molecular Magnets Anchored at Surfaces. *Nano Lett.*, 12 (1):518–521, January 2012. ISSN 1530-6984. doi:10/cqn9hd. Cited on page 3.

[19] Gillard, D.J., *et al.* Strong exciton-photon coupling in large area MoSe$\less$sub$\greater$2$\less$/sub$\greater$ and WSe$\less$sub$\greater$2$\less$/sub$\greater$ heterostructures fabricated from two-dimensional materials grown by chemical vapor deposition. *2D Mater.*, 8(1):011002, November 2020. ISSN 2053-1583. doi:10/gpqfzr. Cited on pages 4 and 144.

[20] Giriunas, L., *et al.* Formation of a macroscopically occupied polariton state in a tunable open-access microcavity under resonant excitation. *J. Appl. Phys.*, 124(2):025703, July 2018. ISSN 0021-8979. doi:10/gqvrgt. Cited on pages 4 and 144.

[21] Betzold, S., *et al.* Tunable Light–Matter Hybridization in Open Organic Microcavities. *ACS Photonics*, 5(1):90–94, January 2018. doi:10.1021/acsphotonics.7b00552. Cited on pages 4 and 144.

[22] Coles, D.M., *et al.* Strong Exciton–Photon Coupling in a Nanographene Filled Microcavity. *Nano Lett.*, 17(9):5521–5525, September 2017. ISSN 1530-6984. doi:10/gdwrns. Cited on pages 4 and 144.

[23] Abragam, A., and Bleaney, B. *Electron Paramagnetic Resonance of Transition Ions*. Oxford Classic Texts in the Physical Sciences. Oxford University Press, Oxford, New York, June 2012. ISBN 978-0-19-965152-8. Cited on pages 6, 11, and 30.

[24] Weil, J.A., and Bolton, J.R. *Electron Paramagnetic Resonance: Elementary Theory and Practical Applications*. Wiley-Interscience, Hoboken, N.J, second edition, 2007. ISBN 978-0-471-75496-1. Cited on page 7.

[25] Christiane Görller-Walrand, and Koen Binnemans. Rationalization of crystal-field parametrization. In Karl A. Gschneidner, Jr, and LeRoy Eyring, editors, *Handbook on the Physics and Chemistry of Rare Earths*, volume 23, pages 121–283. Elsevier, Amsterdam, Lausanne, New York, Oxford, Shannon, Tokyo, 1996. ISBN 978-0-444-82507-0. doi:10/d6jc4h. Cited on pages 10 and 15.

[26] Briganti, M., *et al.* Covalency and magnetic anisotropy in lanthanide single molecule magnets: The DyDOTA archetype. *Chem. Sci.*, 10 (30):7233–7245, July 2019. ISSN 2041-6539. doi:10/grsmcz. Cited on page 13.

[27] Su, S.Q., *et al.* Water-oriented magnetic anisotropy transition. *Nat. Commun.*, 12(1):2738, May 2021. ISSN 2041-1723. doi:10/grsmcx. Cited on page 13.

[28] Choppin, G.R. Structure and thermodynamics of lanthanide and actinide complexes in solution. *Pure Appl. Chem.*, 27(1–2):23–42, January 1971. ISSN 1365-3075. doi:10/d9zb6g. Cited on page 13.

[29] Neidig, M.L., Clark, D.L., and Martin, R.L. Covalency in f-element complexes. *Coord. Chem. Rev.*, 257(2):394–406, January 2013. ISSN 0010-8545. doi:10/f4jz59. Cited on pages 13 and 18.

[30] (((Gould))), C.A., *et al.* Ultrahard magnetism from mixed-valence dilanthanide complexes with metal-metal bonding. *Science*, 375 (6577):198–202, January 2022. doi:10/grsmcw. Cited on page 14.

[31] Demir, S., *et al.* Giant coercivity and high magnetic blocking temperatures for N2 3- radical-bridged dilanthanide complexes upon ligand dissociation. *Nat. Commun.*, 8(1):2144, December 2017. ISSN 2041-1723. doi:10/grsmcv. Cited on page 14.

[32] Bethe, H. Termaufspaltung in Kristallen. *Ann. Phys.*, 395(2):133–208, 1929. ISSN 1521-3889. doi:10/fdsbtt. Cited on page 14.

[33] Van Vleck, J.H. Theory of the variations in paramagnetic anisotropy among different salts of the iron group. *Phys. Rev.*, 41(2):208–215, July 1932. doi:10/cg2643. Cited on page 14.

[34] Van Vleck, J.H. Valence strength and the magnetism of complex salts. *J. Chem. Phys.*, 3(12):807–813, December 1935. ISSN 0021-9606. doi:10/dr8ckv. Cited on page 14.

[35] Racah, G. Theory of complex spectra. IV. *Phys. Rev.*, 76(9):1352–1365, November 1949. doi:10/cpzvjj. Cited on page 14.

[36] Stevens, K.W.H. Matrix elements and operator equivalents connected with the magnetic properties of rare earth ions. *Proc. Phys. Soc. A*, 65(3):209–215, March 1952. ISSN 0370-1298. doi:10/bzc2z4. Cited on page 14.

[37] Wybourne, B.G., and Meggers, W.F. Spectroscopic properties of rare earths. *Phys. Today*, 18(9):70–72, September 1965. ISSN 0031-9228. doi:10/fd6ggp. Cited on page 14.

[38] Maurice, R., *et al.* Universal theoretical approach to extract anisotropic spin hamiltonians. *J. Chem. Theory Comput.*, 5(11):2977–2984, November 2009. ISSN 1549-9618. doi:10/fjbg77. Cited on page 14.

[39] Notter, F.P., and Bolvin, H. Optical and magnetic properties of the $5f^1$ AnX_6^{q-} series: A theoretical study. *J. Chem. Phys.*, 130(18):184310, May 2009. ISSN 0021-9606. doi:10/d75t2m. Cited on page 15.

[40] Ishikawa, N., *et al.* Lanthanide double-decker complexes functioning as magnets at the single-molecular level. *J. Am. Chem. Soc.*, 125 (29):8694–8695, July 2003. ISSN 0002-7863. doi:10/cqhnsj. Cited on page 15.

[41] AlDamen, M.A., *et al.* Mononuclear lanthanide single-molecule magnets based on polyoxometalates. *J. Am. Chem. Soc.*, 130(28): 8874–8875, July 2008. ISSN 0002-7863. doi:10/fkx7sp. Cited on page 15.

[42] AlDamen, M.A., *et al.* Mononuclear lanthanide single molecule magnets based on the polyoxometalates $[Ln(W_5O_{18})_2]^{9-}$ and $[Ln(B_2\text{-}SiW_{11}O_{39})_2]^{13-}$ (Ln^{III} = Tb, Dy, Ho, Er, Tm, and Yb). *Inorg. Chem.*, 48(8):3467–3479, April 2009. ISSN 0020-1669. doi:10/dcbx3f. Cited on page 15.

[43] Luis, F., *et al.* Spin-lattice relaxation via quantum tunneling in an Er^{3+}-polyoxometalate molecular magnet. *Phys. Rev. B*, 82(6):060403, August 2010. doi:10/c2d4v2. Cited on page 15.

[44] Katoh, K., *et al.* Magnetic relaxation of single-molecule magnets in an external magnetic field: An Ising dimer of a terbium(III)–phthalocyaninate triple-decker complex. *Chem. Eur. J.*, 17(1):117–122, 2011. ISSN 1521-3765. doi:10/br82dk. Cited on page 15.

[45] Sorace, L., Benelli, C., and Gatteschi, D. Lanthanides in molecular magnetism: Old tools in a new field. *Chem. Soc. Rev.*, 40(6):3092–3104, May 2011. ISSN 1460-4744. doi:10/b4cnqd. Cited on page 15.

[46] Gavroglu, K., and Simões, A. *Neither Physics nor Chemistry: A History of Quantum Chemistry*. The MIT Press, 2012. ISBN 978-0-262-01618-6. Cited on page 15.

[47] Pauling, L., and Wilson, E.B. *Introduction to Quantum Mechanics: With Applications to Chemistry*. Dover Publications Inc., 1935. ISBN 978-0-486-64871-2. Cited on page 15.

[48] Eyring, H., Walter, J., and Kimball, G.E. *Quantum Chemistry*. Ulan Press, 1944. Cited on page 15.

[49] Heitler, W. *Elementary Wave Mechanics with Applications to Quantum Chemistry*. Oxford University Press, 1945. ISBN 978-0-19-851115-1. Cited on page 15.

[50] Coulson, C.A., and McWeeny, R. *Valence*. Oxford University Press, 1952. ISBN 978-0-19-855145-4. Cited on page 15.

[51] Atanasov, M., Comba, P., and Daul, C.A. Combined ligand field and density functional theory analysis of the magnetic anisotropy in oligonuclear complexes based on Fe^{III}-CN-M^{II} exchange-coupled pairs. *Inorg. Chem.*, 47(7):2449–2463, April 2008. ISSN 0020-1669. doi:10/dfds95. Cited on page 16.

[52] Chibotaru, L.F., *et al.* Magnetic anisotropy of $[Mo(CN)_7]^{4-}$ anions and fragments of cyano-bridged magnetic networks. *J. Phys. Chem. A*, 109(32):7251–7257, August 2005. ISSN 1089-5639. doi:10/bh6knm. Cited on page 16.

[53] Ungur, L., and Chibotaru, L.F. Ab initio crystal field for lanthanides. *Chem. Eur. J.*, 23(15):3708–3718, 2017. ISSN 1521-3765. doi:10/f3tmw9. Cited on page 16.

[54] Richard A. Layfield, and Muralee Murugesu, editors. *Lanthanides and Actinides in Molecular Magnetism*. John Wiley & Sons, Ltd, Weinheim, 2015. ISBN 978-3-527-67347-6. doi:10.1002/9783527673476.ch1. Cited on page 16.

[55] Chibotaru, L.F., and Ungur, L. Ab initio calculation of anisotropic magnetic properties of complexes. I. unique definition of pseudospin Hamiltonians and their derivation. *J. Chem. Phys.*, 137(6):064112, August 2012. ISSN 0021-9606. doi:10/f3542k. Cited on pages 16 and 18.

[56] Cucinotta, G., *et al.* Magnetic Anisotropy in a Dysprosium/DOTA Single-Molecule Magnet: Beyond Simple Magneto-Structural Correlations. *Angew. Chem. Int. Ed.*, 51(7):1606–1610, 2012. ISSN 1521-3773. doi:10/c5ddw4. Cited on page 16.

[57] Boulon, M.E., *et al.* Angular-Resolved Magnetometry Beyond Triclinic Crystals: Out-of-Equilibrium Studies of Cp*ErCOT Single-Molecule Magnet. *Chem. Eur. J.*, 19(41):13726–13731, 2013. ISSN 1521-3765. doi:10/f2dt73. Cited on pages 16 and 69.

[58] Boulon, M.E., *et al.* Magnetic Anisotropy and Spin-Parity Effect Along the Series of Lanthanide Complexes with DOTA. *Angew. Chem. Int. Ed.*, 52(1):350–354, 2013. ISSN 1521-3773. doi:10/fz9knf. Cited on page 16.

[59] Marx, R., *et al.* Spectroscopic determination of crystal field splittings in lanthanide double deckers. *Chem. Sci.*, 5(8):3287–3293, June 2014. ISSN 2041-6539. doi:10/gmnrmj. Cited on page 16.

[60] Ding, Y.S., *et al.* On Approaching the Limit of Molecular Magnetic Anisotropy: A Near-Perfect Pentagonal Bipyramidal Dysprosium(III) Single-Molecule Magnet. *Angew. Chem. Int. Ed.*, 55(52): 16071–16074, 2016. ISSN 1521-3773. doi:10/f3s8ps. Cited on pages 16 and 66.

[61] Denning, R.G., *et al.* Covalency in the uranyl ion: A polarized x-ray spectroscopic study. *J. Chem. Phys.*, 117(17):8008–8020, November 2002. ISSN 0021-9606. doi:10/bkdcrx. Cited on page 18.

[62] Altman, A.B., *et al.* Evidence for 5d-σ and 5d-π covalency in lanthanide sesquioxides from oxygen K-edge X-ray absorption spectroscopy. *Dalton Trans.*, 45(24):9948–9961, June 2016. ISSN 1477-9234. doi:10/gmnqqt. Cited on page 18.

[63] Gupta, T., Singh, M.K., and Rajaraman, G. Role of ab initio calculations in the design and development of lanthanide based single molecule magnets. In Chandrasekhar, V., and Pointillart, F., editors, *Organometallic Magnets*, volume 64 of *Topics in Organometallic Chemistry*, pages 281–354. Springer International Publishing, Cham, 2019. ISBN 978-3-030-26009-5. doi:10/gtfh. Cited on page 18.

[64] Chibotaru, L.F. Ab initio methodology for pseudospin hamiltonians of anisotropic magnetic complexes. volume 153 of *Advances in Chemical Physics*, pages 397–519. John Wiley & Sons, Ltd, 2013. ISBN 978-1-118-57176-7. doi:10/gtfj. Cited on page 18.

[65] Gendron, F., *et al.* Magnetic coupling in the Ce(III) dimer $Ce_2(COT)_3$. *Inorg. Chem.*, 58(1):581–593, January 2019. ISSN 0020-1669. doi:10/gmnrbv. Cited on page 18.

[66] Dubé, M., and Stamp, P.C.E. Mechanisms of decoherence at low temperatures. *Chem. Phys.*, 268(1):257–272, June 2001. ISSN 0301-0104. doi:10/ft54h8. Cited on page 22.

[67] Devoret, M.H., and Schoelkopf, R.J. Superconducting circuits for quantum information: An outlook. *Science*, 339(6124):1169–1174, March 2013. ISSN 0036-8075, 1095-9203. doi:10/f4ps6n. Cited on page 22.

[68] Monroe, C., and Kim, J. Scaling the ion trap quantum processor. *Science*, 339(6124):1164–1169, March 2013. ISSN 0036-8075, 1095-9203. doi:10/gddjvn. Cited on page 22.

[69] Drillon, M., *et al.* Classical treatment of a Heisenberg linear chain with spin alternation; application to the MnNi(EDTA)·6H_2O complex. *Chem. Phys.*, 79(3):449–453, September 1983. ISSN 0301-0104. doi:10/bbv3vz. Cited on page 22.

[70] Kahn, O. *Molecular Magnetism*, volume 98. VCH-Verlag, New York, 1993. ISBN 3-527-89566-3. Cited on page 22.

[71] Hanson, R., *et al.* Coherent dynamics of a single spin interacting with an adjustable spin bath. *Science*, 320(5874):352–355, April 2008. ISSN 0036-8075, 1095-9203. doi:10/b58p4c. Cited on page 22.

[72] Steger, M., *et al.* Quantum information storage for over 180 s using donor spins in a ^{28}Si "semiconductor vacuum". *Science*, 336(6086): 1280–1283, June 2012. ISSN 0036-8075, 1095-9203. doi:10/f3z7zm. Cited on page 22.

[73] Seiden, J. Static properties of an alternating isotropic chain of one-half quantum spins and classical spins. *J. Physique Lett.*, 44(23): 947–952, December 1983. ISSN 0302-072X, 2777-3434. doi:10/d76jbf. Cited on page 22.

[74] Jelezko, F., *et al.* Observation of Coherent Oscillations in a Single Electron Spin. *Phys. Rev. Lett.*, 92(7):076401, February 2004. doi:10/cvnpk8. Cited on page 22.

[75] Pla, J.J., *et al.* A single-atom electron spin qubit in silicon. *Nature*, 489(7417):541–545, September 2012. ISSN 1476-4687. doi:10/gf2mw4. Cited on page 22.

[76] Morioka, N., *et al.* Spin-controlled generation of indistinguishable and distinguishable photons from silicon vacancy centres in silicon carbide. *Nat. Commun.*, 11(1):2516, May 2020. ISSN 2041-1723. doi:10/gjbkpf. Cited on page 22.

[77] Nagy, R., *et al.* High-fidelity spin and optical control of single silicon-vacancy centres in silicon carbide. *Nat. Commun.*, 10(1):1954, April 2019. ISSN 2041-1723. doi:10/ggdwtn. Cited on page 22.

[78] Astakhov, G.V., *et al.* Spin Centres in SiC for Quantum Technologies. *Appl. Magn. Reson.*, 47(7):793–812, July 2016. ISSN 1613-7507. doi:10/f8tg4h. Cited on page 22.

[79] Castelletto, S., and Boretti, A. Silicon carbide color centers for quantum applications. *JPhys Photonics*, 2(2):022001, March 2020. ISSN 2515-7647. doi:10/ghhjtg. Cited on page 22.

[80] Morello, A., Stamp, P.C.E., and Tupitsyn, I.S. Pairwise Decoherence in Coupled Spin Qubit Networks. *Phys. Rev. Lett.*, 97(20):207206, November 2006. doi:10/bzt6wm. Cited on page 23.

[81] Zadrozny, J.M., *et al.* Millisecond Coherence Time in a Tunable Molecular Electronic Spin Qubit. *ACS Cent. Sci.*, 1(9):488–492, December 2015. ISSN 2374-7943. doi:10/ggcht4. Cited on page 24.

[82] Luis, F., *et al.* Observation of quantum coherence in mesoscopic molecular magnets. *Phys. Rev. Lett.*, 85(20):4377–4380, November 2000. ISSN 1079-7114. doi:10/bd77hg. Cited on page 24.

[83] Hill, S., *et al.* Quantum coherence in an exchange-coupled dimer of single-molecule magnets. *Science*, 302(5647):1015–1018, November 2003. ISSN 0036-8075, 1095-9203. doi:10/bhts3m. Cited on page 24.

[84] Wernsdorfer, W., *et al.* Resonant photon absorption and hole burning in Cr_7Ni antiferromagnetic rings. *Phys. Rev. B*, 72(6):060409, August 2005. doi:10/dxgvbw. Cited on page 24.

[85] Mitrikas, G., *et al.* Electron spin–lattice and spin–spin relaxation study of a trinuclear iron(III) complex and its relevance in quantum computing. *Phys. Chem. Chem. Phys.*, 10(5):743–748, January 2008. ISSN 1463-9084. doi:10/fpt26b. Cited on page 24.

[86] Schlegel, C., *et al.* Direct observation of quantum coherence in single-molecule magnets. *Phys. Rev. Lett.*, 101(14):147203, October 2008. doi:10/fwj6x2. Cited on page 24.

[87] Takahashi, S., *et al.* Coherent manipulation and decoherence of $S = 10$ single-molecule magnets. *Phys. Rev. Lett.*, 102(8):087603, February 2009. ISSN 0031-9007. doi:10/dnbfvq. Cited on page 24.

[88] Schlegel, C., *et al.* Origin of superhyperfine interactions in the antiferromagnetic ring Cr_7Ni. *Phys. Rev. B*, 83(13):134407, April 2011. doi:10/cw4vxf. Cited on page 24.

[89] Wedge, C.J., *et al.* Chemical engineering of molecular qubits. *Phys. Rev. Lett.*, 108(10):107204, March 2012. doi:10/gffjhc. Cited on page 24.

[90] Martínez-Pérez, M.J., *et al.* Gd-based single-ion magnets with tunable magnetic anisotropy: Molecular design of spin qubits. *Phys. Rev. Lett.*, 108(24):247213, June 2012. doi:10/gjkrsv. Cited on page 24.

[91] Kaminski, D., *et al.* Quantum spin coherence in halogen-modified Cr_7Ni molecular nanomagnets. *Phys. Rev. B*, 90(18):184419, November 2014. doi:10/gknfb6. Cited on page 24.

[92] Warner, M., *et al.* Potential for spin-based information processing in a thin-film molecular semiconductor. *Nature*, 503(7477):504–508, November 2013. ISSN 1476-4687. doi:10/f5hv84. Cited on page 24.

[93] Gómez-Coca, S., *et al.* Origin of slow magnetic relaxation in Kramers ions with non-uniaxial anisotropy. *Nat. Commun.*, 5(1): 4300, July 2014. ISSN 2041-1723. doi:10/f6cdh6. Cited on page 24.

[94] Liu, J., *et al.* Electric Field Control of Spins in Molecular Magnets. *Phys. Rev. Lett.*, 122(3):037202, January 2019. doi:10/grsmc2. Cited on page 24.

[95] Bogani, L., and Wernsdorfer, W. Molecular spintronics using single-molecule magnets. *Nat. Mater.*, 7(3):179–186, March 2008. ISSN 1476-4660. doi:10/dnmqdn. Cited on page 25.

[96] Fleury, B., *et al.* A new approach to grafting a monolayer of oriented Mn_{12} nanomagnets on silicon. *Chem. Commun.*, (15):2020–2022, April 2005. ISSN 1359-7345. doi:10/bz4p2g. Cited on page 25.

[97] Naitabdi, A., *et al.* Self-assembly and magnetism of Mn_{12} nanomagnets on native and functionalized gold surfaces. *Adv. Mater.*, 17(13): 1612–1616, 2005. ISSN 1521-4095. doi:10/cq25z8. Cited on page 25.

[98] Coronado, E., *et al.* Polycationic Mn_{12} single-molecule magnets as electron reservoirs with $S > 10$ ground states. *Angew. Chem. Int. Ed.*, 43(45):6152–6156, 2004. ISSN 1521-3773. doi:10/c5fdz2. Cited on page 25.

[99] Timco, G.A., *et al.* Engineering the coupling between molecular spin qubits by coordination chemistry. *Nat. Nanotechnol.*, 4(3):173–178, March 2009. ISSN 1748-3395. doi:10/fmnx82. Cited on page 25.

[100] Luis, F., *et al.* Molecular prototypes for spin-based CNOT and SWAP quantum gates. *Phys. Rev. Lett.*, 107(11):117203, September 2011. doi:10/cfmrfk. Cited on page 25.

[101] Fernandez, A., *et al.* Making hybrid [n]-rotaxanes as supramolecular arrays of molecular electron spin qubits. *Nat. Commun.*, 7(1):10240, January 2016. ISSN 2041-1723. doi:10/gmhsgc. Cited on page 25.

[102] Yamabayashi, T., *et al.* Scaling up electronic spin qubits into a three-dimensional metal–organic framework. *J. Am. Chem. Soc.*, 140(38): 12090–12101, September 2018. ISSN 0002-7863. doi:10/gd97qj. Cited on page 25.

[103] Gedik, Z., *et al.* Computational speed-up with a single qudit. *Sci. Rep.*, 5(1):14671, October 2015. ISSN 2045-2322. doi:10/f7s462. Cited on page 25.

[104] Richart, D., Fischer, Y., and Weinfurter, H. Experimental implementation of higher dimensional time–energy entanglement. *Appl. Phys. B*, 106(3):543–550, March 2012. ISSN 1432-0649. doi:10/fzfx42. Cited on page 25.

[105] O'Leary, D.P., Brennen, G.K., and Bullock, S.S. Parallelism for quantum computation with qudits. *Phys. Rev. A*, 74(3):032334, September 2006. doi:10/fw4d2v. Cited on page 26.

[106] Gottesman, D. Fault-tolerant quantum computation with higher-dimensional systems. In Williams, C.P., editor, *Quantum Computing and Quantum Communications*, Lecture Notes in Computer Science, pages 302–313, Berlin, Heidelberg, 1999. Springer. ISBN 978-3-540-49208-5. doi:10/cx5vqn. Cited on page 26.

[107] Kues, M., *et al.* On-chip generation of high-dimensional entangled quantum states and their coherent control. *Nature*, 546(7660):622–626, June 2017. ISSN 1476-4687. doi:10/gbmsxp. Cited on page 26.

[108] Ralph, T.C., Resch, K.J., and Gilchrist, A. Efficient Toffoli gates using qudits. *Phys. Rev. A*, 75(2):022313, February 2007. doi:10/fwt466. Cited on page 26.

[109] Mohammadi, M., Niknafs, A., and Eshghi, M. Controlled gates for multi-level quantum computation. *Quantum Inf. Process.*, 10(2): 241–256, April 2011. ISSN 1573-1332. doi:10/bcxchz. Cited on page 26.

[110] Woodruff, D.N., Winpenny, R.E.P., and Layfield, R.A. Lanthanide single-molecule magnets. *Chem. Rev.*, 113(7):5110–5148, July 2013. ISSN 0009-2665. doi:10/gdm9cs. Cited on page 26.

[111] Sessoli, R., *et al.* High-spin molecules: $[Mn_{12}O_{12}(O_2CR)_{16}(H_2O)_4]$. *J. Am. Chem. Soc.*, 115(5):1804–1816, March 1993. ISSN 0002-7863. doi:10/ddf47c. Cited on pages 26 and 98.

[112] Ruiz, E., *et al.* Can large magnetic anisotropy and high spin really coexist? *Chem. Commun.*, (1):52–54, December 2007. ISSN 1364-548X. doi:10/cxrxzv. Cited on page 26.

[113] Goodwin, C.A.P., *et al.* Molecular magnetic hysteresis at 60 kelvin in dysprosocenium. *Nature*, 548(7668):439–442, August 2017. ISSN 1476-4687. doi:10/ccdm. Cited on page 27.

[114] Guo, F.S., *et al.* Magnetic hysteresis up to 80 kelvin in a dysprosium metallocene single-molecule magnet. *Science*, 362(6421):1400–1403, December 2018. ISSN 0036-8075, 1095-9203. doi:10/gffmp8. Cited on page 27.

[115] Escalera-Moreno, L., *et al.* Spin states, vibrations and spin relaxation in molecular nanomagnets and spin qubits: A critical perspective. *Chem. Sci.*, 9(13):3265–3275, March 2018. ISSN 2041-6539. doi:10/gmkhgx. Cited on page 27.

[116] L. D. Landau, and E. M. Lifshitz. *Quantum Mechanics— Non-Relativistic Theory*, volume 3 of *Course of Theoretical Physics*. Pergamon Press, Oxford, United Kingdom, third edition, 1977. ISBN 978-0-08-020940-1. Cited on page 31.

[117] Wernsdorfer, W., Murugesu, M., and Christou, G. Resonant Tunneling in Truly Axial Symmetry Mn_{12} Single-Molecule Magnets: Sharp Crossover between Thermally Assisted and Pure Quantum Tunneling. *Phys. Rev. Lett.*, 96(5):057208, February 2006. doi:10/cj5ztr. Cited on page 33.

[118] Cervetti, C., *et al.* The classical and quantum dynamics of molecular spins on graphene. *Nat. Mater.*, 15(2):164–168, February 2016. ISSN 1476-4660. doi:10/ghcm3c. Cited on page 34.

[119] Jaynes, E., and Cummings, F. Comparison of quantum and semiclassical radiation theories with application to the beam maser. *Proc. IEEE*, 51(1):89–109, January 1963. ISSN 1558-2256. doi:10/ccmfdq. Cited on pages 36 and 38.

[120] Raizen, M.G., *et al.* Normal-mode splitting and linewidth averaging for two-state atoms in an optical cavity. *Phys. Rev. Lett.*, 63(3):240–243, July 1989. doi:10/bwjswg. Cited on page 39.

[121] Kaluzny, Y., *et al.* Observation of self-induced Rabi oscillations in two-level atoms excited inside a resonant cavity: The ringing regime of superradiance. *Phys. Rev. Lett.*, 51(13):1175–1178, September 1983. doi:10/bzspmh. Cited on page 39.

[122] Kubo, Y., *et al.* Strong Coupling of a Spin Ensemble to a Superconducting Resonator. *Phys. Rev. Lett.*, 105(14):140502, September 2010. doi:10/bbr9sp. Cited on pages 39 and 45.

[123] Huebl, H., *et al.* High cooperativity in coupled microwave resonator ferrimagnetic insulator hybrids. *Phys. Rev. Lett.*, 111(12):127003, September 2013. doi:10/ggnkd5. Cited on page 39.

[124] Mergenthaler, M., *et al.* Strong coupling of microwave photons to antiferromagnetic fluctuations in an organic magnet. *Phys. Rev. Lett.*, 119(14):147701, October 2017. ISSN 0031-9007, 1079-7114. doi:10/gcghp7. Cited on pages 39 and 131.

[125] Fink, J.M., *et al.* Dressed collective qubit states and the Tavis-Cummings model in circuit QED. *Phys. Rev. Lett.*, 103(8):083601, August 2009. doi:10/fj6ggd. Cited on page 39.

[126] Zollitsch, C.W., *et al.* High cooperativity coupling between a phosphorus donor spin ensemble and a superconducting microwave resonator. *Appl. Phys. Lett.*, 107(14):142105, October 2015. ISSN 0003-6951. doi:10/ggz3zb. Cited on page 39.

[127] Wesenberg, J.H., *et al.* Quantum computing with an electron spin ensemble. *Phys. Rev. Lett.*, 103(7):070502, August 2009. doi:10/b7985h. Cited on page 39.

[128] Raimond, J.M., Brune, M., and Haroche, S. Manipulating quantum entanglement with atoms and photons in a cavity. *Rev. Mod. Phys.*, 73(3):565–582, August 2001. doi:10/cpwvw3. Cited on pages 39 and 42.

[129] Thompson, R.J., Rempe, G., and Kimble, H.J. Observation of normal-mode splitting for an atom in an optical cavity. *Phys. Rev. Lett.*, 68 (8):1132–1135, February 1992. doi:10/d3kdjz. Cited on page 39.

[130] Nakamura, Y., Pashkin, Y.A., and Tsai, J.S. Coherent control of macroscopic quantum states in a single-Cooper-pair box. *Nature*, 398(6730):786–788, April 1999. ISSN 1476-4687. doi:10/fwmc3t. Cited on page 39.

[131] Vion, D., *et al.* Manipulating the quantum state of an electrical circuit. *Science*, 296(5569):886–889, May 2002. ISSN 0036-8075, 1095-9203. doi:10/fcvmmk. Cited on page 39.

[132] Chiorescu, I., *et al.* Coherent quantum dynamics of a superconducting flux qubit. *Science*, 299(5614):1869–1871, March 2003. ISSN 0036-8075, 1095-9203. doi:10/bjhkzz. Cited on page 39.

[133] Yamamoto, T., *et al.* Demonstration of conditional gate operation using superconducting charge qubits. *Nature*, 425(6961):941–944, October 2003. ISSN 1476-4687. doi:10/dnf3c9. Cited on page 39.

[134] Wallraff, A., *et al.* Strong coupling of a single photon to a superconducting qubit using circuit quantum electrodynamics. *Nature*, 431 (7005):162–167, September 2004. ISSN 1476-4687. doi:10/bq2bn8. Cited on page 40.

[135] Boca, A., *et al.* Observation of the vacuum rabi spectrum for one trapped atom. *Phys. Rev. Lett.*, 93(23):233603, December 2004. ISSN 0031-9007, 1079-7114. doi:10/bww63q. Cited on pages 40 and 44.

[136] Leuenberger, M.N., and Loss, D. Spin tunneling and phonon-assisted relaxation in Mn_{12}-acetate. *Phys. Rev. B*, 61(2):1286–1302, January 2000. doi:10/fq8skt. Cited on pages 40, 41, 108, and 109.

[137] E. M. Purcell. Spontaneous Emission Probabilities at Radio Frequencies. *Phys. Rev.*, 69(11–12):681, June 1946. Cited on page 41.

[138] Hinds, E.A. Cavity Quantum Electrodynamics. volume 28 of *Advances In Atomic, Molecular, and Optical Physics*, pages 237–289. Academic Press, January 1990. doi:10/cgmqg9. Cited on page 41.

[139] Göppl, M., *et al.* Coplanar waveguide resonators for circuit quantum electrodynamics. *J. Appl. Phys.*, 104(11):113904, December 2008. ISSN 0021-8979. doi:10/c82pgb. Cited on page 42.

[140] Blais, A., *et al.* Cavity quantum electrodynamics for superconducting electrical circuits: An architecture for quantum computation. *Phys. Rev. A*, 69(6):062320, June 2004. doi:10/d6xbd2. Cited on page 42.

[141] Sanchez-Mondragon, J.J., Narozhny, N.B., and Eberly, J.H. Theory of spontaneous-emission line shape in an ideal cavity. *Phys. Rev. Lett.*, 51(7):550–553, August 1983. doi:10/d6ns53. Cited on page 43.

[142] Agarwal, G.S. Vacuum-field Rabi splittings in microwave absorption by Rydberg atoms in a cavity. *Phys. Rev. Lett.*, 53(18):1732–1734, October 1984. doi:10/fmdv6f. Cited on page 43.

[143] Agarwal, G.S. Vacuum-field Rabi oscillations of atoms in a cavity. *J. Opt. Soc. Am. B*, 2(3):480–485, March 1985. ISSN 1520-8540. doi:10/dprvzr. Cited on page 43.

[144] Chiorescu, I., *et al.* Magnetic strong coupling in a spin–photon system and transition to classical regime. *Phys. Rev. B*, 82(2):024413, July 2010. doi:10/bhgjcv. Cited on page 43.

[145] Goy, P., *et al.* Observation of cavity-enhanced single-atom spontaneous emission. *Phys. Rev. Lett.*, 50(24):1903–1906, June 1983. doi:10/ffjr57. Cited on page 44.

[146] Stajic, J. Quantum information processing. The future of quantum information processing. Introduction. *Science*, 339(6124):1163, March 2013. ISSN 1095-9203. doi:10/ggf458. Cited on page 44.

[147] Feynman, R.P. Simulating physics with computers. *Int. J. Theor. Phys.*, 21(6):467–488, June 1982. ISSN 1572-9575. doi:10/cpkzhd. Cited on page 44.

[148] Deutsch, D., and Penrose, R. Quantum theory, the Church–Turing principle and the universal quantum computer. *Proc. R. Soc. Lond. A Math. Phys. Sci.*, 400(1818):97–117, July 1985. doi:10/fk6nzc. Cited on page 44.

[149] Deutsch, D., and Jozsa, R. Rapid solution of problems by quantum computation. *Proc. R. Soc. Lond. A Math. Phys. Sci.*, 439(1907):553–558, December 1992. doi:10/fjp4h9. Cited on page 44.

[150] Koch, J., *et al.* Charge-insensitive qubit design derived from the Cooper pair box. *Phys. Rev. A*, 76(4):042319, October 2007. doi:10/b5bt9m. Cited on page 44.

[151] Gambetta, J.M., Chow, J.M., and Steffen, M. Building logical qubits in a superconducting quantum computing system. *npj Quantum Inf.*, 3(1):1–7, January 2017. ISSN 2056-6387. doi:10/f9vx3q. Cited on page 44.

[152] Scarlino, P., *et al.* Coherent microwave-photon-mediated coupling between a semiconductor and a superconducting qubit. *Nat. Commun.*, 10(1):3011, July 2019. ISSN 2041-1723. doi:10/gf5ghf. Cited on page 44.

[153] Barends, R., *et al.* Coherent Josephson qubit suitable for scalable quantum integrated circuits. *Phys. Rev. Lett.*, 111(8):080502, August 2013. doi:10/gf68ss. Cited on page 44.

[154] Yan, F., *et al.* The flux qubit revisited to enhance coherence and reproducibility. *Nat. Commun.*, 7(1):12964, November 2016. ISSN 2041-1723. doi:10/f89v7b. Cited on page 44.

[155] Nakonechnyi, M.A., *et al.* Multi-signal spectroscopy of qubit-resonator systems. *Nature*, 47(5):383–387, May 2021. ISSN 1063-777X. doi:10/gmmg32. Cited on page 44.

[156] Paik, H., *et al.* Observation of high coherence in josephson junction qubits measured in a three-dimensional circuit QED architecture. *Phys. Rev. Lett.*, 107(24):240501, December 2011. doi:10/b7mhmb. Cited on page 44.

[157] Schuster, D.I., *et al.* High-Cooperativity Coupling of Electron-Spin Ensembles to Superconducting Cavities. *Phys. Rev. Lett.*, 105(14): 140501, September 2010. doi:10/dz3bc7. Cited on page 45.

[158] Sandner, K., *et al.* Strong magnetic coupling of an inhomogeneous nitrogen-vacancy ensemble to a cavity. *Phys. Rev. A*, 85(5):053806, May 2012. doi:10/f3sq6w. Cited on page 45.

[159] Abe, E., *et al.* Electron spin ensemble strongly coupled to a three-dimensional microwave cavity. *Appl. Phys. Lett.*, 98(25):251108, June 2011. ISSN 0003-6951. doi:10/d4zrh4. Cited on page 45.

[160] Gagliardi, L., and Roos, B.O. Quantum chemical calculations show that the uranium molecule U_2 has a quintuple bond. *Nature*, 433 (7028):848–851, February 2005. ISSN 1476-4687. doi:10/fhxj6k. Cited on page 57.

[161] Hagberg, D., *et al.* The coordination of uranyl in water: a combined quantum chemical and molecular simulation study. *J. Am. Chem. Soc.*, 127(41):14250–14256, October 2005. ISSN 0002-7863. doi:10/dvfkhf. Cited on page 57.

[162] Gagliardi, L., *et al.* The electronic spectrum of the UO_2 molecule. *J. Am. Chem. Soc.*, 127(1):86–91, January 2005. ISSN 0002-7863. doi:10/b3xckd. Cited on page 57.

[163] Gagliardi, L., Pyykkö, P., and O. Roos, B. A very short uranium–uranium bond: The predicted metastable U_2^{2+}. *Phys. Chem. Chem. Phys.*, 7(12):2415–2417, 2005. doi:10/bd3wn6. Cited on page 57.

[164] Gagliardi, L. Prediction of new inorganic molecules with quantum chemical methods. *Theor. Chem. Acc.*, 116(1):307–315, August 2006. ISSN 1432-2234. doi:10/bvwb3g. Cited on page 57.

[165] Macchia, G.L., Brynda, M., and Gagliardi, L. Quantum chemical calculations predict the diphenyl diuranium compound [PhUUPh] to have a stable ^1A_g ground state. *Angew. Chem. Int. Ed.*, 45(37): 6210–6213, 2006. ISSN 1521-3773. doi:10/c5fhkw. Cited on page 57.

[166] Roos, B.O., and Gagliardi, L. Quantum chemistry predicts multiply bonded diuranium compounds to be stable. *Inorg. Chem.*, 45(2): 803–807, January 2006. ISSN 0020-1669. doi:10/bwpq27. Cited on page 57.

[167] Gagliardi, L., and Roos, B.O. The electronic spectrum of $Re_2Cl_8^{2-}$: a theoretical study. *Inorg. Chem.*, 42(5):1599–1603, March 2003. ISSN 0020-1669. doi:10/dctkm3. Cited on page 57.

[168] Vogiatzis, K.D., *et al.* Pushing configuration-interaction to the limit: Towards massively parallel MCSCF calculations. *J. Chem. Phys.*, 147 (18):184111, November 2017. ISSN 1089-7690. doi:10/gckbst. Cited on page 58.

[169] Kolesov, G., Kaxiras, E., and Manousakis, E. Density functional theory beyond the Born-Oppenheimer approximation: Accurate treatment of the ionic zero-point motion. *Phys. Rev. B*, 98(19):195112, November 2018. doi:10/gfsn62. Cited on page 59.

[170] Giustino, F. *Materials Modelling Using Density Functional Theory: Properties and Predictions*. Oxford University Press, 2014. ISBN 978-0-19-966244-9. Cited on page 59.

[171] Zhang, P., Guo, Y.N., and Tang, J. Recent advances in dysprosium-based single molecule magnets: Structural overview and synthetic strategies. *Coord. Chem. Rev.*, 257(11):1728–1763, June 2013. ISSN 0010-8545. doi:10/f4wfx9. Cited on page 66.

[172] E. J. Mittemeijer, and U. Welzel, editors. *Modern Diffraction Methods*. Wiley-VCH, Berlin, November 2012. ISBN 978-3-527-32279-4. Cited on page 66.

[173] Dobson, P.J. Physical Properties of Crystals – Their Representation by Tensors and Matrices. *Phys. Bull.*, 36(12):506–506, December 1985. ISSN 0031-9112. doi:10/gqhg6d. Cited on pages 66 and 69.

[174] Qian, K., *et al.* Does the thermal evolution of molecular structures critically affect the magnetic anisotropy? *Chem. Sci.*, 6(8):4587–4593, July 2015. ISSN 2041-6539. doi:10/gqhg6c. Cited on page 66.

[175] Chilton, N.F., *et al.* An electrostatic model for the determination of magnetic anisotropy in dysprosium complexes. *Nat. Commun.*, 4 (1):2551, October 2013. ISSN 2041-1723. doi:10/gbd4t2. Cited on pages 66 and 67.

[176] Chilton, N.F., *et al.* Single molecule magnetism in a family of mononuclear β-diketonate lanthanide(III) complexes: Rationalization of magnetic anisotropy in complexes of low symmetry. *Chem. Sci.*, 4(4):1719–1730, March 2013. ISSN 2041-6539. doi:10/gqhg6b. Cited on page 66.

[177] Jiang, S.D., *et al.* A Mononuclear Dysprosium Complex Featuring Single-Molecule-Magnet Behavior. *Angew. Chem. Int. Ed.*, 49(41): 7448–7451, 2010. ISSN 1521-3773. doi:10/ctw3zp. Cited on page 66.

[178] Chen, G.J., *et al.* Enhancing anisotropy barriers of dysprosium(III) single-ion magnets. *Chem. Eur. J.*, 18(9):2484–2487, February 2012. ISSN 1521-3765. doi:10/fx4qbf. Cited on page 66.

[179] Chen, G.J., *et al.* Coordination-perturbed single-molecule magnet behaviour of mononuclear dysprosium complexes. *Dalton Trans.*, 40(20):5579–5583, May 2011. ISSN 1477-9234. doi:10/fm987p. Cited on page 66.

[180] Tong, Y.Z., *et al.* Two mononuclear single molecule magnets derived from dysprosium(III) and tmphen (tmphen = 3,4,7,8-tetramethyl-1,10-phenanthroline). *Dalton Trans.*, 44(19):9020–9026, May 2015. ISSN 1477-9234. doi:10/gqhg59. Cited on page 66.

[181] CSD crystal system statistics, January 2021. Cited on pages 67, 73, 74, and 75.

[182] Horrocks, W.D.W., and Hall, D.D.W. Paramagnetic anisotropy. *Coord. Chem. Rev.*, 6(2):147–186, July 1971. ISSN 0010-8545. doi:10/cjpxgh. Cited on page 69.

[183] Zhu, Z., *et al.* Molecular magnetism of lanthanide: Advances and perspectives. *Coord. Chem. Rev.*, 378:350–364, January 2019. ISSN 0010-8545. doi:10/gpqkpm. Cited on page 70.

[184] Freidzon, A.Y., Kurbatov, I.A., and Vovna, V.I. Ab initio calculation of energy levels of trivalent lanthanide ions. *Phys. Chem. Chem. Phys.*, 20(21):14564–14577, May 2018. ISSN 1463-9084. doi:10/gj3tmn. Cited on page 78.

[185] Boča, R. Mean and differential magnetic susceptibilities in metal complexes. *Coord. Chem. Rev.*, 173(1):167–283, June 1998. ISSN 0010-8545. doi:10/cmbs5x. Cited on page 84.

[186] Boča, R. Zero-field splitting in metal complexes. *Coord. Chem. Rev.*, 248(9):757–815, May 2004. ISSN 0010-8545. doi:10/cx236t. Cited on page 84.

[187] Caneschi, A., *et al.* Alternating current susceptibility, high field magnetization, and millimeter band EPR evidence for a ground $S = 10$ state in $[Mn_{12}O_{12}(CH_3COO)_{16}(H_2O)_4]\cdot 2CH_3COOH\cdot 4H_2O$. *J. Am. Chem. Soc.*, 113(15):5873–5874, July 1991. ISSN 0002-7863. doi:10/dcp533. Cited on page 98.

[188] Sessoli, R., *et al.* Magnetic bistability in a metal-ion cluster. *Nature*, 365(6442):141–143, September 1993. ISSN 1476-4687. doi:10/dwr7g4. Cited on page 98.

[189] Wernsdorfer, W., *et al.* Quantum phase interference (Berry phase) in single-molecule magnets of $[Mn_{12}]^{2-}$. *J. Appl. Phys.*, 91(10):7164–7166, May 2002. ISSN 0021-8979. doi:10/dhcs7x. Cited on page 98.

[190] Thomas, L., *et al.* Macroscopic quantum tunnelling of magnetization in a single crystal of nanomagnets. *Nature*, 383(6596):145–147, September 1996. ISSN 1476-4687. doi:10/cn3hsj. Cited on page 101.

[191] Cornia, A., *et al.* Origin of Second-Order Transverse Magnetic Anisotropy in Mn_{12}-Acetate. *Phys. Rev. Lett.*, 89(25):257201, November 2002. doi:10/dbrncs. Cited on page 102.

[192] Mertes, K.M., *et al.* Distribution of Tunnel Splittings in Mn_{12} Acetate. *Phys. Rev. Lett.*, 87(22):227205, November 2001. doi:10/csctvk. Cited on page 102.

[193] del Barco, E., *et al.* Tunneling splittings in Mn_{12}-acetate single crystals. *EPL*, 60(5):768, December 2002. ISSN 0295-5075. doi:10/frvtxg. Cited on page 102.

[194] Amigó, R., *et al.* Quadratic tranverse anisotropy term due to dislocations in Mn_{12} acetate crystals directly observed by EPR spectroscopy. *Phys. Rev. B*, 65(17):172403, April 2002. doi:10/bm4gjr. Cited on page 102.

[195] Parks, B., *et al.* Linewidth of single-photon transitions in Mn_{12}-acetate. *Phys. Rev. B*, 64(18):184426, October 2001. doi:10/fkv5xq. Cited on page 102.

[196] Luis, F., Bartolomé, J., and Fernández, J.F. Resonant magnetic quantum tunneling through thermally activated states. *Phys. Rev. B*, 57 (1):505–513, January 1998. doi:10/fbwknw. Cited on page 102.

[197] Takahashi, S., *et al.* Discrete easy-axis tilting in ${\mathrm{Mn}}_-{12}$-acetate, as determined by EPR: Implications for the magnetic quantum tunneling mechanism. *Phys. Rev. B*, 70(9):094429, September 2004. doi:10/c64zxg. Cited on page 102.

[198] Chiorescu, I., *et al.* Phonon-Assisted Tunneling in the Quantum Regime of Mn_{12} Acetate. *Phys. Rev. Lett.*, 85(22):4807–4810, November 2000. doi:10/dfrf29. Cited on page 102.

[199] Barra, A.L., *et al.* The Origin of Transverse Anisotropy in Axially Symmetric Single Molecule Magnets. *J. Am. Chem. Soc.*, 129(35): 10754–10762, September 2007. ISSN 0002-7863. doi:10/fhs4b9. Cited on page 102.

[200] Arute, F., *et al.* Quantum supremacy using a programmable superconducting processor. *Nature*, 574(7779):505–510, October 2019. ISSN 1476-4687. doi:10/ggbnb4. Cited on page 105.

[201] Satyajit, S., *et al.* Nondestructive discrimination of a new family of highly entangled states in IBM quantum computer. *Quantum Inf. Process.*, 17(9):212, July 2018. ISSN 1573-1332. doi:10/gdw93s. Cited on page 105.

[202] Behera, B.K., *et al.* Demonstration of entanglement purification and swapping protocol to design quantum repeater in IBM quantum computer. *Quantum Inf. Process.*, 18(4):108, March 2019. ISSN 1573-1332. doi:10/gnx9qp. Cited on page 105.

[203] Conrad Clauß. *On-Chip Broadband Magnetic Resonance Spectroscopy Down to Ultralow Temperatures*. Doctor of Philosophy, Universität Stuttgart, Stuttgart, March 2014. Cited on pages 105 and 124.

[204] Candini, A. *Hall Probes Magnetometry for the Study of Molecular Nanomagnets*. Doctor of Philosophy, Università di Modena e Reggio Emilia, Modena, Italy, 2007. Cited on page 106.

[205] Li, Y., *et al.* Hall magnetometry on a single iron nanoparticle. *Appl. Phys. Lett.*, 80(24):4644–4646, June 2002. ISSN 0003-6951. doi:10/bsvjzs. Cited on page 106.

[206] Timp, G.L. *Nanotechnology*. Springer Science & Business Media, December 2012. ISBN 978-1-4612-0531-9. Cited on page 106.

[207] Carroll, C.E., and Hioe, F.T. Transition probabilities for the three-level Landau-Zener model. *J. Phys. A: Math. Gen.*, 19(11):2061–2073, August 1986. ISSN 0305-4470. doi:10/c2hjqk. Cited on page 113.

[208] Vitanov, N.V., and Suominen, K.A. Time-dependent control of ultracold atoms in magnetic traps. *Phys. Rev. A*, 56(6):R4377–R4380, December 1997. ISSN 1050-2947, 1094-1622. doi:10/b928d6. Cited on page 115.

[209] Larson, J. Level crossings in a cavity QED model. *Phys. Rev. A*, 73 (1):013823, January 2006. doi:10/dg3hkr. Cited on page 115.

[210] Sinitsyn, N.A. Landau-Zener transitions in chains. *Phys. Rev. A*, 87 (3):032701, March 2013. doi:10/gn42qd. Cited on page 115.

[211] Liu, D. *Probing Exotic Boundary Quantum Phases with Tunable Nanostructures*. Doctor of Philosophy, Duke University, Durham, North Carolina, 2012. Cited on page 115.

[212] Beterov, I.M., and Chebotaev, V.P. Three-level gas systems and their interaction with radiation. *Prog. Quantum Electron.*, 3:1–106, January 1974. ISSN 0079-6727. doi:10/cbn433. Cited on page 119.

[213] Jacobsen, S.H., and Jarvis, P.D. Exactly solvable three-level quantum dissipative systems via bosonization of fermion gas-impurity models. *J. Phys. A: Math. Theor.*, 43(25):255305, May 2010. ISSN 1751-8121. doi:10/bws39r. Cited on page 119.

[214] Chilton, N.F., *et al.* PHI: A powerful new program for the analysis of anisotropic monomeric and exchange-coupled polynuclear d- and f-block complexes. *J. Comput. Chem.*, 34(13):1164–1175, May 2013. ISSN 01928651. doi:10/gdb82v. Cited on page 126.

[215] Edén, M., and Levitt, M.H. Computation of Orientational Averages in Solid-State NMR by Gaussian Spherical Quadrature. *J. Magn. Reson.*, 132(2):220–239, June 1998. ISSN 1090-7807. doi:10/cwr93p. Cited on page 126.

[216] Briganti, M., *et al.* Magnetic Anisotropy Trends along a Full 4f-Series: The fn^{+7} Effect. *J. Am. Chem. Soc.*, 143(21):8108–8115, June 2021. ISSN 0002-7863. doi:10/gj596f. Cited on pages 141 and 142.

[217] Mergenthaler, M., *et al.* Strong Coupling of Microwave Photons to Antiferromagnetic Fluctuations in an Organic Magnet. *Phys. Rev. Lett.*, 119(14):147701, October 2017. doi:10/gcghp7. Cited on page 150.

[218] Gómez-León, Á., Luis, F., and Zueco, D. Dispersive Readout of Molecular Spin Qudits. *Phys. Rev. Applied*, 17(6):064030, June 2022. doi:10/gqxdht. Cited on page 150.

[219] Román-Roche, J., Luis, F., and Zueco, D. Photon Condensation and Enhanced Magnetism in Cavity QED. *Phys. Rev. Lett.*, 127(16): 167201, October 2021. doi:10/gqxdhs. Cited on page 150.

[220] Chiesa, A., *et al.* Robustness of quantum gates with hybrid spin-photon qubits in superconducting resonators. *Phys. Rev. A*, 89(5): 052308, May 2014. doi:10/gqxdjx. Cited on page 150.

[221] Chizzini, M., *et al.* Quantum error correction with molecular spin qudits. *Phys. Chem. Chem. Phys.*, 24(34):20030–20039, August 2022. ISSN 1463-9084. doi:10/gqxdjw. Cited on page 150.

[222] Chiesa, A., *et al.* Theoretical Design of Optimal Molecular Qudits for Quantum Error Correction. *J. Phys. Chem. Lett.*, 13(28):6468–6474, July 2022. doi:10/gqxdjv. Cited on page 150.

[223] Lockyer, S.J., *et al.* Targeting molecular quantum memory with embedded error correction. *Chem. Sci.*, 12(26):9104–9113, July 2021. ISSN 2041-6539. doi:10/gqxdjt. Cited on page 150.

[224] Chiesa, A., *et al.* Molecular Nanomagnets as Qubits with Embedded Quantum-Error Correction. *J. Phys. Chem. Lett.*, 11(20):8610–8615, October 2020. doi:10/gqxdjr. Cited on page 150.

[225] Petiziol, F., *et al.* Counteracting dephasing in Molecular Nanomagnets by optimized qudit encodings. *npj Quantum Inf.*, 7(1):1–10, August 2021. ISSN 2056-6387. doi:10/gqxdjs. Cited on page 150.

[226] Jenkins, M.D., *et al.* A scalable architecture for quantum computation with molecular nanomagnets. *Dalton Trans.*, 45(42):16682–16693, October 2016. ISSN 1477-9234. doi:10/gcvjq5. Cited on page 150.

[227] Ferrando-Soria, J., *et al.* A modular design of molecular qubits to implement universal quantum gates. *Nat. Commun.*, 7(1):11377, April 2016. ISSN 2041-1723. doi:10/f8nj9p. Cited on page 150.

[228] Carretta, S., *et al.* A perspective on scaling up quantum computation with molecular spins. *Appl. Phys. Lett.*, 118(24):240501, June 2021. ISSN 0003-6951. doi:10/gqp3mg. Cited on page 150.

[229] Jenkins, M.D., *et al.* Nanoscale constrictions in superconducting coplanar waveguide resonators. *Appl. Phys. Lett.*, 105(16):162601, October 2014. ISSN 0003-6951. doi:10/ggz35n. Cited on page 150.

[230] Heiko Lueken. *Magnetochemie: Eine Einführung in Theorie und Anwendung*. Teubner Studienbücher Chemie. Vieweg+Teubner Verlag, Stuttgart, October 1999. ISBN 978-3-519-03530-5. Cited on page E.34.

A Tables

A.1 General information

k	q	O_k^q
2	0	$3S_z^2 - sI$
	±1	$c_\pm\{S_z, S_+ \pm S_-\}$
	±2	$c_\pm(S_+^2 \pm S_-^2)$
4	0	$35S_z^4 - (30s - 25)S_z^2 + (3s^2 - 6s)I$
	±1	$c_\pm\{7S_z^3 - (3s + 1)I, S_+ \pm S_-\}$
	±2	$c_\pm\{7S_z^2 - (s + 5)I, S_+^2 \pm S_-^2\}$
	±3	$c_\pm\{S_z, S_+^3 \pm S_-^3\}$
	±4	$c_\pm(S_+^4 \pm S_-^4)$
6	0	$231S_z^6 - (315s - 735)S_z^4 + (105s^2 - 525s + 294)S_z^2 - (5s^3 - 40s^2 + 60s)I$
	±1	$c_\pm\{33S_z^5 - (30s - 15)S_z^3 + (5s^2 - 10s + 12)S_z, S_+ \pm S_-\}$
	±2	$c_\pm\{33S_z^4 - (18s + 123)S_z^2 + (s^2 - 10s + 102)I, S_+^2 \pm S_-^2\}$
	±3	$c_\pm\{11S_z^3 - (3s + 59)S_z, S_+^3 \pm S_-^3\}$
	±4	$c_\pm\{11S_z^2 - (s + 38)I, S_+^4 \pm S_-^4\}$
	±5	$c_\pm\{S_z, S_+^5 \pm S_-^5\}$
	±6	$c_\pm(S_+^6 \pm S_-^6)$

Table A.1: A list of the most common Stevens operators in terms of polynomials in $S_z, S_\pm$. The anticommutator is denoted by $\{\cdot,\cdot\}$ (which is defined as $\{a, b\} = ab + ba$), $c_+ = \frac{1}{4}, c_- = \frac{1}{4i}$, $s = S(S + 1)$, and I is the identity operator.

Ln^{3+}	$4f^N$	$^{2S+1}L_J$	g_J	μ_{eff}^{exp} (μ_o)
La^{3+}	$4f^0$	$^1S_0$		
Ce^{3+}	$4f^1$	$^2F_{5/2}$	6/7	2.3–2.5
Pr^{3+}	$4f^2$	$^3H_4$	4/5	3.4–3.6
Nd^{3+}	$4f^3$	$^4I_{9/2}$	8/11	3.4–3.5
Pm^{3+}	$4f^4$	$^5I_4$	3/5	2.9
Sm^{3+}	$4f^5$	$^6H_{5/2}$	2/7	1.6
Eu^{3+}	$4f^6$	$^7F_0$	0	3.5
Gd^{3+}	$4f^7$	$^8S_{7/2}$	2	7.8–7.9
Tb^{3+}	$4f^8$	$^7F_6$	3/2	9.7–9.8
Dy^{3+}	$4f^9$	$^6H_{15/2}$	4/3	10.2–10.6
Ho^{3+}	$4f^{10}$	$^5I_8$	5/4	10.3–10.5
Er^{3+}	$4f^{11}$	$^4I_{15/2}$	6/5	9.4–9.5
Tm^{3+}	$4f^{12}$	$^3H_6$	7/6	7.5
Yb^{3+}	$4f^{13}$	$^2F_{7/2}$	8/7	4.5
Lu^{3+}	$4f^{14}$	$^1S_0$		

Table A.2: The lanthanides' electron configurations $4f^N$, ground multiplets $^{2S+1}L_J$, effective Landé factors g_J, and experimentally determined effective magnetic moments μ_{eff} at 295 K, which is defined according to the paramagnetic susceptibility by $\chi_m = \mu_o N_A \mu_B^2 \mu_{eff}^2/(3k_B T)$.[230]

A.2 Calculation results

All calculations were done in a "molecular frame" converted from the crystal-structure data using Gram–Schmidt, such that $\hat{x} = \hat{a}$, $\hat{y} = \frac{\hat{b}-(\hat{b}\cdot\hat{x})\hat{x}}{|\hat{b}-(\hat{b}\cdot\hat{x})\hat{x}|}$, and $\hat{z} = \frac{\hat{c}-(\hat{c}\cdot\hat{x})\hat{x}-(\hat{c}\cdot\hat{y})\hat{y}}{|\hat{c}-(\hat{c}\cdot\hat{x})\hat{x}-(\hat{c}\cdot\hat{y})\hat{y}|}$.

Table A.3: The Stevens coefficients of $Gd(hfac)_3(^tBubpy)$ as calculated by MOLCAS using the crystal-structure data. The reference frame is, as specified in the beginning of this section, defined in a "molecular coordinate frame" from the crystal coordinate frame. This set of Stevens coefficients results in a 99.999756 % recovery factor of the crystal-field matrix. The VTZP basis set was used for Gd, O, and N, and VDZP for all other atoms. The lowest-lying 1 octet and 48 sextets were considered.

$$B_2^{-2} = -1.12285095195327 \times 10^{-2}\ \mathrm{cm}^{-1}$$

$$B_2^{-1} = -0.20595043050249 \times 10^{-1}\ \mathrm{cm}^{-1}$$

$$B_2^{0} = 0.96437350277891 \times 10^{-2}\ \mathrm{cm}^{-1}$$

$$B_2^{+1} = -0.36030787056676 \times 10^{-1}\ \mathrm{cm}^{-1}$$

$$B_2^{+2} = 0.47087919236293 \times 10^{-4}\ \mathrm{cm}^{-1}$$

$$B_4^{-4} = -1.33967808706875 \times 10^{-5}\ \mathrm{cm}^{-1}$$

$$B_4^{-3} = -0.56851953205806 \times 10^{-5}\ \mathrm{cm}^{-1}$$

$$B_4^{-2} = 0.54988200626423 \times 10^{-5}\ \mathrm{cm}^{-1}$$

$$B_4^{-1} = -0.61494141577799 \times 10^{-6}\ \mathrm{cm}^{-1}$$

$$B_4^{0} = -0.34209953681296 \times 10^{-5}\ \mathrm{cm}^{-1}$$

$$B_4^{+1} = 1.18287494722867 \times 10^{-5}\ \mathrm{cm}^{-1}$$

$$B_4^{+2} = 0.35480896015030 \times 10^{-5}\ \mathrm{cm}^{-1}$$

$$B_4^{+3} = 0.45940895113740 \times 10^{-6}\ \mathrm{cm}^{-1}$$

$$B_4^{+4} = 1.14960143392921 \times 10^{-5}\ \mathrm{cm}^{-1}$$

$$B_6^{-6} = -0.22888795634555 \times 10^{-9}\ \mathrm{cm}^{-1}$$

$$B_6^{-5} = 0.34444372069792 \times 10^{-8}\ \mathrm{cm}^{-1}$$

$$B_6^{-4} = -0.19288383422683 \times 10^{-8}\ \mathrm{cm}^{-1}$$

$$B_6^{-3} = -0.29960229609538 \times 10^{-8}\ \mathrm{cm}^{-1}$$

$$B_6^{-2} = -0.30419530788223 \times 10^{-9}\ \mathrm{cm}^{-1}$$

$$B_6^{-1} = 1.58669877073767 \times 10^{-9}\ \mathrm{cm}^{-1}$$

$$B_6^{0} = 0.36322455330371 \times 10^{-9}\ \mathrm{cm}^{-1}$$

$$B_6^{+1} = -0.22000959833620 \times 10^{-8}\ \mathrm{cm}^{-1}$$

$$B_6^{+2} = 1.23578415053588 \times 10^{-9}\ \mathrm{cm}^{-1}$$

$$B_6^{+3} = 0.99324034310127 \times 10^{-9}\ \mathrm{cm}^{-1}$$

$$B_6^{+4} = -0.85656518605962 \times 10^{-10}\ \mathrm{cm}^{-1}$$

$$B_6^{+5} = 1.19619565001450 \times 10^{-10}\ \mathrm{cm}^{-1}$$

$$B_6^{+6} = -1.02808444552419 \times 10^{-9}\ \mathrm{cm}^{-1}$$

$B_2^{-2} = 0.44065484742706 \times 10^{0}\ \mathrm{cm}^{-1}$

$B_2^{-1} = -0.16533723768821 \times 10^{0}\ \mathrm{cm}^{-1}$

$B_2^{0} = -0.13993071464188 \times 10^{+1}\ \mathrm{cm}^{-1}$

$B_2^{+1} = 0.40076628735697 \times 10^{0}\ \mathrm{cm}^{-1}$

$B_2^{+2} = 0.14572798654955 \times 10^{+1}\ \mathrm{cm}^{-1}$

$B_4^{-4} = -0.86231430794767 \times 10^{-2}\ \mathrm{cm}^{-1}$

$B_4^{-3} = 0.19965361441992 \times 10^{-1}\ \mathrm{cm}^{-1}$

$B_4^{-2} = -0.12204941739085 \times 10^{-1}\ \mathrm{cm}^{-1}$

$B_4^{-1} = -0.19655674103850 \times 10^{-2}\ \mathrm{cm}^{-1}$

$B_4^{0} = -0.47644042312062 \times 10^{-2}\ \mathrm{cm}^{-1}$

$B_4^{+1} = -0.10328513980757 \times 10^{-1}\ \mathrm{cm}^{-1}$

$B_4^{+2} = 0.31132605524407 \times 10^{-1}\ \mathrm{cm}^{-1}$

$B_4^{+3} = 0.18592909109839 \times 10^{-1}\ \mathrm{cm}^{-1}$

$B_4^{+4} = -0.43358663083585 \times 10^{-2}\ \mathrm{cm}^{-1}$

$B_6^{-6} = -0.58015501448146 \times 10^{-4}\ \mathrm{cm}^{-1}$

$B_6^{-5} = -0.32464965035850 \times 10^{-4}\ \mathrm{cm}^{-1}$

$B_6^{-4} = -0.11954206663139 \times 10^{-3}\ \mathrm{cm}^{-1}$

$B_6^{-3} = 0.63668427372981 \times 10^{-4}\ \mathrm{cm}^{-1}$

$B_6^{-2} = 0.87128417890507 \times 10^{-4}\ \mathrm{cm}^{-1}$

$B_6^{-1} = 0.36614698939298 \times 10^{-7}\ \mathrm{cm}^{-1}$

$B_6^{0} = -0.11707988043657 \times 10^{-4}\ \mathrm{cm}^{-1}$

$B_6^{+1} = -0.11311282545912 \times 10^{-3}\ \mathrm{cm}^{-1}$

$B_6^{+2} = -0.13988225537600 \times 10^{-4}\ \mathrm{cm}^{-1}$

$B_6^{+3} = 0.38051217649294 \times 10^{-4}\ \mathrm{cm}^{-1}$

$B_6^{+4} = 0.19567859434457 \times 10^{-3}\ \mathrm{cm}^{-1}$

$B_6^{+5} = -0.41248415044902 \times 10^{-4}\ \mathrm{cm}^{-1}$

$B_6^{+6} = 0.31528830990616 \times 10^{-4}\ \mathrm{cm}^{-1}$

Table A.4: The Stevens coefficients of $Dy(dbm)_3phen$ as calculated by MOLCAS using the crystal-structure data. The reference frame is, as specified in the beginning of this section, defined in a "molecular coordinate frame" from the crystal coordinate frame. This set of Stevens coefficients results in a 97.635878 % recovery factor of the crystal-field matrix (with the calculated coefficients up to $k = 12$ producing a recovery factor of 99.999999 %). The VTZP basis set was used for Dy, VDZP for O and N, and VDZ for all other atoms. The lowest-lying 21 sextets, 128 quartets, and 130 doublets were considered.

$B_2^{-2} = 0.40280605539049 \times 10^{0}\ \mathrm{cm}^{-1}$

$B_2^{-1} = -0.28841532453490 \times 10^{+1}\ \mathrm{cm}^{-1}$

$B_2^{0} = -0.39255023929069 \times 10^{+1}\ \mathrm{cm}^{-1}$

$B_2^{+1} = -0.17783368953503 \times 10^{+1}\ \mathrm{cm}^{-1}$

$B_2^{+2} = 0.57211063837098 \times 10^{0}\ \mathrm{cm}^{-1}$

$B_4^{-4} = -0.49248534597266 \times 10^{-1}\ \mathrm{cm}^{-1}$

$B_4^{-3} = -0.87085879142723 \times 10^{-2}\ \mathrm{cm}^{-1}$

$B_4^{-2} = 0.11628485658577 \times 10^{-1}\ \mathrm{cm}^{-1}$

$B_4^{-1} = -0.35719594970903 \times 10^{-2}\ \mathrm{cm}^{-1}$

$B_4^{0} = -0.15517806889084 \times 10^{-1}\ \mathrm{cm}^{-1}$

$B_4^{+1} = 0.12678095710066 \times 10^{-1}\ \mathrm{cm}^{-1}$

$B_4^{+2} = -0.22716477944588 \times 10^{-2}\ \mathrm{cm}^{-1}$

$B_4^{+3} = 0.22132053611444 \times 10^{0}\ \mathrm{cm}^{-1}$

$B_4^{+4} = -0.46747777586208 \times 10^{-1}\ \mathrm{cm}^{-1}$

$B_6^{-6} = -0.39257413997035 \times 10^{-4}\ \mathrm{cm}^{-1}$

$B_6^{-5} = -0.13374120827760 \times 10^{-4}\ \mathrm{cm}^{-1}$

$B_6^{-4} = 0.31047394293922 \times 10^{-3}\ \mathrm{cm}^{-1}$

$B_6^{-3} = 0.51979956274254 \times 10^{-4}\ \mathrm{cm}^{-1}$

$B_6^{-2} = -0.13557811206257 \times 10^{-3}\ \mathrm{cm}^{-1}$

$B_6^{-1} = 0.90199518979668 \times 10^{-4}\ \mathrm{cm}^{-1}$

$B_6^{0} = 0.26181847432935 \times 10^{-4}\ \mathrm{cm}^{-1}$

$B_6^{+1} = 0.32324346109207 \times 10^{-4}\ \mathrm{cm}^{-1}$

$B_6^{+2} = 0.13813097749326 \times 10^{-4}\ \mathrm{cm}^{-1}$

$B_6^{+3} = -0.67287695580252 \times 10^{-3}\ \mathrm{cm}^{-1}$

$B_6^{+4} = 0.30195804585069 \times 10^{-3}\ \mathrm{cm}^{-1}$

$B_6^{+5} = -0.91205628466852 \times 10^{-4}\ \mathrm{cm}^{-1}$

$B_6^{+6} = 0.65477638537435 \times 10^{-5}\ \mathrm{cm}^{-1}$

Table A.5: The Stevens coefficients of 1-Tb as calculated by MOLCAS using the crystal-structure data. The reference frame is, as specified in the beginning of this section, defined in a "molecular coordinate frame" from the crystal coordinate frame. This set of Stevens coefficients results in a 97.502154 % recovery factor of the crystal-field matrix (with the calculated coefficients up to $k = 12$ producing a recovery factor of 100.000000 %). The VTZP basis set was used for Tb, VDZP for O and N, and VDZ for all other atoms. The lowest-lying 7 septets, 105 quintets, and 112 triplets were considered.

$B_2^{-2} = -0.14676273167657 \times 10^{0}\ \mathrm{cm}^{-1}$

$B_2^{-1} = -0.74363588334734 \times 10^{0}\ \mathrm{cm}^{-1}$

$B_2^{0} = -0.18769334145427 \times 10^{+1}\ \mathrm{cm}^{-1}$

$B_2^{+1} = -0.28697726269892 \times 10^{+1}\ \mathrm{cm}^{-1}$

$B_2^{+2} = -0.90509485598888 \times 10^{0}\ \mathrm{cm}^{-1}$

$B_4^{-4} = -0.12927901606476 \times 10^{-3}\ \mathrm{cm}^{-1}$

$B_4^{-3} = -0.32592057318429 \times 10^{-1}\ \mathrm{cm}^{-1}$

$B_4^{-2} = 0.66404601388390 \times 10^{-2}\ \mathrm{cm}^{-1}$

$B_4^{-1} = 0.11087464702426 \times 10^{-1}\ \mathrm{cm}^{-1}$

$B_4^{0} = 0.46039509831577 \times 10^{-2}\ \mathrm{cm}^{-1}$

$B_4^{+1} = 0.39167914346504 \times 10^{-1}\ \mathrm{cm}^{-1}$

$B_4^{+2} = 0.15669157071111 \times 10^{-1}\ \mathrm{cm}^{-1}$

$B_4^{+3} = -0.17179293611234 \times 10^{-1}\ \mathrm{cm}^{-1}$

$B_4^{+4} = -0.42448135655033 \times 10^{-1}\ \mathrm{cm}^{-1}$

$B_6^{-6} = 0.48095144349877 \times 10^{-4}\ \mathrm{cm}^{-1}$

$B_6^{-5} = 0.23925177858041 \times 10^{-3}\ \mathrm{cm}^{-1}$

$B_6^{-4} = 0.39623950501635 \times 10^{-4}\ \mathrm{cm}^{-1}$

$B_6^{-3} = 0.26369301489216 \times 10^{-3}\ \mathrm{cm}^{-1}$

$B_6^{-2} = -0.64442066869819 \times 10^{-4}\ \mathrm{cm}^{-1}$

$B_6^{-1} = 0.81486532889879 \times 10^{-5}\ \mathrm{cm}^{-1}$

$B_6^{0} = -0.36050878776643 \times 10^{-5}\ \mathrm{cm}^{-1}$

$B_6^{+1} = 0.99386328284964 \times 10^{-4}\ \mathrm{cm}^{-1}$

$B_6^{+2} = 0.18564792460510 \times 10^{-4}\ \mathrm{cm}^{-1}$

$B_6^{+3} = -0.22290047466243 \times 10^{-3}\ \mathrm{cm}^{-1}$

$B_6^{+4} = 0.28540911315305 \times 10^{-3}\ \mathrm{cm}^{-1}$

$B_6^{+5} = 0.13096997874604 \times 10^{-2}\ \mathrm{cm}^{-1}$

$B_6^{+6} = 0.14669504416098 \times 10^{-3}\ \mathrm{cm}^{-1}$

Table A.6: The Stevens coefficients of 1-Dy as calculated by MOLCAS using the crystal-structure data. The reference frame is, as specified in the beginning of this section, defined in a "molecular coordinate frame" from the crystal coordinate frame. This set of Stevens coefficients results in a 98.139189 % recovery factor of the crystal-field matrix (with the calculated coefficients up to $k = 14$ producing a recovery factor of 100.000000 %). The VTZP basis set was used for Dy, VDZP for O and N, and VDZ for all other atoms. The lowest-lying 18 sextets and 99 quartets were considered.

Glossary

ab initio

From the Latin meaning "from the beginning", *ab initio* describes calculations done from first principles, relying only on basic, established laws of nature and no further assumptions or models.

ansatz

From the German word meaning "initial placement of a tool at a work piece", an ansatz is an educated guess or assumption made to help solve a problem. Often, the results of solving the problem verify the validity of the assumption.

antisymmetric

A mathematical property on an operation O that operates on a mathematical object A (such as a function, matrix, or tensor), where performing the operation changes the sign of (negates) the object: $O(A) = -A$. Examples include skew-symmetric matrices, which are antisymmetric on transposition and odd functions, which are antisymmetric on a sign-flip of the function argument.

Born–Oppenheimer

The best-known mathematical approximation in molecular dynamics that assumes that wavefunctions of atomic nuclei and electrons in a molecule can be treated separately since the nuclei are much heavier.

complete-active-space self-consistent field

A particular approach of multi-configurational self-consistent field wherein a particular number of electrons in a particular number of orbitals only are considered in producing a linear combination of configuration state functions.

configuration interaction

A post-Hartree–Fock linear variation method for solving the Schrödinger equation within the Born–Oppenheimer. This method expresses the variational wavefunction as a linear combination of configuration state functions built from spin orbitals, in order to account for electron correlation.

correlation energy

A measure of how much one electron's movement is affected by all other electrons as a result of electron–electron interaction in a quantum system.

crystal-field parameter

A parameter that is part of a set that correspond to operators which are functions of the spin operators. Collectively, they describe the magnetic properties of a system, including its anisotropy and the dependence of its energy levels on an external magnetic field.

density-functional theory

A computational, quantum-mechanical modelling method used in physics to calculate electronic structures of molecules. It uses a choice functional to iteratively converge to some electronic potential, within some acceptable convergence limit.

electron density

The probability distribution of an electron being present at some region of space.

electron paramagnetic resonance

A method of spectroscopy for studying materials that have unpaired electrons. Similarly to nuclear magnetic resonance, the excitation of spins forms the basis of the method, though instead of nuclear spins, the spins are electron spins. The measurement signal arises from electron energies splitting depending on their spin quantum number s in the presence of an external magnetic field, which can then be detected because the energy difference results in interactions with photons when electrons shift between the states corresponding to the split energy levels.

fermion

An indistinguishable particle that follows Fermi–Dirac statistics and obey the Pauli exclusion principle. These include all quarks and leptons, and any particles consisting of an odd number of these, such as baryons. By the spin-statistics theorem, all particles with half-integer spin are fermions, the most notable being the ($1/2$-spin) electron.

full width at half maximum

The width of the distribution at a level that is just half the maximum ordinate of the peak. That is, for some distribution $f(x)$, the value $f_{\max}$ can be defined for which $f(x) \leq f_{\max} \forall x \in \mathbb{R}$. Assuming the distribution increases monotonically to $f_{\max}$ and then decreases monotonically, there will be two values $x_{\leftarrow}$ and $x_{\rightarrow}$(with the latter

greater, without loss of generality) for which $f(x_{\leftrightarrow}) = f_{\max}/2$. The full width at half maximum is then $x_{\rightarrow} - x_{\leftarrow}$.

graphene nanoribbon

Strips with graphene with width less than 100 nm.

Hartree–Fock

Also called the self-consistent field method, this iterative method based on the variational principle finds the Slater determinant of minimal energy.

indistinguishable

A property of certain particles that describes the impossibility of distinguishing them, even in principle. Notable examples include subatomic particles, such as electrons, and their composites, molecules.

Jaynes–Cummings model

A theoretical model in quantum optics, it describes the interaction of a two-level atom with the (usually fundamental) mode of an optical cavity.

multi-configurational self-consistent field

A method in quantum chemistry that combines the self-consistent field and configuration state function methods, to approximate exact electronic wavefunctions of atoms or molecules using linear combinations of configuration state functions.

Pauli exclusion principle

The quantum-mechanical principle stating that two or more fermions cannot occupy the same quantum state within a quantum system simultaneously because of indistinguishability. As a consequence,

any wavefunction must be antisymmetric under exchange of the coordinates of any two electrons.

quantum electrodynamics

While quantum electrodynamics is generally the relativistic quantum field theory of electrodynamics, in the context of this thesis, we are interested specifically in cavity quantum electrodynamics, which is the study of the interaction between light confined in a reflective cavity and matter that interacts with that light. When this interaction is strong, the light and matter is said to be strongly coupled.

quantum tunnelling of the magnetisation

A physical phenomenon where the quantum-mechanical state that describes the magnetisation of a spin system tunnels through an energy barrier.

restricted-active-space self-consistent field

Because of the exponential increase of the computational cost with respect to the number of active orbitals considered, this approach of multi-configurational self-consistent field aims to restrict the number of electrons in certain subspaces. An example is allowing only single and double excitations from a subset of active orbitals.

rotating-wave approximation

An approximation in magnetic resonance wherein terms in a Hamiltonian that oscillate rapidly are neglected. This approximation is valid when the energy of applied electromagnetic radiation is close in energy to that of an atomic transition, if the intensity is low.

Schrödinger equation

A linear partial differential equation that wavefunctions follow in quantum-mechanical systems. This is often separated into time-dependent and time-independent equations, depending on the properties of the system being investigated. The latter governs the evolution of a system's states, and the former governs stationary states.

self-consistent field

See Hartree–Fock.

single-ion magnet

A compound with a single spin centre that is magnetically shielded from its surroundings. In the absence of an applied magnetic field, the magnetisation of their spin centre relaxes slowly.

single-molecule magnet

A compound with metallic centres bearing large spin that is magnetically shielded from its environment by its ligands. Below a certain temperature, single-molecule magnets exhibit superparamagnetic behaviour and magnetic hysteresis. A unique feature is its large anisotropy barrier, through which quantum tunnelling of the magnetisation can occur.

spin-orbital

A one-particle wavefunction taking both position and spin angular momentum of the particle as parameters, usually expressable as a product of a spatial orbital and a spin function. For a single electron, for instance, the complex-valued function may be expressed by the tensor product $\chi(\vec{r}, m_s) = \phi(\vec{r}) \otimes \sigma(m_s)$, where ϕ describes the atomic orbital and σ the electron spinor.

strong coupling

A regime in which interaction between light and matter is high, such that the rate of energy exchange between the molecules and electromagnetic mode far exceeds that of competing dissipative processes.

superconducting quantum-interference device

A very sensitive magnetometer used to measure extremely small magnetic fields, as low as 5×10^{-14} T

superparamagnet

A nanoparticle exhibiting a form of magnetism wherein an external magnetic field is able to magnetise it but the time needed to measure their magnetisation exceeds the typical time it takes for the magnetisation to flip, resulting in an average magnetisation of zero. Its magnetic susceptibility also tends to be very high.

torque magnetometry

An indirect method of magnetic measurement that measures the torque induced on a cantilever by the magnetisation of a sample. It can be more sensitive than superconducting quantum-interference device magnetometry.

variational principle

A principle that allows a problem to be solved using calculus of variations, in order to find functions that optimise quantities that depend on those functions.

wavefunction

A mathematical description of the quantum state of a system, usually expressed as a complex-valued superposition of some basis of quantum states. This complex value is a normalised probability am-

plitude, from which possible results of measurements made on the system (and their probabilities) can be calculated. While the square of the modulus, being a real number, gives a probability density of some measurement of the particle, the imaginary component gives information about its phase.

zero-field splitting

Interaction of the energy levels in a magnetic system from the presence of unpaired spins that results in small energy splits in otherwise degenerate energy levels. When there is no external field, we would expect pairs of $|\pm m_S\rangle$ levels to have the same energy. Because of off-diagonal terms in the Hamiltonian, however, the eigenstates of the system are not pure $|m_S\rangle$ levels but rather admixtures, $\frac{1}{\sqrt{2}}(|m_S\rangle \pm |-m_S\rangle)$. This results in a lifting of the degeneracy whose strength depends on the magnitude of the off-diagonal terms.

Acknowledgements

In the course of the monumental undertaking that is this thesis, innumerable persons have contributed toward its completion. While it is impossible to exhaustively list everyone who has played their part, I should like at least to give my heartfelt thanks to those who have made the most significant contributions.

First, I wish to thank my adviser, Prof. Lapo Bogani for his patient guidance and instruction, understanding, and hospitality throughout my degree. Though Covid was a trying time for all, he was especially encouraging and empathetic about my mental struggles during the initial lockdown, when I foolishly forewent sunlight for months.

I am grateful also to Prof. Nick Chilton, who spent the time to teach me and answer my stupid questions. None of my *ab initio* calculations would have been possible without his help and instruction. Thanks also to Prof. Dieter Jaksch, Martin Kiffner, and Michael Hughes for insightful discussions.

My warm thanks to my coworkers, who provided me with support throughout my thesis. Thanks for the discussions, the help with important forms and deadlines, and even generally for just being there. I will never forget my time spent in this group, even as we move on to our next stages of life. Special thanks to Dimitris and Wenjing for their help with my research, to Federico, Simen, Alessandro, Michael, and Fanmiao for their friendship, and to Michael especially for reading over various parts of my

thesis multiple times.

For faithful Christian friendship in Oxford, in common prayer to almighty God and in common struggle for peace and justice on earth, I thank Jonathan Yeung, Enoch Yiu, and the late Joe Martin; and beyond Oxford, my other brethren in the Holy Order of Saint Stephen First Martyr, and St Stephen himself for his godly example and (I trust) intercession before the throne of God.

For constant support through the years, through setbacks and successes, and hours looking through my unfinished thesis content late at night to improve its clarity of expression, I thank my family, not least my father, Dr K. Y. Tsang, for his advice not only in physics, but also in algorithms.

For her undying love and reverent spirit, I thank my wife Anne, whom God provided as my helper for life in the midst of my studies, and who is already carrying my sweet child.

Most of all, for working all things together for the good of those who love him, I thank the one God, who is ever above and beyond all things, and blessed beyond measure: God the Father, who has made me, and all the world; God the Son, who has redeemed me, and all mankind; and God the Holy Ghost, who sanctifies me, and all the elect people of God. *Soli Deo gloria.*